Universitat Autònoma de Barcelona

INTERFACIAL CHEMISTRY OF CATECHOL-BASED NANOSTRUCTURES

Mireia Guardingo Melian

Ph.D. Thesis

Ph.D. in Chemistry

Supervisors: Dr. Daniel Ruiz Molina

Dr. Félix Busqué Sánchez

Departament de Química

Facultat de Ciències

2015

Memòria presentada per aspirar al Grau de Doctor per Mireia Guardingo Melian.

Mireia Guardingo Melian

Vist i plau:

Dr. Daniel Ruiz Molina

Dr. Félix Busqué Sánchez

Bellaterra, 1 de Setembre de 2015

Abstract

Catechols are aromatic derivatives present in a variety of environments in nature. Due to their broad physicochemical versatility, they play pivotal roles in multiple natural processes. Probably their most popular appearance is in the adhesive proteins of mussels in the form of the rare aminoacid L-DOPA, which is considered to be essential for the strong adhesion of mussels to surfaces under high humidity conditions. This phenomenon has fascinated scientists for decades and intensive research has been carried out in order to understand and mimic these systems. Furthermore, other chemical properties of catechols, such as their metal-chelating and redox behaviour have also been addressed for both fundamental understanding and practical application.

In this thesis we were interested in the obtention of nanoscale catechol-based systems and the study of their properties. For that, a multidisciplinary work was carried out which included the synthesis of new organic compounds, the preparation of nanostructures and the use of advanced microscopies and lithographic techniques.

The role of packing density and orientation of catechol moieties in the interfacial properties of catechol-terminated SAMs was studied at the local scale using an AFM tip or, alternatively, magnetic nanoparticles. The influence that the presence of the catechol ring has on the formation and final structure of SAMs was also addressed. On the other hand, the synthesis of catechol-based polymers in confined volumes was performed using direct-write AFM-assisted lithography. Polydopamine and coordination polymer particles were fabricated directly on surfaces by controlled delivery of their molecular precursors in the shape of femtolitre-sized droplets. With that, we demonstrated the viability of using this technique to place functional amorphous materials on specific areas of surfaces.

The results reported in this thesis have partially been described in the following publications:

"Bioinspired Catechol-Terminated Self-Assembled Monolayers with Enhanced Adhesion Properties." Mireia Guardingo, Elena Bellido, Rosa Miralles-Llumà, Jordi Faraudo, Josep Sedó, Sergio Tatay, Albert Verdaguer, Felix Busqué and Daniel Ruiz-Molina. *Small* **2014**, *10,* 1594–1602. doi:10.1002/smll.201302406.

"Synthesis of Polydopamine at the Femtoliter Scale and Confined Fabrication of Ag Nanoparticles on Surfaces." Mireia Guardingo, Maria José Esplandiu and Daniel Ruiz-Molina. *Chem. Commun.* **2014**, 12548–51. doi:10.1039/c4cc02500h.

"Design and Synthesis of a Non Innocent Multitopic Catechol and Pyridine Mixed Ligand: Nanoscale Polymers and Valence Tautomerism." Mireia Guardingo, Félix Busqué, Fernando Novio and Daniel Ruiz-Molina. *Inorg. Chem.* **2015**, *54*, 6776–6781. doi:10.1021/acs.inorgchem.5b00598.

"Synthesis of nanoscale coordination polymers confined in femtolitre reactors on surfaces" Mireia Guardingo, Pablo González-Monje, Fernando Novio, Elena Bellido, Felix Busqué, Gábor Molnár, Azzedine Bousseksou, Daniel Ruiz-Molina. (Submitted)

Abbreviations

μB	Bohr magneton
μeff	Magnetic moment
ACN	Acetonitrile
AcOEt	Ethyl acetate
AFM	Atomic Force Microscopy
AgNP(s)	Silver Nanoparticle(s)
ATR	Attenuated Total Reflection
AuNP(s)	Gold Nanoparticle(s)
B.E.	Binding Energy
bix	1,4-bis(imidazole-1-ylmethyl)benzene
BTC	1,3,5-benzenetricarboxylate
C.A.	Contact Angle
Co-bipy	$[Co(CH_3COO)_2(\mu\text{-}4,4'\text{-bipy})]$
CP	Coordination Polymer
CPP(s)	Coordination Polymer Particle(s)
DDT	Dodecanethiol
DMF	N,N-dimethylformamide
DMSO	Dimethyl sulfoxide
DOPA	3,4-dihydroxyphenylalanine
DPN®	Dip-Pen Nanolithography
DTBCat/ DTBSQ	3,5-di-tert-butyl-o-catechol/semiquinone
EDX	Energy-dispersive X-ray spectroscopy
EPR	Electron Paramagnetic Ressonance
ESI	Electrospray ionization
Et_2O	Diethylether
EtOH	Ethanol
Fadh	Force of adhesion
F-d	Force-distance (curve)
FE-SEM	Field Emission-Scannin Electron Microscopy
GA-IR	Grazing Angle-Infrared
HMDS	bis(trimethylsilyl)amide (hexamethyldisilazane)
HRMS	High Resolution Mass Spectrometry
HT	Hexanethiol
LFM	Lateral Force Microscopy
ls-/hs-	low spin/high spin
MD	Molecular Dynamics
Mefp/ Mfp	Mytilus edulis foot protein/Mussel foot protein
MeOH	Methanol
MHA	Mercaptohexadecanoic acid
Mp	Melting point
MPL	Microfluidic Pen Lithography
NMR	Nuclear Magnetic Resonance
ODT	Octadecanethiol
OMOM	Methoxymethyl ether
PCC	Pyridinium Chlorochromate
PDA	Polydopamine
PM-IRRAS	Polarization Modulation-Infrared Reflection Absorption Spectroscopy
POM	Polyoxometalate
PPL	Polymer Pen Lithography
PVD	Physical Vapour Deposition
pyz	Pyrazine
R.H.	Relative Humidity
rms	Root mean square
rt	Room Temperature
S	Spin quantum number
SAM	Self-assembled monolayer
SE	Spectroscopic Ellipsometry
SFA	Surface Forces Apparatus
Si/ SiO_2	Silicon bearing a native layer of silicon oxide
SPBCL	Scanning Probe Block Copolymer Lithography
SPL	Scanning Probe Lithography
SPR/ SPB	Surface Plasmon Resonance/Surface Plasmon Band
STEM	Scanning Transmision Electron Microscopy
STM	Scanning Tunneling Microscopy
TBDPS	tert-Butyldiphenylsilyl
TEM	Transmission Electron Microscopy

TGA	Thermogravimetric Analysis
THF	Tetrahydrofuran
TLC	Thin Layer Chromatography
TOA	Take-off angle
TOAB	Tetraoctylammonium bromide
VT	Valence Tautomerism
XPS	X-Ray Photoelectron Spectroscopy

Table of Contents

Chapter 1

Introduction

Catechols (*o*-dihydroxybenzene) are aromatic derivatives featuring two neighbouring (*ortho*-) hydroxyl groups that can be found in a surprisingly wide variety of environments in nature due to their physicochemical versatility. Although the catechol is an apparently simple moiety, its chemistry is more complex and challenging than it could be initially expected. Catechols are able to act as weak acids and establish reversible equilibria between their reduced and oxidized forms. On the other hand, the presence of two hydroxyl groups in vicinal positions makes this moiety ideal for bidentate coordination and hydrogen bonding either to metal ions, surfaces or other organic functional groups. According with such range of functionalities, naturally occurring catechols perform a variety of functions and can exist either as simple molecular systems, forming part of supramolecular structures, coordinated to different metal ions or as macromolecules.[1] For example, catecholamine neurotransmitters like dopamine, adrenaline or noradrenaline occupy key positions in the regulation of physiological processes and the development of neurological, psychiatric, endocrine and cardiovascular diseases.[2] Dopamine influences in motivational and motor functions[3] and its re-uptake process is related to depression and attention-deficit disorders.[4] The secretion of adrenaline is motivated by stress to initiate physiological and behavioural responses to it (fight or flight).[5] Catechols may also serve protective purposes; 3-n-alkylcatechols are secreted by poison ivy and cause severe contact dermatitis to humans.[6] The health benefits of dietary polyphenolics present in wine, tea, chocolate, fruits and vegetables are related to their antioxidant properties, which reduce the risk of chronic and degenerative diseases.[7,8] They have a direct influence on the colour, flavour and astringency (tannin content) of red wine[9] and the cardioprotective effect of moderate consumption of this beverage has been associated to the presence of polyphenols.[10] Some examples of these natural catechol derivatives are shown in Figure 1.1. Next, a detailed description of the chemical properties of the catechol moiety is provided taking both natural and synthetic catechol derivatives as representative examples.

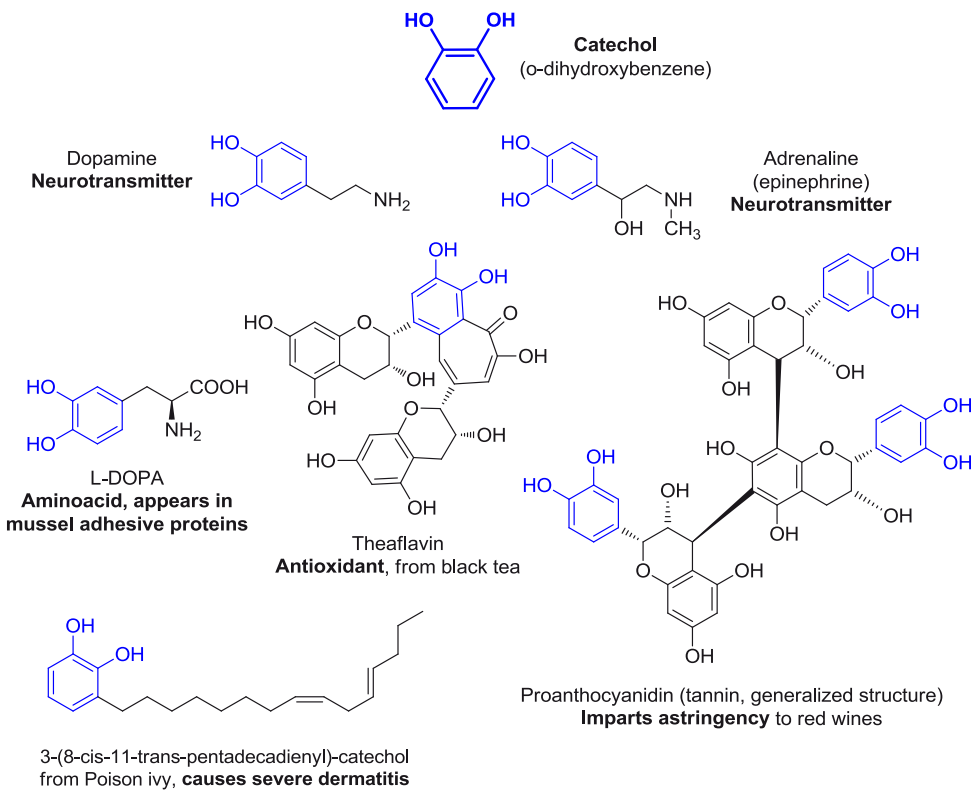

Figure 1.1 Chemical structures of a variety of natural catechol derivatives with different activities and functions.

1.1 Physicochemical properties of catechol derivatives and their role in natural processes

1.1.1 Redox activity and cross-linking

Catechol moieties may exist in three oxidation states: the fully reduced catechol form, the semi-oxidized state called semiquinone and the completely oxidized form, or quinone. (Scheme 1.1) In the presence of oxygen, the oxidation of catechol can occur spontaneously even under mild acidic conditions to give the corresponding semiquinone through a one-electron transfer and the quinone by a two electron process. Quinones are strong electrophiles and can react with nucleophilic moieties such as amines or thiols through reductive addition and Michael-type reactions[11,12] (Scheme 1.1A) or give place to aryl-aryl bonds occurring through radical coupling (Scheme 1.1B).[13,14] In addition, under certain

conditions, tautomeric forms of the quinone may be more stable than their precursor (Scheme 1.1C).[15] Catechols (and phenols in general) have very low ionization potentials and can homolitically release a hydrogen atom (H·) or transfer a single electron to another radicalary species forming a stable catechol radical (Scheme 1.1D). This ability provides polyphenols, especially those containing catechol groups, highly appreciated antioxidant and radical scavenging activity.[7]

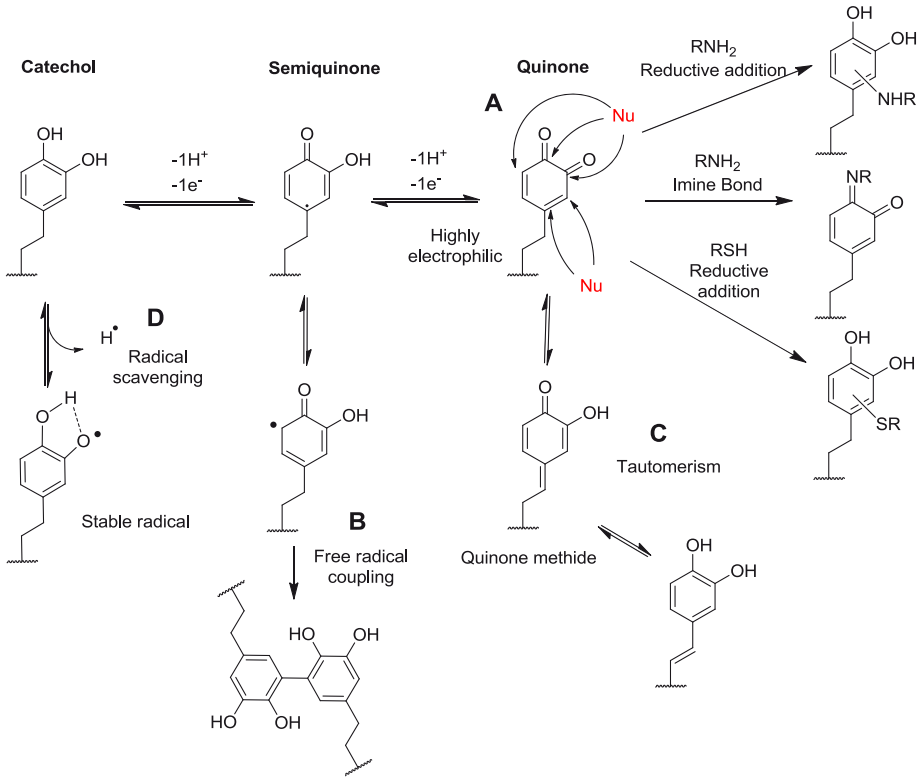

Scheme 1.1 Redox activity and reactivity of the catechol group.

An excellent natural example of the complex redox character of the catechol group is the melanin family. Melanin is a generic term englobing a variety of biopolymers found widespread in nature as pigments, including those from skin, eyes, feathers or the sepia ink. They were long thought of as photoprotectors; however, their presence in other parts of organisms that are not exposed to light, such as the *substantia nigra* of the brain, suggests other functions.[16] The most studied type of melanin is eumelanin which is known to be a product of the oxidative polymerization of 5,6-dihydroxyindole and 5,6-dihydroxyindole-2-carboxylic acid.[17] The first stages of melanogenesis involve several oxidations, reductive additions and tautomerizations that are in some cases enzymatically controlled and lead to

the obtention of the two monomers (Scheme 1.2).[18–20] Little is known about the following polymerization steps though studies with synthetic eumelanin analogs suggest the formation of planar dimers, trimers and tetramers that stack together to form a highly insoluble black-brown material.[17]

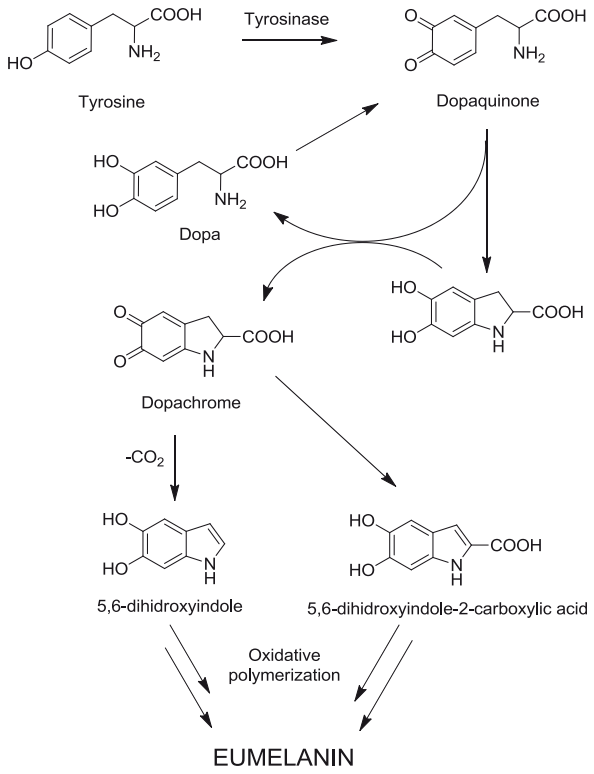

Scheme 1.2 First steps of the oxidation of tyrosine (catalyzed by tyrosinase) to give 5,6-dihydroxyindole and 5,6-dihydroxyindole-2-carboxylic acid, the monomers of eumelanin. Reproduced from ref. 17.

Melanins display a broad range of particularly intriguing physicochemical properties such as broad-band UV-Vis absorption, non-radiative conversion of photo-excited electronic states and electrical conductivity and switching properties. The observation of such a broad range of properties supports the "chemical disorder" model, according to which eumelanin would consist of an ensemble of multiple species comprising completely reduced catecholic moieties together with their oxidation products and their tautomers including radical semiquinone moieties.[1,16] Synthetic melanin analogs have been recently pointed out as promising multifunctional materials; however control over their aggregation state is a key issue for their development.[17]

1.1.2 Metal-coordination

The presence of two hydroxyl groups in the *ortho-* positions provides a strong metal-chelating character to the catechol moiety, being Fe^{3+} the greatest example.[21,22] For instance, melanins can act as metal reservoirs and scavenging agents and are able to strongly coordinate Mg^{2+}, Ca^{2+}, Zn^{2+} and heavy metals *in vivo*.[23,24] In fact, the increase of free Fe^{3+} in neuromelanin has been linked to the pathogenesis of the Parkinson's disease.[25,26] Other powerful chelating agents known as siderophores, are essential for the regulation of Fe^{3+} levels inside the organisms. Enterobactin is the strongest natural siderophore known to date and consists of a tripodal catecholic structure that provides strong octahedral coordination to the metal centre (Figure 1.2).[27] Artificial siderophores inspired by enterobactin and other natural siderophores have been used to treat iron poisoning and for *in vivo* radioisotope decontamination.[28,29]

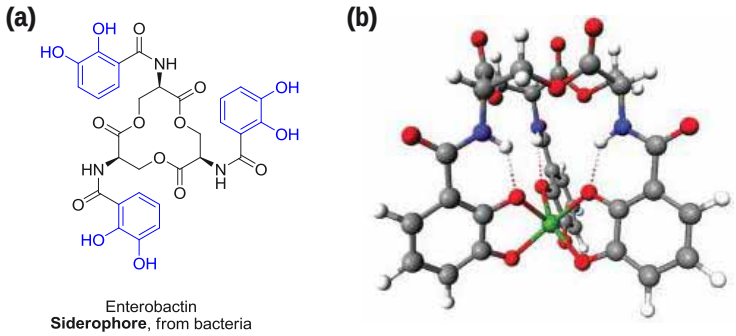

Figure 1.2 (a) Structure of enterobactin. (b) Structure of the Fe-enterobactin triscatecholate complex. Reproduced from ref. 27.

The special redox behaviour of catechol moieties that we have previously pointed out is maintained once they are coordinated to metal ions, which has caused their classification as non-innocent ligands. In transition metal complexes, catechols can be found either as dianions (Cat^{2-}) or radical semiquinones ($SQ^{\cdot-}$). If the coordinated metal ion exhibits more than one stable oxidation state, an intramolecular electron transfer between the ligand and the metal can be induced by different external stimuli, and thus the internal electronic distribution can be modulated.[30] More details on this phenomenon, known as valence tautomerism, are provided Section 1.3. The study of this family of complexes is relevant in molecular electronics but also in biological systems containing complexes bearing non-innocent ligands.[1]

1.1.3 Adhesive properties

The strong underwater adhesion shown by some catechol-containing natural materials has attracted increasing attention during the last decade and has become a source of inspiration for novel synthetic materials. Several marine organisms, like mussels and sandcastle worms[31,32] secrete proteinaceous substances that contain high concentrations of the catecholic aminoacid 3,4-dihydroxyphenyl-L-alanine (L-DOPA), which has been directly associated to their strong adhesion to virtually any substrate.[33]

The role of the DOPA moiety in natural adhesives is two-fold: on one hand it serves as anchor as it can chemisorb onto surfaces by different mechanisms such as metal bidentate coordination[34,35] or hydrogen bonding.[33,36] Also, the oxidized DOPA-quinone form is formed readily at seawater pH (~8.5) and can act as a covalent cross-linker (as detailed above) providing cohesion to the adhesive.[14,37,38] Other physicochemical mechanisms such as the geometry of the adhesive pads,[39] the tautomeric equilibrium with the protein backbone[15] and the presence of metal ions[40–42] or other amino acid residues in the proteins may also contribute to the overall adhesion.[43,44] A more detailed revision of the adhesive interactions measured for mussel adhesive proteins and synthetic analogs is provided in Section 4.1 of this thesis.

Many examples of synthetic catechol-based polymers with adhesive properties have been described in the last decade.[12,45] The main conclusions that can be extracted from those studies agree with the observations made in mussel adhesion: both the catechol content and degree of cross-linking are determinant factors of the adhesive strength. Although high shear strengths have been measured in synthetic mussel-inspired adhesives,[46–48] the underwater adhesive system of mussels is still unrivalled by any synthetic polymer or composite.

In the last years, an important part of the research carried out in our group has involved catechol derivatives. Our efforts have been focused on the formation of functional coatings (adhesives) based on polymeric materials derived from catechol compounds and on the synthesis and study of switchable valence tautomeric systems, where the redox and metal-chelating properties of catechols combine to obtain stimuli-responsive materials. In the following sections we provide a detailed description of the adhesive system of mussels and a revision of reported synthetic bio-inspired adhesives. Also, we describe the valence tautomeric interconversion phenomenon and the work performed in our group using these systems.

1.2 Catechol-based adhesives and coatings

1.2.1 Mussel adhesive proteins: the finest control of catechol chemistry

The adhesive system of mussels is a fascinating example of how nature is able to build architectures that flawlessly perform a specific function. Catechols are an essential moiety in the adhesive proteins of mussels and their chemical properties are perfectly combined and controlled in the mussel *byssus* in order to maximize its performance. The *Mytilus edulis* (blue mussel) is the most studied species of mussel and the proteins that compose its adhesive pad are often called mefps (from *Mytitlus edulis* foot protein) or just mfps (mussel foot proteins).

The collection of threads that connect a mussel to a substrate is called the *byssus*. The threads are formed by collagenous microfibers that extend into the adhesive plaque, which is composed of a proteinaceous solid foam. A cuticle covers both the threads and the adhesive pad and protects them from abrasion (Figure 1.3a).[49] The proteins forming the adhesive plaque are secreted by the "phenol gland" and all of them contain repeated sequence motifs and DOPA residues in different percentages. Mfp-3 (with its two variants, fast and slow) and mfp-5 are the proteins with higher DOPA content (between 10 and 30% DOPA), and are located at the substrate interface with mfp-6 over or mixed with them. On top, and representing much of the plaque bulk are mfp-3 (slow) and mfp-2. Finally, approaching the fibres that form the thread are mfp-4 and the thread matrix proteins (tmps). Mfp-1 is located at the outer part of the adhesive pad and the thread, forming the cuticle (Figure 1.3b).[50]

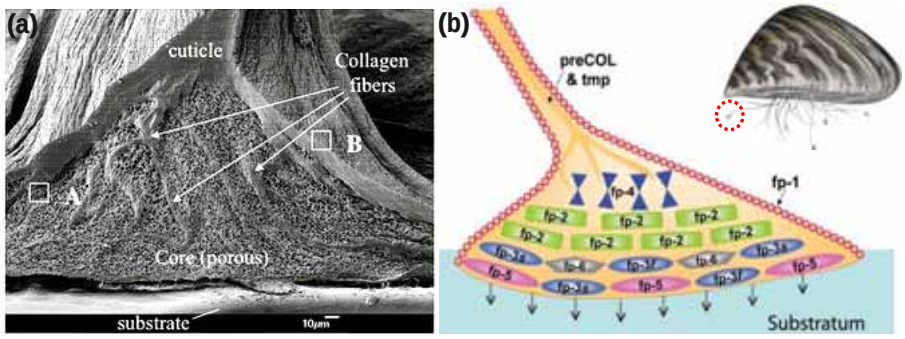

Figure 1.3 (a) Solid foam structure of a byssal adhesive plaque. (b) Approximate distribution of the known plaque proteins in relation to the substratum. Dopa-containing proteins nearest the interface with the substratum are mfp-3 (fast and slow), mfp-5 and mfp-6. Reproduced from ref. 49 and ref. 50.

It has been seen in both adhesive proteins and synthetic protein analogs that the adhesion strength relies on a fragile equilibrium between the interfacial interaction attributed to catechol moieties and internal cohesiveness, associated to quinone formation and

subsequent covalent cross-linking. In that way, absence of oxidation leads to cohesive failure whilst excess quinone formation results in interfacial failure. Exactly how mussels balance these mutually competing needs is still under debate.[51] We do know however, that mussels are able to regulate the conditions in the surrounding microenvironment during plaque formation in order to control the oxidation of the proteins.[50] Also, the non-adhesive protein mfp-6, that mussels produce together with mfp-3 and mfp-5, is rich in cysteine (-SH) residues (11%) which can act as reducing agents to restore oxidized DOPA, either by reductive addition to the aromatic ring or by oxidation to disulfide (Figure 1.4a).[50,52] Thus, by making slight changes in solution conditions and mfp-6, mfp-3 and mfp-5 concentration; mussels can control the environment in which the plaques are formed to precisely regulate byssal adhesion.

Mussels also take profit from the metal-chelating abilities of the catechol group. Adhesion measurements have repeatedly shown that the presence of Fe^{3+} contributes to the cohesion of the adhesive proteins and even proteins that are not adhesive by themselves, such as mfp-2, show strong metal-mediated interactions.[40,41] Catechol-metal complexation is specially important in the cuticle, which is comprised of granular structures dispersed in a protein matrix (Figure 1.4b). The localization of high densities of Fe^{3+}-triscatecholate complexes inside the granules increases the hardness and resistance to failure of the byssus.[53,54]

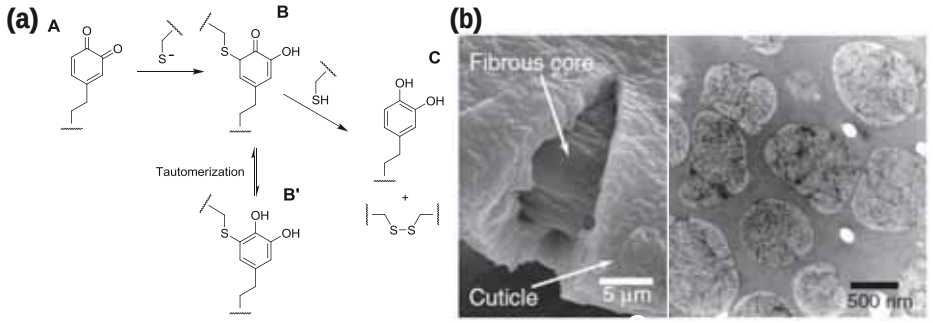

Figure 1.4 (a) Proposed reaction mechanism for the reduction of quinone by thiolates. (A) The first thiolate attacks the DOPA-quinone in a Michael reaction. (B) The C-S bond is prone to further attack by a second thiolate. (C) The leaving S tranfers an electron pair to the aromatic ring regenerating the reduced form of DOPA and forming a disulfide. (B') The thio-quinone intermediate (structure B) is related by tautomerization with structure B'. (b) Structure of the cuticle that covers the byssal threads. Left: Strain-induced rupture of the cuticle showing the fibrous interior in an SEM image. Right: TEM image of the cuticle showing the granular microstructure in an osmium-stained cuticle. Reproduced from ref. 50 and 53.

Summing up, catechol groups are essential for the strong adhesion of mussels to surfaces, as they not only mediate the interaction with the underlying substrate but also control the mechanical properties of the holdfast. However, it is important to note that

several posttranslational modifications other than DOPA are present in the adhesive proteins. The contribution of such modifications to adhesion is not clear but surely exists.[49] Hence, DOPA is unarguably an adhesive residue but not the only one.

Biomimetics seeks to replicate natural adhesives for technological applications, a task that has proved to be difficult. In the following section we provide the reader with examples of mussel-mimetic adhesives and coatings, with special attention to the well-known polydopamine.

1.2.2 Synthetic mussel-inspired coatings and adhesives

Polydopamine (PDA) is currently the most popular catechol-based material among the scientific community and has emerged as a virtually universal adhesive and primer. The synthesis and deposition of PDA was first described in 2007. In their pioneering work Messersmith and co-workers described the in-situ deposition of PDA on a variety of substrates just by immersion in a basic solution of dopamine. This procedure led to the precipitation of a black-brown solid and the deposition of a polymeric film on the surface.[55] Other methodologies to obtain PDA coatings have appeared since then, including enzymatic oxidation[56] and electrodeposition,[57] however the solution oxidation method is the most commonly used. Both the conditions in which the reaction is performed and the characteristics of the final material are clearly related to those of the melanin biopolymers described in Section 1.1.1 of this thesis, therefore PDA shares many properties with natural melanins.[58,59]

The polymerization process and final structure of polydopamine are nowadays still unclear. Initially, PDA was considered a classical polymer of high molecular weight, although this structure was never verified experimentally.[58,60] Later on, a completely opposite model suggested that PDA was an aggregate of monomeric units of 5,6-dihydroxyindoline and its quinone derivative held together by charge transfer, π-stacking and H-bonding interactions.[61] The more recent studies seem to go all in the same direction and agree on polydopamine consisting in an agglomeration of oligomers of different lengths, oxidation and unsaturation degrees held together by non-covalent interactions, a similar structure to that accepted for eumelanin.[62,63] D'Ischia and co-workers further affirmed that the final structure and properties of PDA were dependent on the synthetic conditions and observed the presence of pyrrolecarboxylic acid moieties, typical of the eumelanin structure,

in the final material (Figure 1.5).[64,65] Even though several groups have worked towards the elucidation of the PDA structure, it is still unkown.

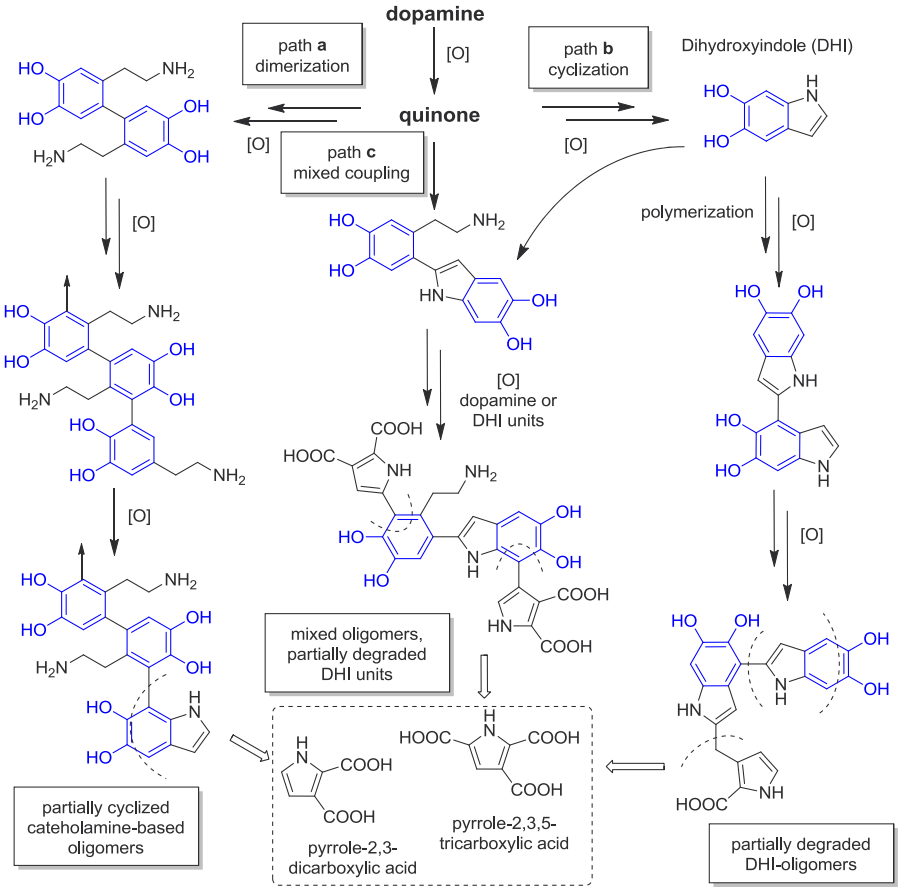

Figure 1.5 Competitive reaction pathways occurring during the synthesis of PDA as described by d'Ischia and co-workers. Reproduced from ref. 64.

The chemical diversity in PDA accounts for a wide variety of chemical properties. As already demonstrated in the initial report on PDA,[55] nucleophiles such as thiols or amines can react with the quinone units in PDA through Schiff base and Michael-type addition reactions. Thus, PDA coatings have been used as universal primers for surface modification and particularly appreciated for the immobilization of biomolecules as an alternative to other less efficient methodologies.[66,67] PDA also shows adhesive properties; although it does not have a specially interesting behaviour as a bulk glue,[68,69] it shows good performance when it comes to immobilizing and coating small objects. Nanoparticles and cells have been directly grafted onto PDA-coated surfaces showing good biocompatibility.[70–72] Finally, PDA

behaves as a strong metal-chelating and reducing agent, being able to reduce metal ions to their zero-valent state and form metal nanoparticles.[73] This property has been exploited to create anti-bacterial coatings and conducive nanomaterials by in situ synthesis and deposition of silver nanoparticles[74–77] or to obtain PDA-coated graphene sheets through reduction of graphene oxide.[78] Many other examples of the use of polydopamine either as a coating or as a dispersed colloid can be found in the literature and have been extensively reviewed.[1,58,59]

Although PDA is clearly the most studied and applied system, many other catechol-based materials have been described in the last years ranging from coatings and adhesives[1,12] to gels[79] or catechol-anchored monolayers.[80–82] Our group synthesized several alkyl-catechols and catechols modified with a fluorinated chain that were used to obtain coatings that inferred oleo-/hydrophobic character to a variety of materials (the synthesis of these compounds is described in Section 3.1.1).[83–85] Robust coatings were obtained by polymerization of the catechol monomers in similar conditions to those used for the formation of PDA coatings. The exposure of heptadecylcatechol **1** and **2** to ammonia under aerobic conditions afforded a dark brown powder that could be re-dissolved in selected organic solvents and used to coat different materials such as glass, cotton or polyester, turning them oleo-/hydrophobic (Figure 1.6).[84] Other alkylcatechols bearing shorter aliphatic chains provided less hydrophobic character. Additionally, the coated materials could be used for water/oil separation.[83]

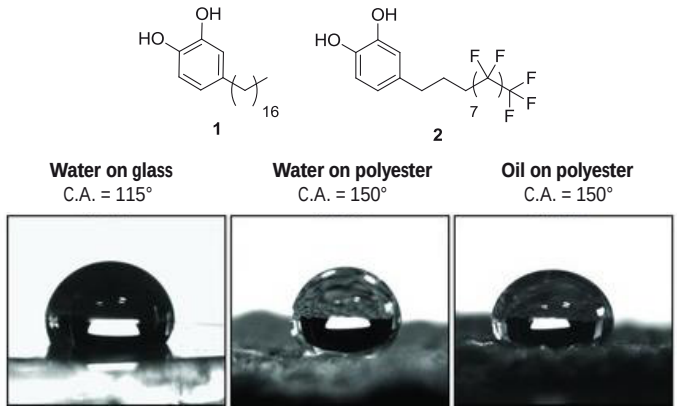

Figure 1.6 (a) Structure of compounds **1** and **2**. (b) Contact angles obtained with different liquids on a variety of substrates coated with the polymerization product of the fluorinated alkylcatechol **2**. Reproduced from ref. 84.

The approach used in our group consisted in inducing the polymerization of functional catechol derivatives to synthesize macromolecular compounds that were able to coat

multiple surfaces and provide functionality. Alternatively, polymeric chains[86] or dendrimers[87] functionalized with pendant catechol groups have been used to obtain catechol-based coatings showing good adhesion to substrates. By using this strategy, functionalizable platforms[88] or antifouling[89,90] and anticorrosive coatings[91] have been prepared.

Adhesive materials based on catechol-modified polymeric structures such as polypeptides,[92] block copolymers[93] or DOPA-ended polymers[94,95] have also been described in multiple reports in the last decade. As an example, biomimetic modification of chitosan afforded an adhesive hydrogel that resisted high shear strengths under water.[96] Also, Wilker and co-workers designed a cationic mussel mimetic adhesive that showed higher adhesion than selected commercial glues under water.[46] Catechol-based adhesives have also shown excellent *in vivo* performance and strong adhesion to wet mucoses and tissues.[97] Interestingly, materials showing strong reversible adhesion were obtained by combining catechol-containing polymers with nanostructured surfaces.[98–100]

1.3 Catechols as redox-active ligands in valence-tautomeric complexes and polymers

Catechols have long been known as electro- and redox-active units and, as already mentioned in Section 1.1.2, their participation in intramolecular electron transfer processes has caused their classification as non-innocent ligands.

Valence tautomeric (VT) complexes that combine redox-active ligands and transition metal ions are known to exhibit two nearly degenerated electronic states with localized electronic structures (Figure 1.7a). The charge distribution in such electronic isomers has an appreciable sensitivity to the environment so an external perturbation like photons, temperature, pressure or pH; may lead to an intramolecular electron transfer between the metal centre and the redox-active ligand and therefore to a reversible interconversion between the two degenerated electronic states in an entropy-driven process.[101,102] Since each electronic isomer exhibits different optical, electronic and/or magnetic properties, these complexes have been suggested as candidates for future use in molecular electronic devices and switches.[30,103]

Most of the VT complexes thus far reported are monomeric and dimeric cobalt complexes containing quinone or quinone-type ligands (catechols), although other ligands such as Schiff-base and phenoxyl radicals have been used.[104–106] When coordinated to the metal centre, the ligands may be present as semiquinone ($SQ^{\cdot}$) or catecholate (Cat^{2-}) moieties and can interconvert between the two forms in response to an external stimulus (e.g. temperature). At the same time, the oxidation state of the metal switches between the *ls*-Co^{III} and the *hs*-Co^{II} isomers (Figure 1.7b).[107] The equilibrium between the two isomers can be monitored by magnetic measurements and spectroscopic techniques such as UV/Vis, NMR and/or EPR spectroscopy.

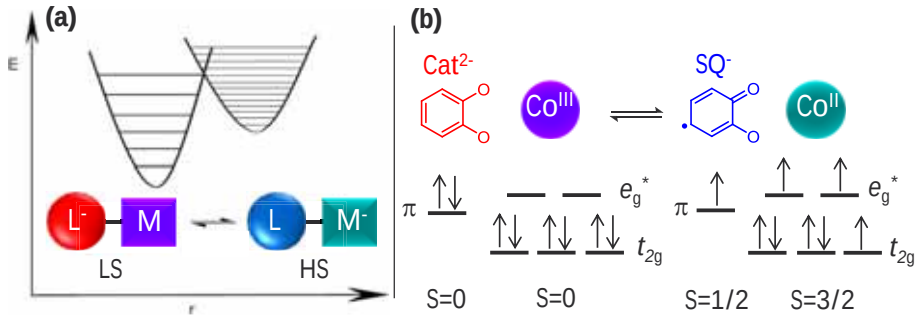

Figure 1.7 (a) Schematic representation of valence tautomerism involving a redox-active ligand and a transition metal ion together with the corresponding potential energy curve plotted as a function of the nuclear coordinate. (b) Representation of the orbital occupancy, both metal and ligand based, of the two different tautomeric forms of a Co-*o*-quinone VT complex. Reproduced from ref. 30 and ref. 103.

The first reported example of a valence tautomeric complex was the cobalt-bis(quinone) complex [Co^{III}(3,5-DTBCat)(3,5-DTBSQ)(bpy)], where 3,5-DTBCat^{2-} stands for the catecholate form of 3,5-di-*tert*-butyl-*o*-quinone, 3,5-DTBSQ$^{\cdot}$ for its semiquinone form and bpy is the 2,2'-bipyridine (Figure 1.8a).[108] Using UV-Vis spectroscopy, the temperature-dependent VT behaviour of a solution of this complex in toluene was monitored (Figure 1.8b). At low temperatures, a band at ~600 nm wavelength was observed, corresponding to the *ls*-Co^{III} tautomer. With increasing temperature, the intramolecular electron transfer occurred and the Cat^{2-} ligand oxidized to the $SQ^{\cdot}$, transferring one electron to the *ls*-Co^{III} metallic centre, which converted into the *hs*-Co^{II} isomer. This translated into the UV-Vis spectrum through the appearance of a characteristic band at ~700 nm, corresponding to the *hs*-Co^{II} tautomer.[103] The electron transfer was also accompanied by changes in the magnetic properties of the complex, which were followed by recording the magnetic susceptibility of the VT complex at different temperatures (Figure 1.8c). At low temperatures the magnetic moment value agreed with the predominant *ls*-Co^{II} isomer, which has an S=1/2 ground state (coming from the unpaired electron of the $SQ^{\cdot}$ ligand), whereas the appearance of the

hs-Co^{II} isomer at higher temperatures caused an increase in the magnetic moment in agreement with the S=3/2+2×1/2 ground state (1 unpaired electron from each of the $SQ^{\cdot}$ ligands and 3 from the metal centre).[101,108]

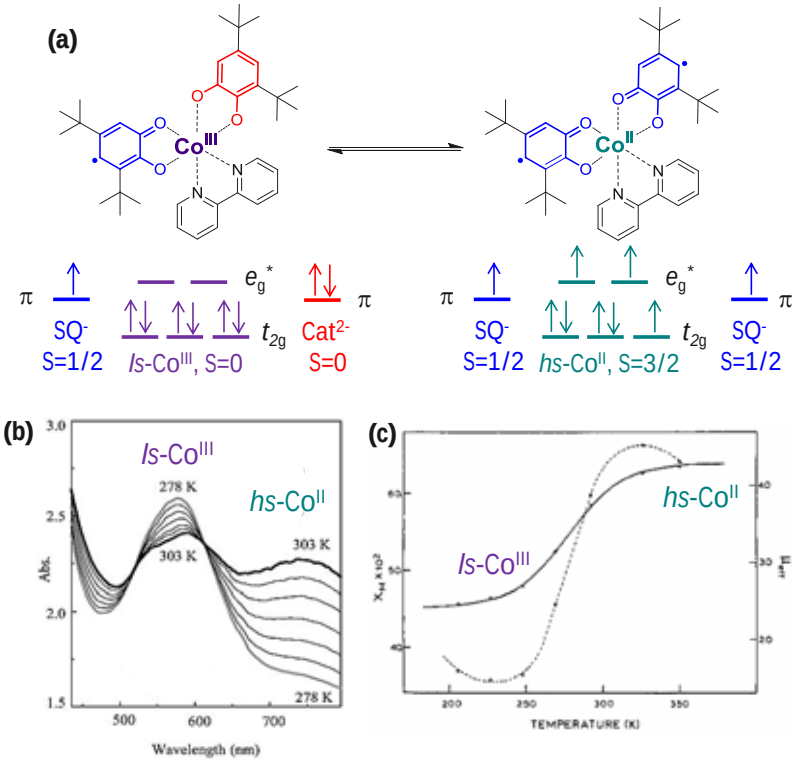

Figure 1.8 (a) VT equilibrium of the [Co^{III}(3,5-DTBCat)(3,5-DTBSQ)(bpy)] complex showing the molecular orbitals involved and the electronic distribution of each one of the VT isomers. (b) Temperature-dependent UV-Vis spectra of the same complex in CH_2Cl_2 showing the variation in absorption associated to the VT process. (c) Magnetic susceptibility (dotted line) and effective magnetic moment of a toluene-d_8 solution of the complex in (a) plotted as a function of temperature. Reproduced from ref. 103 and ref. 108.

Since this pioneering work, multiple VT complexes have been reported and several factors[30] such as the nature of the counterligands,[109] steric hinderance,[110] or the partial oxidation or reduction of the complex[111] proved to have an important effect in the VT properties. Additionally, the matrix and the environment surrounding the system have unpredictable effects on the VT behaviour, which represents a real challenge for the application of VT materials.[112,113]

One of the first advances made towards the synthesis of nanomaterials showing VT behaviour was reported by our group in 2008, when the formation of valence-tautomeric coordination polymer particles (VT-CPP) was described. Coordination polymers (CPs) are a

class of solids obtained through the association of metal ions and multitopic organic ligands [114–116] that, due to their synthetic flexibility, are considered excellent candidates for the fabrication of functional materials (Figure 1.9a). In our case, spherical nanoparticles of the [Co^{III}(3,5-DTBCat)(3,5-DTBSQ)(bix)] coordination polymer, where bix stands for the ditopic flexible ligand 1,4-bis(imidazole-1-ylmethyl)benzene were obtained after mixing both ligands and the metal salt in EtOH and inducing a fast precipitation of the solid by addition of water(Figure 1.9b, c).[117] Variable-temperature magnetization studies of the nanoparticles revealed an incomplete VT transition with gradual conversion, as commonly seen for non-crystalline phases.[118]

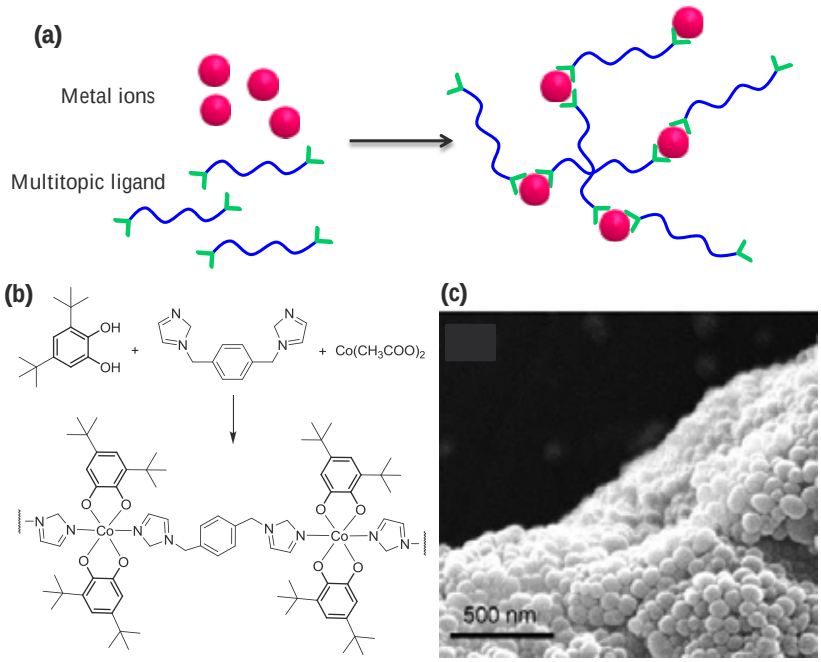

Figure 1.9 (a) Schematic representation of the synthesis of a coordination polymer. (b) Coordination polymerization reaction used to obtain VT-CPPs. (c) SEM image of the obtained particles. Reproduced from ref. 117.

Since then, other examples of VT-CPs have been reported and studied by ourselves and others with the aim of determining the key factors affecting the VT behaviour of this novel class of materials.[119–124] For example, the VT transition of the [Co^{III}(3,5-DTBCat)(3,5-DTBSQ)(4,4'-bipy)] polymer proved to be highly dependent on its crystalline phase but unaffected by changes in particle size and morphology.[125] Also, the use of bis-catechol ligands with pH-sensitive bonds, allowed to obtain pH-sensitive amorphous CPPs with ligand-centered responses.[126]

In any case, one of the most important challenges regarding these materials is to find strategies that make it possible to fabricate VT-based micro-/nano-devices working at room temperature. For that, it is necessary to develop methodologies to integrate these switchable materials on surface in a way that the resulting assemblies are robust enough to be handled without compromising their functionality. With this end, our group has explored several approaches such as the use of polymeric matrices to embed VT compounds,[127] the encapsulation of VT complexes in liquid-filled polymeric capsules[128,129] or the covalent anchoring of VT-CPPs by amide coupling through their surface functionalities.[130] Although great improvements have been made in this direction, much research is still needed in order to establish universal and scalable methodologies that allow the direct integration of VT switching materials on surfaces.

1.4 Scope of the thesis

Considering the different topics reviewed here, this thesis was directed to face two main challenges directly related with the research carried out in our group.

The first one consists in the design and synthesis of a simplified model to study the interaction of catechol moieties positioned at a solid interface. As detailed above, the adhesive character of catechols has been extensively studied in adhesive proteins and catechol-containing polymers but it is still not well understood and its assessment is commonly complicated by the presence of other functional groups in the materials. Our alternative approach is based on supramolecular assemblies of catechol groups; namely, self-assembled monolayers on Au that avoid the presence of other moieties on the surface. In Chapter 4, the study of the interfacial properties of these systems at the local scale will be described. An AFM tip will be used to measure the adhesion of the catechol moieties at the solid interface and their functionality will also be addressed by adsorbing magnetic nanoparticles. Additionally, the influence of the packing density and orientation of the catechol rings and the effect of the catechol moiety on the final structure of the assemblies will be considered.

On the other hand, our second challenge was related to the integration of VT-CPPs on surfaces. Although our group has suggested the use of different strategies to tackle this issue, none of them was directed to achieve the precise positioning of VT-CPPs on surfaces.

Direct-write AFM-assisted lithography was the tool of choice for that purpose, as it is an almost universal technique that allows to precisely position a diversity of materials on virtually any substrate. The use of this lithographic technique to fabricate confined nanoreactors that lead to the formation of single nanostructures (**CPP1**) will be described in Chapter 5. The synthesis of PDA in similar conditions and the study of the adhesive and chemical properties of the obtained material will also be detailed.

Chapter 3 of this thesis has been set as a transitional chapter. There, the synthesis and characterization of two new catechol derivatives will be described (Scheme 1.3). Compound **3** is a catechol-terminated alkanethiol that will be used to obtain the catechol-containing SAMs described in Chapter 4. On the other hand, compound **4** is a bifunctional ligand that combines a catechol and a pyridine moiety in a single molecule. Compound **4** will be used in the synthesis of the VT-CPPs inside femtolitre-sized droplets on surface, as described in Chapter 5. As will be detailed in Chapter 3, the combination of a catechol and a pyridine moiety in a single molecule not only facilitates the experimental procedure during the confined synthesis of the particles but also provides thermal hysteresis to the VT-CPPs. The synthesis and characterization of **CPP1** in bulk will also be described in this chapter.

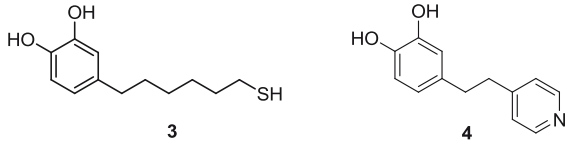

Scheme 1.3 Compounds **3** and **4** synthesized, characterized and used to obtain nanostructures in this thesis.

Due to the multidisciplinarity of this work, apart from the general introduction that we just provided, an introduction to the specific materials and methodologies used in each part of this thesis project has been included at the beginning of each chapter.

1.5 References

(1) Sedó, J.; Saiz-Poseu, J.; Busqué, F.; Ruiz-Molina, D. *Adv. Mater.* **2013**, *25*, 653–701.

(2) Eisenhofer, G.; Kopin, I. J.; Goldstein, D. S. *Pharmacol. Rev.* **2004**, *56*, 331–349.

(3) Wise, R. A. *Nat. Rev. Neurosci.* **2004**, *5*, 483–494.

(4) Torres, G. E.; Gainetdinov, R. R.; Caron, M. G. *Nat. Rev. Neurosci.* **2003**, *4*, 13–25.

(5) Wong, D. L.; Tai, T. C.; Wong-Faull, D. C.; Claycomb, R.; Siddall, B. J.; Bell, R. A.; Kvetnansky, R. *Cell. Mol. Neurobiol.* **2010**, *30*, 1451–1457.

(6) Vogl, O. *J. Polym. Sci. Part A Polym. Chem.* **2000**, *38*, 4327–4335.

(7) Quideau, S.; Deffieux, D.; Douat-Casassus, C.; Pouységu, L. *Angew. Chem. Int. Ed.* **2011**, *50*, 586–621.

(8) Pandey, K. B.; Rizvi, S. I. *Oxid. Med. Cell. Longev.* **2009**, *2*, 270–278.

(9) Kennedy, J. A.; Saucier, C.; Glories, Y. *Am. J. Enol. Vitic.* **2006**, *57*, 239–248.

(10) Cordova, A. C.; Sumpio, B. E. *Int. J. Angiol.* **2009**, *18*, 111–117.

(11) Abul-Hajj, Y. J.; Tabakovic, K.; Gleason, W. B.; Ojala, W. H. *Chem. Res. Toxicol.* **1996**, *9*, 434–438.

(12) Lee, B. P.; Messersmith, P. B.; Israelachvili, J. N.; Waite, J. H. *Annu. Rev. Mater. Res.* **2011**, *41*, 99–132.

(13) McDowell, L. M.; Burzio, L. A.; Waite, J. H.; Schaefer, J. *J. Biol. Chem.* **1999**, *274*, 20293–20295.

(14) Burzio, L. A.; Waite, J. H. *Biochemistry* **2000**, *39*, 11147–11153.

(15) Yu, J.; Wei, W.; Danner, E.; Israelachvili, J. N.; Waite, J. H. *Adv. Mater.* **2011**, *23*, 2362–2366.

(16) Meredith, P.; Powell, B. J.; Riesz, J.; Nighswander-Rempel, S. P.; Pederson, M. R.; Moore, E. G. *Soft Matter* **2006**, *2*, 37–44.

(17) D'Ischia, M.; Napolitano, A.; Pezzella, A.; Meredith, P.; Sarna, T. *Angew. Chem. Int. Ed.* **2009**, *48*, 3914–3921.

(18) Ito, S.; Wakamatsu, K. *Photochem. Photobiol.* **2008**, *84*, 582–592.

(19) Raper, H. S. *Biochem. J.* **1927**, *21*, 89–96.

(20) Mason, H. S. *J. Biol. Chem.* **1947**, *172*, 83–99.

(21) Xu, Z. *Sci. Rep.* **2013**, *3*, 2914.

(22) Yamahara, R.; Ogo, S.; Masuda, H.; Watanabe, Y. *J. Inorg. Biochem.* **2002**, *88*, 284–294.

(23) Hong, L.; Simon, J. D. *J. Phys. Chem. B* **2007**, *111*, 7938–7947.

(24) Meredith, P.; Sarna, T. *Pigment Cell Res.* **2006**, *19*, 572–594.

(25) Berg, D.; Gerlach, M.; Youdim, M. B. H.; Double, K. L.; Zecca, L.; Riederer, P.; Becker, G. *J. Neurochem.* **2008**, *79*, 225–236.

(26) Hare, D. J.; Lei, P.; Ayton, S.; Roberts, B. R.; Grimm, R.; George, J. L.; Bishop, D. P.; Beavis, A. D.; Donovan, S. J.; McColl, G.; Volitakis, I.; Masters, C. L.; Adlard, P. A.; Cherny, R. A.; Bush, A. I.; Finkelstein, D. I.; Doble, P. A. *Chem. Sci.* **2014**, *5*, 2160–2169.

(27) Raymond, K. N.; Dertz, E. A.; Kim, S. S. *Proc. Natl. Acad. Sci. USA* **2003**, *100*, 3584–3588.

(28) Scarrow, R. C.; Riley, P. E.; Abu-Dari, K.; White, D. L.; Raymond, K. N. *Inorg. Chem.* **1985**, *24*, 954–967.

(29) Gorden, A. E. V; Xu, J.; Raymond, K. N.; Durbin, P. *Chem. Rev.* **2003**, *103*, 4207–4282.

(30) Evangelio, E.; Ruiz-Molina, D. *C. R. Chimie* **2008**, *11*, 1137–1154.

(31) Stewart, R. J.; Weaver, J. C.; Morse, D. E.; Waite, J. H. *J. Exp. Biol.* **2004**, *207*, 4727–4734.

(32) Waite, J. H.; Jensen, R. A.; Morse, D. E. *Biochemistry* **1992**, *31*, 5733–5738.

(33) Anderson, T. H.; Yu, J.; Estrada, A.; Hammer, M. U.; Waite, J. H.; Israelachvili, J. N. *Adv. Funct. Mater.* **2010**, *20*, 4196–4205.

(34) Li, S.-C.; Chu, L.-N.; Gong, X.-Q.; Diebold, U. *Science* **2010**, *328*, 882–884.

(35) Mcbrlde, M. B.; Wessellnk, L. G. *Environ. Sci. Technol.* **1988**, *22*, 703–708.

(36) Waite, J. H.; Housley, T. J.; Tanzer, M. L. *Biochemistry* **1985**, *24*, 5010–5014.

(37) Yu, M.; Hwang, J.; Deming, T. J. *J. Am. Chem. Soc.* **1999**, *121*, 5825–5826.

(38) Yu, J.; Wei, W.; Menyo, M. S.; Masic, A.; Waite, J. H.; Israelachvili, J. N. *Biomacromolecules* **2013**, *14*, 1072–1077.

(39) Lin, Q.; Gourdon, D.; Sun, C.; Holten-Andersen, N.; Anderson, T. H.; Waite, J. H.; Israelachvili, J. N. *Proc. Natl. Acad. Sci. USA* **2007**, *104*, 3782–3786.

(40) Zeng, H.; Hwang, D. S.; Israelachvili, J. N.; Waite, J. H. *Proc. Natl. Acad. Sci. USA* **2010**, *107*, 12850–12853.

(41) Hwang, D. S.; Zeng, H.; Masic, A.; Harrington, M. J.; Israelachvili, J. N.; Waite, J. H. *J. Biol. Chem.* **2010**, *285*, 25850–25858.

(42) Sever, M. J.; Weisser, J. T.; Monahan, J.; Srinivasan, S.; Wilker, J. J. *Angew. Chem. Int. Ed.* **2004**, *43*, 448–450.

(43) Stewart, R. J.; Ransom, T. C.; Hlady, V. *J. Polym. Sci. Part B Polym. Phys.* **2011**, *49*, 757–771.

(44) Waite, J. H.; Qin, X. *Biochemistry* **2001**, *40*, 2887–2893.

(45) Ye, Q.; Zhou, F.; Liu, W. *Chem. Soc. Rev.* **2011**, *40*, 4244–4258.

(46) White, J. D.; Wilker, J. J. *Macromolecules* **2011**, *44*, 5085–5088.

(47) Matos-Pérez, C. R.; White, J. D.; Wilker, J. J. *J. Am. Chem. Soc.* **2012**, *134*, 9498–9505.

(48) Li, A.; Jia, M.; Mu, Y.; Jiang, W.; Wan, X. *Macromol. Chem. Phys.* **2015**, *216*, 450–459.

(49) Waite, J. H.; Andersen, N. H.; Jewhurst, S.; Sun, C. *J. Adhes.* **2005**, *81*, 297–317.

(50) Nicklisch, S. C. T.; Waite, J. H. *Biofouling* **2012**, *28*, 865–877.

(51) Waite, J. H. *Integr. Comp. Biol.* **2002**, *42*, 1172–1180.

(52) Zhao, H.; Waite, J. H. *J. Biol. Chem.* **2006**, *281*, 26150–26158.

(53) Harrington, M. J.; Masic, A.; Holten-Andersen, N.; Waite, J. H.; Fratzl, P. *Science* **2010**, *328*, 216–220.

(54) Holten-Andersen, N.; Mates, T. E.; Toprak, M. S.; Stucky, G. D.; Zok, F. W.; Waite, J. H. *Langmuir* **2009**, *25*, 3323–3326.

(55) Lee, H.; Dellatore, S. M.; Miller, W. M.; Messersmith, P. B. *Science* **2007**, *318*, 426–430.

(56) Tan, Y.; Deng, W.; Li, Y.; Huang, Z.; Meng, Y.; Xie, Q.; Ma, M.; Yao, S. *J. Phys. Chem. B* **2010**, *114*, 5016–5024.

(57) Ouyang, R.; Lei, J.; Ju, H.; Xue, Y. *Adv. Funct. Mater.* **2007**, *17*, 3223–3230.

(58) Liu, Y.; Ai, K.; Lu, L. *Chem. Rev.* **2014**.

(59) Ball, V.; Frari, D.; Michel, M.; Buehler, M. J.; Toniazzo, V.; Singh, M. K.; Gracio, J.; Ruch, D. *Bionanoscience* **2011**, *2*, 16–34.

(60) Wang, X.; Jin, B.; Lin, X. *Anal. Sci.* **2002**, *18*, 931–933.

(61) Dreyer, D. R.; Miller, D. J.; Freeman, B. D.; Paul, D. R.; Bielawski, C. W. *Langmuir* **2012**, *28*, 6428–6435.

(62) Hong, S.; Na, Y. S.; Choi, S.; Song, I. T.; Kim, W. Y.; Lee, H. *Adv. Funct. Mater.* **2012**, *22*, 4711–4717.

(63) Liebscher, J.; Mrówczyński, R.; Scheidt, H. A.; Filip, C.; Hădade, N. D.; Turcu, R.; Bende, A.; Beck, S. *Langmuir* **2013**, *29*, 10539–10548.

(64) Della Vecchia, N. F.; Avolio, R.; Alfè, M.; Errico, M. E.; Napolitano, A.; D'Ischia, M. *Adv. Funct. Mater.* **2013**, *23*, 1331–1340.

(65) Della Vecchia, N. F.; Luchini, A.; Napolitano, A.; D'Errico, G.; Vitiello, G.; Szekely, N.; D'Ischia, M.; Paduano, L. *Langmuir* **2014**, *30*, 9811–9818.

(66) Lee, Y. Bin; Shin, Y. M.; Lee, J.-H.; Jun, I.; Kang, J. K.; Park, J.-C.; Shin, H. *Biomaterials* **2012**, *33*, 8343–8352.

(67) Kang, K.; Choi, I. S.; Nam, Y. *Biomaterials* **2011**, *32*, 6374–6380.

(68) Zhang, W.; Yang, F. K.; Han, Y.; Gaikwad, R.; Leonenko, Z.; Zhao, B. *Biomacromolecules* **2013**, *14*, 394–405.

(69) Yang, F. K.; Zhao, B. *Open Surf. Sci. J.* **2011**, *3*, 115–122.

(70) Chien, H.-W.; Kuo, W.-H.; Wang, M.-J.; Tsai, S.-W.; Tsai, W.-B. *Langmuir* **2012**, *28*, 5775–5782.

(71) Ku, S. H.; Lee, J. S.; Park, C. B. *Langmuir* **2010**, *26*, 15104–15108.

(72) Ku, S. H.; Park, C. B. *Biomaterials* **2010**, *31*, 9431–9437.

(73) Ball, V.; Nguyen, I.; Haupt, M.; Oehr, C.; Arnoult, C.; Toniazzo, V.; Ruch, D. *J. Colloid Interface Sci.* **2011**, *364*, 359–365.

(74) Saidin, S.; Chevallier, P.; Abdul Kadir, M. R.; Hermawan, H.; Mantovani, D. *Mater. Sci. Eng. C. Mater. Biol. Appl.* **2013**, *33*, 4715–4724.

(75) Son, H. Y.; Ryu, J. H.; Lee, H.; Nam, Y. S. *Macromol. Mater. Eng.* **2013**, *298*, 547–554.

(76) Fu, Y.; Liu, L.; Zhang, L.; Wang, W. *ACS Appl. Mater. Interfaces* **2014**, *6*, 4–11.

(77) Long, Y.; Wu, J.; Wang, H.; Zhang, X.; Zhao, N.; Xu, J. *J. Mater. Chem.* **2011**, *21*, 4875–4881.

(78) Xu, L. Q.; Yang, W. J.; Neoh, K. G.; Kang, E. T.; Fu, G. D. *Macromolecules* **2010**, *43*, 8336–8339.

(79) Huang, K.; Lee, B. P.; Ingram, D. R.; Messersmith, P. B. *Biomacromolecules* **2002**, *3*, 397–406.

(80) Rodenstein, M.; Zürcher, S.; Tosatti, S. G. P.; Spencer, N. D. *Langmuir* **2010**, *26*, 16211–16220.

(81) Weinhold, M.; Soubatch, S.; Temirov, R.; Rohlfing, M.; Jastorff, B.; Tautz, F. S.; Doose, C. *J. Phys. Chem. B* **2006**, *110*, 23756–23769.

(82) Rībena, D.; Alekseev, A.; van Asselen, O.; Mannie, G. J. A.; Hendrix, M. M. R. M.; van der Ven, L. G. J.; Sommerdijk, N. A. J. M.; de With, G. *Langmuir* **2012**, *28*, 16900–16908.

(83) García, B.; Saiz-Poseu, J.; Gras-Charles, R.; Hernando, J.; Alibés, R.; Novio, F.; Sedó, J.; Busqué, F.; Ruiz-Molina, D. *ACS Appl. Mater. Interfaces* **2014**, *6*, 17616–17625.

(84) Saiz-Poseu, J.; Sedó, J.; García, B.; Benaiges, C.; Parella, T.; Alibés, R.; Hernando, J.; Busqué, F.; Ruiz-Molina, D. *Adv. Mater.* **2013**, *25*, 2066–2070.

(85) Saiz-Poseu, J. Ph.D. Thesis, Universitat Autónoma de Barcelona, 2011.

(86) Gong, Y.-K.; Liu, L.-P.; Messersmith, P. B. *Macromol. Biosci.* **2012**, *12*, 979–985.

(87) Wei, Q.; Achazi, K.; Liebe, H.; Schulz, A.; Noeske, P.-L. M.; Grunwald, I.; Haag, R. *Angew. Chem. Int. Ed.* **2014**, *53*, 11650–11655.

(88) Wang, X.; Ye, Q.; Gao, T.; Liu, J.; Zhou, F. *Langmuir* **2012**, *28*, 2574–2581.

(89) Saxer, S.; Portmann, C.; Tosatti, S.; Gademann, K.; Zürcher, S.; Textor, M. *Macromolecules* **2010**, *43*, 1050–1060.

(90) Lee, H.; Lee, K. D.; Pyo, K. B.; Park, S. Y.; Lee, H. *Langmuir* **2010**, *26*, 3790–3793.

(91) Faure, E.; Halusiak, E.; Farina, F.; Giamblanco, N.; Motte, C.; Poelman, M.; Archambeau, C.; Van De Weerdt, C.; Martial, J.; Jérôme, C.; Duwez, A.-S.; Detrembleur, C. *Langmuir* **2012**, *28*, 2971–2978.

(92) Yu, M.; Deming, T. *Macromolecules* **1998**, *31*, 4739–4745.

(93) Lee, B. P.; Chao, C. Y.; Nelson Nunalee, F.; Motan, E.; Shull, K. R.; Messersmith, P. B. *Macromolecules* **2006**, *39*, 1740–1748.

(94) Burke, S. A.; Ritter-Jones, M.; Lee, B. P.; Messersmith, P. B. *Biomed. Mater.* **2007**, *2*, 203–210.

(95) Barrett, D. G.; Fullenkamp, D. E.; He, L.; Holten-Andersen, N.; Lee, K. Y. C.; Messersmith, P. B. *Adv. Funct. Mater.* **2013**, *23*, 1111–1119.

(96) Yamada, K.; Chen, T.; Kumar, G.; Vesnovsky, O.; Topoleski, L. D.; Payne, G. F. *Biomacromolecules* **2000**, *1*, 252–258.

(97) Ryu, J. H.; Lee, Y.; Kong, W. H.; Kim, T. G.; Park, T. G.; Lee, H. *Biomacromolecules* **2011**, *12*, 2653–2659.

(98) Lee, H.; Lee, B. P.; Messersmith, P. B. *Nature* **2007**, *448*, 338–341.

(99) Glass, P.; Chung, H.; Washburn, N. R.; Sitti, M. *Langmuir* **2009**, *25*, 6607–6612.

(100) Glass, P.; Chung, H.; Washburn, N. R.; Sitti, M. *Langmuir* **2010**, *26*, 17357–17362.

(101) Gütlich, P.; Dei, A. *Angew. Chem. Int. Ed.* **1997**, *36*, 2734–2736.

(102) Pierpont, C. G.; Jung, O.-S. *Inorg. Chem.* **1995**, *34*, 4281–4283.

(103) Evangelio, E.; Ruiz-Molina, D. *Eur. J. Inorg. Chem.* **2005**, *2005*, 2957–2971.

(104) Pierpont, C. G. *Coord. Chem. Rev.* **2001**, *216-217*, 99–125.

(105) Tezgerevska, T.; Alley, K. G.; Boskovic, C. *Coord. Chem. Rev.* **2014**, *268*, 23–40.

(106) Dei, A.; Gatteschi, D.; Sangregorio, C.; Sorace, L. *Acc. Chem. Res.* **2004**, *37*, 827–835.

(107) Hendrickson, D. N.; Pierpont, C. G. *Top. Curr. Chem.* **2004**, *234*, 63–95.

(108) Buchanan, R. M.; Pierpont, C. G. *J. Am. Chem. Soc.* **1980**, *102*, 4951–4957.

(109) Adams, D. M.; Dei, A.; Rheingold, A. L.; Hendrickson, D. N. *J. Am. Chem. Soc.* **1993**, *115*, 8221–8229.

(110) Beni, A.; Dei, A.; Laschi, S.; Rizzitano, M.; Sorace, L. *Chem. Eur. J.* **2008**, *14*, 1804–1813.

(111) Ruiz-Molina, D.; Veciana, J.; Wurst, K.; Hendrickson, D. N.; Rovira, C. *Inorg. Chem.* **2000**, *39*, 617–619.

(112) Evangelio, E.; Rodriguez-Blanco, C.; Coppel, Y.; Hendrickson, D. N.; Sutter, J. P.; Campo, J.; Ruiz-Molina, D. *Solid State Sci.* **2009**, *11*, 793–800.

(113) Dapporto, P.; Dei, A.; Poneti, G.; Sorace, L. *Chem. Eur. J.* **2008**, *14*, 10915–10918.

(114) Kitagawa, S.; Kitaura, R.; Noro, S. *Angew. Chem. Int. Ed.* **2004**, *43*, 2334–2375.

(115) Maspoch, D.; Ruiz-Molina, D.; Veciana, J. *Chem. Soc. Rev.* **2007**, *36*, 770–818.

(116) Carne, A.; Carbonell, C.; Imaz, I.; Maspoch, D. *Chem. Soc. Rev.* **2011**, *40*, 291–305.

(117) Imaz, I.; Maspoch, D.; Rodríguez-Blanco, C.; Pérez-Falcón, J.; Campo, J.; Ruiz-Molina, D. *Angew. Chem. Int. Ed.* **2008**, *47*, 1857–1860.

(118) Bodnar, S. H.; Caneschi, A.; Dei, A.; Shultz, D. A.; Sorace, L. *Chem. Commun.* **2001**, 2150–2151.

(119) Chen, X.; Wei, R.; Zheng, L.; Tao, J. *Inorg. Chem.* **2014**, *53*, 13212–13219.

(120) Chen, L.; Wei, R.; Tao, J.; Huang, R.; Zheng, L. *Sci. China Chem.* **2012**, *55*, 1037–1041.

(121) Cheng, W.-Q.; Li, G.-L.; Zhang, R.; Ni, Z.-H.; Wang, W.-F.; Sato, O. *J. Mol. Struct.* **2015**, *1087*, 68–72.

(122) Goswami, S.; Panja, A.; Butcher, R. J.; Shaikh, N.; Banerjee, P. *Inorg. Chim. Acta* **2011**, *370*, 311–321.

(123) Li, B.; Chen, L. Q.; Wei, R. J.; Tao, J.; Huang, R. Bin; Zheng, L. S.; Zheng, Z. *Inorg. Chem.* **2011**, *50*, 424–426.

(124) Calzolari, A.; Chen, Y.; Lewis, G. F.; Dougherty, D. B.; Shultz, D.; Buongiorno Nardelli, M. *J. Phys. Chem. B* **2012**, *116*, 13141–13148.

(125) Novio, F.; Campo, J.; Ruiz-Molina, D. *Inorg. Chem.* **2014**, *53*, 8742–8748.

(126) Nador, F.; Novio, F.; Ruiz-Molina, D. *Chem. Commun.* **2014**, *50*, 14570–14572.

(127) Novio, F.; Evangelio, E.; Vazquez-Mera, N.; González-Monje, P.; Bellido, E.; Mendes, S.; Kehagias, N.; Ruiz-Molina, D. *Sci. Rep.* **2013**, *3*, 1708.

(128) Vázquez-Mera, N. A.; Roscini, C.; Hernando, J.; Ruiz-Molina, D. *Adv. Funct. Mater.* **2015**, *25*, 4129–4134.

(129) Vázquez-Mera, N. A. Ph.D. Thesis, Universitat Autónoma de Barcelona, 2015.

(130) González-Monje, P.; Novio, F.; Ruiz-Molina, D. *Chem. Eur. J.* **2015**, *21*, 10094–10099.

Chapter 2

Objectives

In accordance with the precedents in catechol chemistry described in the introduction, the **general objectives** set for the present PhD thesis are:

1. To gain deeper understanding on the adhesive and interfacial properties of catechol groups by organizing them as self-assembled monolayers on gold substrates.
2. To achieve the confined synthesis of different catechol-based polymers in femtolitre volumes using tip-assisted methodologies with precise control over the XY positioning on a surface

To achieve this, the following **specific objectives** were set:

I. To synthesize and characterize two new catechol derivatives, namely the catechol-terminated alkanethiol 4-(6'-mercaptohexyl)catechol (**3**) and the ditopic ligand 4-(2-(pyridin-4-yl)ethyl)catechol (**4**).

II. To synthesize and characterize valence tautomeric coordination polymer particles (**CPP1**) obtained through the coordination of **4** with Co^{2+} in order to induce thermal hysteresis.

III. To position catechol moieties at the interface of gold surfaces in an organized manner through the assembly of **3** on both planar and curved (nanoparticulate) gold.

IV. To study the interfacial properties of the previous structures obtained on planar Au, concretely their interaction (adhesion) with an AFM tip and the influence that the molecular orientation and packing have on their functionality.

V. To assess the stability and functionality of Au nanoparticles functionalized with outward-facing catechol moieties and study the influence of the catechol moiety on the formation and final structure of the assemblies.

VI. To synthesize catechol-based materials through confined reactions in droplets generated by direct write AFM-assisted lithography. As a proof-of-concept to demonstrate the viability of this approach two different families of catechol-based polymers, polydopamine and coordination polymer nanoparticles, were used.

VII. To characterize the materials synthesized in confined environments in both chemical structure and functionality.

Chapter 3

Synthesis of catechol derivatives and coordination polymer particles

In this Chapter we describe the synthesis of two new catechol derivatives. The catechol-terminated thiol **3**, of interest to obtain self-assembled monolayers on gold surfaces, and the bifunctional ligand **4**, used in the synthesis of VT-CPPs in confined environments. The synthesis of such VT-CPPs by classical methodologies is also described in this chapter.

3.1 Introduction

In the last few years, an important part of the research efforts made in our group has been based on the use of catechol derivatives. A variety of catechol-containing compounds have been synthesized and their pH-switching,[1–3] assembly on surfaces[4,5] or coating ability of their polymeric derivatives have been explored.[6–8] In the following paragraphs we summarize the synthetic strategies used for their construction, as we will see, the use of a Wittig methodology is recurrent.

3.1.1 Group precedents on the synthesis of functional catechol derivatives

The first catechol derivatives synthesized were designed to behave as fluorescent chemosensors with wide-range pH-induced response. To that effect the catechol unit was covalently coupled to other aromatic rings, thus obtaining π-delocalized systems with both pH-responsive groups and fluorescence emission in the visible region. Both compounds **5** and **6** were obtained through the coupling of the aldehyde **7** with the appropriate phosphorane derivative in a Wittig reaction[1]. Whilst **5** presents two stable protonation states with distinct optical properties, compound **6** shows up to three different luminescent protonation states (Scheme 3.1).

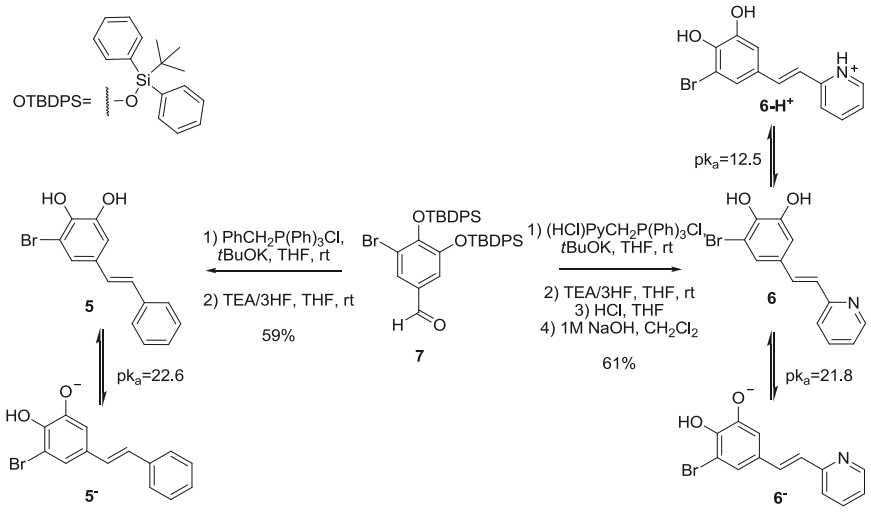

Scheme 3.1 Synthesis and acid-base equilibrium of compounds **5** and **6**.

Later on, catechol derivatives bearing alkylic chains were synthesized. The synthetic strategy employed to obtain these compounds was based once again in a Wittig reaction

between a protected catechol ring bearing one or two aldehyde groups and appropriate phosphoranes. The heptadecylcatechol, **1** was the first compound of the family and was obtained through the coupling of compound **8** and 1-hexadecyltriphenylphosphonium bromide in the presence of *t*BuOK, followed by standard hydrogenation and deprotection procedures.[4] Other catechol derivatives bearing shorter alkylic chains, **9** and **10** were synthesized in an analogous way (Scheme 3.2).[7] Also, following similar synthetic strategies a perfluorinated chain or two alkyl chains (instead of only one) were attached to the catechol rings to obtain compound **2** with a fluorinated chain,[6] **11** bearing two identical alkyl chains and **12**, with a long alkyl chain and a *tert*-butyl group (Scheme 3.3).[5]

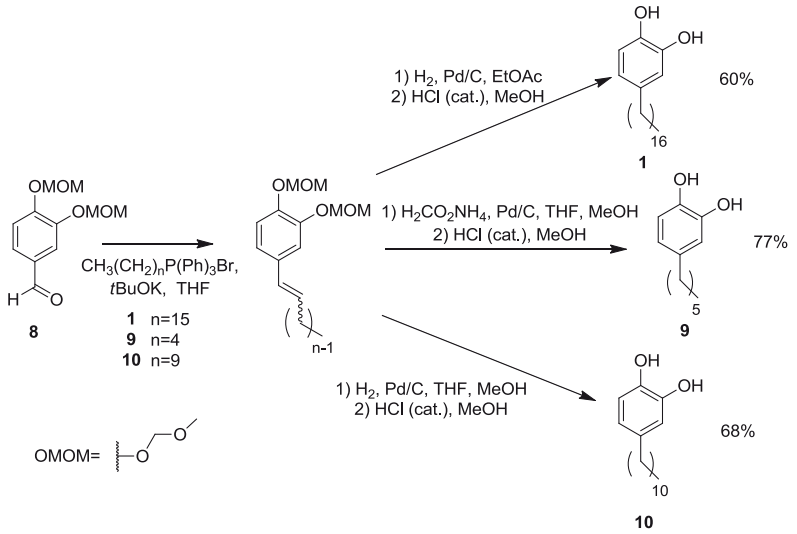

Scheme 3.2 Synthesis of the alkylcatechols **1**, **9** and **10**.

The adsorption of **1**, **11** and **12** on surfaces was studied by STM and both **1** and **11** proved to interact strongly with the surface forming ordered domains.[4,5] Additionally, as already pointed out in the introduction, when compound **1** was exposed to basic media in aerobic conditions a dark polymeric derivative of unknown chemical structure was obtained. This material was then used to coat a variety of substrates and impart them hydrophobic properties due to the presence of the long alkyl chains. Structure-property relationships between hydrophobic character or coating capability and the structure of the catechol monomers were established using the oxidation products of compounds **2**, **9**, **10** and **11** to coat different types of surfaces and nano-objects.[6,7]

Here we have summarized the work performed in our group in the synthesis of catechol derivatives for different applications. As seen, the Wittig methodology was

employed in all cases as a strategy to couple the catechol ring to other functionalities. By doing so, in the group we have been able to explore the properties of the catechol moiety from a fundamental point of view and also as building block of new functional materials.[9]

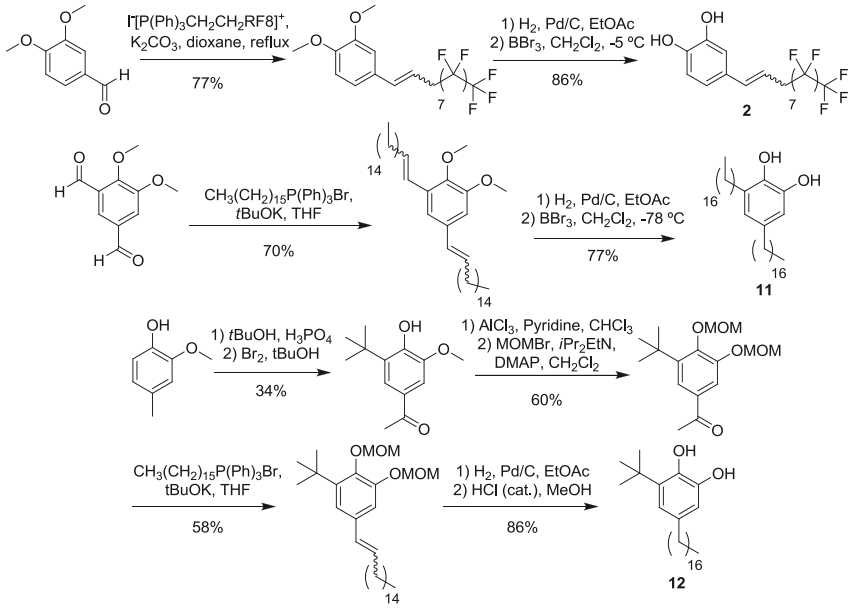

Scheme 3.3 Synthesis of the catechol derivatives **2**, **11** and **12**.

3.1.2 Catechol ligands in valence-tautomeric coordination polymers

As already addressed in Section 1.3 of this thesis, catechols are interesting redox-active ligands that can participate in reversible intramolecular electron transfer processes when they are coordinated to an appropriate metal ion.[10] This electron transfer process occurs in response to an external perturbation such as temperature,[11] pressure,[12] irradiation[13] or pH[14] and results in the existence of two degenerated electronic states.[15] The presence of two stable electronic isomers makes these complexes, termed valence tautomers (VT), potential building blocks of molecular electronic devices and switches.[10,16]

However, there exists an important limitation of the potential application of these VT complexes, which is the lack of thermal hysteresis. In the cases where the intramolecular electron transfer is triggered by temperature changes, thermal hysteresis occurs when the temperature of the *ls*→*hs* transition in the warming mode is higher than the *hs*→*ls* transition in the cooling mode and is an essential prerequisite for having memory effects.[17] Indeed, even though hysteresis in a few monomeric[18–20] and dimeric[21–23] VT complexes has been

reported and associated with their supramolecular packing,[24,25] a set of basic laws to design molecular systems with hysteresis is still lacking. The synthesis of VT polymeric systems that induce thermal hysteresis through cooperative effects is nowadays the most frequent approach.[17]

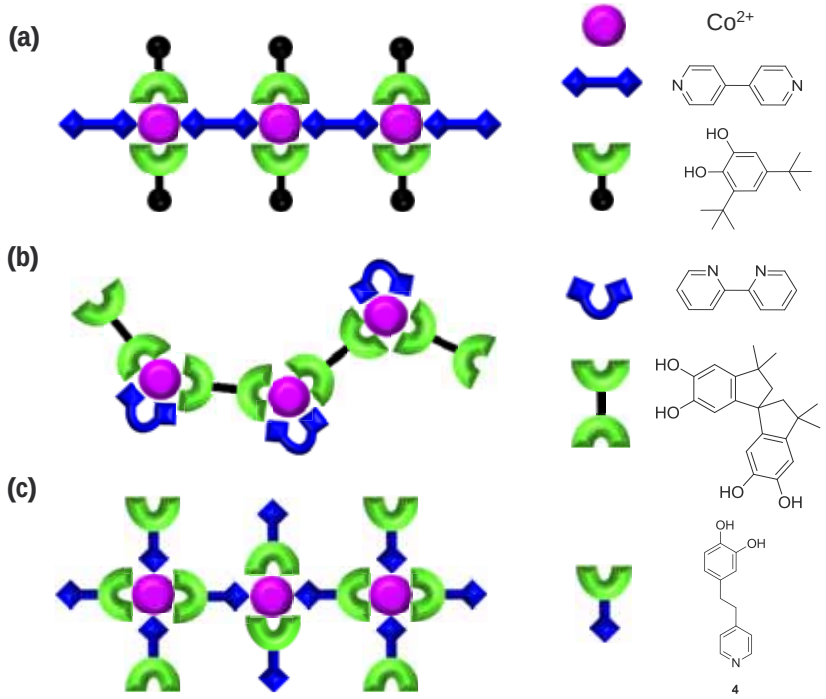

Figure 3.1 Schematic representation of the different approaches so far followed for the formation of VT coordination polymers and the one used in this thesis: (a) Combination of catechol ligands with bipyridil/pyrazol ligands (example from ref. 26). (b) Bisbidentate catechol and bypiridine as ancillary ligand (example from ref. 27).(c) Catechol and pyridine moieties combined in a single molecule (this work).

In this context, the synthesis of valence-tautomeric coordination polymers (VT-CPs) arises as a promising methodology to obtain solid materials with VT interconversion and thermal hysteresis. In Figure 3.1, a schematic representation of the different approaches so far followed for the preparation of VT-CPs is shown. Within the framework of the first approach (see Figure 3.1a), one-dimensional[26,28] and two-dimensional[29] coordination polymers were obtained by linking the cobalt-*o*-quinone complex units using multitopic pyridyl or pyrazol ligands. Whilst the catechol ligand provides the switchable behaviour through the thermally induced intramolecular electron transfer with the cobalt ion, the non-electroactive multitopic bridging ligand acts as polymerizing agent. Pierpont et al. followed this approach to obtain the photomechanical polymer $[Co(3,6\text{-}DTBSQ)_2(pyz)]_n$, where pyz stands for pyrazine.[30] This coordination polymer exhibited a temperature-induced

tautomeric interconversion in the solid state derived from a mechanical process attributed to the variation of the bond lengths. More recently, three novel polymeric complexes with different bidentate-bridging pyridine ligands were synthesized and their VT behaviour was studied in terms of solvent effects and photoinduced transition.[31] In the same way, a series of 1-D polymer structures ranging from amorphous spherical nanoparticles to crystals with several different morphologies were obtained.[32] The experimental results indicated that the degree of crystallinity and the crystalline phase critically determine the VT process, independently of the morphology and/or dimensions of the crystals. However, in any of the reported examples relevant hysteresis effects were observed.

In the second approach (see Figure 3.1b) bis-bidentate catechol-based ligands are used. In this way, the catechol-containing ligand plays a double role, acting as both polymerizing and electroactive unit. An additional ancillary ligand is also included to complete the coordination sphere and achieve a proper balance between the frontier orbitals of the quinone and the metal ion involved in the intramolecular electron transfer process.[15] Using this approach, Schultz and Dei and co-workers reported the synthesis of VT-CPs showing small hysteresis width (between 5 and 13 K),[27,33] associated to the cooperativity between the cobalt centres.[34,35]

We have envisioned a third approach to synthesize VT-CPs using a single ditopic ligand that combines in the same molecule a redox-active and a polymerizing unit (see Figure 3.1c). For this, ligand **4** was designed to combine a catechol and a pyridine moiety in the same molecule.

3.1.3 Aim of the work

In the next section we will describe the synthesis of two new catechol derivatives (Scheme 3.4). The first one is the 4-(6'-mercaptohexyl)catechol **3**, a catechol-terminated alkanethiol that will be used later in this thesis (See Chapter 4) for the construction of self-assembled monolayers on gold exposing catechol moieties to the outer interface. The second novel compound is the 4-(2-(pyridin-4-yl)ethyl)catechol **4**, which is a bi-functional ligand that combines the catechol and pyridine functionalities in a single molecule. As explained above, the design of this molecule was motivated by the interest in inducing hysteresis effects on the VT-CPs derived from the coordination of ligand **4** to cobalt ions. Additionally, the combination of the two moieties in a single molecule avoids the use of an auxiliary N-donor ligand to complete the coordination sphere of the metal centre, thus the synthetic

procedure is simplified. This is important for the development of processes that lead to the integration of these materials on functional devices, as will be discussed in Chapter 5.

The synthesis and characterization of the valence tautomeric coordination polymer particles (VT-CPPs) obtained from the combination of the synthesized ligand cobalt ions will also be reported here.

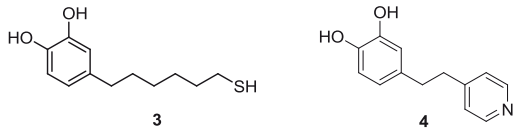

Scheme 3.4 Chemical structure of the two catechol derivatives synthesized in this thesis

3.2 Synthesis of the catechol-terminated thiol 4-(6'-mercaptohexyl)catechol, 3

One of the objectives of the present PhD project consisted on the preparation of SAMs exposing catechol moieties to the outside in order to study the interfacial properties of highly ordered and homogeneous catechol-modified surfaces. Our goal was to obtain catechol-functionalized gold surfaces with the simplest possible chemical composition in order to guarantee that the interfacial properties of the obtained material were defined almost exclusively by the catechol group and avoiding any significant interferences. In order to do so, a compound that combined in the same structure the catechol moiety and a thiol group was synthesized.

The final objective molecule was formed by a catechol moiety, which provided surface functionality, a thiol group to act as anchor and an alkyl chain connecting both moieties and adding stability to the SAM. The chain length was decided on the basis of preliminary theoretical calculations that suggested that the optimal structure should contain between five and eight carbon atoms in the chain. Therefore, the catechol-terminated thiol **3**, which bears a six carbon chain as a linker between the two moieties, was synthesized.

The synthetic pathway towards the obtention of the target molecule consisted in a convergent synthesis having a Wittig reaction as a key step to combine the phosphonium ylide derived from compound **13** and the aldehyde **14** (Scheme 3.5). The synthesis was intentionally designed in this way so that the same strategy could be extended to obtain a whole family of catechol derivatives having compound **13** as a common intermediate.

Considering the vast amount of commercially available aldehyde-bearing compounds as well as primary alcohols that can be easily oxidized to aldehydes, there is a myriad of possible compounds that could be obtained using this approach.

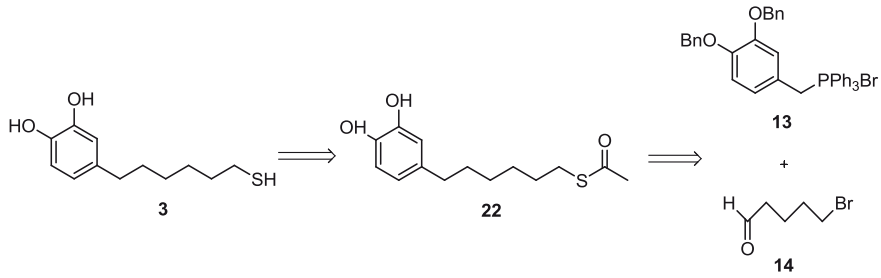

Scheme 3.5 Retrosynthetic analysis of the catechol-terminated thiol **3**.

3.2.1 Synthesis of the phosphonium salt, 13

The synthesis of the phosphonium salt was already described in the literature and could be easily reproduced after minimal adjustments.[36–38] The aldehyde moiety of commercially available 3,4-dibenzyloxybenzaldehyde **15** was reduced with $NaBH_4$ to give the corresponding alcohol **16**, which was then treated with PBr_3 to afford the bromoderivative **17** in 89% overall yield. Afterwards, compound **17** was quantitatively transformed in the corresponding phosphonium bromide by reaction with triphenylphosphine in CH_2Cl_2 reflux. Therefore, the intermediate **13** was afforded in three steps with 83% overall yield (Scheme 3.6).

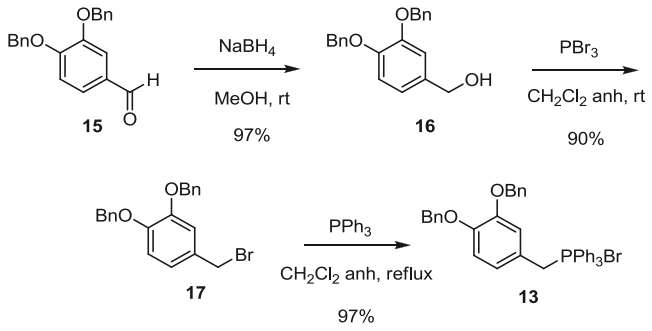

Scheme 3.6 Synthesis of the phosphonium salt **13** in three steps.

It is important to point out that the intermediates where obtained with high purity and that it was not necessary to use flash column chromatography after any of the synthetic

steps. Also, the synthesis of **13** could be scaled up to multigram amounts and the solid product was stable over long periods of time, which facilitates its use as a common intermediate of a generalized synthetic strategy.

3.2.2 Synthesis of 5-bromopentanal, 14

In parallel experiments, the synthesis of 5-bromopentanal, **14** by oxidation of 5-bromobutanol, **18** was explored. Three classical oxidation methodologies were assayed: the use of Dess-Martin periodinane, the Swern methodology and pyridinium chlorochromate (PCC), being the latter the method that provided better results.[39] In that way, **14** was obtained in 87% yield through reaction with PCC in dichloromethane at room temperature (Scheme 3.7). The ^{1}H-NMR spectrum of the obtained product clearly indicated the formation of an aldehyde by the appearance of a singlet at δ 9.77 ppm.

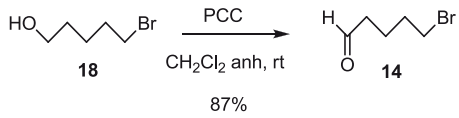

Scheme 3.7 Synthesis of the aldehyde **14**.

3.2.3 Wittig reaction between 13 and 14 to obtain the olefin mixture (Z)- and (E)-19

The next synthetic step consisted in the coupling of the two fragments that had been constructed previously using the Wittig methodology. The experimental procedure consists in exposing the phosphonium salt to basic media to promote the formation of the corresponding phosphonium ylide, which subsequently reacts with the aldehyde moiety to give the desired olefin as a mixture of (*Z*)- and (*E*)- isomers in variable ratios, depending on the reaction conditions and the nature of the reagents. Also, phosphine oxide is obtained as a by-product (Scheme 3.8).

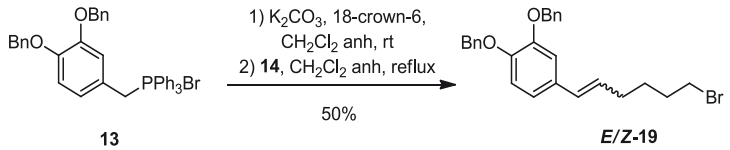

Scheme 3.8 Wittig reaction combining the two fragments, **13** and **14** to from the olefin mixture (*E*)-/(*Z*)-**19** as an intermediate of the final product.

In a first approximation an excess of *n*BuLi was used as a base to generate the ylide and THF was employed as solvent, as described in the literature for similar reactions.[36] The resulting reaction crude showed the presence of a complex mixture of compounds, including the (*E*)- and (*Z*)- isomers of compound **19** in low yields. One of the main by-products of the reaction was identified as the reduction product of the phosphonium salt, **20**. The ^{1}H-NMR spectrum of compound **20** isolated from the reaction crude appears in Figure 3.2 and shows a sharp singlet signal at δ 2.35 ppm corresponding to the methyl group generated.

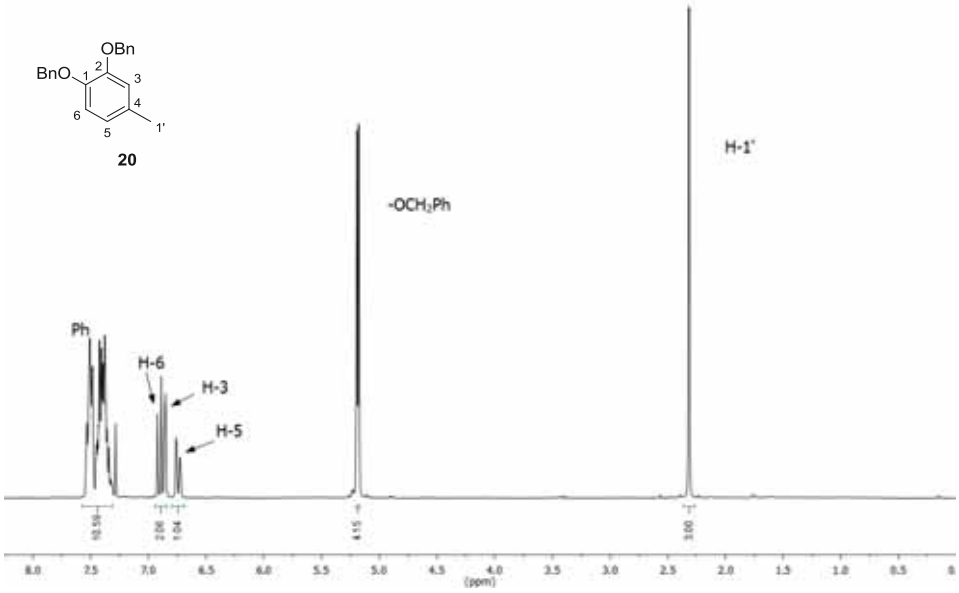

Figure 3.2 ^{1}H-NMR spectra and structure of the by-product **20** obtained during the Wittig reaction performed using strong bases.

In order to improve the reaction yield and minimize the appearance of compound **20**, a study of the influence of the reaction conditions (nature of the used base, equivalents of base and temperature) on the reaction yield based on isolated **19** was carried out. The results are summarized in Table 3.1.

As can be seen in the table, first the *n*BuLi equivalents were varied as well as the temperature at which the reaction was performed (entries 1-5). As observed, a reduction in the equivalents of *n*BuLi resulted in an increase of the reaction yield and the **19:20** ratio, thus favouring the obtention of the desired product (entry 3). Also, if the reaction was carried out at low temperature, the amount of **20** substantially increased (entry 2). It was

decided then to use a non-nucleophilic base with the objective of minimizing the amount of by-products.[40,41] For that bis(trimethylsilyl)amide (HMDS) salts were used (entries 6, 7), and yields of **19** similar to those in the previous experiments were obtained but the amount of by-products formed during the reaction was significantly reduced. Finally, the best results were obtained when the reaction was performed in mild basic medium by using a weaker base such as K_2CO_3 under reflux of a low boiling point solvent like CH_2Cl_2 (entries 8, 10, 12).[37,42] Use of higher boiling point solvents[6] (entries 9, 11) resulted in low yields and the formation of impurities. A large excess of base and long reaction times (24 hours) were necessary to achieve complete conversion of the reactants. After all these considerations a 1:1 mixture of olefins (*E*)- and (*Z*)-**19** in 50% yield was afforded while significantly reducing the formation of by-products, even to the point that compound **20** was not observed

Table 3.1 Optimization of reaction conditions for the obtention of **19**.[a]

Entry	Base	Solvent	Base equivalents	Temperature	19 Yield (%)	Ratio (19:20)
1	*n*BuLi	THF	1.5	RT	26	1:2.6
2	*n*BuLi	THF	1.5	-25 ºC	--[b]	1:6
3	*n*BuLi	THF	1.3	RT	40	2.1:1
4	*n*BuLi	THF	1.3	40 ºC	35	1:1
5	*n*BuLi	THF	2.0	RT	--[b]	1:1.2
6	KHMDS	THF	1.1	RT	28	2.8:1
7	LiHMDS	THF	1.4	RT	40	1:1.6
8[c]	K_2CO_3	CH_2Cl_2	1.35	40 ºC	22	1:0
9	K_2CO_3	1,4-dioxane	2.7	101 ºC	--[b]	1:0
10[c]	K_2CO_3	CH_2Cl_2	3	40 ºC	38	1:0
11	K_2CO_3	THF	3	66 ºC	23	1:2.1
12[c]	K_2CO_3	CH_2Cl_2	5.8	40 ºC	50	1:0

[a] All the reactions were performed under N_2. [b]In these cases the ^{1}H-NMR spectra of the crude showed a very small amount of the desired product and it was not purified. [c] To the experiments in CH_2Cl_2 a small amount of 18-crown-6-ether was added.

3.2.4 Deprotection of the hydroxyl groups and reduction of the double bond

Next, the mixture of olefins was subjected to hydrogenation under palladium catalyst. In this way the reduction of the double bond formed in the previous step could be carried out simultaneously with the deprotection of the two hydroxyl moieties of the aromatic ring

(Scheme 3.9). First, ammonium formate was used as a source of hydrogen, which resulted in the obtention of **21** in low yields. This problem was overcome by using molecular hydrogen at a pressure of three atmospheres in the presence of the same palladium supported on carbon catalyst, achieving the simultaneous deprotection of the alcohol groups and reduction of the double bond to afford the corresponding ω-bromocatechol **21** in 86% yield.

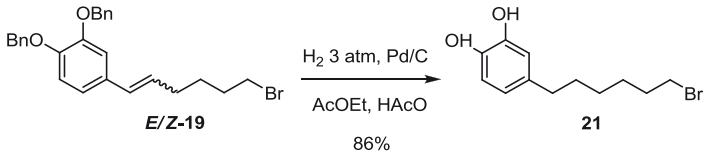

Scheme 3.9 Deprotection of the hydroxyl groups and reduction of the double bond.

The ^{1}H-NMR spectrum of the hydrogenated product (Figure 3.3) shows the disappearance of the signals corresponding to the olefinic protons along with the aromatic and methylene signals from the protective groups. At the same time, a new triplet appears at δ 2.49 ppm, corresponding to the protons in the benzylic position.

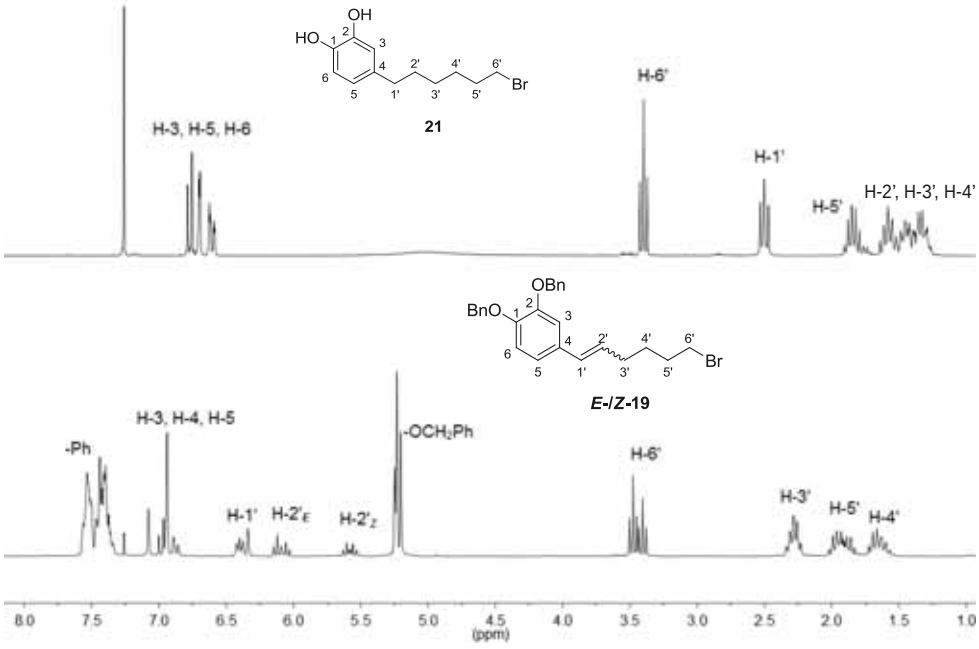

Figure 3.3 ^{1}H-NMR spectra of the mixture of isomers of **19** and the hydrogenated product **21** showing the disappearance of the signals corresponding to the protective groups and the olefin protons.

3.2.5 Introduction of the thiol moiety

Finally, the introduction of the thiol moiety in the molecule was tackled. With that aim, an already reported methodology was used consisting on the treatment of the bromo-derivative with potassium thioacetate in anhydrous DMF.[43] This procedure afforded the thioacetate precursor **22** in 85% yield (Scheme 3.10).

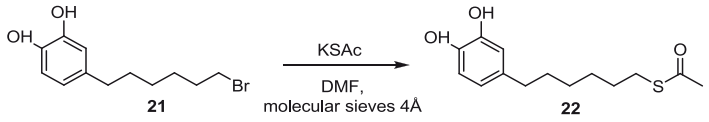

Scheme 3.10 Introduction of the thiol moiety as a thioacetate to obtain **22**.

After that, the hydrolysis of the thioacetate was carried out (Scheme 3.11). In previous synthetic work performed in our lab, the best results were obtained by performing the hydrolysis in a 1:1 mixture of EtOH and NaOH 0.2 M. However, in our case the use of these conditions afforded a mixture of the target thiol **3** (49% yield) and its corresponding disulphide **23** (21% of total weight), which could be separated by column chromatography. The overall performance of the reaction was improved by carrying out the hydrolysis in mild acidic media using MeOH containing a few drops of concentrated HCl, which provided **3** in higher yield (64%) and a diminished occurrence of the by-product **23** (13% of total weight). It was also observed that minimizing the amount of oxygen present in the solvent by bubbling Ar through it before carrying out the reaction led to a decrease in the amount of disulphide obtained.

In order to increase the overall yield of the synthesis, the reduction of the disulphide by-product **23** to the aimed thiol **3** was performed. The first methodology tested with this objective made use of metallic Zn in the presence of trifluoroacetic acid.[44] However, using this procedure total conversion was not achieved and the reactant was partially recovered along with the objective compound **3** (35% yield). Alternatively, by using tributyl phosphine as reducing agent in degassed methanol[45] the objective thiol **3** was obtained in 75% yield without compound **23** being observed in the crude (Scheme 3.11).

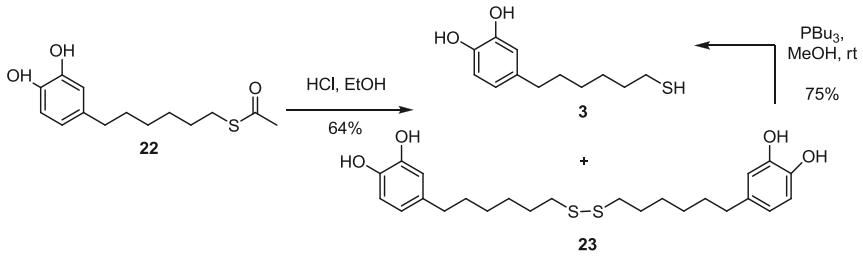

Scheme 3.11 Final steps towards the synthesis of the objective compound **3** including the hydrolysis of the thioacetate moiety and the reduction of the disulphide by-product **23** to the thiol.

Overall, we were able to synthesize the catechol-terminated thiol **3** in 9 steps with 16% overall yield. The product was obtained with high purity and used later on for self-assembly on gold surfaces, as detailed in Chapter 4.

3.3 Synthesis of the bifunctional ligand 4-(2-(pyridin-4-yl)ethyl)catechol, 4

The catechol moiety has been long known for its metal chelating and redox properties. Because of that, it has been widely used as redox-active ligand participating in valence-tautomeric (VT) processes.[10] Our group has a large experience in the synthesis and characterization of coordination polymer particles showing valence VT properties (VT-CPPs), as exposed earlier in this thesis.[26,46] As detailed in Section 3.1.2, the most commonly used strategy for the construction of such particles consists in combining one metal ion and two ligands, one of them acting as a redox-active unit (catechol) and the other (usually bis-pyridine or bis-imidazole) as linker between the metal centres. One of the objectives of this thesis was to obtain VT-CPPs using a single ligand that showed both redox-active properties and bridging capabilities. Therefore, compound **4** was chosen as target molecule to obtain a new hetero-ditopic ligand bearing a catechol moiety (redox-active) and a non-electroactive coordination moiety (bridging), in this case a pyridine unit.

The synthetic strategy was based in the procedure described in Section 3.2. As already mentioned, the intermediate **13** was designed to be used as a common precursor of a family of catechol derivatives. Therefore the retrosynthetic analysis that appears in Scheme 3.12 shows how the objective compound **4** could be obtained through the combination of two fragments, **13** and **24**, each one bearing one of the functionalities present in the final ditopic ligand.

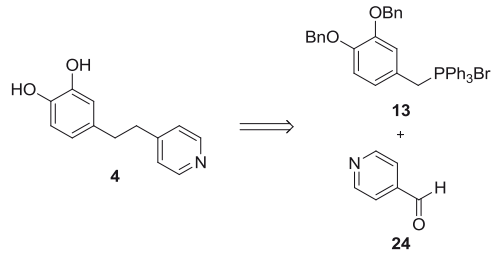

Scheme 3.12 Retrosynthetic analysis of the bifunctional ligand **4**

3.3.1 Synthesis of the olefin mixture (Z)- and (E)-25

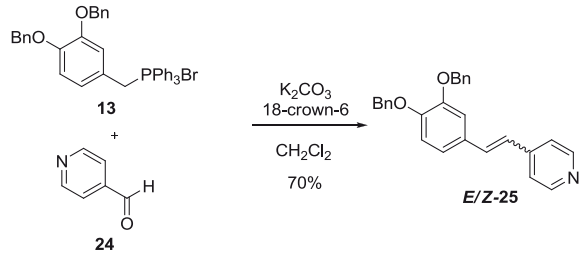

Scheme 3.13 Synthesis of the mixture of olefins *E*- and *Z*-**25**.

The first step of the synthesis that was performed was the Wittig reaction between the phosphonium ylide derived from **13** and the commercially available 4-pyridinecarboxaldehyde, **24**. With that aim, the reaction conditions previously optimized were used; i.e. an excess of K_2CO_3 as a base in refluxing CH_2Cl_2 in the presence of a small amount of 18-crown-6-ether (Scheme 3.13). The reaction was carried out overnight and the crude was purified by column chromatography, providing a 1:1 mixture of the *(Z)*- and *(E)*-isomers of the olefin **25** in 70% yield.

3.3.2 Synthesis of the ditopic ligand 4

The second and last step towards the obtention of the ligand **4** consisted in the deprotection of the hydroxyl groups with concomitant reduction of the double bond, which was achieved by hydrogenation using a palladium catalyst. In this case, the mixture of olefins was dissolved in MeOH and ammonium formate was added as a source of hydrogen in the presence of Pd supported on carbon. The reaction mixture was kept under reflux for

three hours and then the catalyst was removed by filtering through a Celite® pad (Scheme 3.14).

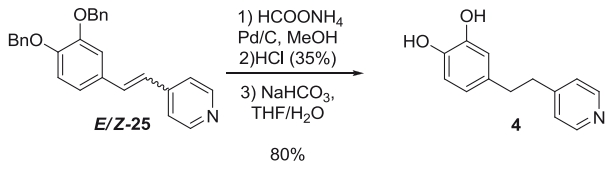

Scheme 3.14 Hydrogenation of the olefin precursor to obtain the objective ligand, **4**.

The most significant difficulty that was encountered in this step was the purification of the objective compound **4**. This catechol-pyridine, a small molecule slightly soluble in water, resulted hard to separate from the remaining ammonium formate. A somewhat simple solution was found to overcome this problem, just by allowing the reaction to continue for a slightly longer time, between 4 and 5 hours; in that way all the ammonium formate was decomposed and it was not necessary to separate it from the product, which was obtained in 80% yield.

In Figure 3.4 the ^{1}H-NMR spectra of the *(Z)*-**25** before the hydrogenation (a) is shown together with the spectra obtained from the crude of the hydrogenation reaction after refluxing for 3 hours (b) and for 5 hours (c). It can be clearly seen that the signals corresponding to the olefinic protons and those of the protecting groups are not present in the spectra of the reduced products. Also, in spectrum (b) a signal appears at δ 8.5 ppm, corresponding to the proton in the formate anion. This signal is not present in spectrum (c), probing that a longer reaction time resulted in complete decomposition of the ammonium formate.

Once the reaction was completed and the catalyst removed, the final product was precipitated from MeOH by adding a few drops of concentrated HCl. This afforded the pyridinium salt derivative of the desired ligand that was filtered and washed with MeOH. In order to recover the deprotonated form of the ligand, the pyridinium derivative was dissolved in THF and mixed with an equivalent of $NaHCO_3$ under nitrogen atmosphere, resulting in the quantitative conversion to the neutral form of the ligand that was then used for the synthesis of VT-CPPs.

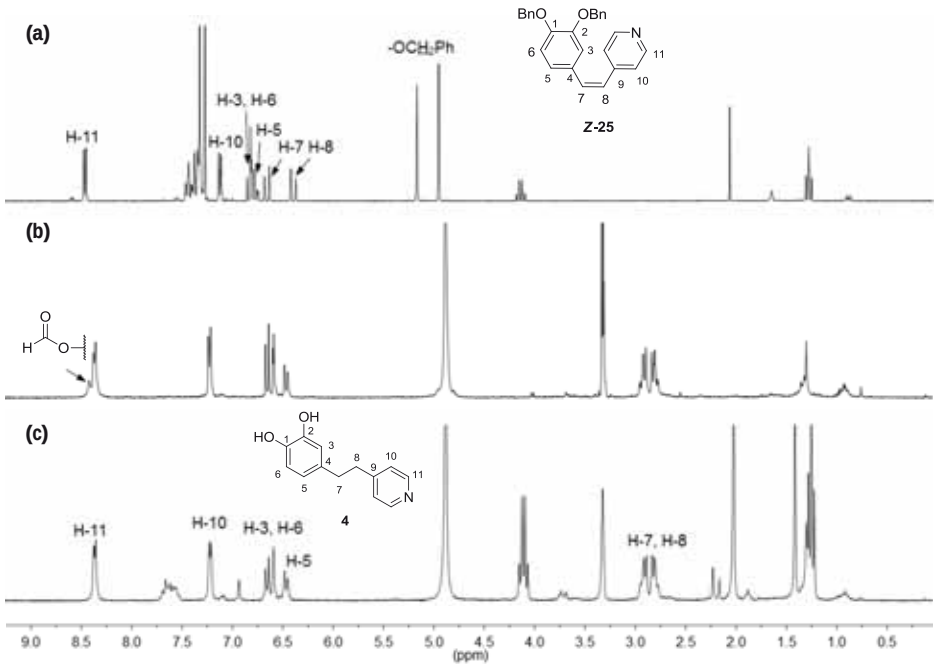

Figure 3.4 (a) ^{1}H-NMR spectra in $CDCl_3$ of the protected olefin ***(Z)*-25** before the hydrogenation. (b) ^{1}H-NMR spectra in MeOD of the reaction crude after performing the hydrogenation under reflux for 3 hours. The presence of a small amount of ammonium formate was still observed after that time. (c) ^{1}H-NMR spectra in MeOD of the reaction crude after performing the hydrogenation under reflux for 5 hours. In this case the ammonium formate was completely decomposed and its characteristic signal was not observed.

Overall, we were able to synthesize the bifunctional ligand **4** in 56% overall yield (from **13**) in two simple steps taking advantage from our previous work.

3.4 Synthesis and characterization of valence-tautomeric coordination polymer particles, CPP1

Once ligand **4** was obtained we moved on to the synthesis of the nanoscale coordination polymer particles (from here on, **CPP1**) obtained through the reaction of the bifunctional ligand with a cobalt salt. The following experiments were carried out in collaboration with Dr. Fernando Novio, from ICN2. An aqueous solution of $Co(COOCH_3)_2$ was mixed with an ethanolic solution of **4** (2 equivalents) under magnetic stirring (800 rpm) (Figure 3.5). The coordination reaction took place spontaneously and a dark precipitate started to appear almost immediately. The precipitate was collected after 30 minutes, washed several times with H_2O and EtOH and dried under vacuum. Examination of the

resulting material under FE-SEM revealed the formation of spherical particles with diameters ranging between 60 and 130 nm (mean size 110 nm).

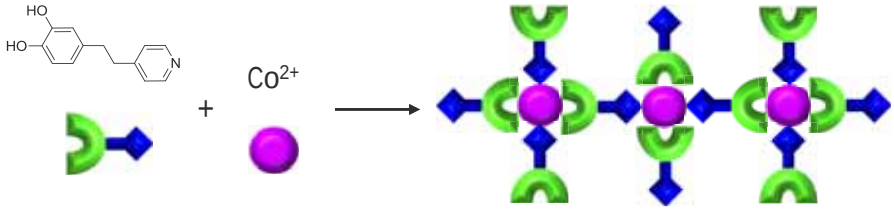

Figure 3.5 Synthesis of **CPP1** by reaction of the ditopic ligand **4** and $Co(COOCH_3)_2$. The connectivity represented in the final structure is tentative.

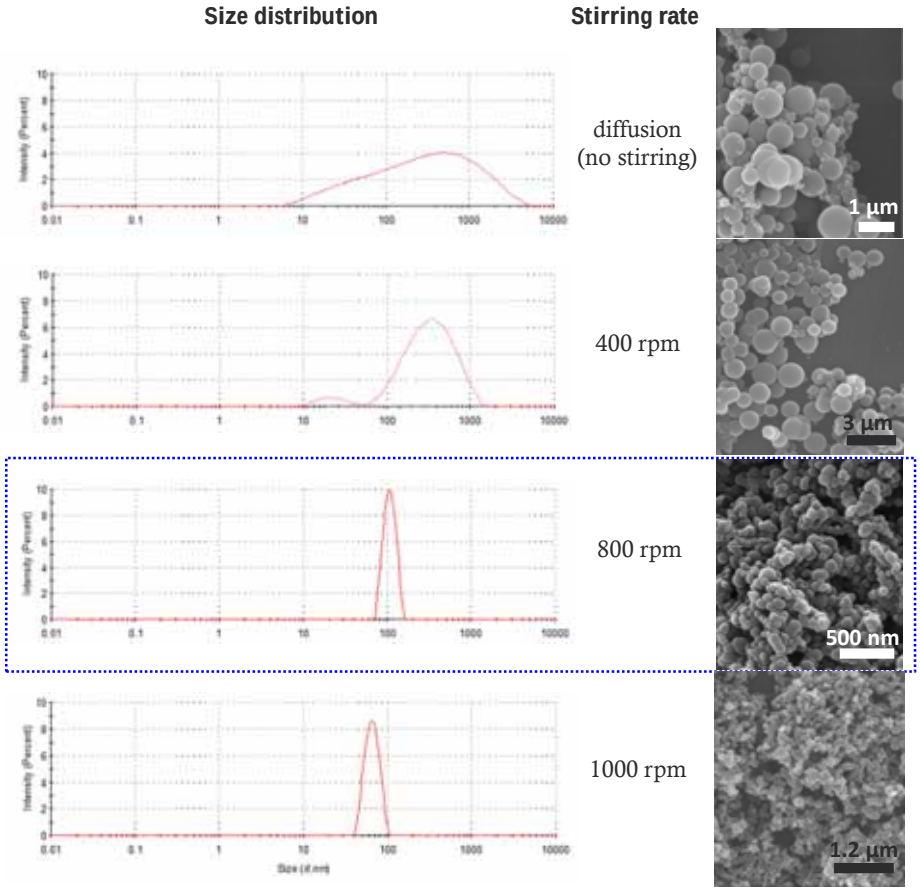

Figure 3.6 Series of experiments performed for the synthesis of **CPP1** using different stirring rates, particles with different dimensions were obtained in this way. We have highlighted the conditions used for the preparation of the material employed in the subsequent experiments.

CPPs are considered highly versatile materials, not only because of the possibility of introducing an enormous amount of functionalities on their structure but also because of their size tuneability.[26,32,47] The dimensions of **CPP1** particles could be controlled by regulating the stirring rate; in that way, using high stirring speeds resulted in the formation of smaller particles. On the other hand, when the metal and ligand solutions were mixed by diffusion and stirring was avoided, bigger nanoparticles with a high dispersion in size were obtained (Figure 3.6). The different batches of nanoparticles were analysed through X-ray powder diffraction, which showed the amorphous nature of the material (see the Annex). Unfortunately, this prevented a precise determination of the structural connectivity between the ligands and the metal ion.

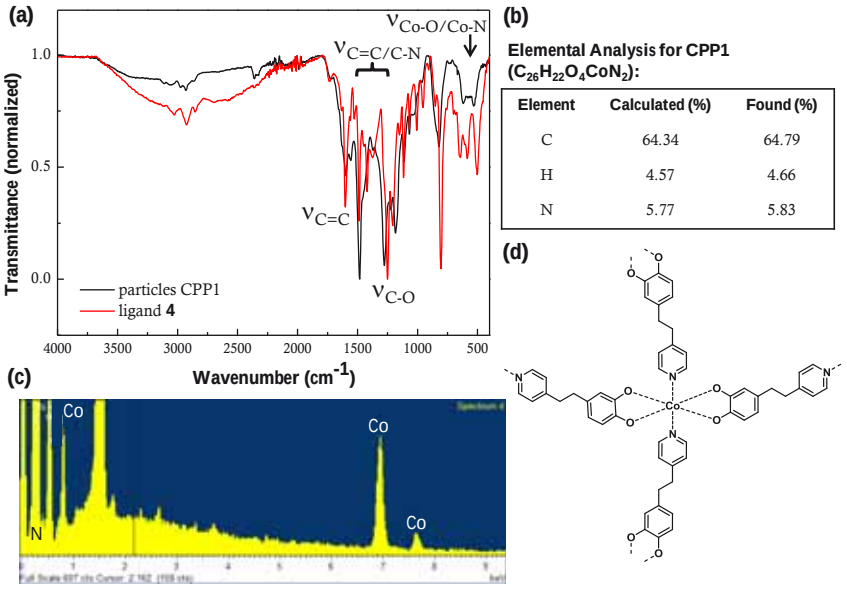

Figure 3.7 (a) IR-ATR spectra of **4** and **CPP1** showing the shifting of the bands upon coordination. (b) Elemental analysis results showing good agreement between the expected and obtained results. (c) EDX spectra of **CPP1** denoting the presence of cobalt. (d) Tentative connectivity of **CPP1**.

The infrared spectra of the obtained particles showed the displacement of the bands attributed to the C-O stretching of the catechol ring (1280-1250 cm^{-1} range) with respect to the free ligand **4**. Also, the signals corresponding to the C=C and C-N stretching modes (1530-1400 cm^{-1}) and the bands in the 900-750 cm^{-1} range, attributed to the C–H bending in the aromatic ring, were slightly shifted. The signals appearing in the 700-500 cm^{-1} region were attributed to Co-O and Co-N vibrations (Figure 3.7a).[46] The elemental analysis was consistent with the stequiometry of the proposed polymeric structure, which corresponds to 2 ligands per each metal centre (Figure 3.7b) and Energy Dispersive X-ray spectroscopy

(EDX) confirmed that the material contained cobalt, carbon, oxygen, and nitrogen (Figure 3.7c). Although all these results point towards the formation of a polymeric structure composed of six-coordinate complex units having two chelating catechols (Co-dioxolene rings) and two Co-N bonds per metal centre (as depicted in Figure 3.7d) this can only be tentatively suggested due to the lack of an informative X-Ray diffraction pattern. The thermogravimetric analysis (TGA) performed under N_2 atmosphere indicated a good stability up to 175 °C with only a small weight loss of around 5% at temperatures over 75 °C, tentatively assigned to the evaporation of entrapped solvent (water or most likely ethanol) within the polymer. From 175 to 325 ºC a gradual weight loss attributed to the decomposition of **4** was observed and a sudden thermal decomposition of the material occurred at 400 ºC (see Annex).

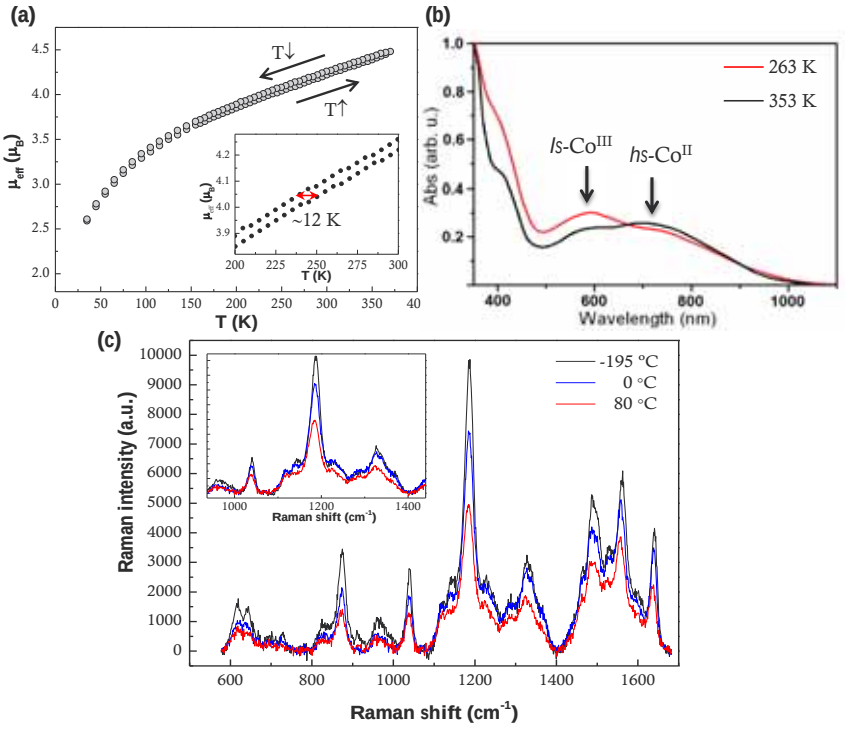

Figure 3.8 (a) Variable-temperature magnetization measurements of **CPP1** in the 35-370 K temperature range. Inset: Difference in the measured μ_{eff} between heating (bottom line) and cooling (upper line) processes. The arrow in the inset figure shows the maximum width of thermal hysteresis, ca. 12 K at 250 K. (b) Absorption spectra of **CPP1** nanoparticles in toluene at 263 K (red) and 353 K (black) showing the characteristic band at 590 nm for *ls*-Co^{III} isomer and the band at 740 nm corresponding to the *hs*-Co^{II} isomer.(c) Raman spectra of **CPP1** particles recorded at different temperatures showing an increase in intensity of the signals related to the ligand vibrations with decreasing temperature.

Finally, the VT interconversion of the material was explored in the 35-370 K temperature range (see Figure 3.8). At the highest experimental temperature, **CPP1** showed a μ_{eff} value of 4.4 μ_B, within the range of expected values for an S= 3/2+2×1/2 (*hs*-Co^{II}) species with a large orbital contribution (4.1-5.2 μ_B)[48] and in agreement with the values reported for other similar VT compounds in the *hs*-Co^{II} state.[49,50] Upon cooling, the μ_{eff} value monotonically decreased to 2.6 μ_B at 35 K. A fit to a line through the lowest temperature points determined a y-intercept around 1.90 μ_B, close to the 1.73 μ_B theoretical value for an S=1/2 (*ls*-Co^{III}) ground state.[48,49] The gradual interconversion, which is commonly observed in non-crystalline phases and tautomeric coordination polymers,[16,26,33,51,52] was tentatively attributed to the gradual interconversion from the *hs*-Co^{II} to the *ls*-Co^{III} isomer in the different metal centres together with spin-orbit coupling effects[53] or the presence of an additional structural transition.[54] Additionally, small thermal hysteresis effects were observed by subjecting the nanoparticles to thermal cycling over the whole temperature range (see inset in Figure 3.8a). The curves corresponding to increasing and decreasing temperature differed by almost 12 K at the midpoints. Such hysteresis was reproducible over repeated cycles and was independent of the sweeping rate, which discarded any influence of small composition variations or a spin frustration mechanism.

The VT interconversion was confirmed using UV-Vis spectroscopy. The spectrum of a dispersion of **CPP1** particles in toluene was recorded at two different temperatures and appears in Figure 3.8b. In both spectra the bands corresponding to the *ls*-Co^{III} isomer (590 nm) and the *hs*-Co^{II} isomer (740 nm) were observed. With increasing temperature the intensity of the band at 590 nm decreased while the band at 740 nm became more intense, in agreement with the existence of VT equilibrium.[32,55,56] Additionally, we attempted the characterization of the VT using Raman spectroscopy. This technique has been successfully used for the characterization of spin-crossover transitions, closely related to VT.[57–59] The bands observed in the Raman spectrum of **CPP1** were assigned to the bending mode of the C-H bond in the aromatic ring (1190 cm^{-1}) and the stretching of the aromatic C-C bonds (1320 cm^{-1}). The low intensity signal at around 630 cm^{-1} was assigned to the Co-O bond.[60] In the assessment of spin-crossover transitions, the shifting of the low frequency bands (< 600 cm^{-1}) is normally used to study the interconversion.[57,58] The bands at higher frequencies correspond to intraligand vibrations and are less affected by the spin conversion of the metallic centres, thus their positions are not shifted but changes in the intensity of some of these bands can be observed. In our case, a slight increase in the intensity of the signals assigned to catecholate vibrations was observed as the temperature decreased, (Figure 3.8c) which could be attributed to an increase of the *ls*-Co^{III} isomer population at low

temperatures.[59] However, the observed differences were very small and we cannot fully affirm that those changes were related to the VT process. The assessment of the VT behaviour of CPPs using Raman spectroscopy will be an exciting challenge to face in the future.

The observation of VT on the **CPP1** nanoparticles is not only important for their application in future molecular electronic devices but also for the structural characterization of the material. Indeed, even though the amorphous nature of **CPP1** nanoparticles precluded any accurate structural characterization by classical diffraction techniques, the occurrence of VT corroborates the expected [Co(nitrogen)(*o*-quinone)] connectivity required to ensure the energy balance between the antibonding orbital (e_g* orbital) of the metal ion and the frontier orbitals of catechol ligands necessary for the intramolecular electron transfer.[15,61]

3.5 Summary

In this chapter we have described the synthesis of two new catechol derivatives; the catechol-terminated alkanethiol **3** and the bifunctional ligand **4**. Both compounds were obtained with high overall yields following a convergent synthetic strategy through the common intermediate **13**. This key intermediate was easily synthesized in three steps with high yields (Scheme 3.15) and could be obtained in multigram amounts and stored for long periods of time. In following chapters (Chapter 4), we will describe the use of compound **3** for the formation of catechol-terminated SAMs on gold surfaces and gold nanoparticles, together with the study of the interfacial properties of the resulting materials.

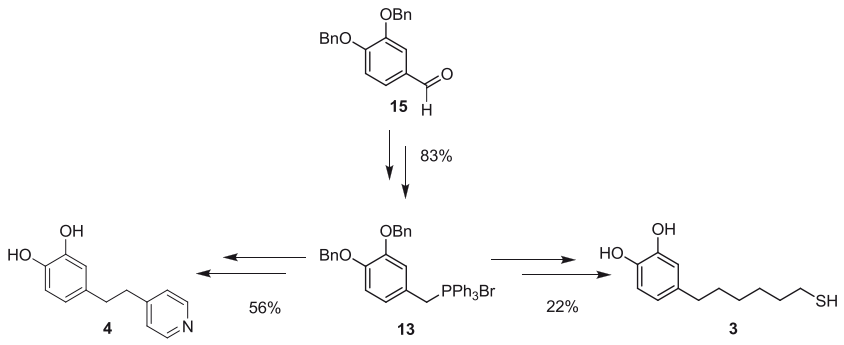

Scheme 3.15 Summary of the synthesis of the two objective compounds, the catechol-terminated thiol **3** and the bifunctional ligand **4**

We have also described the synthesis of VT-CPPs using the custom-designed ligand **4**, which combines polymerizing and redox-active properties. The coordination of **4** upon reaction with a Co^{2+} salt and its subsequent polymerization and precipitation lead to the formation of nanoparticles a few hundred nanometers in diameter exhibiting a gradual VT interconversion upon temperature variation. Significantly, a small hysteresis effect was observed probably related to the cooperative effect between valence tautomeric units forming the coordination polymer. The difference measured at the midpoints of the cooling and heating curves was almost 12 K, which is close to the hysteresis measured using bis-catecholate ligands.[33,54] This observation, suggests the need for the catechol to be involved in the polymerization process to induce the hysteresis effect. These promising results obtained in bulk will be applied later to the confined synthesis of **CPP1** in femtolitre-sized droplets fabricated using direct-write AFM-assisted lithography (See Chapter 5).

3.6 Experimental section

All commercially available reagents were used as received. Solvents were dried by distillation over the appropriate drying agents: CH_2Cl_2 (CaH_2), THF (Na^0). When needed, reactions were performed avoiding moisture by standard procedures and under N_2 atmosphere.

In NMR spectroscopy proton chemical shifts (δ) are reported in ppm ($CDCl_3$, 7.26 ppm, MeOH-d_4, 3.31 ppm and DMSO-d_6, 2.50 ppm). Carbon chemical shifts are reported in ppm ($CDCl_3$, 77.16 ppm, MeOH-d_4, 49.00 ppm and DMSO-d_6, 39.52 ppm). NMR signals were assigned with the help of COSY, DEPT 135 HSQC, and HMBC experiments. All spectra were measured at 298 K.

The abbreviations used to describe signal multiplicities are: s (singlet), br s (broad singlet), d (doublet), t (triplet), q (quartet), dd (double doublet), qd (quadruple doublet), m (multiplet), and *J* (coupling constant).

Further information of the equipment and procedures used for characterization can be found in Chapter 7. The NMR and IR spectra of the intermediates are provided in the Annex.

3.6.1 Synthesis of 4-(6'-mercaptohexyl)catechol, 3

*3.6.1.1 Synthesis of [3,4-bis(benzyloxy)phenyl]methanol, **16***

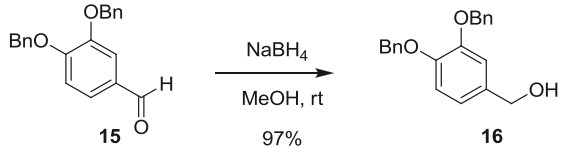

To a stirred solution of 3,4-bis(benzyloxy)-benzaldehyde (5.03 g, 15.8 mmol) in MeOH (72 mL) at 0 ºC, sodium borohydride (1.6 g, 42.3 mmol) was added in small portions and the reaction mixture was stirred for 4 h, allowing it to warm to room temperature. At this time, the reaction was quenched by the addition of saturated $NaHCO_3$ solution (30 mL diluted with 30 mL of water), and extracted with $CHCl_3$ (4 x 30 mL). The combined organic extracts were dried ($MgSO_4$), filtered and concentrated under reduced

pressure to furnish the target alcohol (4.9 g, 15.3 mmol, 97% yield) as a white solid. The ^{1}H- and ^{13}C-NMR spectra of the product were in good agreement with previously reported data.[36,62]

^{1}H NMR (360 MHz, $CDCl_3$) δ 7.46 (t, *J* = 6.6 Hz, 4H: H-Ar benzyl), 7,41-7.7.27 (m, 6H: H-Ar benzyl), 7.00 (s, 1H: H-3), 6.92 (d, *J* = 8.1 Hz, 1H: H-6), 6.85 (d, *J* = 8.1 Hz, 1H: H-5), 5.16 (s, 4H: -OCH_2Ph), 4.55 (s, 2H: H-1'), 1.82 (bs, 1H: -OH).

3.6.1.2 Synthesis of 1,2-bis(benzyloxy)-4-(bromomethyl)benzene, ***17***

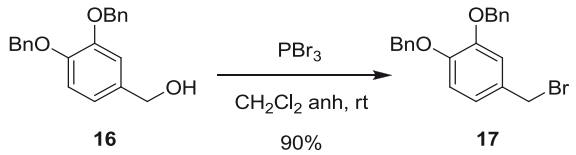

16 **17**

To a solution of [3,4-bis(benzyloxy)phenyl]-methanol, **16** (4.35 g, 13.6 mmol) in anhydrous CH_2Cl_2 (85 mL) at 0 ºC, phosphorus tribromide (2.7 mL, 28.7 mmol) was added dropwise under nitrogen atmosphere. The mixture was allowed to warm to room temperature and stirred for 3 h. Then, it was quenched by the addition of water (65 mL), and the aqueous phase was extracted with $CHCl_3$ (3 x 63 mL). The combined organic extracts were washed with brine (2 x 40 mL), dried ($MgSO_4$), filtered and concentrated under reduced pressure to provide **17** (4.57 g, 11.9 mmol, 90% yield) as a pale brown solid. The ^{1}H- and ^{13}C-NMR spectra of the product were in good agreement with previously reported data.[36,62]

^{1}H NMR (250 MHz, $CDCl_3$) δ 7.48 – 7.30 (m, 10H: H-Ar benzyl), 7.00 (d, *J* = 1.8 Hz, 1H: H-3), 6.92 (dd, *J* = 8.2, 1.9 Hz, 1H: H-5), 6.87 (d, *J* = 8.2 Hz, 1H: H-6), 5.16 (s, 4H: -OCH_2Ph), 4.44 (s, 2H: H-1').

3.6.1.3 Synthesis of [3,4-bis(benzyloxy)benzyl](triphenyl)phosphonium bromide, ***13***

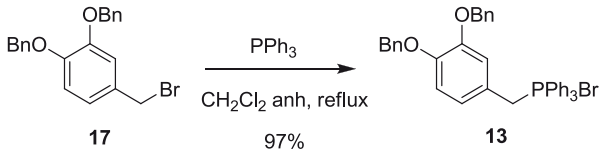

17 **13**

A solution of **17** (3.06 g, 7.98 mmol) and triphenylphosphine (2.77 g, 10.6 mmol) in anhydrous CH_2Cl_2 (30 mL) was refluxed under nitrogen atmosphere for 4 h. After allowing

the reaction mixture to cool to room temperature, the solvent was removed under reduced pressure. The resulting solid was washed with diethyl ether, filtered and dried to afford **13** (4.99 g, 7.73 mmol, 97% yield) as a white solid.[36]

^{1}H NMR (250 MHz, $CDCl_3$) δ 7.79 – 7.65 (m, 10H: H-PPh_3), 7.61 (dd, *J* = 7.3, 3.6 Hz, 5H: H-PPh_3), 7.40 – 7.26 (m, 10H: H-Ar benzyl), 6.89 (s, 1H: H-3), 6.67 (d, *J* = 8.1 Hz, 1H: H-6), 6.59 (d, *J* = 8.3 Hz, 1H: H-5), 5.38 (s, 1H: H-1'), 5.32 (s, 1H: H-1'), 5.06 (s, 2H: -OCH_2Ph), 4.80 (s, 2H: -OCH_2Ph).

3.5.1.4 Synthesis of 5-bromopentanal, ***14***

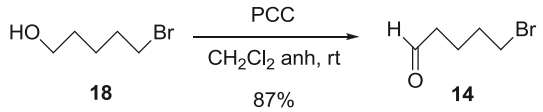

To a suspension of PCC (504 mg, 2.34 mmol) in anhydrous CH_2Cl_2 (15 mL) was added a solution of 5-bromo-1-pentanol, **18** (0.22 mL, 1.82 mmol) in anhydrous CH_2Cl_2 (5 mL) under nitrogen atmosphere. The mixture was stirred at room temperature for three hours and then 20 mL of Et_2O were added to the mixture and stirred for 10 min. The organic fraction was separated and the precipitate washed with Et_2O. The combined organic fractions were evaporated under reduced pressure to the half their original volume and then filtered over a Celite pad. After evaporation of the solvents 5-bromopentanal (262 mg, 1.58 mmol, 87% yield) was obtained as a pale yellow oil. The ^{1}H- and ^{13}C-NMR spectra of the product were in good agreement with previously reported data.[39,63]

^{1}H NMR (250 MHz, $CDCl_3$) δ 9.78 (s, 1H: -CHO), 3.41 (t, *J* = 6.4 Hz, 2H: H-5), 2.49 (td, *J* = 6.9, 1.0 Hz, 2H: H-2), 1.96 – 1.71 (m, 4H: H-3,4).

3.6.1.5 Synthesis of Z- and E-1,2-bis-(benzyloxy)-4-(6-bromo-1-hexenyl)benzene, ***19***

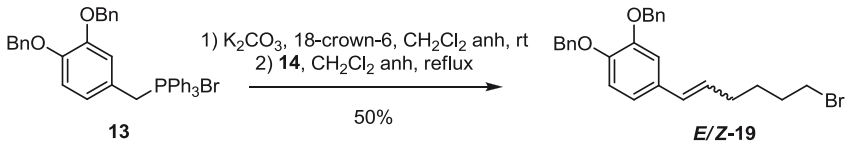

To a suspension of K_2CO_3 (1.76 g, 12.77 mmol) in dry CH_2Cl_2 (15 mL) was added a small amount of 18-crown-6-ether and **13** (1.75g, 2.71 mmol) under nitrogen atmosphere.

To the resulting mixture a solution of aldehyde **14** (362.2 mg, 2.19 mmol) in dry CH_2Cl_2 was added (5 mL) and the mixture was refluxed under nitrogen for 24 hours. After that time, the solvent was decanted and evaporated and the crude was purified by flash column chromatography (hexane/ EtOAc 97:3) to provide a mixture 1:1 of ***Z-*** and ***E*-19** (496 mg, 1.09 mmol, 50% yield) as a colorless oil.

***(Z)*-19: ^{1}H NMR** (400 MHz, $CDCl_3$) δ 7.46 (m, 4H: H-Ar benzyl), 7.40 – 7.28 (m, 6H: H-Ar benzyl), 6.91 (d, *J* = 8.3 Hz, 1H: H-6), 6.86 (d, *J* = 1.8 Hz, 1H: H-3), 6.79 (dd, *J* = 8.3, 1.9 Hz, 1H: H-5), 6.31 (d, *J* = 11.6 Hz, 1H: H-1'), 5.51 (dt, *J* = 11.6, 7.2 Hz, 1H: H-2'), 5.18 (s, 4H: -OCH_2Ph), 3.36 (t, *J* = 6.8 Hz, 2H: H-6'), 2.22 (qd, *J* = 7.3, 1.7 Hz, 2H: H-3'), 1.89 – 1.78 (m, 2H: H-4'), 1.58 – 1.49 (m, 2H: H-5').

^{13}C NMR (101 MHz, $CDCl_3$) δ 148.6 (C-2), 148.0 (C-1), 137.6, 137.5 (C-Ph), 131.4 (C-4), 131.0 (C-2'), 129.1 (C-1'), 128.6, 127.9, 127.9, 127.5, 127.4 (C-Ar benzyl), 122.3 (C-5), 116.2 (C-3), 115.0 (C-6), 71.6, 71.5 (-OCH_2Ph), 33.7 (C-6'), 32.4 (C-5'), 28.5 (C-4'), 27.6 (C-3').

(*E*)-19: **^{1}H NMR** (400 MHz, $CDCl_3$) δ 7.49 – 7.41 (m, 4H: H-Ar benzyl), 7.40 – 7.29 (m, 6H: H-Ar benzyl), 6.99 (d, *J* = 1.5 Hz, 1H: H-3), 6.88 (d, *J* = 8.3 Hz, 1H: H-6), 6.85 (dd, *J* = 8.3, 1.7 Hz, 1H: H-5), 6.29 (d, *J* = 15.8 Hz, 1H: H-1'), 6.01 (dt, *J* = 15.7, 6.9 Hz, 1H: H-2'), 5.16 (s, 2H: -OCH_2Ph), 5.14 (s, 2H: -OCH_2Ph), 3.43 (t, *J* = 6.8 Hz, 2H: H-6'), 2.22 (qd, *J* = 7.3, 1.2 Hz, 2H: H-3'), 1.96 – 1.87 (m, 2H: H-4'), 1.65-1.56 (m, 2H: H-5').

^{13}C NMR (101 MHz, $CDCl_3$) δ 149.4 (C-2), 148.6 (C-1), 137.6, 137.6 (C-Ph), 131.9 (C-4), 130.1 (C-2'), 128.6 (C-1'), 128.6, 127.9, 127.9, 127.6, 127.5 (C-Ar benzyl), 119.8 (C-5), 115.6 (C-3), 113.1 (C-6), 71.7, 71.7 (-OCH_2Ph), 33.7 (C-6'), 32.4 (C-5'), 32.1 (C-3'), 28.1 (C-4').

HRMS (ESI+) *m/z:* calcd for $C_{26}H_{27}BrO_2$: 475.1068 $[M+nNa]^+$; found: 475.1062.

IR (ATR): υ (cm^{-1}) 3031, 2925, 2857, 1735, 1601, 1023.

By-product 20: **^{1}H NMR** (360 MHz, $CDCl_3$) δ 7.46 (t, *J* = 7.1 Hz, 4H: H- Ar. benzyl), 7.41 – 7.27 (m, 6H: H-Ar. benzyl), 6.85 (d, *J* = 8.1 Hz, 1H: H-6), 6.80 (s, 1H: H-3), 6.69 (d, *J* = 8.0 Hz, 1H: H-5), 5.14 (d, *J* = 5.7 Hz, 4H: -OCH_2Ph), 2.27 (s, 3H: H-1').

^{13}C NMR (91 MHz, $CDCl_3$) δ 149.1 (C-2), 146.9 (C-1), 137.7, 137.6 (C-Ph), 131.6, 128.6, 128.6, 127.9, 127.8, 127.6, 127.5 (C-Ar benzyl), 121.9 (C-5), 116.3 (C-3), 115.7 (C-6), 71.8, 71.4 (C-OCH_2Ph), 21.1 (C-1').

HRMS (ESI+) *m/z:* calcd for $C_{21}H_{20}O_2$: 427.1356 $[M+nNa]^+$; found: 327.1349.

Mp: 42-44ºC ($CHCl_3$)

IR (ATR): υ (cm^{-1}) 2919, 2873, 1719, 1588.

3.6.1.6 Synthesis of 4-(6'-bromohexyl)catechol, ***21***

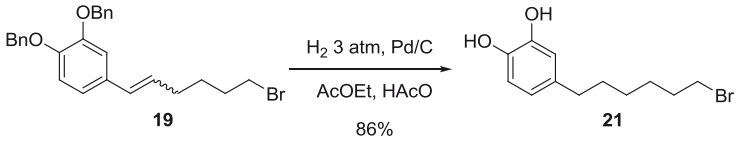

To a solution of a 1:1 mixture of ***Z-*** and ***E*-19** (436 mg, 0.965 mmol) in EtAcO, were added 10% Pd/C (235 mg) and a small amount of acetic acid (8 μL). The mixture was stirred at room temperature under hydrogen atmosphere (3 atm) for 24 hours. Then, the suspension was filtered over a Celite® pad and the filtrate was evaporated to dryness to obtain **21** (227.8mg, 0.832 mmol, 86% yield) as a white solid.

^{1}H NMR (360 MHz, $CDCl_3$) δ 6.77 (d, *J* = 8.0 Hz, 1H: H-6), 6.70 (d, *J* = 1.9 Hz, 1H= H-3), 6.61 (dd, *J* = 8.0, 1.9 Hz, 1H: H-5),5.47 (bs, 2H: -OH), 3.40 (t, *J* = 6.8 Hz, 2H: H-6'), 2.52 (t, *J* = 7.4 Hz, 2H: 1'), 1.92 – 1.78 (m, 2H: H-5'), 1.66 – 1.50 (m, 2H: H-2'), 1.50 – 1.24 (m, 4H: H-3',4').

^{13}C NMR (63 MHz, $CDCl_3$) δ 143.5 (C-2), 141.4 (C-1), 136.0 (C-4), 120.9 (C-5) , 115.7, 115.4 (C-3,6), 35.1 (C-1'), 34.12 (C-6'), 32.85 , 31.40 (C-2',5'), 28.4, 28.1 (C-3',4').

HRMS (ESI+) *m/z:* calcd for $C_{12}H_{17}O_2Br$: 271.0339 $[M+nNa]^+$; found: 271.0345.

Mp: 45-49ºC (MeOH)

IR (ATR): υ (cm^{-1}) 3328, 2930, 2856, 1606, 1110.

3.6.1.7 Synthesis of 4-(6'-thioacetyl)hexylcatechol, ***22***

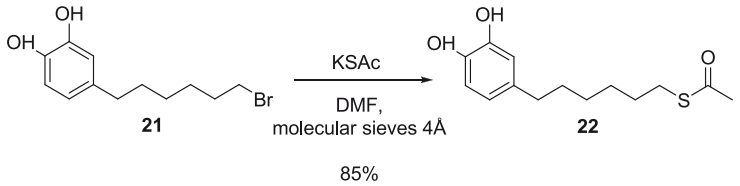

To a solution of 4-(6'-bromohexyl)catechol (258 mg, 0.945 mmol), **21** in anhydrous DMF (10 mL) were added 4Å molecular sieves and KSAc (195 mg, 1.707 mmol) under nitrogen atmosphere and the mixture was stirred at room temperature for six hours. Then,

15 mL of water were added and the aqueous phase was extracted with EtAcO (3x10 mL). The combined organic extracts where washed with water, dried ($MgSO_4$) and filtered. The crude obtained after evaporation of the solvent was purified by flash column chromatography (hexane/ EtAcO 4:1) to furnish 4-(7'-thioacetyl)hexylcatechol, **22 (**210 mg, 0.782 mmol, 85% yield) as a clear oil.

^{1}H NMR (250 MHz, $CDCl_3$) δ 6.77 (d, *J* = 8.0 Hz, 1H: H-6), 6.70 (d, *J* = 1.6 Hz, 1H: H-3), 6.58 (dd, *J* = 7.9, 1.5 Hz, 1H: H-5), 2.85 (t, *J* = 7.3 Hz, 2H: H-6'), 2.48 (t, *J* = 7.5 Hz, 2H: H-1'), 2.33 (s, 3H: -SC(O)CH_3), 1.65 – 1.28 (m, 8H: H-2',3',4',5').

^{13}C NMR (63 MHz, $CDCl_3$) δ 197.3 (-SC(O)), 143.6 (C-2), 141.6 (C-1), 135.8 (C-4), 120.8 (C-5), 115.6 (C-3), 115.3 (C-6), 35.1 (C-1'), 31.3 (C-6'), 30.8 (-SC(O)CH_3), 29.4, 29.3 (C-2',5'), 28.6, 28.6 (C-4',3').

HRMS (ESI+) *m/z:* calcd for $C_{14}H_{20}O_3S$: 267.1060 $[M+nNa]^+$; found: 267.1051.

IR (ATR): υ (cm^{-1}) 3370, 2928, 2855, 1664, 1606.

3.6.1.8 Synthesis of 4-(6'-mercaptohexyl)catechol, ***3***

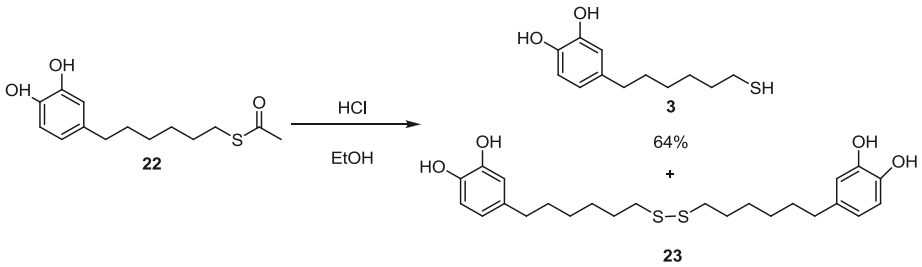

4-(6'-thioacetyl)hexylcatechol, **22** (240 mg, 0.894 mmol) was dissolved in degassed MeOH (20 mL), then a small amount (~10 drops) of concentrated HCl (35%) was added and the resulting solution was stirred under argon at room temperature for 24 hours. After that time, the crude was concentrated and 30 mL EtOAc were added and the organic phase was washed with water. The organic fraction was dried ($MgSO_4$), filtered and evaporated to dryness. The crude was purified by flash column chromatography (hexane/EtAcO 2:1) to provide **Y1** (130 mg, 0.57 mmol, 64% yield) together with the corresponding disulphide **23** (20 mg, 0.04 mmol).

3: ^{1}H NMR (250 MHz, MeOD): δ 6.65 (d, *J* = 8.0 Hz, 1H), 6.59 (d, *J* = 2.0 Hz, 1H), 6.47 (dd, *J* = 8.0, 2.0 Hz, 1H), 2.46(td, *J* = 7.3, 5.4 Hz, 4H), 1.65 – 1.48 (m, 4H), 1.48 – 1.23 (m, 4H).

^{13}C NMR (101 MHz, MeOD): δ 145.8 (C-2), 143.9 (C-1), 135.5 (C-4), 120.6 (C-5), 116.4 (C-6), 116.1 (C-3), 36.1 (C-1'), 35.1, 32.7 (C-2', 5'), 29.6, 29.2 (C-3', 4'), 24.9 (C-6').

HRMS (ESI-)*: m/z* calcd for $C_{12}H_{18}O_2S$: 225.0955 $[M\text{-}H^+]^-$; found: 225.0949.

Mp: 58-61ºC (EtOAc)

IR (ATR): υ (cm^{-1}) 3318, 2925, 2854, 2459, 1517, 874.

23: ^{1}H NMR (250 MHz, $CDCl_3$) δ 6.65 (d, *J* = 8.0 Hz, 1H: H-6), 6.60 (d, *J* = 2.0 Hz, 1H: H-3), 6.47 (dd, *J* = 8.0, 2.0 Hz, 1H: H-5), 2.66 (t, *J* = 7.2 Hz, 2H: H-6'), 2.45 (t, *J* = 7.5 Hz, 2H: H-1'), 1.73 – 1.48 (m, 4H: H-2', 5'), 1.48 – 1.25 (m, 4H: H-3', 4').

^{13}C NMR (63 MHz, $CDCl_3$) δ 146.0 (C-2), 144.1 (C-1), 135.6 (C-4), 120.6 (C-5), 116.5 (C-3), 116.2 (C-6), 39.8 (C-6'), 36.1 (C-1'), 32.7, 30.1 (C-2', 3'), 29.8 (C-3'), 29.3 (C-4').

HRMS (ESI+) *m/z:* calcd for $C_{24}H_{34}O_4S_2$: 449.1826 $[M+nNa]^+$; found: 449.1820.

Mp: 67-71ºC (EtOAc)

IR (ATR): υ (cm^{-1}) 3255, 2920, 2850, 1603.

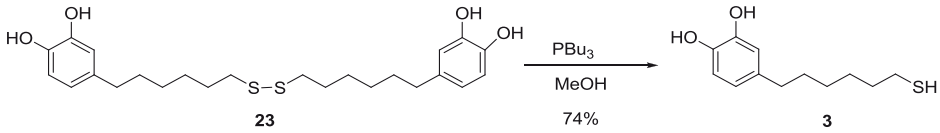

23 **3**

In order to improve the overall yield, the disulfide was reduced to obtain the thiol **3**. To a solution of **23** (21 mg, 0.047 mmol) in degassed MeOH (5 mL), was added PBu_3 (15 μL, 0.06 mmol) and the mixture was stirred at room temperature under argon atmosphere for four hours. Then, the reaction was quenched by the addition of water (5 mL) and the aqueous phase was extracted with EtAcO. The combined organic fractions were dried ($MgSO_4$), filtered and concentrated by evaporation under reduced pressure. The crude was purified by flash column chromatography (hexane/ EtOAc 2:1) to obtain **3** (16 mg, 0.07 mmol, 74% yield) as a white solid.

3.6.2 Synthesis of the bifunctional ligand 4-(2-(pyridin-4-yl)ethyl)catechol, 4

3.6.2.1 Synthesis of Z- and E-4-(2-(pyridin-4-yl)ethenyl)benzene-1,2-bis(benzyloxy), ***25***

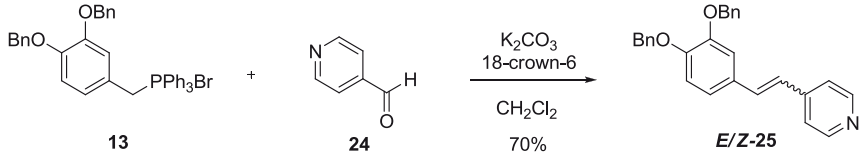

13 **24** ***E/Z*-25**

To a suspension of K_2CO_3 (0.522 g, 3.77 mmol) in dry CH_2Cl_2 (4 mL) was added a small amount of 18-crown-6-ether and **13** (0.527 g, 0.816 mmol) under nitrogen atmosphere. To the resulting mixture a solution of 4-pyridinecarboxaldehyde, **24** (70, 0.652 mmol) in dry CH_2Cl_2 (2 mL) was added and the mixture was refluxed under nitrogen for 24 hours. After that time, the solvent was evaporated and the crude was purified by flash column chromatography (hexane/ EtOAc 80:20) to provide a mixture 1:1 of ***Z-*** and ***E*-25** (219 mg, 0.557 mmol, 68% yield) as a colorless oil (*Z*-isomer) and white solid (*E*-isomer).

***Z*-(25): ^{1}H-NMR** (400 MHz, $CDCl_3$): δ 8.55 (s, 2H: H-11), 7.50 – 7.29 (m, 12H: H-Ar benzyl, H-10), 7.19 (d, *J* = 17.1 Hz, 1H: H-7), 7.16 (s, 1H: H-3), 7.07 (dd, *J* = 8.3, 1.9 Hz, 1H: H-5), 6.94 (d, *J* = 8.3 Hz, 1H: H-6), 6.81 (d, *J* = 16.2 Hz, 1H: H-8) , 5.22 (s, 2H: -OCH_2Ph), 5.20 (s, 2H: -OCH_2Ph).

^{13}C-NMR (100.6 MHz, $CDCl_3$): δ 150.2 (C-11), 149.9 (C-1), 149.2 (C-2), 145.0 (C-9), 137.2 (C-Ar benzyl), 137.1 (C-7), 132.1 (C-4), 129.9, 128.7, 128.7, 128.1, 128.0, 127.5, 127.4, (C- Ar benzyl) 124.4 (C-10), 121.5 (C-5), 120.8 (C-8), 114.9, 113.4 (C-3,6), 71.6, 71.3 (-OCH_2Ph).

***E*-(25): ^{1}H-NMR** (400 MHz, $CDCl_3$): δ 8.40 (d, *J* = 4.2 Hz, 2H: H-11), 7.44 – 7.16 (m, 10H: H- Ar benzyl), 7.06 (d, *J* = 5.6 Hz, 2H: H-10), 6.76 (m, 2H: H-3,6), 6.70 (dd, *J* = 8.3, 1.8 Hz, 1H: H-5), 6.58 (d, *J* = 12.2 Hz, 1H: H-7), 6.32 (d, *J* = 12.2 Hz, 1H: H-8), 5.09 (s, 2H: -OCH_2Ph), 4.88 (s, 2H: -OCH_2Ph).

^{13}C-NMR (100.6 MHz, $CDCl_3$): 149.8 (C-11), 148.8, 148.6 (C-1,2), 145.5 (C-9), 137.1, 137.0 (C-Ar benzyl), 133.6 (C-7), 129.4 (C-4), 128.6, 128.5, 127.9, 127.8, 127.3 (C-Ar benzyl), 127.2 (C-10), 126.3 (C-8), 123.6 (C-8), 122.6 (C-5), 115.3, 114.6 (C-3,6), 71.2, 71.1 (-CH_2Ph).

HRMS (ESI+): *m/z* calcd for $C_{27}H_{23}NO_2$: 394.1802 $[M+H]^+$; found: 394.1807

Mp: 126-130°C (EtOAc)

IR (ATR): υ (cm^{-1}) 3065, 3027, 2970, 2920, 2856, 1590, 1511, 1267, 1229, 967, 810, 731, 693.

3.6.2.2 Synthesis of 4-(2-(pyridin-4-yl)ethyl)catechol, ***4***

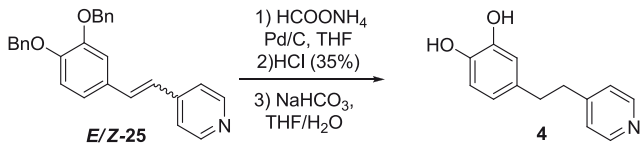

A 1:1 mixture of ***(Z)*-25** and ***(E)*-25** (439 mg, 1.11 mmols) was dissolved in 10 ml of THF. Then, ammonium formate (391 mg, 6.2 mmols) and Pd/C (111 mg) where added to the mixture and it was refluxed for four hours. Then, the suspension was filtered over a Celite pad and a few drops of HCl (35%) where added, resulting in the precipitation of the pyridinium derivative of the final product as a white solid that was filtrated and rinsed with THF (213 mg, 0.848 mmol, 82% yield). To deprotonate the salt, a suspension of the pyridinium chloride (20.4 mg, 0.081 mmols) in THF was prepared and $NaHCO_3$ (9.1 mg, 0.108 mmols) and a few drops of water were added and the mixture was stirred at room temperature under nitrogen for 10 minutes. Then the solvent was evaporated and compound **4** was obtained as a pale orange solid (17 mg, 85% yield)

4: ^{1}H-NMR (400 MHz, MeOD): δ 8.35 (d, *J* = 5.7 Hz, 2H: H-11), 7.20 (d, *J* = 6.1 Hz, 2H: H-10), 6.65 (d, *J* = 8.0 Hz, 1H: H-6), 6.58 (d, *J* = 2.0 Hz, 1H: H-3), 6.45 (dd, *J* = 8.0, 2.0 Hz, 1H: H-6), 2.90 (t, *J* = 7.4 Hz, 2H: H-8), 2.78 (t, *J* = 7.7 Hz, 2H: H-7).

^{13}C-NMR (100.6 MHz, MeOD): δ 153.9 (C-9), 149.6 (C-11), 146.2 (C-2), 144.6 (C-1), 133.6 (C-4), 125.8 (C-10), 120.8 (C-5), 116.6, 116.3 (C-3,6), 38.4, 36.9 (C-7,8).

HRMS (ESI+): *m/z* calcd for $C_{13}H_{14}NO_2$, 216.1019 $[M+H]^+$; found: 216.1025.

Mp: 170-174ºC (THF)

IR (ATR): υ (cm^{-1}) = 3028, 2923, 2853, 1632, 1602, 1527, 1486, 1250, 805.

4H$^+$Cl$^-$: ^{1}H-NMR (400 MHz, DMSO): δ 8.79 (d, *J* = 6.6 Hz, 2H: H-11), 7.88 (d, *J* = 6.5 Hz, 2H: H-10), 6.63 (d, *J* = 8.0 Hz, 1H: H-6), 6.59 (d, *J* = 2.0 Hz, 1H: H-3), 6.43 (dd, *J* = 8.0, 2.0 Hz, 1H: H-5), 3.11 (t, *J* = 7.7 Hz, 2H: H-8), 2.81 (t, *J* = 7.7 Hz, 2H: H-7).

^{13}C-NMR (100.6 MHz, DMSO): δ 162.3 (C-9), 145.1 (C-2), 143.6 (C-1), 141.0 (C-11), 130.6 (C-4), 127.0 (C-10), 118.1 (C-5), 115.9, 115.5 (C-3,6), 36.9, 34.4 (C-7,8).

HRMS (ESI+): *m/z* calcd for $C_{13}H_{15}NO_2$, 216.1019 $[M+H]^+$; found: 216.1028.

Mp: 173-180ºC (THF)

IR (ATR): υ(cm^{-1}) = 3336, 3197, 2690, 1633, 1610, 1528, 1503, 1202, 811.

3.6.3 Synthesis of VT coordination polymer particles, CPP1

An aqueous solution (4 mL) of $Co(COOCH_3)_2 \cdot 4H_2O$ (121.4 mg, 0.50 mmol) was added dropwise to a solution of the bifunctional ligand **4** (216.1 mg, 1 mmol) in EtOH (20 mL). A black precipitate formed immediately. After 30 min the precipitate was centrifuged and washed several times with water and EtOH, and dried under vacuum. The resulting solid product was obtained in 70% yield. SEM analysis showed the formation of spherical-shaped particles (mean size: 109 ± 12 nm), and XRD measurements indicate the amorphous nature of the particles.

IR (ATR) $\upsilon(cm^{-1})$ = 3350, 2957, 2924, 2856, 1597, 1482, 1277, 1222, 1184, 1112, 1068, 821, 620, 533.

Elemental Analysis: calcd for $C_{26}H_{22}O_4CoN_2$: C=64.34%; H=4.57%; N,=5.77%. Found: C=64.79%; H=4.66%; N=5.83%.

3.7 References

(1) Evangelio, E.; Hernando, J.; Imaz, I.; Bardají, G. G.; Alibés, R.; Busqué, F.; Ruiz-Molina, D. *Chem. Eur. J.* **2008**, *14*, 9754–9763.

(2) Martínez-Otero, A.; Evangelio, E.; Alibés, R.; Bourdelande, J. L.; Ruiz-Molina, D.; Busqué, F.; Hernando, J. *Langmuir* **2008**, *24*, 2963–2966.

(3) Martínez-Otero, A. Ph.D. Thesis, Universitat Autónoma de Barcelona, 2010.

(4) Saiz-Poseu, J.; Faraudo, J.; Figueras, A.; Alibés, R.; Busqué, F.; Ruiz-Molina, D. *Chem. Eur. J.* **2012**, *18*, 3056–3063.

(5) Saiz-Poseu, J.; Alcón, I.; Alibés, R.; Busqué, F.; Faraudo, J.; Ruiz-Molina, D. *CrystEngComm* **2012**, *14*, 264–271.

(6) Saiz-Poseu, J.; Sedó, J.; García, B.; Benaiges, C.; Parella, T.; Alibés, R.; Hernando, J.; Busqué, F.; Ruiz-Molina, D. *Adv. Mater.* **2013**, *25*, 2066–2070.

(7) García, B.; Saiz-Poseu, J.; Gras-Charles, R.; Hernando, J.; Alibés, R.; Novio, F.; Sedó, J.; Busqué, F.; Ruiz-Molina, D. *ACS Appl. Mater. Interfaces* **2014**, *6*, 17616–17625.

(8) Saiz-Poseu, J. Ph.D. Thesis, Universitat Autónoma de Barcelona, 2011.

(9) Busqué Sánchez, F.; Sedó Vegara, J.; Garcia Martínez, B.; Saiz Poseu, J.; Ruiz Molina, D. A process for preparing a material having hydrophobic and/or oleophobic properties and material thus obtained. EP2589578A1, 2013.

(10) Evangelio, E.; Ruiz-Molina, D. *Eur. J. Inorg. Chem.* **2005**, *2005*, 2957–2971.

(11) Tezgerevska, T.; Alley, K. G.; Boskovic, C. *Coord. Chem. Rev.* **2014**, *268*, 23–40.

(12) Roux, C.; Adams, D. M.; Itié, J. P.; Polian, A.; Hendrickson, D. N.; Verdaguer, M. *Inorg. Chem.* **1996**, *35*, 2846–2852.

(13) Sato, O.; Cui, A.; Matsuda, R.; Tao, J.; Hayami, S. *Acc. Chem. Res.* **2007**, *40*, 361–369.

(14) Nador, F.; Novio, F.; Ruiz-Molina, D. *Chem. Commun.* **2014**, *50*, 14570–14572.

(15) Gütlich, P.; Dei, A. *Angew. Chem. Int. Ed.* **1997**, *36*, 2734–2736.

(16) Evangelio, E.; Ruiz-Molina, D. *C. R. Chimie* **2008**, *11*, 1137–1154.

(17) Kahn, O.; Martinez, C. J. *Science* **1998**, *279*, 44–48.

(18) Schmidt, R. D.; Shultz, D. A.; Martin, J. D.; Boyle, P. D. *J. Am. Chem. Soc.* **2010**, *132*, 6261–6273.

(19) Pierpont, C. G. *Coord. Chem. Rev.* **2001**, *216-217*, 99–125.

(20) Jung, O.-S.; Jo, D. H.; Lee, Y.-A.; Conklin, B. J.; Pierpont, C. G. *Inorg. Chem.* **1997**, *36*, 19–24.

(21) Yu, F.; Xiang, M.; Wu, Q.; He, H.; Cheng, S.; Cai, X.; Li, A.; Zhang, Y.; Li, B. *Inorg. Chim. Acta* **2015**, *426*, 146–149.

(22) Li, B.; Tao, J.; Sun, H.-L.; Sato, O.; Huang, R.-B.; Zheng, L.-S. *Chem. Commun.* **2008**, *2*, 2269–2271.

(23) Tao, J.; Maruyama, H.; Sato, O. *J. Am. Chem. Soc.* **2006**, *128*, 1790–1791.

(24) Adams, D. M.; Dei, A.; Rheingold, A. L.; Hendrickson, D. N. *J. Am. Chem. Soc.* **1993**, *115*, 8221–8229.

(25) Schmidt, R. D.; Shultz, D. A.; Martin, J. D. *Inorg. Chem.* **2010**, *49*, 3162–3168.

(26) Imaz, I.; Maspoch, D.; Rodríguez-Blanco, C.; Pérez-Falcón, J.; Campo, J.; Ruiz-Molina, D. *Angew. Chem. Int. Ed.* **2008**, *47*, 1857–1860.

(27) Affronte, M.; Beni, A.; Dei, A.; Sorace, L. *Dalton Trans.* **2007**, 5253–5259.

(28) Cheng, W.-Q.; Li, G.-L.; Zhang, R.; Ni, Z.-H.; Wang, W.-F.; Sato, O. *J. Mol. Struct.* **2015**, *1087*, 68–72.

(29) Li, B.; Chen, L. Q.; Wei, R. J.; Tao, J.; Huang, R. Bin; Zheng, L. S.; Zheng, Z. *Inorg. Chem.* **2011**, *50*, 424–426.

(30) Jung, O.; Pierpont, C. G. *J. Am. Chem. Soc.* **1994**, *116*, 2229–2230.

(31) Chen, X.; Wei, R.; Zheng, L.; Tao, J. *Inorg. Chem.* **2014**, *53*, 13212–13219.

(32) Novio, F.; Campo, J.; Ruiz-Molina, D. *Inorg. Chem.* **2014**, *53*, 8742–8748.

(33) Bodnar, S. H.; Caneschi, A.; Dei, A.; Shultz, D. A.; Sorace, L. *Chem. Commun.* **2001**, 2150–2151.

(34) Kiriya, D.; Nakamura, K.; Kitagawa, S.; Chang, H.-C. *Chem. Commun.* **2010**, *46*, 3729–3731.

(35) Kiriya, D.; Chang, H. C.; Nakamura, K.; Tanaka, D.; Yoneda, K.; Kitagawa, S. *Chem. Mater.* **2009**, *21*, 1980–1988.

(36) Venkateswarlu, S.; Satyanarayana, B.; Sureshbabu, C. V; Subbaraju, G. V. *Biosci. Biotechnol. Biochem.* **2003**, *67*, 2463–2466.

(37) Motoshima, K.; Noguchi-Yachide, T.; Sugita, K.; Hashimoto, Y.; Ishikawa, M. *Bioorg. Med. Chem.* **2009**, *17*, 5001–5014.

(38) Alonso, F.; Riente, P.; Yus, M. *Eur. J. Org. Chem.* **2009**, *2009*, 6034–6042.

(39) Miesch, M.; Miesch, L.; Horvatovich, P.; Burnouf, D.; Delincée, H.; Hartwig, A.; Raul, F.; Werner, D.; Marchioni, E. *Radiat. Phys. Chem.* **2002**, *65*, 233–239.

(40) Kong, Y.; Grembecka, J.; Edler, M. C.; Hamel, E.; Mooberry, S. L.; Sabat, M.; Rieger, J.; Brown, M. L. *Chem. Biol.* **2005**, *12*, 1007–1014.

(41) Lautens, M.; Paquin, J.-F.; Piguel, S.; Dahlmann, M. *J. Org. Chem.* **2001**, *66*, 8127–8134.

(42) Sun, B.; Yuan, H.; Xi, G.; Ma, Y.; Lou, H. *Bioorg. Med. Chem.* **2009**, *17*, 4981–4989.

(43) Wijtmans, M.; Rosenthal, S. J.; Zwanenburg, B.; Porter, N. A. *J. Am. Chem. Soc.* **2006**, *128*, 11720–11726.

(44) Kelleman, A.; Mattern, R.-H.; Pierschbacher, M. D.; Goodman, M. *Biopolymers* **2003**, *71*, 686–695.

(45) Bourdier, T.; Fookes, C. J. R.; Pham, T. Q.; Greguric, I.; Katsifis, A. *J. Label. Compd. Radiopharm.* **2008**, *51*, 369–373.

(46) Novio, F.; Lorenzo, J.; Nador, F.; Wnuk, K.; Ruiz-Molina, D. *Chem. Eur. J.* **2014**, *20*, 15443–15450.

(47) Masoomi, M. Y.; Morsali, A. *RSC Adv.* **2013**, *3*, 19191–19218.

(48) Drago, R. S. *Physical Methods for Chemists. 2nd Edition*; Saunders College Pub.: Florida, 1992.

(49) Buchanan, R. M.; Pierpont, C. G. *J. Am. Chem. Soc.* **1980**, *102*, 4951–4957.

(50) Buchanan, R. M.; Fitzgerald, B. J.; Pierpont, C. G. *Inorg. Chem.* **1979**, *18*, 3439–3444.

(51) Evangelio, E.; Rodriguez-Blanco, C.; Coppel, Y.; Hendrickson, D. N.; Sutter, J. P.; Campo, J.; Ruiz-Molina, D. *Solid State Sci.* **2009**, *11*, 793–800.

(52) Chen, L.; Wei, R.; Tao, J.; Huang, R.; Zheng, L. *Sci. China Chem.* **2012**, *55*, 1037–1041.

(53) Lloret, F.; Julve, M.; Cano, J.; Ruiz-García, R.; Pardo, E. *Inorg. Chim. Acta* **2008**, *361*, 3432–3445.

(54) Beni, A.; Dei, A.; Shultz, D. A.; Sorace, L. *Chem. Phys. Lett.* **2006**, *428*, 400–404.

(55) Katayama, K.; Hirotsu, M.; Kinoshita, I.; Teki, Y. *Dalt. Trans.* **2014**, *43*, 13384.

(56) Novio, F.; Evangelio, E.; Vazquez-Mera, N.; González-Monje, P.; Bellido, E.; Mendes, S.; Kehagias, N.; Ruiz-Molina, D. *Sci. Rep.* **2013**, *3*, 1708.

(57) Bousseksou, A.; McGarvey, J. J.; Varret, F.; Real, J. A.; Tuchagues, J.-P.; Dennis, A. C.; Boillot, M. L. *Chem. Phys. Lett.* **2000**, *318*, 409–416.

(58) Moliner, N.; Salmon, L.; Capes, L.; Muñoz, M. C.; Létard, J.-F.; Bousseksou, A.; Tuchagues, J.; McGarvey, J. J.; Dennis, A. C.; Castro, M.; Burriel, R.; Real, J. A. *J. Phys. Chem. B* **2002**, *106*, 4276–4283.

(59) Molnár, G.; Niel, V.; Gaspar, A. B.; Real, J. a.; Zwick, A.; Bousseksou, A.; McGarvey, J. J. *J. Phys. Chem. B* **2002**, *106*, 9701–9707.

(60) Hartl, F.; Barbaro, P.; Bell, I. M.; Clark, R. J. H.; Snoeck, T. L.; Vlček, A. *Inorg. Chim. Acta* **1996**, *252*, 157–166.

(61) Tokarev, A.; Salmon, L.; Guari, Y.; Molnár, G.; Bousseksou, A. *New J. Chem.* **2011**, *35*, 2081.

(62) Brun, K. A.; Linden, A.; Heimgartner, H. *Helv. Chim. Acta* **2002**, *85*, 3422–3443.

(63) Dolbier Jr., W. R.; Rong, X. X.; Bartberger, M. D.; Koroniak, H.; Smart, B. E.; Yang, Z.-Y. *J. Chem. Soc. Perkin Trans. 2* **1998**, 219–232.

Chapter 4

Self-assembled monolayers as model systems for the study of the interfacial properties of catechols

In the following Chapter, the formation of molecular assemblies of the catechol-terminated thiol **3** on gold surfaces will be described. These materials will be used as a model to study the interfacial properties of the catechol moiety at the local scale by means of Force-distance curves and iron oxide nanoparticle assembly. Additionally, the attempts to use compound **3** to functionalize AuNPs will be reported.

4.1 Introduction

As already addressed in Chapter 1, the strong adhesion of mussels to surfaces is a relevant and intriguing phenomenon. This extraordinary ability of mussels has been generally attributed to the presence of high percentages of the aminoacid L-DOPA in their adhesive proteins and the elucidation of the adhesive forces exerted by catechol moieties has become a matter of general interest.[1] The surface interactions of the plaque proteins extracted directly from living mussels as well as of catechol-containing synthetic analogues have been extensively studied using the Surface Forces Apparatus (SFA).[2] A clear explanation on how DOPA imparts adhesiveness has not been extracted from these experiments, but metal bidentate surface complexation[3–6] and H-bonding[7–11] are assumed to be the stronger interactions whenever the adhesion takes place on purely inorganic surfaces like mica, Au or TiO_2. Other weak interactions such as electrostatic forces[12–14] or π-π stacking[7] can also participate in catechol-mediated adhesion.

Even though much information has been gathered on catechol adhesion after years of research, there are still a lot of questions to be answered. The large tendency of catechols to oxidize even under acidic conditions, together with the structural complexity of proteins and the variation between samples from different individuals, turns the study of the adhesive proteins and the establishment of structure-property relationships in a real challenge.[15] Most of the adhesion measurements reported in the literature to date were performed in complex systems like polymers or proteins containing multiple functional groups, but the studies reporting adhesion values exclusively of catechol moieties are still scarce.

4.1.1 Studies of the adhesion of the catechol group

One of the most direct approaches to understand catechol adhesion consists on the study at the single molecule level, where no cooperative effect or interference of other chemical functionalities can occur. Lee and co-workers reported the adhesion of a single DOPA residue for the first time in 2006.[16] In that work, the authors used an AFM tip functionalized with a single catechol moiety to record Force-distance (F-d) curves on different surfaces (Figure 4.1a). Forces of interaction as strong as 800 pN were measured between the catechol moiety and a TiO_2 surface, which were attributed to bidentate coordination of the Ti atoms by the catechol ring. As opposite, diminished adhesion was detected on the same substrate when the catechol moiety was oxidized to its quinone

counterpart. When the surface was functionalized with nucleophilic groups (amines), the quinone attached covalently to the surface through nucleophilic attack of the amines. Those results showed that the chemical versatility of the catechol-quinone system provides strong adhesion to both organic and inorganic substrates by forming covalent bonds on organic surfaces and reversible yet strong bonds on inorganic substrates (coordination or H-bonds).

Two independent studies were released more recently in which catechol-containing polymers were gradually detached form the surface using an AFM tip in order to detect and measure single catechol-surface interaction ruptures (Figure 4.1b).[17,18] Interestingly, both reported similar interaction forces between 60 and 90 pN, which considerably differ from the values measured earlier by Lee and co-workers. However, these adhesion values agree much better with the occurrence of interactions such as H-bonds and bidentate coordination to the substrates. An explanation for the discrepancy between these results has not been suggested.

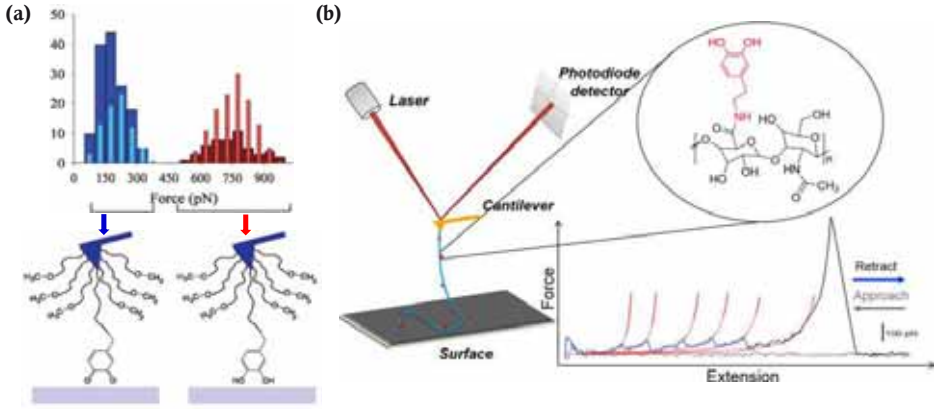

Figure 4.1 (a) Single-molecule interaction force measurements of a catechol and a quinone moiety over TiO_2. The adhesion force measured for the catechol was higher than that of the quinone counterpart. (b) Scheme of single molecule AFM experiments on DOPA−surface interactions using a catechol-modified polymer (Hyaluronan). Using this methodology, detachment events were detected individually. Reproduced from ref. 16 and ref. 18.

In order to gain deeper understanding of the basic behaviour of catechols and their interaction with surfaces, our group reported the study of the adsorption and self-assembly of long chain alkylcatechols on surfaces using Scanning Tunnelling Microscopy (STM) and Molecular Dynamics (MD) simulations. The obtained results indicated that alkylcatechols had a high tendency to adsorb onto surfaces with their aromatic rings oriented parallel to the substrate (flat position). The assembly process was driven by energetic factors related to the adsorption of the molecules on the substrate and highly affected by the solvent, which

seemed to play a crucial role.[19] Moreover, the temperature was also a decisive parameter that could be used to switch between two different self-assembly patterns.[20]

As we have summarized here, significant efforts have been made towards the elucidation of the mechanisms that rule the strong interaction of catechols with surfaces, going from the study of proteins secreted by mussels[21] to the measurement of single molecule interactions.[16–18] It is known that in mussel adhesion the interfacial chemistry of catechols plays a key role; as a consequence, exploring ways to introduce this moiety at the interface of synthetic materials is essential for the design of biomimetic interfaces with adhesive properties. With this perspective, in the present thesis the use of self-assembled monolayers (SAMs) on flat and curved surfaces was suggested as an alternative approach to gain deeper understanding of the interfacial properties of the catechol moiety using ideal model systems. Our approach also explored a different way of introducing this moiety at the interface of synthetic materials with control over the order and orientation of the catechol groups, which is not possible when polymeric coatings are used. In the following pages we provide basic information on SAMs on both flat surfaces and nanoparticles.

4.1.2 Self-assembled monolayers: formation and structure

Self-assembled monolayers are organic assemblies formed by the adsorption of molecular constituents from solution or the gas phase onto the surface of solids or in regular arrays on the surface of liquids. SAMs obtained on flat substrates are used to place specific functionalities at the interface or modify the properties of the surface.[22] When SAMs are formed on the surface of nanoparticles they play a dual role; they present functional groups at the interfaces and simultaneously stabilize the nanoparticles, which is essential to maintain their size-dependent properties.[23]

The molecules that form SAMs have normally three structural components, as represented in Figure 4.2: the headgroup anchors the adsorbate to the substrate, the methylene spacer stabilizes the monolayer and the tailgroup (located at the outer interface) provides functionality to the surface. There are a number of headgroups that bind strongly to specific substrates but the most extensively studied family of SAMs derives from the adsorption of alkanethiols on gold surfaces.[22]

The first contribution to a stable thin film formed at an air/solid or liquid/solid interface comes from the attachment of the headgroup to the surface, as the anchoring of the individual adsorbates provides significant stability. Concretely, the Au-S bond strength has

been calculated to be between 40 and 50 kcal/mol.[24] To minimize the free energy of the organic layer, the molecules adopt conformations that maximize the van der Waals attractive forces between the organic chains until they reach a quasi-crystalline structure. In alkanethiol monolayers on gold surfaces the stabilizing interactions are maximized when the fully extended chains are slightly tilted from the surface normal by an angle of ~30º. In general, purely hydrocarbon chains are preferred to form stable monolayers although amide moieties present in the chains can provide additional stability thanks to the occurrence of H-bonds between the chains.[25] It is generally accepted that long methylene chains (n>10) provide more robust assemblies because of the additive effect of the lateral interchain van der Waals forces.[22]

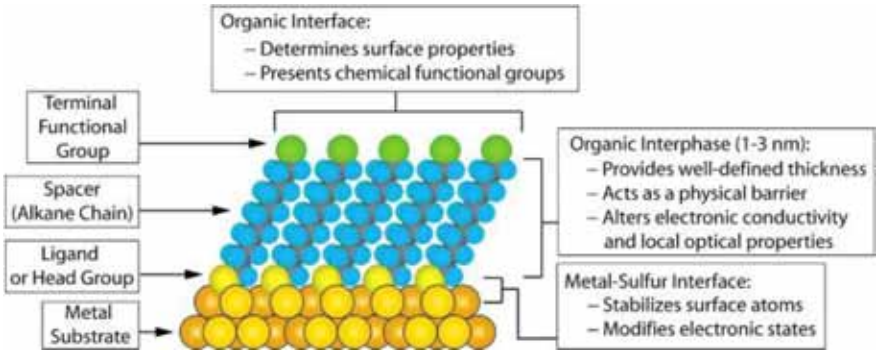

Figure 4.2 Schematic representation of an ideal SAM of alkanethiolates on Au. The characteristics of each part of the SAM are highlighted. Reproduced from ref. 22.

When SAMs are formed on nanoparticle surfaces however, their structure is strongly influenced by the amount of defects on the surface and its curvature. Due to the higher percentage of atoms present at the surface, AuNPs tend to have higher coverage densities than SAMs formed on planar substrates.[26] Also, as a consequence of the high surface curvature of nanoparticles, there is a decrease in the chain density moving away from the surface because the chains occupy a conical segment. This is translated into an enhanced mobility of the terminal groups (Figure 4.3), that acquire a liquid-like behaviour.[27] It has been demonstrated that the amount of deviations from the all-trans conformation (gauche defects) on alkanethiol chains increases with decreasing particle size[28,29] (higher surface curvature) and that the internal atoms of stabilizing chains are more exposed to the solvent in small nanoparticles.[30]

One of the main advantages of the use of SAMs for surface functionalization relies on the possibility of introducing almost any functional group at the interface of valuable materials, thus altering their surface properties and reactivity.[31] However, the presence of

such functional moieties can diminish the interchain attractive forces between the methylene spacers of neighbouring chains by pushing them apart due to steric hindrance, which results in the formation of low-density and poorly packed monolayers.[32] Therefore, we have to be aware that the density of functional groups on the surface may not be maximum (i.e. as high as with methyl groups) and that this parameter will have to be assessed for each individual case.

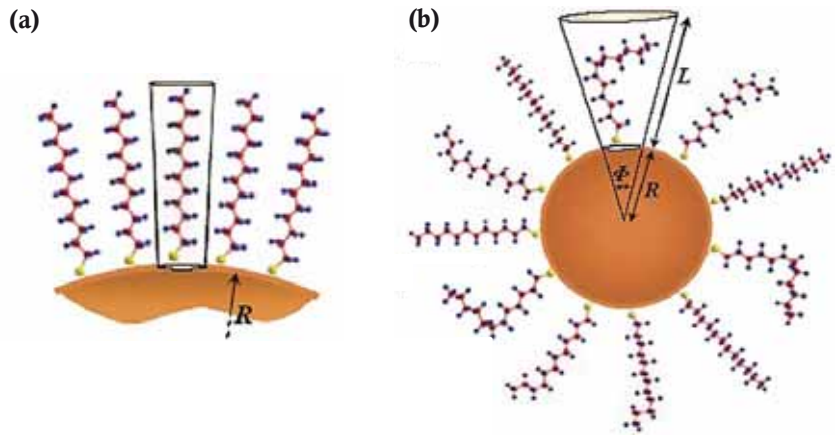

Figure 4.3 Schematic representation of the thiol space occupation in AuNPs with different radius. (a) Large nanoparticles have smaller surface curvature so the thiols are organized in a similar way as SAMs on flat surfaces. (b) In smaller nanoparticles the chain ends have more space to occupy and fill up a conical segment. The final methylene groups have a liquid-like behaviour in this environment and present a larger amount of defects. Reproduced from ref. 28.

4.1.2.1 Catechol-terminated SAMs on planar surfaces

Although one can find in the literature several examples of catechol-terminated SAMs, the main goal of positioning this moiety at the interface has not been the exploration of its adhesive properties but of its redox and chelating activity.

A few works have studied the structural characteristics of catechol-terminated SAMs on gold surfaces with special attention to the orientation of the catechol ring with respect to the surface. Simmons et. al. used XPS and IR spectroscopy to study the assembly of a catechol-terminated alkanethiol bearing a short methylene chain (3,4-dihydroxyphenethyl mercaptan) and determined that a tightly-packed monolayer was formed after self-assembly on gold substrates with the aromatic ring plane aligned close to the surface normal.[33] As opposite, catechol terminated monolayers containing an amide group in their alkyl chains showed a different orientation of the aromatic ring. Whilst the C=O bond from the amide moiety was oriented parallel to the surface, the catechol rings were tilted between 51 and 64º with respect to the surface normal.[34,35]

The incorporation of catechol moieties at the end of thiolated organic chains is a common strategy for the formation of electroactive SAMs due to the reversible catechol/quinone redox reaction (Figure 4.4a). The redox behaviour of catechol-modified electrodes probed to be pH-sensitive and showed metal-ion recognition properties[36,37] and electrocatalytic activity during the oxidation of NADH[38] and dopamine.[39,40] Another possible application of catechol-terminated SAMs relies on their ability to chelate the metal atoms present at the surface of metallic and ceramic nanostructures so they can be used as intermediate layer to form nanoparticle assemblies on surfaces. This method was used to form highly crystalline CeO[41] and maghemite[42] nanoparticle films. Alternatively, gold nanoparticles bearing boronic acid residues on the surface were also assembled on catechol-modified patterns through the formation of a catechol-boron complex (Figure 4.4b).[42]

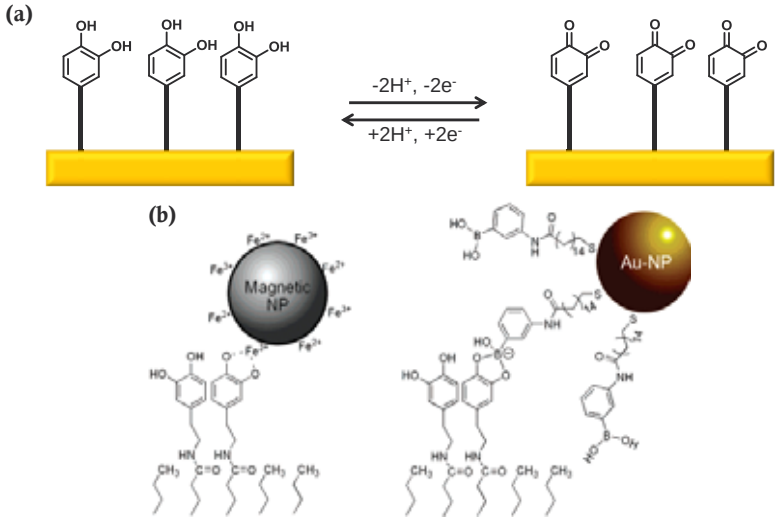

Figure 4.4 (a) Schematic representation of the electrochemical reaction occurring at the interface of a catechol-functionalized electrode. (b) Examples of nanoparticles assembled over catechol-terminated monolayers by coordination of surface metal ions or by complexation of the surface stabilizer. Reproduced from ref. 42.

4.1.3 Gold nanoparticles

During the last two decades, considerable effort has been devoted to the synthesis of AuNPs, focussing on control over their size, shape, solubility, stability and functionality.[43]

The first reported synthesis of colloidal gold is attributed to Michael Faraday, back in 1857.[44] More recently, in 1951 Turkevich and co-workers described one of the most popular methods for the synthesis of gold nanoparticles[45] which was refined by Frens et. al. later

on.[46] The procedure, based on the reduction of $HAuCl_4$ by citrate ions in aqueous media, leads to the formation of AuNPs electrostatically stabilized by weakly-bound citrate ions that can be easily replaced by other chemical entities binding more strongly to the AuNP surface. In 1994, Brust and Schiffrin reported a different methodology for the synthesis of small AuNPs in organic solvents.[47] In this procedure the Au precursor is first transferred from the aqueous to the organic phase using a quaternary ammonium salt (typically tetraoctylammonium bromide, TOAB) in the presence of dodecanethiol (DDT). On addition of $NaBH_4$ the AuNPs rapidly nucleate and are stabilised by the thiols present in the solution. Other alkanethiols (with different chain lengths and functionalities) can also act as stabilizers of AuNPs obtained by this method.[48–50] Alternatively, the AuNPs can be synthesized in the absence of the thiol ligand, solely with the organic quaternary ammonium ion stabilizing the nanoparticles.[51] In this way functional thiols, or other capping agents,[52] can be introduced in the surface of the AuNPs in subsequent steps. In thiol-stabilized AuNPs place exchange reactions can be carried out in order to modify the nanoparticle surface, as reported by Murray et al.[27,53] In this method, the originally anchored thiol ligands are replaced by free thiols of a different nature. The reaction time and the feed ratio of the incoming ligands control the efficiency of the replacement, so AuNPs bearing multiple functionalities on the surface may be obtained in this way.

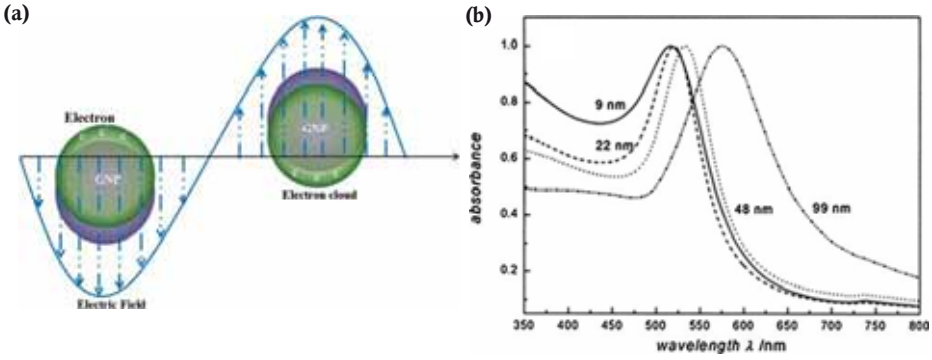

Figure 4.5 (a) Schematic representation of SPR in AuNPs, where the conduction electrons coherently oscillate due to strong interaction with incident light. (b) UV-Vis absorption spectra of 9, 22, 48, and 99 nm gold nanoparticles in water showing the increase in maximum absorption wavelength. Reproduced from ref. 54 and ref. 55.

The deep-red colour of colloidal AuNP solutions is probably one of their most attractive features and is caused by the surface plasmon resonance (SPR). This phenomenon can be described as the coherent oscillation of the electrons in the conduction band caused by the interaction with an electromagnetic field (Figure 4.5a) (when the diameter $d<<\lambda$, where λ is the light wavelength). When the frequency of the electromagnetic field is resonant with the electron motion, a strong absorption is seen in the UV-Vis spectrum,

which is the origin of the observed colour.[54,56,57] Thus, AuNP dispersions show characteristic bands in their UV-Vis spectra, often called surface plasmon resonance band (SPRB) or just surface plasmon band (SPB). The maximum absorption wavelength is found at around 520 nm and its position and bandwidth are directly related to the nanoparticle size. The SPB shifts to longer wavelengths and broadens as the particle diameter increases (Figure 4.5b). This trend is only true for nanoparticles with diameters larger than ~5 nm due to the increasing quantum size effects taking place in smaller particles.[55,58] Apart from the size, other factors can influence the SPR such as the refractive index of the medium or the interaction of the ligand shell with the electron cloud.[59] The SPB position and width are also sensitive to the proximity of other particles. Interparticle plasmon coupling occurs when metal nanoparticles are placed in close proximity to one another and results in distance-dependent shifting of the SPB[60,61] and change of solution colour from red to blue upon particle aggregation.[62,63] Optical spectroscopy is then an excellent tool to routinely assess the size, stability and aggregation (either spontaneous or intentionally induced) of the nanoparticles. Note here that the shifting of the SPB to longer wavelengths is commonly named red-shifting in the literature and this terminology will be used from here on in this manuscript.

4.1.3.1 Catechol-functionalized gold nanoparticles

Only a few examples of AuNPs containing catechol groups on their surface have been described in the literature. The metal-chelating properties of the catechol moiety have been exploited to construct metal ion colorimetric sensors based on AuNPs bearing catechol moieties on the surface. In the presence of metal ions, the AuNPs tend to aggregate due to the formation of metal complexes bridging the nanoparticles.[64] This forces a change of colour in the dispersion and red-shifting of the SPR band, as represented in Figure 4.6.[65]

Ye and co-workers used AuNPs modified with mixed SAMs of mercaptosuccinic acid and catechol-modified thiouracil to perform colorimetric detection of Cu^{2+}.[65] Recently, Phillips and co-workers used a catechol-terminated polymeric stabilizer to detect the presence of Fe^{3+} at serum concentration (8-25 μM) in saline solutions.[66] On the other hand dopamine dithiocarbamate was used to functionalize AuNPs that, even though they aggregated upon functionalization, could be used as matrix in laser desorption/ionization analysis techniques.[67]

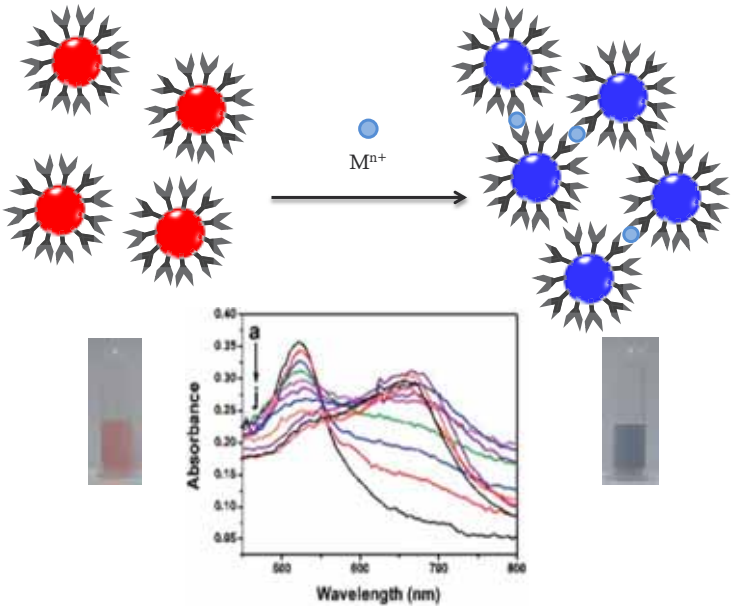

Figure 4.6 Schematic representation of red-to-blue colorimetric sensing using AuNPs functionalized in such a way that aggregation is caused by the presence of a metal ion. The graph shows the evolution of the UV-Vis spectra of metal-chelating AuNP upon addition of increasing amounts of metal ions, in the pictures the colour change from red to blue can be easily observed. Adapted from ref. 65.

4.1.4 Aim of the work

In the following section we will describe the formation of self-assembled monolayers on gold substrates exposing catechol moieties to the interface. With that aim; compound **3**, whose synthesis has been described in Section 3.2, was assembled on flat gold surfaces and the interfacial properties of the resulting SAMs were studied. First, the adhesive strength of the assemblies was measured at the local scale by recording F-d curves using an AFM. Alternatively, magnetic nanoparticles were used to assess the functionality of the interfaces in the cases were the adhesion could not be measured. The results were compared to those of other model systems like hydrophobic monolayers or the catechol-based coating polydopamine. The assembly of compound **3** was also attempted on the surface of AuNPs. In this case an added difficulty was faced, which was the stabilization of the AuNPs. Finally, the differences in the structure of SAMs formed on flat and curved substrates were rationalized in terms of geometry and equilibration time.

4.2 Catechol-terminated Self-Assembled Monolayers on planar gold surfaces

In this section we describe the study of the interfacial properties of catechol groups located at the interface of self-assembled monolayers. As we have detailed in Section 4.1 multiple studies can be found in the literature concerning the adhesive and interfacial properties of catechols either as single molecules or forming part of complex macromolecules like proteins. As an alternative approach, we designed a simplified model material based on a SAM that exposes exclusively catechol moieties to the interface in an organized manner (Figure 4.7a). For that, the catechol-terminated thiol **3** was assembled on gold surfaces (Figure 4.7c) and the properties of the obtained SAM were compared to those of polydopamine, an amorphous polymer with multiple functionalities including catechols and quinones (Figure 4.7b). Moreover, the influence of orientation and density of catechol moieties in the adhesive properties of catechol-based materials had not been considered before the writing of this thesis. By using the SAM approach we were able to construct a system where the adhesive moieties have consistent orientation. Additionally, we studied the influence of the catechol moiety on the formation process and final structure of the SAM.

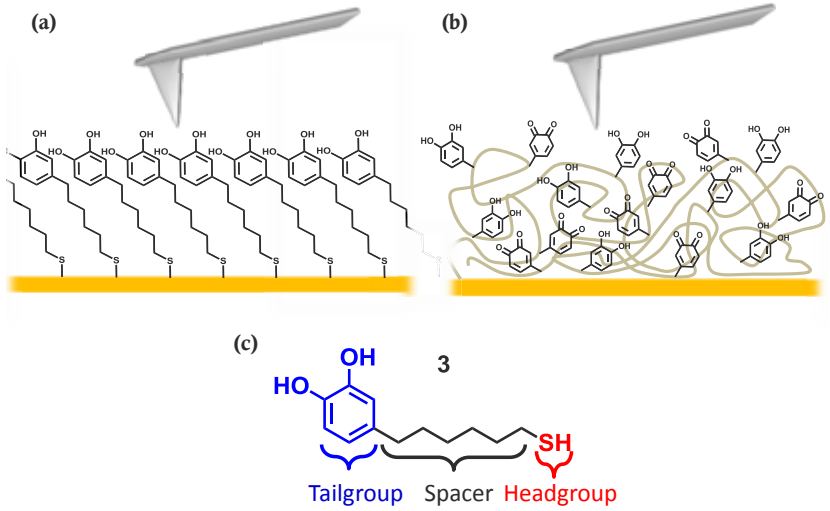

Figure 4.7 Schematic representation of the studied surfaces. (a) SAM of compund **3** on gold (b) PDA coating showing the presence of catechol and quinone moieties in a disordered manner. (c) Structure of the alkanethiol **3** used to form SAMs on gold and the different parts of the molecule.

4.2.1 Self-assembly and characterization of catechol-terminated SAMs on flat Au surfaces

Catechol-terminated SAMs were obtained using standard methodologies by immersion of clean gold substrates in a 1 mM ethanolic solution of compound **3** overnight under ambient conditions.[68] The gold substrates were activated prior to functionalization by exposing them to O_3/UV for 10 minutes and immersed in the thiol solution immediately afterwards. After the incubation, the substrates where thoroughly rinsed with EtOH and Milli-Q water. Catechol-terminated SAMs were obtained by this method in two types of substrates, namely polycrystalline gold (40 nm thick) deposited by Physical Vapour Deposition (PVD) on Si chips bearing a native oxide layer (from here on Si/SiO_2) and epitaxial gold (300 nm thick) supported on mica. Polycrystalline gold shows a rough topography on the surface (rms ~1 nm, Figure 4.8a, b) whilst epitaxial gold has a highly smooth topography with atomically flat terraces (rms ~0.3 nm) (Figure 4.8c, d). Whilst polycrystalline gold is much more robust and easier to handle than epitaxial gold, its higher roughness affects the local adhesion measurements. Thus, each of the substrates was used with different purposes, as detailed next.

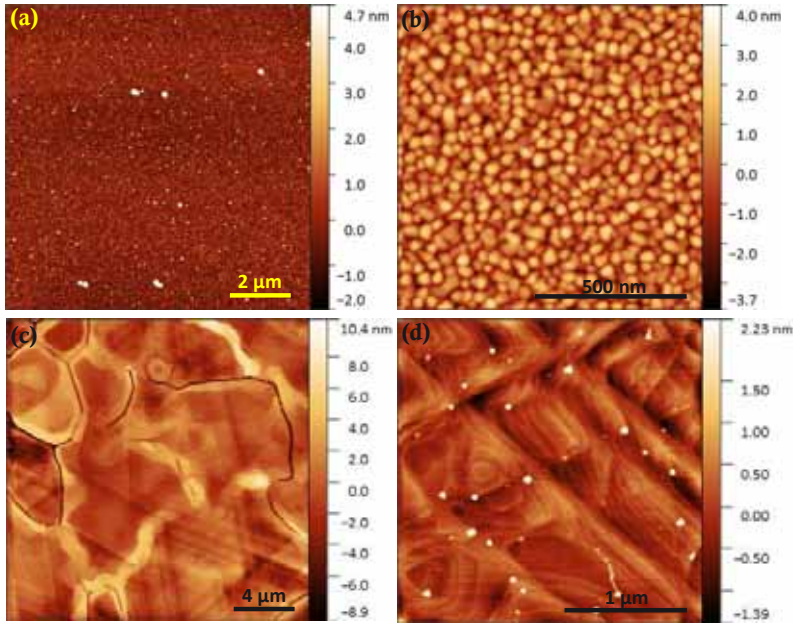

Figure 4.8 Tapping mode AFM topography images of the two types of gold substrates used in this thesis. Panels (a) and (b) correspond to polycrystalline gold and the grains are visible in panel (b). Panels (c) and (d) correspond to epitaxial gold and show the atomically flat terraces.

The obtained SAMs were characterized using Polarization Modulation-Infrared Reflection-Absorption Spectroscopy (PM-IRRAS), X-Ray Photoelectron Spectroscopy (XPS) and Spectroscopic Ellipsometry (SE). The PM-IRRAS spectrum (Figure 4.9a) was in agreement with other spectra previously reported for related catechol-terminated SAMs.[33,34,38,69] The bands ranging from 2960 to 2855 cm^{-1}, which were also present in the corresponding ATR spectrum of the free thiol, were assigned to the stretching modes of C-H bonds in the alkyl chain. Importantly, the band around 2500 cm^{-1}, assigned to the stretching of the S-H bond, was not observed in the monolayer spectra, which is fully consistent with the formation of a Au-S bond and subsequent loss of the thiol moiety. The presence of the hydroxyl groups was confirmed by the bands at 3462 cm^{-1}, 1264 and 1113 cm^{-1}, assigned to O-H stretching and in-plane bending, and C-O stretching modes. Peaks at 1522 and 1458 cm^{-1} were assigned to the in-plane stretching of the C=C bonds present in the aromatic ring.[34,70]

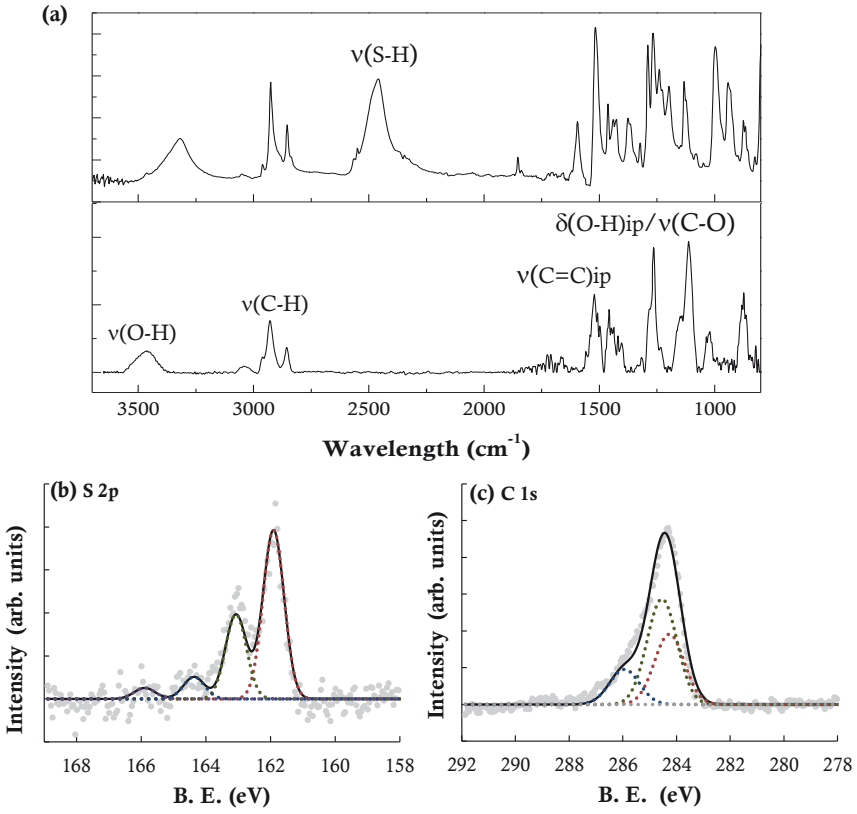

Figure 4.9 (a) IR-ATR spectrum of compound **3** (above) and PM-IRRAS spectrum obtained for a monolayer of **3** on polycrystalline gold (below). (b) and (c) XPS spectrum of a **3** SAM on polycrystalline gold; (d) S 2p region, (e) C 1s region.

Besides the chemical composition of the organic layer, the PM-IRRAS spectrum can also provide information about the relative position of the functional groups in the SAM with respect to the surface.[71] Because the high sensitivity of the technique is associated to the electric field oriented normal (perpendicular) to the surface (p-polarized); only those vibrational modes having a component of their transitional dipole normal to the surface will interact strongly with the electric field. This is commonly known as the surface selection rule. In our case, the strong signals associated to the in plane vibrations of the C-O, O-H, and C=C bonds (1264, 1113, 1522 and 1458 cm^{-1}) discarded the possibility of a parallel orientation of the aromatic ring with regard to the surface (if that was the case, these signals should not appear), and suggested that the thiols in the SAM were standing in an orderly fashion with a certain tilt angle. This observation is in agreement with the results obtained for other structurally related monolayers.[33]

The XPS results were also in agreement with those found for similar catechol-terminated monolayers.[33,34] The deconvoluted regions of the spectrum corresponding to the S 2p and C 1s core levels appear in Figure 4.9b and c. The S 2p region of the spectrum clearly fitted two intense peaks with a 2:1 area ratio positioned at 161.9 ($2p_{3/2}$) and 163.1 eV ($2p_{1/2}$), the characteristic binding energy of sulphur atoms chemically bound to gold surfaces as thiolate species.[72] The observation of a double peak is due to the spin-orbit splitting of the *p* level. A more detailed deconvolution of this spectral region showed the presence of a low intensity signal with its main component centred at 164.4 eV and associated to the presence of a small amount (less than 10%) of unbound sulphur species. This signal could correspond to either physisorbed thiol molecules or disulfide derivatives that spontaneously generate in solution, which are undistinguishable by XPS.[73] The C 1s core level was deconvoluted into three peaks at ~284.3, 284.5 and 286.0 eV (intensity ratio 2:3:1), corresponding to four aromatic carbons, six aliphatic, and two O-bound aromatic carbons respectively, in agreement with the structure of the thiol **3**. The presence of quinone was discarded because our trials to include a fourth peak corresponding to the C=O group (~287 eV) in the deconvolution did not provide a better fit for the experimental data. Additionally, by analysing the electrons emitted with different take-off angles (TOA), it was possible to obtain information about the element distribution along the layer thickness.[74] Importantly, the C/S intensity ratio measured at a TOA=60º was higher than that obtained at 0º. This indicated that S atoms were preferentially located close to the surface, while C atoms tent to position away from it, in agreement with the formation of a tilted S-bound monolayer.[75]

Finally, the estimation of layer thickness was performed using spectroscopic ellipsometry, which was carried out by Dr. S. Tatay at the Instituto de Ciencia Molecular in

Valencia. The ellipsometry was measured in the 300–400 nm range. The UV–vis spectra of compound **3** did not show any bands in this wavelength range, so the SAM was modelled as a transparent medium with a refractive index of 1.49.[76,77] Film thickness was found to be approximately 5 Å, being slightly dependent on the point of sampling. Since this value is well below the length of the fully extended molecule (ca. 12 Å), the formation of multilayers was ruled out. Using the same molecular length value, an approximate tilt angle of ~60° with respect to the surface normal could be estimated. This tilt angle is quite high compared to those reported for linear alkanethiols self-assembled on gold surfaces, which is around 30°[22] but close to the orientation of catechol rings measured on other catechol-terminated monolayers.[34,35] Seems then that the catechol moiety plays an important role in the final structure of the monolayer; this issue will be discussed later in the manuscript.

4.2.2 Measurement of adhesion at the local scale: Force-distance curves

AFM force-distance curves have become a fundamental tool in various fields of research, including surface science, materials engineering, biochemistry and biology and are routinely used in several types of measurements.[78] A model F-d curve recorded in air is depicted in Figure 4.10. In a typical experiment, an AFM tip is brought into contact with the surface at a constant speed (approach) and then pressed against it to a fixed load; afterwards, the tip is retracted from the surface. During the whole process, the deflection of the cantilever is registered and plotted as a function of the extension of the piezoelectric actuator. The resulting curve consists of a noncontact region where no tip–sample interaction is observed (Figure 4.10, region 1) due to the long distance between them, as the tip and the surface come closer long range forces start dominating their interaction until they exceed the spring constant of the cantilever; at this point the tip "jumps" into contact with the surface (2). After contact, the tip enters a repulsive regime as it is pressed against/into the surface until a predetermined load setting is reached (3). The retraction movement starts right afterwards and the adhesive forces maintain the tip-sample contact (4) until the load on the cantilever overcomes the attractive forces between the tip and sample, at this point the "jump out" of contact is observed (5). The adhesion (F_{adh}) is extracted from the difference in cantilever deflection between the contact break and the resting position of the tip.

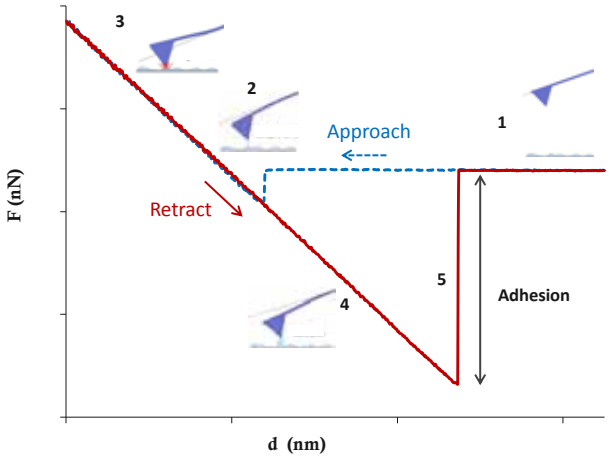

Figure 4.10 (a) Model F-d curve showing each of the stages of of an experiment. (1) First the tip and the sample are far from each other and no interaction exists between them, then the tips "jumps into contact" with the surface (2) and the tip is pressed against the surface (3). When the maximun load is reached, the retraction starts and and adhesive forces act (4) until the tip "jumps out" of contact.

Repeated F-d curves were registered along the surface of catechol-functionalized epitaxial gold substrates. Two additional samples were also studied by this method for comparison purposes, namely bare epitaxial gold and gold modified with a hydrophobic monolayer (octadecanethiol, ODT). The experiments were performed on the same experimental session, in order to minimize temperature and humidity fluctuations and the obtained results are summarized in Figure 4.11.

Bare gold substrates presented a F_{adh} histogram centred at small values of 8-9 nN (Figure 4.11b), most likely arising from capillary forces originated by the presence of a thin layer of water on top of the bare Au surface.[79] ODT-modified substrates showed adhesion force values around 5-6 nN (Figure 4.11d). Such small adhesion values are consistent with the absence of functional moieties that are able to interact strongly with the tip through specific interactions. It was also observed that the F-d curves obtained for the ODT monolayer presented a different shape for the retraction movement, with a softer and less vertical jump-out than bare Au substrates. This was attributed to deformation of the monolayer caused by the tip, as well as to irregularities of the thin water layer adsorbed on the surface. Finally, the adhesion measurements on catechol-terminated monolayers afforded a set of F_{adh} values centred at 45 nN (Figure 4.11f), which was a considerably higher value than the ones obtained on the other two systems. Specifically, the catechol-terminated monolayer showed an average adhesion force at the nanoscale level five times higher than that measured for bare gold, and eight times higher than that of an ODT monolayer, denoting a strong interaction of the tip with the catechol groups on the surface.

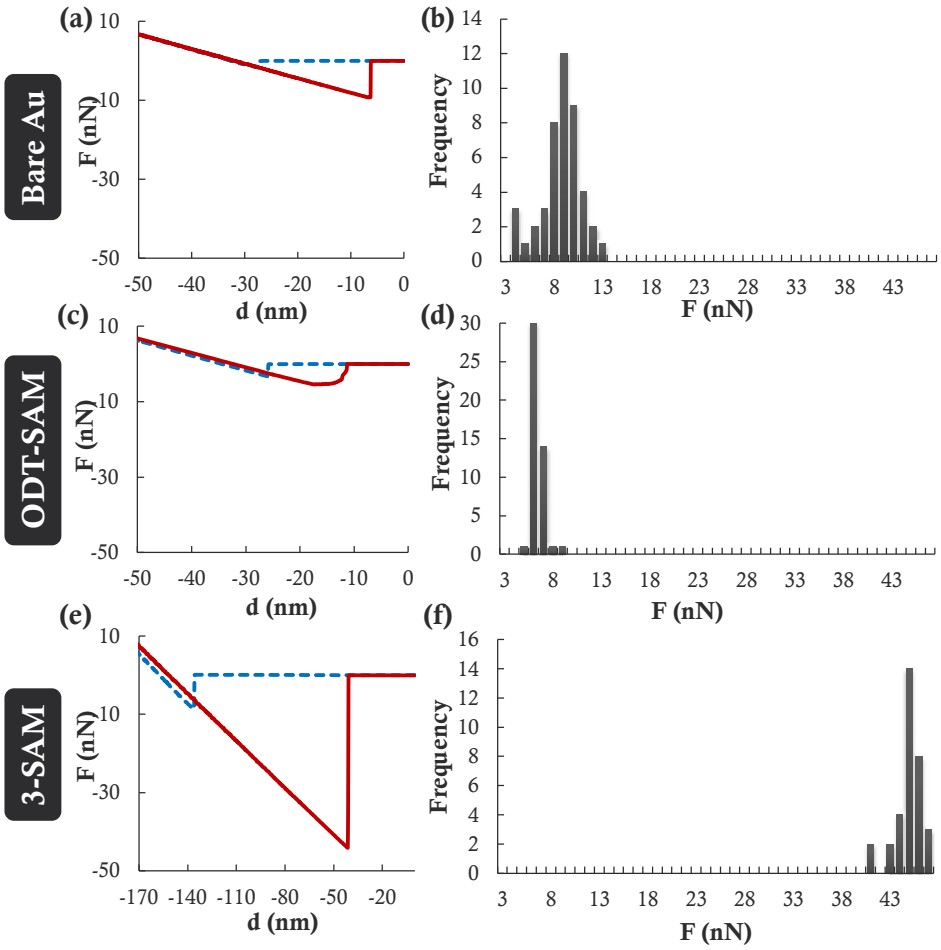

Figure 4.11 Adhesion measurements on epitaxial gold on mica substrates. Representative force curves for each of the substrates are displayed in the left column. The blue dashed line and the red solid line indicate the approach and retract movements, respectively. Histograms of the obtained adhesion force values are showed in the right column. Panels (a) and (b) unmodified gold, (c) and (d) ODT monolayer, (e) and (f) **3** monolayer. The histograms have been represented with the same x-axis for easier comparison.

For comparison purposes, additional F-d measurements were recorded on a PDA film that was deposited on gold following a procedure already described in the literature.[80] Briefly, clean epitaxial gold substrates were immersed in a buffered solution of dopamine hydrochloride (pH 8.5) and kept in vertical orientation while stirring the solution for an hour. Afterwards they were rinsed with Milli-Q water. Tapping mode AFM imaging of the PDA-coated substrates revealed an irregular topography formed by small aggregates deposited on the surface, in agreement with previously reported data (Figure 4.12a,b).[81] To measure the thickness of the coating a scratch was carefully made on the film using a needle as shown in Figure 4.12a. The coating thickness was ~15 nm (Figure 4.12c) although this

value varied considerably depending on the site of measurement, as did the surface roughness (rms) which, depending on the location, showed values between 1.5 and 20 nm.

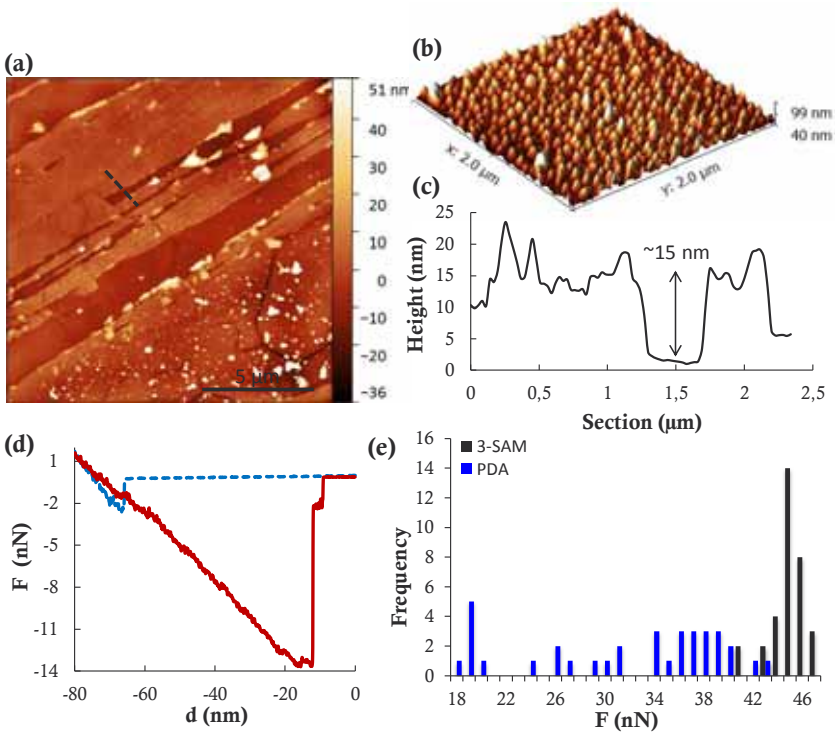

Figure 4.12 (a) Tapping mode AFM topography of a PDA film on epitaxial gold showing a scratch intentionally made to measure the thickness of the coating. (b) 3-D AFM topography image of the coating showing the rough topography. (c) Height profile corresponding to the dashed line in panel (a). (d) Representative F-d curve on a PDA film. (h) Combined histogram showing the Fadh values obtained for the **3** monolayer and the PDA film.

The results extracted from F-d curves recorded on the PDA-coated substrate are represented in the histogram shown in Figure 4.12e. In some experiments, PDA coatings showed multiple jump-off or deformed curves and; as seen in the histogram, the results presented a high degree of statistical dispersion. If the adhesion values obtained for the two catechol-based systems are compared, it can be seen that the average F_{adh} measured on the catechol-terminated monolayer was slightly higher than the maximum F_{adh} recorded on the PDA thin film. Significantly, the statistical dispersion of the results was much lower on the catechol-terminated SAM. These differences were attributed to the superior chemical and topographical homogeneity of the SAM, which is a well-defined system in terms of composition and structure. PDA, on the contrary is a soft and amorphous material with a complicated topography that contains a large amount of functional groups[82–84] able to interact with the tip. Because of that, the forces acting on the tip significantly varied between

measurements in the PDA film whilst they were much more reproducible in the catechol-terminated SAMs.

Further studies were carried out to assess the effect of surface roughness on the monolayer properties. For this, SAMs of **3** were prepared on polycrystalline gold substrates exhibiting rough topographies, as opposed to the atomically flat surfaces studied before. The F-d curves recorded on polycrystalline gold afforded a highly disperse set of values and the measured F_{adh} was far from that measured in SAMs obtained on flat gold surfaces (Figure 4.13a). This difference could be attributed to several reasons. First, the increased surface roughness impedes the establishment of strong interactions between the chains,[85] leading to the formation of a poorly packed monolayer of randomly oriented molecules showing a decreased F_{adh}. Moreover, the rougher topography of the substrate is expected to cause important variations in the contact geometry between the tip and the sample, thus adding uncertainty to the results.[86] We have ideally represented the two situations in Figure 4.13b.

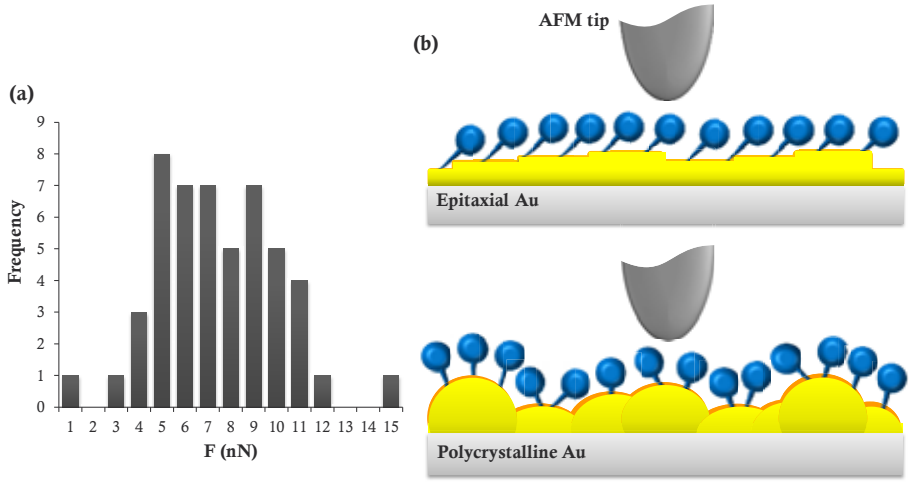

Figure 4.13 (a) Histogram obtained from the F_{adh} measured on a SAM of **3** on polycrystalline gold showing no enhanced adhesion. (b) Schematic representation of the SAM on the two gold surfaces used in the study; epitaxial gold (top) and polycrystalline gold (below). Both of them are ideal representations and are not made to scale.

4.2.3 Adsorption of iron oxide nanoparticles on catechol-functionalized substrates

Alternatively, the functionality of catechol-terminated monolayers on polycrystalline gold substrates was studied by assembling maghemite (γ-Fe_2O_3) nanoparticles on the modified surface. The high affinity of catechols to iron oxide nanoparticles is well known and has been extensively used as a strategy to stabilize and functionalize magnetic

nanoparticles.[87] For that, differently functionalized polycrystalline gold substrates were immersed in a colloidal dispersion of maghemite nanoparticles (8-10 nm in diametre), sonicated for 15 min and then thoroughly rinsed with Milli-Q water.[69] Attempts to carry out this procedure in epitaxial gold substrates led to the detachment of the gold film from the support.

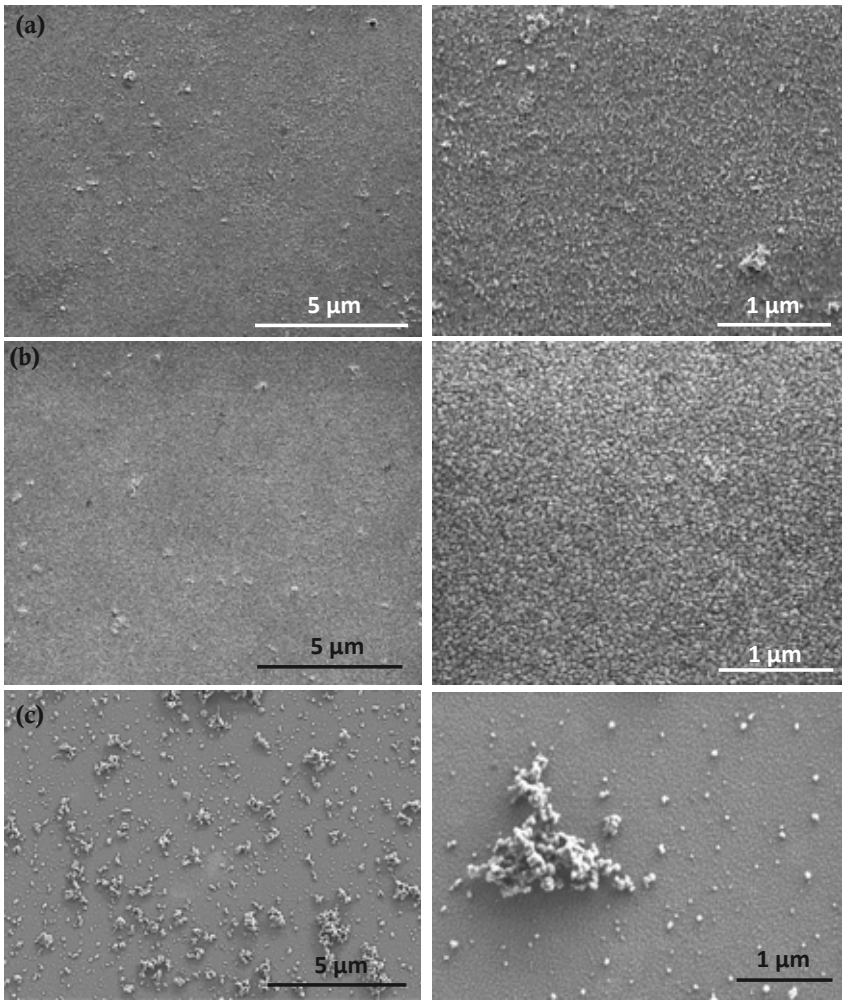

Figure 4.14 SEM images of different substrates after inmersing them in a 0.3 mg/mL dispersion of maghemite nanoparticles and sonicating for 15 minutes. Images on the right column are magnified views of the samples in the left column. (a) **3**-SAM on polycrystalline gold. (b) Bare polycrystalline gold. (c) PDA deposited on a polycrystalline gold substrate. Note that in the magnified image in (a), the high density of nanoparticles does not allow seeing the gold grains that are clearly visible in (b). In (c), the roughness of the PDA coating can be distinguished.

In the experiments performed using a polycrystalline gold substrate functionalized with a monolayer of **3**, an homogeneous distribution of nanoparticles was observed across the whole surface area with high coverage. As can be seen in the SEM images in Figure 4.14a,

the nanoparticles adsorbed on the surface cover the gold grains, which cannot be distinguished. This procedure was repeated for comparison purposes with an unmodified gold substrate and a PDA-coated substrate. Very few nanoparticles were found randomly adsorbed on the bare gold (Figure 4.14b), whilst on the PDA-coated samples we observed a highly inhomogeneous distribution of aggregates on the surface. Most probably these correspond to the magnetic nanoparticles that get aggregated due to the partial desorption of PDA from the surface upon to sonication (Figure 4.14c). Overall, despite the fact that the roughness of the substrate impeded a precise assessment of the F_{adh} by AFM, the catechol moieties appeared to be homogeneously distributed on the SAMs obtained on polycrystalline gold and provided functionality to the surface by acting as anchors for iron oxide nanoparticles.

4.2.4 Monolayer formation process

The formation process of alkanethiol monolayers has been extensively studied and is generally considered to occur in a two-step mechanism. First, a very fast step (~ 1 minute in 1 mM alkanethiol solutions) takes place where the thiols assemble on the surface in a disordered way with low tilt angles; by the end of this step the thickness is about 80-90% of its maximum. The second step takes a few hours and can be described as a surface crystallization process where the chains get out of the disordered state and form a two-dimensional crystal. While the first step is governed by the surface-head group reactivity, the kinetics of the second step is related to chain disorder, chain-chain interactions, and surface mobility of the alkanethiols. In linear alkanethiols, the masking of adsorption sites by disordered chains is not considered a serious problem. However, when the chains contain bulky groups the chemisorption kinetics is greatly impeded by the chain disorder. This is attributed to the additive effects of the stabilizing van der Waals interactions that are stablished between the chains of linear alkanethiols to form tightly-packed monolayers and that are hindered when bulky groups are present.[31]

In order to assess the effect of the catechol moiety in the formation of the SAM the importance of equilibration time on the adhesive properties of the monolayer was studied. For that, a clean epitaxial gold substrate was immersed in a 1 mM ethanolic solution of **3** at ambient conditions for only 15 minutes. Then, F-d curves were recorded following the experimental procedure described above and F_{adh} values centered at around 5-6 nN were measured (see Figure 4.15a), far below those found for catechol-terminated SAMs obtained

after longer immersion time. Also, the obtained results were highly dispersed, consistent with the formation of a disordered and inhomogeneous coating; and the F_{adh} values were similar to those obtained for ODT monolayers.

Early stage monolayers were also obtained on polycrystalline gold substrates by immersion in a 1 mM solution of **3** in EtOH for 15 minutes, and their ability to assemble iron oxide nanoparticles was evaluated. The functionalized substrate was immersed in a dispersion of iron oxide nanoparticles and then thoroughly rinsed with water. The particle coverage obtained on this substrate was shown to be poor and inhomogeneous as seen in Figure 4.15b and c and strongly dependent on the observed area, confirming that short equilibration times led to transient monolayers where the catechol moieties at the end of the alkyl chains were unable to effectively interact with other surfaces.

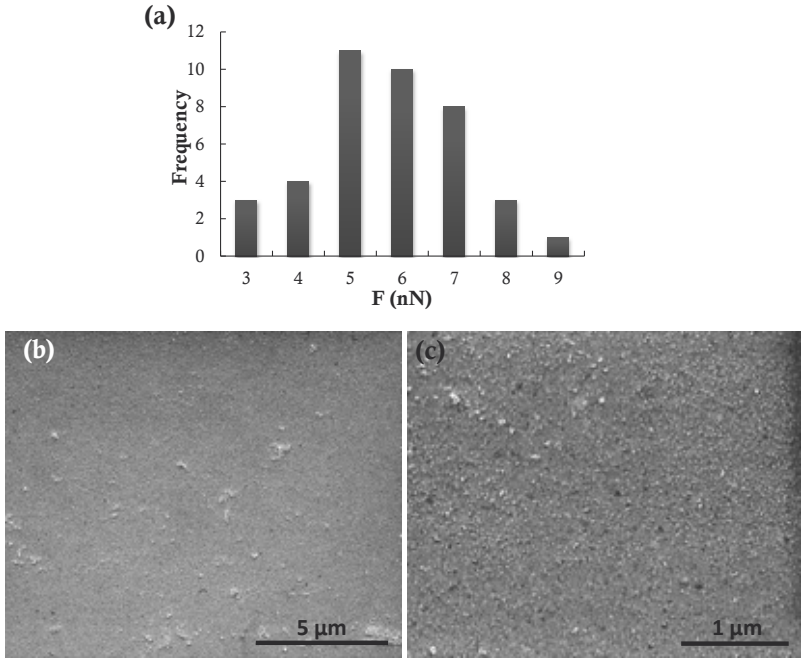

Figure 4.15 (a) Histogram obtained from the F_{adh} measurements performed on a SAM of **3** equilibrated for 15 minutes showing diminished adhesion. (b), (c) SEM images of a polycrystalline gold substrate modified with a SAM of **3** equilibrated for 15 minutes and then immersed in a 0.3 mg/mL dispersion of maghemite nanoparticles, some particles can be seen on the surface with uneven distribution.

Confirmation of the need of having sufficiently prolonged immersion times to obtain good quality monolayers was obtained by using an alternative method to obtain the SAMs. Sub-monolayer dot-like features of **3** were fabricated on epitaxial gold substrates by Direct-Write AFM-assisted lithography and then the F_{adh} was measured on the resulting patterns.

An introduction to the Direct-Write AFM-assisted lithography technique is provided in Section 5.1.1.

In this lithographic technique, an AFM tip coated with the thiols is brought into close contact with a gold surface and the thiols coating the tip diffuse to the surface through the water meniscus that forms between them.[88] The intrinsic nature of the diffusion mechanism implies that the sub-monolayers are formed in highly concentrated micro-environments, which can result in higher packing densities of the alkanethiols.[89] This methodology has been previously shown to form close-packed and highly ordered SAMs with commonly used thiols such as ODT and mercaptohexadecanoic acid (MHA), normally by using prolonged contact times (or low writing speeds in the case of dynamic writing) to promote the establishment of effective chain-chain interactions.[90,91] For that, an AFM tip was functionalized with **3** by using a standard procedure based in dipping the tip in a thiol solution and blow-drying it with nitrogen after a treatment with steam. Afterwards, the functionalized tip was brought into contact with the gold surface under ambient conditions (~25 ºC, ~40% R.H.) and dot-like feature arrays were fabricated by traversing the tip over the surface in the shape of the desired patterns. Contact mode AFM images obtained immediately after the deposition using the same coated tip showed a difference in friction on the spots where the tip had contacted the surface, proving that the catechol-terminated thiol had been successfully transferred (Figure 4.16a).

After the patterning process, the quality of the obtained monolayers was adressed. As we have exposed before, notable differences can be observed when the local adhesion of well equilibrated and primitive monolayers is measured. Therefore, the F_{adh} values registered on the patterned areas were used to evaluate the quality of the sub-monolayers. For that the Flex-Grid option of PicoScan software (used for controlling the AFM) was employed to record F-d curves on selected points of an area while scanning the surface in contact mode. First, the obtained dot-like feature arrays of **3** were located by lateral force microscopy (LFM) imaging using a clean tip (Figure 4.16b) and then F-d curves were recorded immediately afterwards on both functionalized and pristine areas while scanning the surface with the same probe. Unfortunately, no significant differences were observed between the F_{adh} values of bare gold and the functionalized spots. Additionally, square motifs were fabricated by scanning the surface with a **3**-coated tip at slow speeds and even with repeated passes (Figure 4.16c). The use of these conditions should have contributed to improve the monolayer quality, as longer equilibration times are achieved in this way; however in our case it was not possible to detect any enhanced adhesion in those areas. Therefore, poor-

quality sub-monolayers of **3** without any adhesive character were obtained by direct-write AFM-assisted lithography.

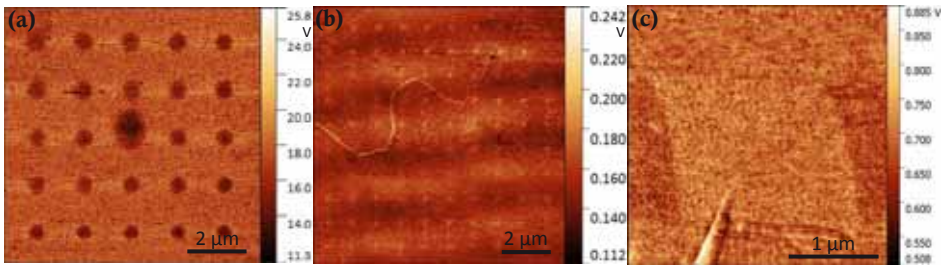

Figure 4.16 LFM images of different motifs (dot arrays and areas) obtained by direct-write AFM-assisted lithography on gold substrates using a tip coated with compound **3**. (a) LFM image of a 5x5 dot array of **3** obtained with the same tip used for patterning. (b) LFM image of a 10x10 dot array recorded using a clean tip. (b) LFM image of a 2x2 µm square written on a gold surface by scanning the area with an AFM tip coated with **3**.

It is important to point out here that the small dimensions of the obtained features highly complicated the task of locating them in the substrate after the patterning process. At least one preliminary scan of the area was always required to locate them but frequently several scans were necessary. In those cases, a new AFM tip was used for the adhesion measurements but still one scan of the area was needed. The possibility that during these previous scans the surface suffers some modifications that affect the results cannot be discarded, as has been reported before that the "history" of the system can be determinant when the interfacial properties of modified surfaces are studied.[86] Also, the tip used for the adhesion measurements may also get dirty or damaged during the previous scan, thus affecting the subsequent measurements. Nevertheless, the obtained results agree with those of monolayers equilibrated for short times, as no localized adhesion was detected although we cannot consider them fully conclusive.

All these observations combined suggest that the presence of the catechol moiety at the end of the alkyl chain slows down the formation process of the monolayer. For SAMs of linear alkanethiols we could expect that after 15 minutes the interfacial properties of the monolayers were almost identical to those of completely equilibrated ones. However, our system needs longer equilibration times. This may be due to the strong interaction of the catechol moiety with the surface that we reported in our group a few years ago (see Section 4.1.1).[19,20] Also, the presence of the catechol group can hinder the van der Waals chain-chain interactions that are essential to form a tightly-packed monolayer. As we have seen, exposing the gold substrates to the thiol solutions for long periods of time (overnight) results in the formation of SAMs with adhesive capabilities; although according to the

ellipsommetry measurements, the tilt angle of the chains is still far from that obtained for linear alkanethiols.

4.2.5 Molecular Dynamics simulations

In order to get some atomistic insight into the formation of the studied monolayers, all-atomic Molecular Dynamics (MD) simulations were carried out. The calculations were performed by Dr. J. Faraudo, from the Institut de Ciència de Materials de Barcelona (ICMAB-CSIC). Atomically flat gold surfaces with different coverage degrees of **3** were considered both in vacuum and with water as solvent. All MD simulations were performed at 25 °C and, whenever present in the simulation, the solvent was kept at 1 atm of pressure. The quality of the monolayer was characterized by measuring the tilt angle α between the gold surface and the extended alkyl chain of **3**. The dependence of α with the surface coverage is shown in Figure 4.17a.

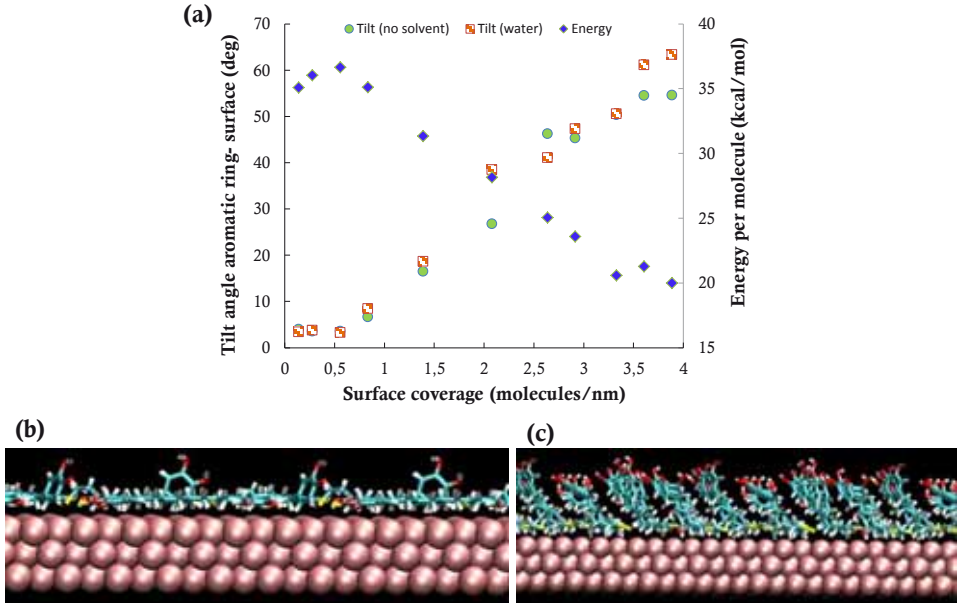

Figure 4.17 Results from MD simulations. (a) Evolution of the angle between the catechol group of adsorbed **3** molecules and the gold surface with increasing surface coverage. Stripped orange squares correspond to simulations with water and filled green circles correspond to simulations without solvent (left axis). Energy per molecule calculated with increasing surface coverage (blue diamonds, right axis). The snapshots correspond to a simulation with a surface coverage of 0.83 molecules/nm^2 (b) and 2.64 molecules/nm^2 (c) with water as solvent (water molecules are not shown for clarity).

As observed, at very low coverage values (<1 molecule/nm^2), the molecules of **3** tend to lay roughly flat on the surface ($\alpha \approx 0°$), with catechol groups in contact with the gold interface, as expected for a monolayer in its first formation stages (Figure 4.17b). Higher surface coverages of **3** resulted in equilibrium configurations with higher tilt angles; and values of $\alpha \approx 30°$ were measured when the surface coverage was around 2 molecules/nm^2 (Figure 4.17c). This trend continued at least up to a surface coverage of ca. 3.6 molecules/nm^2 (the largest coverage simulated) for which a tilt value of $\alpha \approx 60°$ was obtained. As can be seen in Figure 4.17a, the effect of ambient water was not very important except at large coverage values, when the presence of water tent to induce larger tilts as compared to the simulations in vacuum. During the simulations, the energy per molecule was also computed; meaning the sum of the interactions with other molecules, solvent and surface, plus the conformational energy, and the kinetic energy due to thermal agitation (Figure 4.17a). For SAMs in the presence of water and very low coverages (<1 molecule/nm^2) the molecular energy was found to be roughly constant and consistent with a low coverage of independent, randomly oriented and flat-lying molecules. For higher surface coverages, favourable intermolecular interactions were stablished, resulting in a consistent decrease in the molecular energy, concomitant to increasing tilt angles; this suggested that the spontaneous formation of monolayers of **3** should be energetically favoured. According to the MD calculations, the energy seemed to reach a minimum when the surface coverage was about 3.33 molecules/nm^2 (corresponding to a tilt angle of $\alpha \approx 60°$). The energy per molecule increased for larger coverages, which was attributed to packing constraints and steric interactions between adjacent molecules.

Summing up, the MD simulations indicate that the formation of SAMs with higher tilt angles should be theoretically feasible. Although it was not possible to achieve that conformation experimentally, the simulation results are encouraging, as they suggest that an ideal situation with high surface coverage and molecular orientation closer to the surface normal is possible.

4.3 Attempts to obtain catechol- functionalized gold nanoparticles

Up until now, we have explored the interfacial properties of catechol-terminated monolayers formed on planar gold surfaces. Considering the increasing attention that AuNPs have received in the last decades we considered it appropriate to also address the assembly of the catechol-terminated alkanethiol **3** on the surface of AuNPs. An ideal representation of the formation of catechol-terminated SAMs on both flat surfaces and AuNPs is shown in figure 4.18. Working with AuNPs we had to face the added difficulty of stabilizing them whilst simultaneously providing functionality. Some of this work was performed in the Laboratory for Inorganic Colloidal Nanocrystals and Applications, led by Dr. A. Kanaras at the University of Southampton.

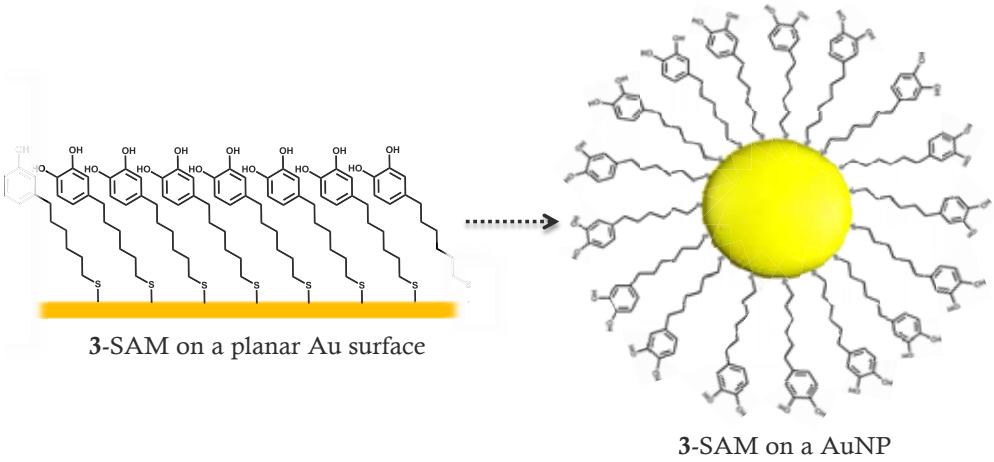

Figure 4.18 Ideal representation of the evolution from catechol-terminated SAMs to catechol-functionalised AuNPs using compound **3**. The representations are not made to scale.

4.3.1 Attempts to functionalize AuNPs with 3

The first strategy employed consisted in synthesizing AuNPs stabilized by tetraoctylammonium bromide (TOAB) (from here on AuNP-TOAB) and then replace the stabilizer with the catechol-terminated ligand **3**, as represented in Figure 4.19.

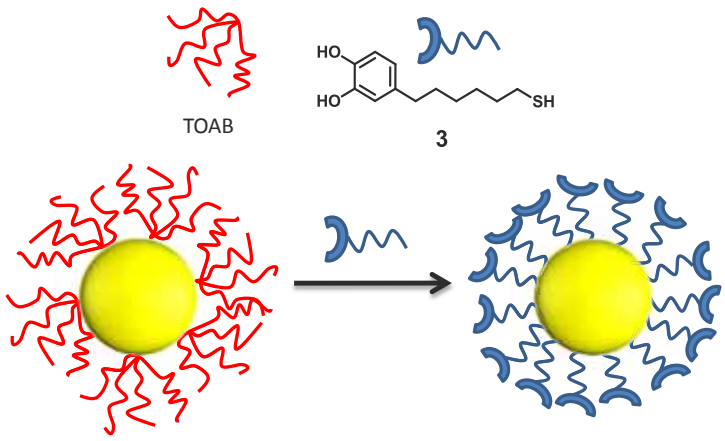

Figure 4.19 Schematic representation of the replacement of TOAB by thiol **3**.

AuNP-TOAB were obtained by the Brust-Schiffrin method[47] with a slight modification to avoid the use of toluene (see Experimental Section 4.5). Briefly, an aqueous solution of $HAuCl_4$ (30 mM) was mixed with a solution of TOAB in Hexane/CH_2Cl_2 1:1 and stirred until the gold precursor was totally transferred to the organic phase. Then a solution of $NaBH_4$ (1 mmol) in water was added dropwise and the reaction mixture turned dark red immediately. After stirring for 30 minutes, the nanoparticles were subjected to successive washes to remove the TOAB excess and the AuNP-TOAB were obtained as a stable dark red dispersion in CH_2Cl_2/Hexane 1:1. The median size of the particles was 6.3 nm (1.9 sd) as observed by TEM (Figure 4.20a) and they showed a SPR band centred at 517 nm (Figure 4.20b).

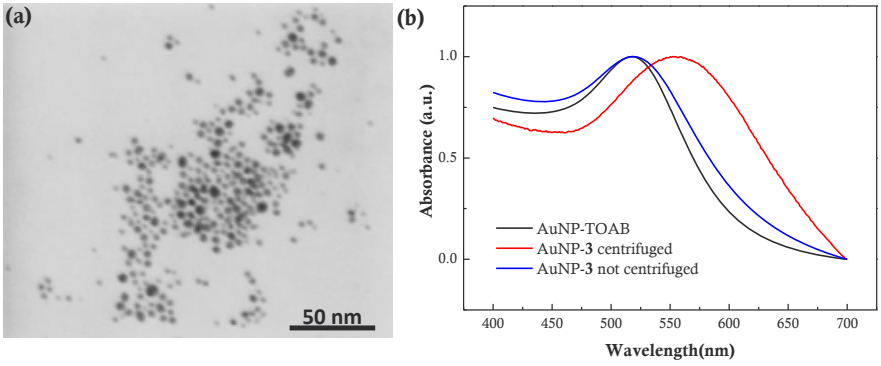

Figure 4.20 a) STEM image of AuNP-TOAB. (b) UV-VIS spectra of the as-synthesized AuNPs stabilized by TOAB and functionalized by **3** (after mixing for 3 hours) before and after centrifugation.

Once the AuNP-TOAB nanoparticles were obtained, the functionalization of their surface with **3** was attempted by a replacement process. For that, a dispersion of the as-

prepared AuNP-TOAB (500 μL) was mixed with increasing amounts (5, 15, 35 and 75 μL) of a 0,1 mg/mL solution of compound **3** in CH_2Cl_2. After a few hours the nanoparticles were centrifuged in order to remove the excess thiol and free TOAB, which resulted in the irreversible aggregation of the particles in all the samples, as observed by the shifting of the SPR band to longer wavelengths (see Figure 4.20b). If the nanoparticles were not centrifuged and left to exchange for longer periods of time (aprox. 48 hours), they spontaneously precipitated. Further trials to functionalise the AuNPs in this way by increasing the concentration of the thiol solution (10-fold) provided the same results.

Seeing that it was not possible to obtain stable catechol-coated nanoparticles in organic non-polar solvents the use polar solvents was attempted. Citrate-stabilized water-dispersible nanoparticles (from here on AuNP-cit) were used as starting material with that aim and the citrate stabilizer was then replaced by **3**. This kind of AuNPs is frequently used in phase transfer procedures, where the citrate-stabilized nanoparticles in water are transferred to the organic phase through the substitution of the citrate ions by organic ligands (normally thiols or amines).[92,93] Given the high solubility of **3** in EtOH, polar solvents appeared as a good alternative dispersive media for the **3**-coated nanoparticles.

Water-dispersible AuNPs were synthesized using a previously described procedure that employed $NaBH_4$ as reducing agent and citrate as stabilizer.[92] A 5 mM solution of $HAuCl_4$ was mixed with a 38.3 mM solution of sodium citrate; then $NaBH_4$ (50 mM) was added dropwise and the mixture was stirred for two hours. Using this method a dispersion in water of AuNP-cit of around 7.5 nm (1.5 sd) in diameter was obtained showing a well-defined SPR band centred at 518 nm (Figure 4.21a). Substitution of citrate ions by the catechol-terminated ligand **3** was attempted then by mixing 500 μL of the obtained AuNP-cit dispersion with a solution of **3** (400 μL, 1 mg/100 μL) in EtOH and stirring the mixture overnight. No precipitation or drastic colour change was observed after that time, indicating that no spontaneous aggregation of the AuNPs occurred. Then, the functionalized AuNPs were washed by centrifugation after adding an equal amount of EtOH to the mixture. After this procedure, and as observed by UV-Vis spectroscopy (Figure 4.21a), the nanoparticles showed slight red-shifting of their SPR band, showing their tendency to aggregate. It was observed that consecutive washing cycles led to a decrease in the stability of the nanoparticles, which irreversibly aggregated after more than two centrifugation/re-dispersion cycles. The IR-ATR spectrum of the sample after the washings showed good agreement with that of the catechol-terminated ligand, suggesting the functionalization of the nanoparticles by **3** (Figure 4.21b). XPS measurements were also carried out in order to

confirm the incorporation of ligand **3** to the AuNPs surface; however it was not possible to extract any conclusions from those experiments due to sample charging. In XPS, this phenomenon occurs in samples containing insulating or semiconducting regions, which develop varying surface potentials during the analysis that affect the position and shape of the XPS peaks, causing the obtention of low resolution spectra and hampering the analysis of the results.[94] In our case, sample charging was most probably due to the presence of high amounts of organic impurities that remained in the AuNPs dispersion because the washing procedure was not effective enough.

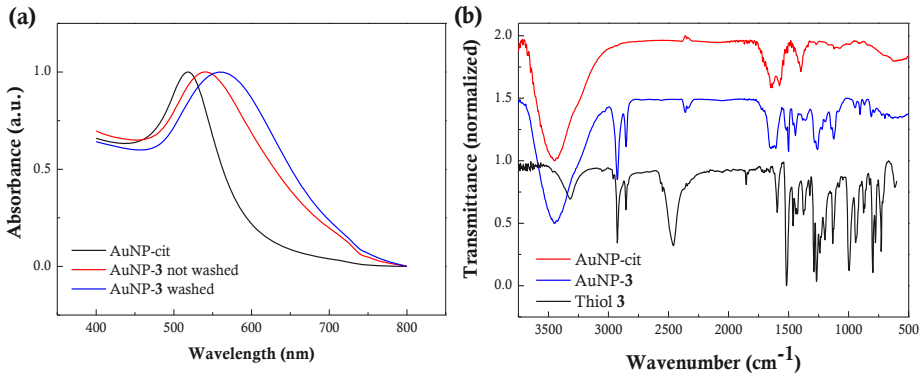

Figure 4.21 Functionalization of citrate-stabilized nanoparticles with **3**. (a) UV-VIS spectra of the particles shows slight blue-shifting after functionalization that increases after the washings. (b) IR-ATR spectra of the AuNPs showing the presence of the catechol-terminated thiol **3** in the sample after the functionalization and confirming the replacement of the citrate ligands (at least partially).

Worth to mention, the stability of the nanoparticles varied between the different samples after the replacement of the citrate ions by the thiol **3**; moreover the IR spectra recorded from identical samples were not in good agreement, especially in the 1600-1100 cm^{-1} range, denoting a low reproducibility of the procedure.

4.3.2 Combination of 3 and alkanethiols in mixed monolayers

Due to the impossibility to obtain stable AuNPs functionalized with **3**, further attempts to introduce the catechol functionality on the AuNPs surface were based on the formation of mixed monolayers. With that aim, **3** was combined with linear alkanethiols, as it is well known the ability of alkyl chains to stabilize AuNPs in organic solvents when they are anchored to the gold surface through Au-S bonds.[23,95] By using this strategy we tried to improve the stability of the AuNPs without interfering in the desired catechol-induced properties of the surface.[29,96]

Two alkanethiols with different chain lengths were suggested as co-stabilizers for the AuNP-**3**, hexanethiol (HT) and dodecanethiol (DDT). Due to its chain length, DDT provides higher stability to the nanoparticles[97] but its longer methylene chain may also be counter-productive, as the interaction of the catechol moieties with the media may be slightly hindered by the alkyl chains, as schematically represented in Figure 4.22. Because of that, hexanethiol was also tested as co-stabilizer as the shorter chain would allow better accessibility to the catechol moieties

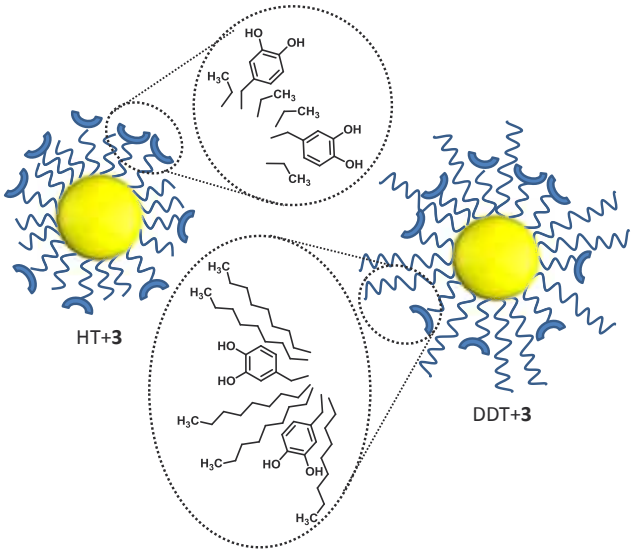

Figure 4.22 Schematic representation of the surface of the AuNPs after functionalization with mixed monolayers of **3** and HT or **3** and DDT. The longer chain of DDT enhances the stability of the AuNPs but could also diminish the exposure of the catechol groups to the media, thus affecting the functionality of the surface groups.

Initally, four samples were prepared by mixing a dispersion of AuNP-TOAB with thiol solutions in CH_2Cl_2, as summarized in Table 4.1. In all the experiments the total amount of thiol was kept constant and equal to 10 μmols either of a pure thiol or a 1:1 mixture of two thiols. To calculate the amount of thiol necessary for the functionalization, data reported in the literature were used. According to Murray et. al. AuNPs of 5-6 nm in diameter are composed of approximately 4800 Au atoms and covered by 520 linear alkanethiols each.[98] The total amount of AuNPs synthesized in each batch was calculated assuming that all the $HAuCl_4$ was reduced during the synthesis and the amount of thiol needed to functionalize the AuNPs was calculated from there. In order to ensure a full coverage of the nanoparticles surfaces, a large excess of thiols was used in all the experiments.

Table 4.1 Set of experiments carried out to form **3**/alkanethiol mixed-monolayers on AuNPs.

Reaction	AuNp (nmols)[a]	HT (μmols)	3 (μmols)	DDT (μmols)	Mol ratio RSH:3[b]
1	3.1	10	0	0	1:0
2	3.1	5	5	0	1:1
3	3.1	0	0	10	1:0
4	3.1	0	5	5	1:1

[a] Considering that each AuNP is coated by 520 thiols, at least 1.6 μmols of thiol would be necessary to functionalize this amount of AuNPs. A large excess was used in all cases. [b] R = alkyl chain.

After stirring the mixtures for 3 hours, reactions **1** (HT) and **3** (DDT) in Table 4.1 provided stable nanoparticles that could be centrifuged and re-dispersed easily. On the contrary, reaction **2** (HT/**3**) showed the spontaneous precipitation of the AuNPs whilst the rest of the samples did not show any visual changes and remained stable. However, when sample **4** (DDT/**3**) was centrifuged to remove excess thiols, a purple solution with significant red-shifting of its SPR was obtained (see Figure 4.23a), denoting severe aggregation of the AuNPs.. Therefore, none of the mixed monolayers were able to stabilise the nanoparticles.

These preliminary results showed that DDT was a better co-stabilizer than HT for the AuNPs, as the samples did not precipitate spontaneously. Therefore, additional experiments were performed in order to obtain stable nanoparticles by increasing the amount of DDT with respect to **3**. The presence of higher percentages of long alkyl chains on the surface of the AuNPs was expected to provide enhanced stability. Although the decision of decreasing the concentration of catechol groups on the outer surface of the AuNPs may seem contradictory with our goal, we considered that the catechol moiety would still have a determinant role in the properties of the resulting particles, as it has been demonstrated before that a content as small as 10% of functional groups on the surface of AuNPs already provides specific reactivity.[99] With this aim, four additional reactions were carried out in which the DDT:**3** ratio was systematically varied (Table 4.2).

Table 4.2 Set of experiments performed to optimise the DTT/**3** ratio in mixed monolayers on AuNPs.

Reaction	AuNP (nmols)	3 (μmols)	DDT (μmols)	Mol ratio DDT:3	3 (%)
5	1.8	2.08	4.17	2:1	33
6	1.8	0.57	5.7	10:1	10
7	1.8	0.12	6.13	50:1	2
8	1.8	0.06	6.2	100:1	1

After overnight reaction no changes were observed in any of the samples (no precipitation or change in colour). The nanoparticles were then washed by centrifugation after adding an equivalent volume of EtOH to the nanoparticle dispersions. After at least three consecutive washing cycles, samples **7** (2% **3**) and **8** (1% **3**) could be easily re-dispersed in CH_2Cl_2/Hexane mixtures and their UV-VIS spectra showed that their maximum absorbance was not shifted after functionalization, probing the stability of the obtained particles (Figure 4.23b). However, samples **5** (33% **3**) and **6** (10% **3**) precipitated irreversibly after the washings, proving that higher **3** contents in the thiol mixture led to unstable nanoparticles.

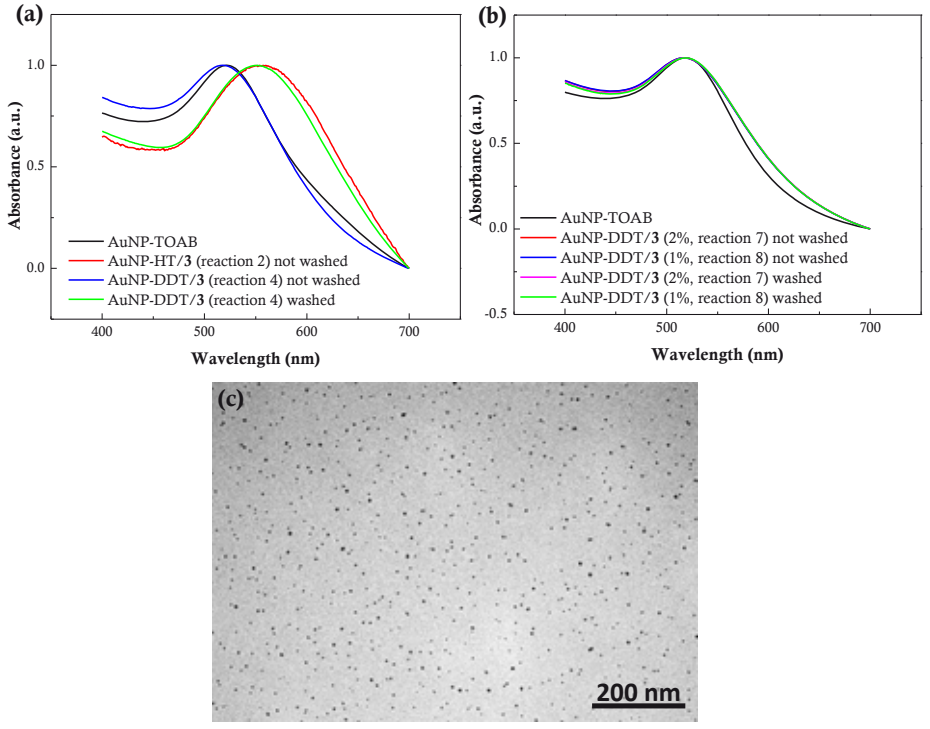

Figure 4.23 UV-VIS spectra of AuNPs functionalized by mixed monolayers. (a) Results obtained after the formation of mixed monolayers of **3** with either HT or DDT. As observed in the spectra, the combination of HT with **3** led to spontaneous aggregation. (b) UV-Vis spectra of the experiments performed towards the optimization of the DDT/**3** ratio to obtain stable NPs. (c) TEM micrograph of the AuNP-DDT/**3** (1%, reaction **8**) sample.

In order to determine the exact composition of the monolayer coating the AuNPs, several NMR experiments were carried out. Indeed, it has been shown before that the thiol ratios present in the solutions used to functionalize AuNPs with mixed monolayers are not exactly reproduced on the AuNP shell.[100,101] For that, a previously described method to etch the nanoparticles using I_2 was used.[29,102] The procedure consisted in simply mixing a

dispersion of AuNPs with a small amount of I_2 and stirring for a few minutes. After that time, a solution containing the disulphide derivatives of the thiols present on the AuNPs surface was obtained, which could be analysed by NMR to determine the ratios of the thiols present in the mixed monolayers. Analysis of the ^{1}H-NMR spectra of the samples resulting from reactions **4** to **8** revealed the lack of signals in the 6-7 ppm range, where the aromatic protons of the catechol moiety should appear (Figure 4.24). Actually, only signals in the alkyl range were observed in all the samples, even in the ones where the linear alkanethiol and the aromatic ligand **3** were present in equimolar amounts in the solution used to functionalize the AuNPs (reaction **4**).

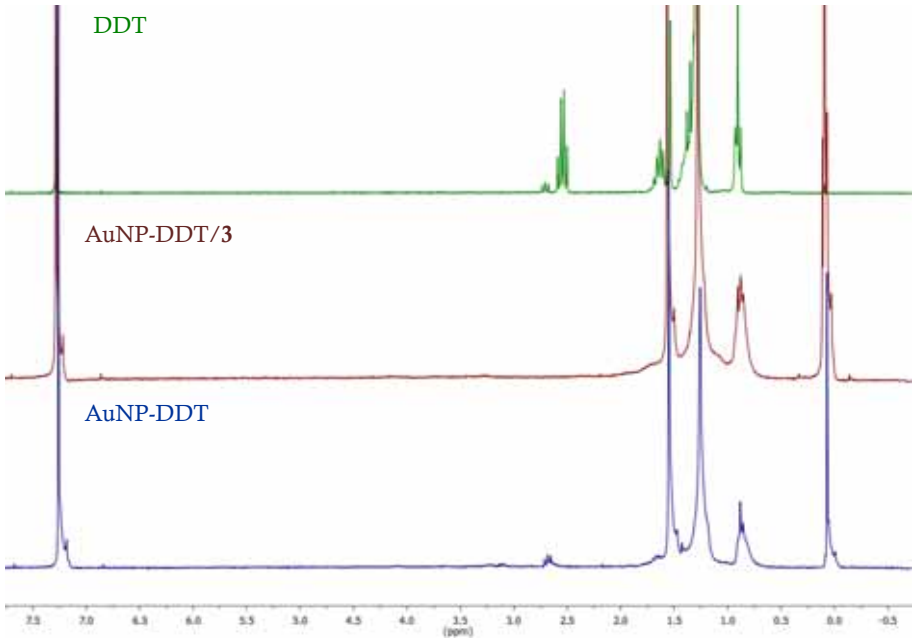

Figure 4.24 ^{1}H-NMR spectra in $CDCl_3$ of the thiol coating of AuNPs functionalized with a 1:1 mixture of DDT and **3** and only with DDT. No aromatic signals were observed in the mixed-monolayer sample.

The lack of aromatic signals or other characteristic signals indicating the presence of **3** in the NMR spectra was mainly attributed to two reasons. On one hand, ligand **3** may not be present in the monolayer in detectable amounts because of its inability to compete with DDT and form mixed monolayers with a significant percentage of catechol moieties. This can be explained by analysing the chemical structure of both ligands; dodecanethiol has a long linear carbon chain which is able to form tightly-packed monolayers much more easily than compound **3**, which is composed of a shorter chain and a bulky substituent. Hence, the DDT moieties quickly assemble on the gold surfaces in a close-packed manner leaving most of the **3** molecules out of the shell. Another possibility would be that ligand **3** was initially

present in the AuNPs shell but the treatment with I_2 caused the oxidation of the catechol groups forming insoluble products that were not detected by NMR. Whilst the first explanation seems the most reasonable one for samples **7** and **8**, due to the small percentages of the catechol-terminated ligand used for functionalization; the second one agrees better with the results observed in reaction **4**, where the behaviour of the AuNPs was clearly affected by the presence of the catechol-terminated ligand.

4.3.3 Attempts to introduce the catechol group in the AuNPs shell by thiol replacement

So far, the introduction of the catechol functionality in the AuNPs surface by coating AuNP-TOAB or AuNP-cit with ligand **3** either alone or in combination with linear alkanethiols had proved to be unsuccessful. As an alternative, DDT-stabilized nanoparticles (from here on AuNP-DDT) were used as a starting material and the alkanethiols on the surface were replaced by exposing the AuNPs to a solution of **3**. [27,96] The process is schematically represented in Figure 4.25. This approach has been used before to include other specific functionalities on the surface of AuNPs and proved to be effective even at low feed ratios. As an example, ω-phenylbutanethiol was able to displace DDT from the stabilizing layer of AuNPs even at a feed ratio as low as 1:4 (ω-phenylbutanethiol:DDT).[27]

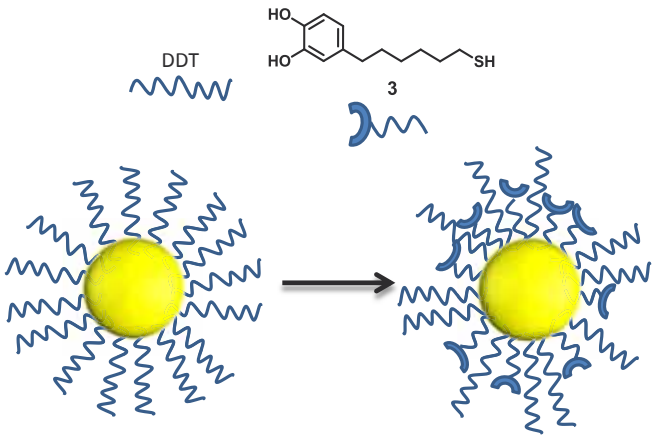

Figure 4.25 Schematic representation of the functionalization of AuNPs by thiol replacement.

To perform these experiments, DDT-stabilized gold nanoparticles of 6.3 nm (1.2 sd) diameter were synthesized following the procedure described by Murray and co-workers.[98] Briefly, a 30 mM solution of $HAuCl_4$ in water was mixed with a solution of TOAB in toluene and the mixture was stirred until the aqueous phase was completely colourless. The aqueous phase was then removed and 1.8 μL of DDT were added under stirring. Finally the

$NaBH_4$ (34 mg) was added quickly and the AuNPs-DDT formed, as seen by the drastic colour change of the solution, which turned dark red. After the synthesis, the excess reagents were removed and three thiol exchange reactions were performed, as summarized in Table 4.3.

Table 4.3 Set of experiments performed to explore the introduction of **3** in the nanoparticles shell through thiol replacement.

Reaction	AuNP (nmols)	DDT (μmols)[a]	3 (μmols)	Mol ratio DDT:3
9	9.5	4.9	4.9	1:1
10	9.5	4.9	2.5	2:1
11	9.5	4.9	9.9	1:2

[a] Amount of DDT bound to AuNPs calculated considering each nanoparticle is coated by 520 thiol ligands.

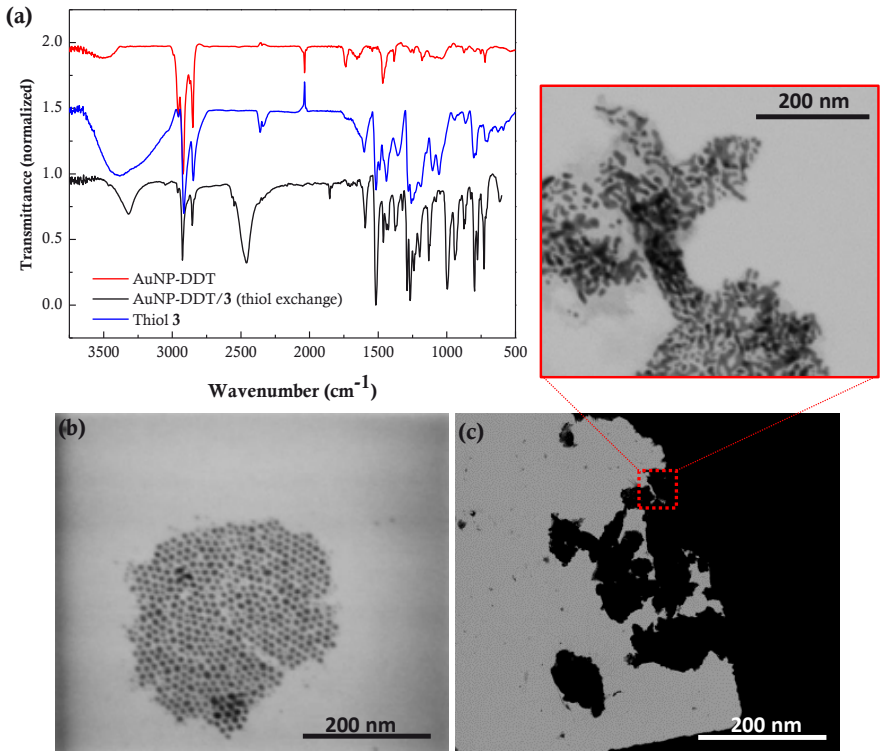

Figure 4.26 (a) IR spectra of the AuNPs after thiol replacement (reaction **9**) showing the presence of the catechol-terminated thiol. (b) STEM image of the DDT-stabilized AuNPs before thiol replacement. (c) STEM image of the AuNPs after the thiol replacement showing irreversible aggregation. In the magnified image (red box) it can be seen how the AuNPs lose their rounded shape.

In the first one (reaction **9**) an equimolar ratio between the entering thiols and those already present in the nanoparticle shell was employed, in the second one (reaction **10**) a two-fold excess of the DDT present in the AuNPs was used and in the third one (reaction **11**) a two-fold excess of the substituting thiol was added. The exchange reactions were carried out overnight and resulted in complete irreversible aggregation and precipitation of the three samples. The obtained black powder was washed by centrifugation/sonication cycles using EtOH and afterwards it was examined by IR-ATR spectroscopy (Figure 4.26a). The IR spectrum of the powder (resulting from reaction **9**) clearly showed the presence of compound **3** on the sample. The absence of the intense band at ~2500 cm^{-1} associated to the S-H bond suggested that the ligand was covalently attached to the gold substrate. Therefore, the replacement reaction successfully occurred but it lead to the complete aggregation of the AuNPs, as seen in the STEM image in Figure 4.26c. An additional experiment was carried out using high dilution conditions (10 times more diluted) and maintaining a 1:1 thiol ratio, unfortunately irreversible aggregation of the nanoparticles also occurred in this case.

4.4 Summary

In this work we have demonstrated the capability of the custom-designed catechol-terminated thiol **3** to self-assemble on flat gold surfaces providing adhesive capabilities to the interface. The formation of self-assembled monolayers on different gold substrates (polycrystalline and epitaxial gold) was demonstrated by several spectroscopic techniques. Then, the interfacial properties of the catechol-modified substrates were studied. Local adhesion measurements performed using an AFM showed enhanced adhesion of the tip on epitaxial gold substrates modified with **3**, overpassing the results obtained on a PDA film in both absolute value and reproducibility due to the highly homogeneous interface created by the SAM. The availability and functionality of the catechol groups at the interface was further studied by adsorbing maghemite nanoparticles on the modified surfaces. This showed that the catechol moieties assembled at the interface were homogeneously distributed and available for interaction with the surface of iron oxide nanoparticles.

The influence of the catechol tailgroup on the formation process and final structure of the monolayer was also addressed. We found that long equilibration times were necessary in order to form tightly packed monolayers showing a strong adhesive character. Even with that, the ellipsommetry results indicated that the tilt angle of the chains was still low (~30º).

This was attributed to the strong interaction of the catechol ring with the substrate as well as to the steric hinderance caused by the aromatic moiety, which difficults the establishment of effective interactions between the chains. Molecular dynamics simulations also provided information about the formation of the SAM from an atomistic point of view. According to the results, a tightly-packed catechol-terminated monolayer with high tilt angles (~60º) should be energetically favoured. Although this is not in accordance with the experimental results, it is an encouraging finding that supports the possibility of reaching higher F_{adh} values using catechol-terminated SAMs if larger tilt angles are induced. This was not possible to achieve during the course of this thesis, but it would be an exciting challenge to face in the future.

The use of AuNPs as substrates for the formation of SAMs of **3** confirmed the difficulty to form tightly-packed monolayers of this compound. The catechol-terminated thiol was grafted on the surface of AuNPs alone and in combination with other co-stabilizers and in any case was possible to obtain stable AuNPs containing compound **3** on the surface. Even when the catechol-terminated thiol was introduced in the AuNP surface by displacement of DDT, it effectively coated the AuNPs forming Au-S bonds but gave place to aggregation. These results confirmed that the presence of the catechol moiety in compound **3**, the steric hindrance that it exerts and its high tendency to interact with surfaces, hampers the formation of tightly-packed monolayers. Overcoming this tendency was relatively easy when SAMs were constructed on planar gold surfaces, as long equilibration times lead to tightly-packed monolayers of thiols exposing catechol moieties. However, when the case of study was AuNPs the equilibration time could not be prolongued, as it was limited by the nature of the system. AuNPs need to be coated by a stabilizing layer as quickly as possible, in order to avoid their aggregation. The tendency of catechols to lay flat on the surface together with the longer distances between the thiolated chains caused by the surface curvature, presumably gave place to AuNPs coated with a disordered monolayer of **3** that was unable to stabilize the AuNPs. The catechol-terminated thiols were unable to form tightly-packed stabilizing monolayers fast enough to avoid the aggregation of the nanoparticles. Therefore, AuNPs functionalized with **3** could be obtained but their instability made it unfeasible to handle the materials.

4.5 Experimental section

Materials: Dopamine hydrochloride , Tris(hydroxymethyl)aminomethane (99.0%), Tris(hydroxymethyl)aminomethane hydrochloride (99.0%), octadecanethiol (ODT, 98%), tetraoctylammonium bromide (TOAB, 98%), dodecatethiol (DDT, ≥ 98%) and hexanethiol (HT, 95%) were purchased from Sigma-Aldrich. Toluene, dichloromethane and hexane (ACS reagent grade) were purchased from Scharlab. Tetrachloroauric acid (99.999% trace metals basis) was purchased form Sigma-Aldrich and right after receiving, it was dissolved in Milli-Q water (18.2 mΩ.cm) to obtain a 50 mM solution that was stored in the fridge and covered in foil to be used as a stock solution.

4.5.1 SAMs on planar Au surfaces

4.5.1.1 Formation of the SAMs: All the substrates were cleaned by sonication in Acetone, EtOH (HPLC grade) and Milli-Q water. After drying under a flow of N_2, they were placed in a UV/O_3 cleaner for 10 min (Novascan Technologies) and immediately immersed in the corresponding solutions. SAM formation was performed by a standard procedure, as follows. Clean gold substrates were immersed overnight in 1 mM solutions of the corresponding thiols in EtOH. Then, the substrates were rinsed with copious amounts of EtOH and Milli-Q water and dried by a nitrogen flow. For the force-distance measurements, the modified substrates were allowed to dry overnight; for the rest of the experiments, they were immediately used as prepared.

4.5.1.2 PDA synthesis and deposition on substrates: Polydopamine was obtained following the previously described procedure.[80] Dopamine hydrochloride (2 mg/mL) was dissolved in 10 mM Tris·HCl (pH 8.6) solution. The previously cleaned substrates were placed in vertical orientation in the freshly-prepared solution and for 1 hour while stirring to minimize non-specific deposition. Afterwards, the substrates were rinsed with Milli-Q water and dried under a nitrogen stream.

4.5.1.3 Iron oxide nanoparticles. Synthesis and adsorption on surfaces: Maghemite nanoparticles were synthesized by Dr. J. Simmchen at the ICN2 using the coprecipitation method.[103] $FeCl_2 \cdot 4H_2O$ (10.21g , 52 mmol) was dissolved in Milli-Q water (1L). Then, a solution of $FeCl_3 \cdot 6H_2O$ (28.35g, 104 mmol) in HCl 1.5 M (57 mL) was added under strong stirring to yield nanometric magnetite (Fe_3O_4). To the previous solution, 25% NH_3 (100 mL)

was added and stirring was stopped after 15 minutes, followed by a two days decantation on a magnet. The black flocculate was dispersed to a 2 M HNO_3 solution and stirred for 2-3 minutes. After decantation, the particles were oxidized to maghemite by adding a solution of $Fe(NO_3)_3 \cdot 9H_2O$ (27.2g, 67.3 mmol) in Milli-Q water (200 mL) and stirring for 30 minutes at 100ºC. After that, a magnetic decantation (2-3 hours) was carried out and the product was dispersed to a 2M HNO_3 solution and stirred during 15 min. The average diameter of the obtained magnetic nanoparticles was 8-10 nm, as estimated from TEM (Figure 4.27). The obtained nanoparticle suspension was diluted to a concentration of Fe_2O_3 ~65 mg/L in Milli-Q water and it was sonicated for 15 min. This dispersion was used as mother solution to prepare the different magnetite dispersions used for the adsorption experiments, being 0.3 mg/ml the concentration that provided better results. For that, differently functionalized polycrystalline gold substrates were immersed in the suspension, sonicated during 15 minutes and rinsed with Milli-Q water. Then they were dried by nitrogen flow.

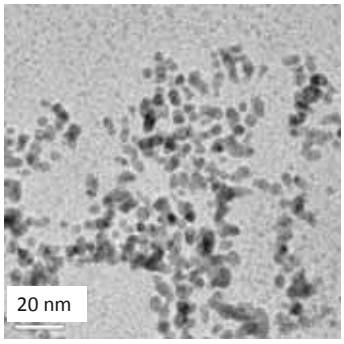

Figure 4.27 TEM image of the maghemite nanoparticles used for adsorption on surfaces

4.5.1.4 Direct-write AFM-assisted lithography: All the lithographic experiments were carried out under ambient conditions (~40% relative humidity, room temperature) using the Nscriptor™ DPN System from Nanoink. For the localized monolayer formation, thiol-coated tips were obtained following a previously described method form Nanoink Inc. Briefly, a UV/O_3 cleaned silicon nitride tip (A-type) was immersed in a saturated solution of **3** in ACN for about 10 seconds and dried with gentle nitrogen flow. After that, the tip was exposed to water vapour for 5 min and then left to dry. Once dry, the tip was re-dipped again in the same solution and blow-dried with nitrogen. The functionalized tip was mounted on the instrument and the laser reflected on the back of the cantilever was aligned with the photodetector. Then the tip was brought into contact with the surface to perform the lithographies by traversing the tip over the surface in the shape of the desired patterns. After the writing procedure, the same coated tip could be used to scan the patterned area,

which was done only in the first lithographies performed in each experimental session to ensure the effective transfer of thiols from the tip to the substrate. In the following lithographies the patterns were written and localized afterwards by scanning the areas with a clean tip. It is worth noting that epitaxial gold surfaces are quite fragile and soft, so careful adjustment of the parameters of the processes, such as laser alignment and deflection setpoint, was required when performing the lithographies and subsequent characterization steps to avoid indentation of the surface.

4.5.1.5 Local F_{adh} measurements using F-d curves: The F-d curves were recorded using SiN cantilevers with nominal force constants of 42 $N \cdot m^{-1}$. The F-d curves were performed by approaching the tip to the substrate and pressing against it until a maximum load was reached (~ 0.5 V) and then retracted while recording the deflection of the cantilever.

At least 45 experiments were performed on each sample to provide an average value. Initially, a unique AFM tip was used in order to obtain directly comparable data for all the studied samples. However, we detected that contamination and damaging of the tip with the experiments resulted in an increase of the dispersion, and decided to use a new tip for each sample.

4.5.1.6 Molecular Dynamics (MD) simulations were based on the numerical solution of the Newtonian equations of motion for all the atoms of the molecular system constrained to the given thermodynamic conditions. All MD simulations were performed using the NAMD software,[104] version 2.9 running in parallel at the Finisterrae Supercomputer (CESGA Supercomputing Center). The equations of motion were solved with a 2 fs time step. The temperature was kept constant at 25 ºC using the Langevin thermostat with a relaxation constant of 1 ps^{-1}. In simulations with water as a solvent, the liquid was also maintained at constant pressure of 1 atm employing the Nosé-Hoover-Langevin piston in the vertical direction with an oscillation period of 100 fs and a decay time of 50 fs (which are standard parameters for NAMD). Periodic boundary conditions in all directions were employed in all the simulations. The snapshots of the simulations and the energy calculations were obtained from the MD trajectories by using the Visual Molecular Dynamics (VMD) software.[105]

4.5.2 Catechol-functionalized AuNPs

4.5.2.1 Synthesis of TOAB-stablised AuNPs: Organic solvent-soluble AuNP were obtained by the well-known Brust-Schiffrin method[47] with a slight modification.

In a 25 ml Erlenmeyer flask, 3 ml of a 30 mM aqueous solution of $HAuCl_4$ (0.09 mmols) were mixed with 210 mg of tetraoctylammonium bromide (TOAB, 0.38 mmols) dissolved in 8 mL of a 1:1 Hexane/CH_2Cl_2 mixture under vigorous stirring. After a few minutes all the gold precursor had been transferred to the organic phase, which showed a bright orange colour. After that, 38 mg of $NaBH_4$ (1 mmol) in 2.5 mL of water were added to the mixture dropwise, which caused the change of colour of the organic phase form orange to deep dark red.

After 30 minutes the two phases were separated and the organic fraction was successively washed with 20 mL of H_2SO_4 0.1 M, 20 mL of Na_2CO_3 1 M (twice) and 20 mL of H_2O (three times). Then the organic phase was dried over $MgSO_4$ and filtered through filter paper.

4.5.2.2 Replacement of TOAB by thiol ligands: For the functionalization of the nanoparticle surfaces with thiol ligands, a dispersion of AuNPs-TOAB in CH_2Cl_2/Hex (1:1), (AuNP concentration between 1 and 10 μM) was mixed with a solution of the ligand or mixture of ligands in CH_2Cl_2. The concentration of each solution as well as the ratios in which they were mixed and the reaction time were varied in order to optimise the process. However, in all the cases, a large molar excess (about 10-fold) of thiol was used to ensure complete displacement of the TOAB molecules. After the exchange, the excess thiols and displaced TOAB were removed by centrifugation.

*4.5.2.3 Functionalization of water-dispersible AuNPs with **3**:* Water-soluble AuNPs stabilized by citrate ions were obtained using a reported procedure.[92] A 50 mM solution of $HAuCl_4$ (0.4 mL) was diluted by adding 9.6 mL of H_2O and then 1 mL of a 38.8 mM solution of sodium citrate was added followed by the dropwise addition of 1.2 mL of a 50 mM solution of $NaBH_4$ in H_2O under vigorous stirring that was maintained for two hours.

For the functionalization with the catechol-terminated ligand **3**, 500 μL of the obtained AuNP-cit dispersion in water were mixed with a large excess of **3** (4 mg) in 400 μL EtOH and stirred overnight. After that time, an equivalent volume of EtOH was added to the mixture and it was centrifuged and washed with EtOH and finally re-dispersed in a H_2O/EtOH mixture.

*4.5.2.4 Introduction of ligand **3** through thiol replacement:* For the experiments where the catechol functionality was inserted in the AuNP shell using a thiol replacement procedure our starting material were AuNPs-DDT that were obtained following a previously described procedure based on the Brust-Schiffrin method.[98]

Briefly, 3 mL of a 30 mM solution of $HAuCl_4$ (0,09 mmols) were mixed with 120 mg of TOAB in 8 mL toluene under stirring. After approximately ten minutes all the gold had been transferred to the organic phase. The aqueous phase was removed and 1.8 µL (7.51 µmols) of DDT were added and the solution was stirred for ten more minutes. Finally, a freshly prepared solution of $NaBH_4$ in water (34 mg in 2,5 mL H_2O) was quickly added, which resulted in a drastic change of colour of the solution form orange to dark red. The reaction mixture was stirred for three more hours to ensure full transformation of the reagents.

After that time, the aqueous phase was removed and the solvent evaporated. To the obtained solid, about 6 mL of EtOH were added and the mixture was sonicated briefly. The dark suspension was filtered through filter paper and washed with EtOH (8 mL) and acetone (25 mL) and left to dry overnight. The solid could then be easily re-dispersed in non-polar solvents.

For the thiol exchange experiments, 5 mL of 2 mg/mL solutions of AuNP-DDT in CH_2Cl_2 were mixed with variable volumes of 2 mg/ml solution of **3** in CH_2Cl_2 (276 µL, 560 µL, 1.12 mL) and the mixtures were kept under stirring overnight. The ratios between bound and entering thiols were varied from 2:1 to 1:2, and experiments in diluted conditions (0,2 and 0,02 mg/mL) were also carried out.

Whenever the nanoparticles did not precipitate spontaneously, the mixture was centrifuged and the precipitate washed with EtOH. When the AuNPs did precipitate, the supernatant was removed and the powder was washed with EtOH. In any case the materials were re-dispersible.

4.5.2.5 AuNP etching: To etch the AuNP and release the thiols present in the shell, ~50 mg of AuNPs in CH_2Cl_2 were mixed with 3 mg of I_2 and stirred for 1-2 hours. The obtained solution was evaporated to dryness and the residue was dissolved in CD_3Cl and analysed by NMR.

4.6 References

(1) Waite, J. H.; Andersen, N. H.; Jewhurst, S.; Sun, C. *J. Adhes.* **2005**, *81*, 297–317.

(2) Israelachvili, J.; Min, Y.; Akbulut, M.; Alig, A.; Carver, G.; Greene, W.; Kristiansen, K.; Meyer, E.; Pesika, N.; Rosenberg, K.; Zeng, H. *Reports Prog. Phys.* **2010**, *73*, 036601.

(3) Li, S.-C.; Chu, L.-N.; Gong, X.-Q.; Diebold, U. *Science* **2010**, *328*, 882–884.

(4) Mcbrlde, M. B.; Wessellnk, L. G. *Environ. Sci. Technol.* **1988**, *22*, 703–708.

(5) Guvendiren, M.; Messersmith, P. B.; Shull, K. R. *Biomacromolecules* **2008**, *9*, 122–128.

(6) Hwang, D. S.; Harrington, M. J.; Lu, Q.; Masic, A.; Zeng, H.; Waite, J. H. *J. Mater. Chem.* **2012**, *22*, 15530.

(7) Anderson, T. H.; Yu, J.; Estrada, A.; Hammer, M. U.; Waite, J. H.; Israelachvili, J. N. *Adv. Funct. Mater.* **2010**, *20*, 4196–4205.

(8) Danner, E. W.; Kan, Y.; Hammer, M. U.; Israelachvili, J. N.; Waite, J. H. *Biochemistry* **2012**, *51*, 6511–6518.

(9) Yu, J.; Wei, W.; Danner, E.; Israelachvili, J. N.; Waite, J. H. *Adv. Mater.* **2011**, *23*, 2362–2366.

(10) Yu, J.; Wei, W.; Menyo, M. S.; Masic, A.; Waite, J. H.; Israelachvili, J. N. *Biomacromolecules* **2013**, *14*, 1072–1077.

(11) Mian, S. A.; Yang, L. M.; Saha, L. C.; Ahmed, E.; Ajmal, M.; Ganz, E. *Langmuir* **2014**, *30*, 6906–6914.

(12) Lin, Q.; Gourdon, D.; Sun, C.; Holten-Andersen, N.; Anderson, T. H.; Waite, J. H.; Israelachvili, J. N. *Proc. Natl. Acad. Sci. USA* **2007**, *104*, 3782–3786.

(13) Wei, W.; Yu, J.; Gebbie, M. A.; Tan, Y.; Martinez Rodriguez, N. R.; Israelachvili, J. N.; Waite, J. H. *Langmuir* **2015**, *31*, 1105–1112.

(14) White, J. D.; Wilker, J. J. *Macromolecules* **2011**, *44*, 5085–5088.

(15) Nicklisch, S. C. T.; Waite, J. H. *Biofouling* **2012**, *28*, 865–877.

(16) Lee, H.; Scherer, N. F.; Messersmith, P. B. *Proc. Natl. Acad. Sci. USA* **2006**, *103*, 12999–13003.

(17) Wang, J.; Tahir, M. N.; Kappl, M.; Tremel, W.; Metz, N.; Barz, M.; Theato, P.; Butt, H.-J. *Adv. Mater.* **2008**, *20*, 3872–3876.

(18) Li, Y.; Qin, M.; Li, Y.; Cao, Y.; Wang, W. *Langmuir* **2014**, *30*, 4358–4366.

(19) Saiz-Poseu, J.; Alcón, I.; Alibés, R.; Busqué, F.; Faraudo, J.; Ruiz-Molina, D. *CrystEngComm* **2012**, *14*, 264–271.

(20) Saiz-Poseu, J.; Faraudo, J.; Figueras, A.; Alibés, R.; Busqué, F.; Ruiz-Molina, D. *Chem. Eur. J.* **2012**, *18*, 3056–3063.

(21) Lee, B. P.; Messersmith, P. B.; Israelachvili, J. N.; Waite, J. H. *Annu. Rev. Mater. Res.* **2011**, *41*, 99–132.

(22) Love, J. C.; Estroff, L. A.; Kriebel, J. K.; Nuzzo, R. G.; Whitesides, G. M. *Chem. Rev.* **2005**, *105*, 1103–1169.

(23) Templeton, A. C.; Wuelfing, W. P.; Murray, R. W. *Acc. Chem. Res.* **2000**, *33*, 27–36.

(24) Lawrence, H.; Ralph, G. *Annu. Rev. Chem.* **1992**, *43*, 437–463.

(25) Hsu, S.-H.; Reinhoudt, D. N.; Huskens, J.; Velders, A. H. *J. Mater. Chem.* **2011**, *21*, 2428.

(26) Hill, H. D.; Millstone, J. E.; Banholzer, M. J.; Mirkin, C. A. *ACS Nano* **2009**, *3*, 418–424.

(27) Ingram, R. S.; Hostetler, M. J.; Murray, R. W.; Hill, C.; Carolina, N. *J. Am. Chem. Soc.* **1997**, *119*, 9175–9178.

(28) Weeraman, C.; Yatawara, A. K.; Bordenyuk, A. N.; Benderskii, A. V. *J. Am. Chem. Soc.* **2006**, *128*, 14244–14245.

(29) Templeton, A. C.; Hostetler, M. J.; Kraft, C. T.; Murray, R. W.; Hill, C.; Carolina, N. *J. Am. Chem. Soc.* **1998**, *7863*, 1906–1911.

(30) Lucarini, M.; Franchi, P.; Pedulli, G. F.; Gentilini, C.; Polizzi, S.; Pengo, P.; Scrimin, P.; Pasquato, L. *J. Am. Chem. Soc.* **2005**, *127*, 16384–16385.

(31) Ulman, A. *Chem. Rev.* **1996**, *96*, 1533–1554.

(32) Srisombat, L.; Jamison, A. C.; Lee, T. R. *Colloid Surface A* **2011**, *390*, 1–19.

(33) Simmons, N. J.; Chin, K. O. A.; Harnisch, J. A.; Vaidya, B.; Trahanovsky, W. S.; Porter, M. D.; Angelici, R. J. *J. Electroanal. Chem.* **2000**, *482*, 178–187.

(34) Vahlberg, C.; Linares, M.; Villaume, S.; Norman, P.; Uvdal, K. *J. Phys. Chem. C* **2011**, *115*, 165–175.

(35) Petoral, R. M.; Uvdal, K. *J. Phys. Chem. B* **2003**, *107*, 13396–13402.

(36) Tian, Y.; Ye, S.; Ran, Q.; Xian, Y.; Xu, J.; Peng, R.; Jin, L. *Phys. Chem. Chem. Phys.* **2010**, *12*, 13287–13295.

(37) Brooksby, P. A.; Schiel, D. R.; Abell, A. D. *Langmuir* **2008**, *24*, 9074–9081.

(38) Nakano, K.; Ohkubo, K.; Taira, H.; Takagi, M.; Imato, T. *Anal. Chim. Acta* **2008**, *619*, 30–36.

(39) Salmanipour, A.; Taher, M. A. *Analyst* **2011**, *136*, 545–549.

(40) Kang, J.; Zhuo, L.; Lu, X.; Wang, X. *J. Solid State Electrochem.* **2004**, *9*, 114–120.

(41) Shultz, M. D.; Reveles, J. U.; Khanna, S. N.; Carpenter, E. E. *J. Am. Chem. Soc.* **2007**, *129*, 2482–2487.

(42) Basnar, B.; Xu, J.; Li, D.; Willner, I. *Langmuir* **2007**, *23*, 2293–2296.

(43) Saha, K.; Agasti, S. S.; Kim, C.; Li, X.; Rotello, V. M. *Chem. Rev.* **2012**, *112*, 2739–2779.

(44) Faraday, M. *Philos. Trans. R. Soc. London* **1857**, *147*, 145–181.

(45) Turkevich, J.; Stevenson, P. C.; Hillier, J. *Discuss. Faraday Soc.* **1951**, *11*, 55.

(46) Frens, G. *Nat. Phys. Sci.* **1973**, *241*, 20–22.

(47) Brust, M.; Walker, M.; Bethell, D.; Schiffrin, D. J.; Whyman, R. *J. Chem. Soc. Chem. Commun.* **1994**, 801–802.

(48) Hostetler, M. J.; Stokes, J. J.; Murray, R. W. *Langmuir* **1996**, *12*, 3604–3612.

(49) Brust, M.; Fink, J.; Bethell, D.; Schiffrin, D. J.; Kiely, C. *J. Chem. Soc. Chem. Commun.* **1995**, 1655–1656.

(50) Badia, A.; Gao, W.; Singh, S.; Demers, L.; Cuccia, L.; Reven, L. *Langmuir* **1996**, *12*, 1262–1269.

(51) Fink, J.; Kiely, C. J.; Bethell, D.; Schiffrin, D. J. *Chem. Mater.* **1998**, *10*, 922–926.

(52) Neouze, M.-A.; Schubert, U. *Monatshefte für Chemie - Chem. Mon.* **2008**, *139*, 183–195.

(53) Hostetler, M. J.; Templeton, A. C.; Murray, R. W. *Langmuir* **1999**, *15*, 3782–3789.

(54) Choudhary, A.; Singh, G.; Biradar, A. M. *Nanoscale* **2014**, *6*, 7743–7756.

(55) Zeng, S.; Yong, K.-T.; Roy, I.; Dinh, X.-Q.; Yu, X.; Luan, F. *Plasmonics* **2011**, *6*, 491–506.

(56) Link, S.; El-Sayed, M. A. *Annu. Rev. Phys. Chem.* **2003**, *54*, 331–366.

(57) Daniel, M.-C.; Astruc, D. *Chem. Rev.* **2004**, *104*, 293–346.

(58) Kamat, P. V. *J. Phys. Chem.* **2002**, *106*, 7729–7744.

(59) Ghosh, S. K.; Nath, S.; Kundu, S.; Esumi, K.; Pal, T. *J. Phys. Chem. B* **2004**, *108*, 13963–13971.

(60) Yoon, J. H.; Yoon, S. *Langmuir* **2013**, *29*, 14772–14778.

(61) Ghosh, S. K.; Pal, T. *Chem. Rev.* **2007**, *107*, 4797–4862.

(62) Su, K. H.; Wei, Q. H.; Zhang, X.; Mock, J. J.; Smith, D. R.; Schultz, S. *Nano Lett.* **2003**, *3*, 1087–1090.

(63) Srivastava, S.; Frankamp, B. L.; Rotello, V. M. *Chem. Mater.* **2005**, *17*, 487–490.

(64) Lin, Y.-W.; Huang, C.-C.; Chang, H.-T. *Analyst* **2011**, *136*, 863–871.

(65) Ye, S.; Shi, X.; Gu, W.; Zhang, Y.; Xian, Y. *Analyst* **2012**, *137*, 3365–3371.

(66) Phillips, D. J.; Davies, G.-L.; Gibson, M. I. *J. Mater. Chem. B* **2014**, *3*, 270–275.

(67) Kailasa, S. K.; Wu, H.-F. *Analyst* **2012**, *137*, 1629–1638.

(68) Tao, E. B. T. Y.; Evall, J. *J. Am. Chem. Soc.* **1989**, *335*, 321–335.

(69) Hojo, D.; Togashi, T.; Iwasa, D.; Arita, T.; Minami, K.; Takami, S.; Adschiri, T. *Chem. Mater.* **2010**, *22*, 1862–1869.

(70) Weinhold, M.; Soubatch, S.; Temirov, R.; Rohlfing, M.; Jastorff, B.; Tautz, F. S.; Doose, C. *J. Phys. Chem. B* **2006**, *110*, 23756–23769.

(71) Porter, M. D. *Anal. Chem.* **1988**, *60*, 1143–1155.

(72) Zharnikov, M. *J. Electron Spectros.* **2010**, *178-179*, 380–393.

(73) Cavalleri, O.; Oliveri, L.; Daccà, A.; Parodi, R.; Rolandi, R. *Appl. Surf. Sci.* **2001**, *175-176*, 357–362.

(74) Mielczarski, J. a.; Dong, J.; Mielczarski, E. *J. Phys. Chem. B* **2008**, *112*, 5228–5237.

(75) Moulder, J. F.; Stickle, W. E.; Sobol, P. E.; Bomben, K. D. *Handbook of X-ray Photoelectron Spectroscopy*; Perkin-Elmer Corp.: Eden Prairie, MN, 1992.

(76) Ulman, A. *An Introduction to Ultrathin Organic Films: from Langmuir-Blodgett to Self-Assembly*; Academic Press: New York, NY, 1991.

(77) Tompkins, H. G.; McGahan, W. A. *Spectroscopic EIlipsommetry and reflectommetry: A User's Guide*; John Wiley & Sons: New York, NY, 1999.

(78) Cappella, B.; Dietler, G. *Surf. Sci. Rep.* **1999**, *34*, 1–104.

(79) Verdaguer, A.; Sacha, G. M.; Bluhm, H.; Salmeron, M. *Chem. Rev.* **2006**, *106*, 1478–1510.

(80) Lee, H.; Dellatore, S. M.; Miller, W. M.; Messersmith, P. B. *Science* **2007**, *318*, 426–430.

(81) Zangmeister, R. A.; Morris, T. A.; Tarlov, M. J. *Langmuir* **2013**, *29*, 8619–8628.

(82) Della Vecchia, N. F.; Avolio, R.; Alfè, M.; Errico, M. E.; Napolitano, A.; D'Ischia, M. *Adv. Funct. Mater.* **2013**, *23*, 1331–1340.

(83) Hong, S.; Na, Y. S.; Choi, S.; Song, I. T.; Kim, W. Y.; Lee, H. *Adv. Funct. Mater.* **2012**, *22*, 4711–4717.

(84) Liebscher, J.; Mrówczyński, R.; Scheidt, H. A.; Filip, C.; Hădade, N. D.; Turcu, R.; Bende, A.; Beck, S. *Langmuir* **2013**, *29*, 10539–10548.

(85) Browne, K. P.; Grzybowski, B. a. *Langmuir* **2011**, *27*, 1246–1250.

(86) Xu, C.; Jones, R. L.; Batteas, J. D. *Scanning* **2008**, *30*, 106–117.

(87) Yuen, A. K. L.; Hutton, G. A.; Masters, A. F.; Maschmeyer, T. *Dalton Trans.* **2012**, *41*, 2545–2559.

(88) Sheehan, P. E.; Whitman, L. J. *Phys. Rev. Lett.* **2002**, *88*, 156104.

(89) Rozhok, S.; Piner, R.; Mirkin, C. A. *J. Phys. Chem. B* **2003**, *107*, 751–757.

(90) Barsotti, R. J.; O'Connell, M. S.; Stellacci, F. *Langmuir* **2004**, *20*, 4795–4798.

(91) Campiglio, P.; Campione, M.; Sassella, A. *J. Phys. Chem. C* **2009**, *113*, 8329–8335.

(92) Yang, J.; Lee, J. Y.; Deivaraj, T. C.; Too, H.-P. *J. Colloid Interface Sci.* **2004**, *277*, 95–99.

(93) Liu, J.; Anand, M.; Roberts, C. B. *Langmuir* **2006**, *22*, 3964–3971.

(94) Tielsch, B. J.; Fulghum, J. E.; Surman, D. J. *Surf. Interface Anal.* **1996**, *24*, 459–468.

(95) Azcárate, J. C.; Corthey, G.; Pensa, E.; Vericat, C.; Fonticelli, M. H.; Salvarezza, R. C.; Carro, P. *J. Phys. Chem. Lett.* **2013**, *4*, 3127–3138.

(96) Hostetler, M. J.; Green, S. J.; Stokes, J. J.; Murray, R. W. *J. Am. Chem. Soc.* **1996**, *118*, 4212–4213.

(97) Gutiérrez-Wing, C.; Ascencio, J. A.; Pérez-Alvarez, M.; Marín-Almazo, M.; José-Yacamán, M. *J. Clust. Sci.* **1998**, *9*, 529–545.

(98) Hostetler, M. J.; Wingate, J. E.; Zhong, C.; Harris, J. E.; Vachet, R. W.; Clark, M. R.; Londono, J. D.; Green, S. J.; Stokes, J. J.; Wignall, G. D.; Glish, G. L.; Porter, M. D.; Evans, N. D.; Murray, R. W. *Langmuir* **1998**, *14*, 17–30.

(99) Zheng, M.; Huang, X. *J. Am. Chem. Soc.* **2004**, *126*, 12047–12054.

(100) Itoh, H.; Tahara, A.; Naka, K.; Chujo, Y. *Langmuir* **2004**, *20*, 1972–1976.

(101) Stewart, A.; Bell, S. E. J. *Chem. Commun.* **2011**, *47*, 4523–4525.

(102) Templeton, A. C.; Hostetler, M. J.; Warmoth, E. K.; Chen, S.; Hartshorn, C. M.; Krishnamurthy, V. M.; Forbes, M. D. E.; Murray, R. W.; Hill, C.; Carolina, N. *J. Am. Chem. Soc.* **1998**, *7863*, 4845–4849.

(103) Ruiz-Hernández, E.; Baeza, A.; Vallet-Regí, M. *ACS Nano* **2011**, *5*, 1259–1266.

(104) Phillips, J. C.; Braun, R.; Wang, W.; Gumbart, J.; Tajkhorshid, E.; Villa, E.; Chipot, C.; Skeel, R. D.; Kalé, L.; Schulten, K. *J. Comput. Chem.* **2005**, *26*, 1781–1802.

(105) Humphrey, W.; Dalke, A.; Schulten, K. *J. Mol. Graph.* **1996**, *14*, 33–38.

Chapter 5

Synthesis of catechol-based materials confined in femtolitre volumes

Direct-write AFM-assisted lithography will be used in this Chapter to confine the synthesis of two catechol-based functional polymers. The systems of choice are polydopamine, a well-known adhesive and functionalizable platform; and **CPP1** particles, which show VT interconversion and are potential building-blocks of future molecular electronic devices.

5.1 Introduction

The Electronic Numerical Integrator and Computer (ENIAC) was built in the 1940s at the University of Pennsylvania and was one of the first electronic programmable computers. Its weight was 27 tons and it occupied an area of 680 square feet.[1] Today, computers deal with much more complex operations in a fraction of the time while we carry them in our pockets. Since the burst of the so called "information era" there is an ever-growing demand of devices that perform faster and better, that means higher densities of integration, less power consumption, more information storage and reduction of cost. This trend towards higher levels of complexity and integration is not only found in the electronics and computing field but also in applications such as micro-electromechanical systems (MEMs), sensors, microfluidic devices and biochips.[2] A direct consequence of this trend is the need to reduce the size of the individual components of the device (materials). Because of that, (micro-)patterning has become one of the most intensively studied technologies and continuous advances are made towards the building of stable, precisely controlled and reproducible micro- and nanostructures.[3–7]

Femtolitre chemistry has arisen in the last few years as an exciting way to synthesize nanoscale materials in a highly controlled manner. In combination with patterning and micro/nano-fabrication techniques, it has opened the door to the creation of large and dense arrays of parallelized small volumes for high-throughput screening, combinatorial chemistry and biology, or chemical synthesis.[8] Beyond the need for nanostructured materials, there are several other scientific motivations to conduct chemistry at this scale. A femtolitre (fL= 10^{-15} L, 1 μm^3) is approximately the volume of the bacterial cell *Escherichia coli*, therefore the ultimate chemistry of life takes place in confined volumes that range from picolitres (pL= 10^{-12} L, 10 μm^3) to attolitres (aL=10^{-18} L, 100 nm^3).[9] It is important then to reproduce these highly crowded and confined conditions in order to understand their effect on the thermodynamics and kinetics of the reactions.[10] Also, confined reaction volumes can act as templates and have an influence on parameters such as particle size, particle shape or surface texture of nanomaterials,[11] allowing to tune the morphology-size-property correlations.

So far, miniaturized reactors have mostly been contructed using either self-contained structures[9,10] (emulsions, liposomes, micelles or protein cages) (Figure 5.1a) or microfluidic-generated droplets (Figure 5.1b).[12–14] Multiple (bio)chemical reactions[15–20] as well as synthesis of different types of nanoparticles[21–27] have been performed using these methods to study the confined reactions or produce high-quality materials.

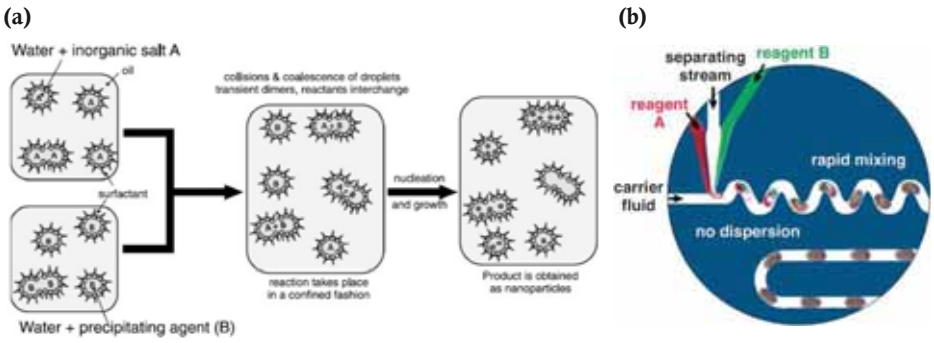

Figure 5.1 (a) Schematic representation of the synthesis of inorganic nanoparticles using water-in-oil emulsions. For purely inorganic materials, the precipitating agent (B) is usually a reducing agent such as $NaBH_4$, in the case of metal-organic particles, (B) corresponds to the organic ligand(s). (b) Mixture of reagents inside droplets generated in microfluidic channels. The mixture of the reagents occurs in a very reproducible and fast way which leads to monodisperse structures. Reproduced from ref. 27 and ref. 12.

Among the different approaches, the confined synthesis of functional materials directly on specific areas of a surface is of special relevance, as it opens the door to the direct integration of those materials into working devices. In this context, direct-write AFM-assisted lithography and other derived tip-based lithographies appear as valuable tools.

5.1.1 Direct-write AFM-assisted lithography: a brief introduction

Also referred to as Scanning Probe Lithography (SPL), AFM lithography or tip-assisted lithography; AFM-assisted lithography is a high-resolution technique that uses a sharp tip to pattern nano-to-microscale features on a surface. Actually, the category Scanning Probe Lithography comprises a wide range of techniques that have in common the use of an AFM tip to mediate the patterning process.[7] Direct-write AFM lithography is one of those techniques and it resembles the normal writing process, where the AFM tip is used as "pen", a solid state substrate acts as "paper" and a solution containing the material(s) as "ink".

The first example of molecular transport from a tip to a surface was reported in 1995 by Jaschke and Butt,[28] who deposited aggregates of ODT onto freshly cleaved mica. A few years later, in 1999, Mirkin and co-workers demonstrated the enormous potential of direct-write AFM lithography by arranging alkanethiol molecules onto a gold surface in the shape of well-defined SAMs with excellent resolution (down to 12 nm).[29,30] Importantly, the same authors demonstrated the capability of the method to fabricate multi-component nanostructures made of monolayers of different alkanethiols with only 5 nm of separation.[31,32] These results led to the invention of a commercialized process named Dip-

Pen Nanolithography® (abbreviated as DPN®), that became a registered trademark of NanoInk, Inc. (Chicago, IL). In the subsequent years the technique became increasingly popular[33,34] and since then a myriad of materials has been successfully structured in a variety of substrates.[35–43]

The experimental procedure of direct-write AFM lithography is relatively simple. The molecules or nanostructures acting as inks are first coated on the tip and then transported to the substrate by engaging and traversing the tip over the surface in the form of the desired patterns. Although at the experimental level the technique can be seen as relatively easy, the fundamentals of the writing mechanism are much more complex and still under debate.[44–46] A number of factors have been reported to influence the ink transport during the patterning of ODT and mercaptohexadecanoic acid (MHA) on gold.[35,47] The transport of these small organic molecules is known to occur by diffusion through the water meniscus that is formed due to capillary condensation under ambient conditions, as shown in Figure 5.2a.[48–53] However, the ink delivery mechanism for more complex systems, such as nanoparticles or the deposition of liquids, is still unclear.[54,55]

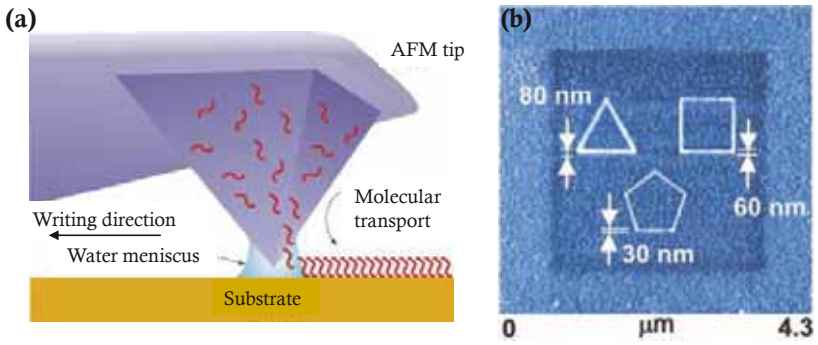

Figure 5.2 (a) Schematic representation of the writing process of direct-write AFM-assisted lithography. A functionalised AFM tip dispenses the ink onto the substrate by diffusion through the water meniscus. (b) LFM images of SAMs in the shapes of polygons drawn by direct-write AFM-assisted lithography with MHA on an amorphous Au surface. An ODT SAM overwritten around the polygons can be seen thanks to the difference in friction. Reproduced from ref. 31.

According to the ink's physical state, direct-write AFM lithography experiments can be categorized into two types: dry and liquid.[56] In classic (dry) writing, the patterned materials are present on the tip in the solid state, as described in the previous Chapter for the deposition of the catechol-terminated thiol **3** on gold. This methodology was originally developed for the deposition of alkanethiols,[29] but it has extended to more complex inks such as nanoparticles,[57] biomolecules[58,59] and materials supported on matrix carriers.[60,61] A completely different methodology and the one used in the experiments described in this Chapter, consists in dipping the tip into an ink solution for a given time and immediately

using it. In this case, the ink is transferred to the substrate through the delivery of less than femtoliter droplets of the solution previously loaded on the tip. After the patterning process, the solvents evaporate and motifs of solid materials are obtained. In order to ensure an efficient and controlled transfer from the tip to the surface, the inks must fulfil several requirements. First, the solution must exhibit an adequate viscosity to ensure an homogeneous coating of the tip and a controlled transference of the material to the surface,[62] also the ink must be in its liquid state over the whole writing process. For that, high boiling point solvents and viscous additives can be used as well as control of the environmental conditions (relative humidity and temperature). Additionally, the surface affinity of the ink should be neither too weak nor too strong to guarantee a controlled delivery and the deposited materials should be highly soluble and stable in the solvents

The main advantage of direct-write AFM assited lithography in comparison with other structuration techniques is that it allows the precise positioning of materials onto virtually any substrate without the need of previous surface or material modification. However, the utility of AFM-assisted lithography has always been limited by its low throughput; i.e. its inability to pattern large areas in a reasonable time due to its inherent serial writing nature. Because of that, it has been considered a technique restricted to proof-of-concept studies and basic science. In order to expand the limits of the technique, 2D cantilever arrays[63,64] and cantilever-free printing tools have been designed,[65–67] resulting in the appearance of new tip-based lithographic techniques such as Polymer Pen Lithography (PPL).[60,68–70]

Although direct-write AFM lithography has been mostly used to position materials in the same chemical state as they are present in the inks, this technique can be also used to fabricate femtolitre-sized containers and promote the transformation of the materials inside them to induce the growth of nanostructures. By precisely controlling parameters such as concentration of the ink solutions, deposited volume, temperature or solvent evaporation; the formation of nanostructures inside the features can be achieved. In the next paragraphs we describe some examples of the use of femtolitre-sized vessels fabricated by tip-assisted lithography to confine crystallization and self-assembly processes, as well as nanoparticle growth.

In 2011, our group reported one of the first examples of confined crystal growth using direct-write AFM lithography. An AFM tip was used to deliver femtolitre droplets of the soluble precursors of metal-organic nanostructures onto a target surface.[71,72] In that way, crystals of the well-known metal-organic framework HKUST-1 ($[Cu_3(BTC)_2]$, BTC= 1,3,5-benzenetricarboxylate)[73] were grown directly on gold surfaces after incubation of the patterned precursors in a DMF atmosphere (Figure 5.3, left panel). Also, hollow structures

of polyoxometallates (POMs) were obtained through surface-confined self-assembly. A reduction in the volume of the deposited droplets, together with the precise control of solvent evaporation afforded the formation of a single nanostructure per deposited droplet. Carbonell and co-workers also described the formation of single HKUST-1 crystals inside femtolitre-sized droplets[74] obtained by Microfluidic Pen Lithography (MPL).[75]

On the other hand, the controlled growth of metallic and semiconductor nanoparticles directly on surface has received much attention. Since 2010, the Mirkin group has released several papers using Scanning Probe Block Copolymer Lithography (SPBCL) to obtain a diversity of nanoparticles by patterning their precursors and confining the synthesis and growth of the structures.[76] By using this methodology single nanoparticles were obtained in each lithographic feature with precise control over their size and position. This method was successfully employed to obtain metallic, metal oxide and metal alloy nanoparticles[77] (Figure 5.3, right panel) as well as CdS quantum dots.[78] They were also able to monitorize the growth of the nanostructures and study the influence of temperature by in-situ TEM experiments.[79]

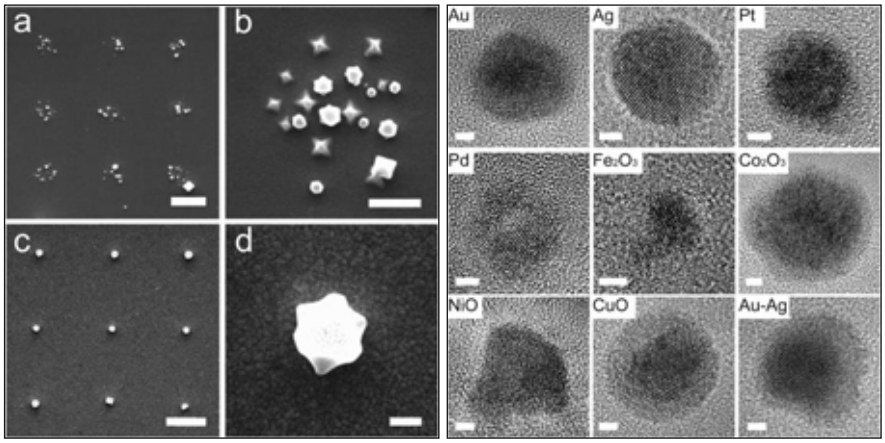

Figure 5.3 Left panel: FE-SEM images of HKUST-1 nanocrystals grown inside confined solution droplets deposited by direct-write AFM_assisted lithography. (a) Nanoarray; scale bar 2 μm. (b) Details of the nanocrystals grown inside each dot-like feature; scale bar 1 μm. Growth of a single crystal per dot nanoarray viewed from above (c) and at a 45º tilt angle (d); scale bars 2 μm and 200 nm respectively. Right panel: HR-TEM images of different inorganic nanoparticles obtained in confined environments fabricated by SPBCL, scale bars 2 nm. Reproduced from ref. 71 and ref. 77.

5.1.2 Direct-write AFM-assisted lithography for confined reactions in femtolitre volumes

A highly challenging and novel application of direct-write AFM-assisted lithography consists in the fabrication of femtolitre reaction vessels and the performance of confined reactions inside these ultrasmall volumes. This methodology is not only scientifically

challenging but can also be applied to the positioning of nanostructures on surface that cannot be patterned otherwise. Although this use of AFM-assisted lithography is only at its infancy stages, some examples can be found in the literature. After reviewing them, we have classified these works in three groups. The different approaches are schematically represented in Figure 5.4:

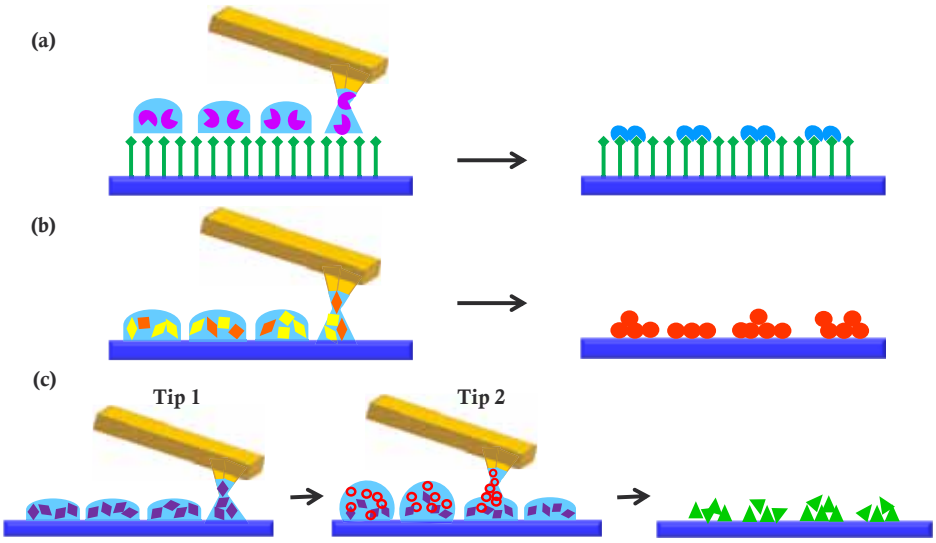

Figure 5.4 Schematic representation of the different methodologies employed to carry out reactions confined into femtolitre droplets using tip-assisted lithography. (a) Reaction with the substrate. (b) Transformation of deposited precursors. (c) Mixture of reagents by sequential deposition of inks.

a) **Reaction between the ink components and the substrate** (Figure 5.4a): This is the most commonly reported approach of the three and consists in the reaction of the delivered material with the surface. This strategy has been extensively used to anchor functional materials or entities to the surface, commonly through click-chemistry. By doing so the patterns can resist subsequent washing steps and wet treatments.[80–84] Also, the redox properties of the substrate can be exploited to in situ transform the patterned materials.[85,86] As an example metallic gold motifs were obtained by in situ reduction of a Au^{+3} precursor upon its deposition on an activated Si substrate (Figure 5.5a).[87]

b) **Transformation of patterned materials** (Figure 5.4b)**:** In this case, the inks are composed of a mixture of precursors of the final objective materials. For this strategy to be successful the reaction must either triggered after the patterning through an external stimulus[88] or occur spontaneously at a slow rate, so the patterning can be performed without the ink being changed substantially during the process.[89,90] Using this strategy, nanostructures of Al_2O_3, SiO_2 and SnO_2 were

fabricated on Si and SiO_2 surfaces by patterning chloride precursors of the metal oxides that slowly hydrolyzed upon contact with the water condensed at the meniscus (Figure 5.5b).[91]

c) **Mixture of reagents on surface** (Figure 5.4c)**:** In the last approach, mixed droplets containing the reagents are formed directly on surface by sequentially delivering two different inks onto the same position of the substrate to form femtolitre-sized reactors.

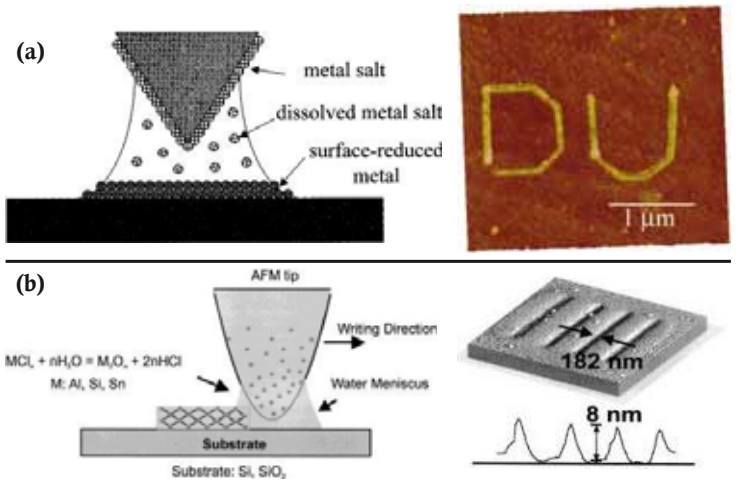

Figure 5.5 (a) Schematic diagram of the fabrication of Au patterns through the reduction of a Au^{3+} precursor caused by the surface and AFM topography image of a fabricated motif. (b) Representation of the lithographic process used to fabricate metal-oxide patterns and topographic AFM image of SnO_2 nanostructures fabricated on a silicon substrate. Reproduced from ref. 87 and ref. 91.

Let us note here an important observation that we detected on reviewing the literature regarding surface-confined reactions. The chemical characterization of the materials resulting from them can be quite complicated due to the extremely small amount of analyte contained in the patterns and their location on small areas of a surface. Therefore, apart from the commonly used probe-based, electron and optical microscopies; the characterization techniques employed are mostly restricted to fluorescence microscopy[92] and X-ray based methods,[93] which have a limited application. Therefore, much research is still needed not only to extend the use of tip-assisted lithography for directed synthesis on surfaces but also to develop techniques that facilitate the characterization of the obtained materials.

Here, we will focus on chemical reactions performed in femtolitre-sized vessels using the third methodology (Figure 5.4c); although it is clearly the less popular out of the three it

is also the more challenging one because it requires a high level of precision in the positioning of the reagents as well as in the control of the reaction conditions.

5.1.3 Reactions confined in femtolitre droplets by sequential addition of reagents

This singular methodology consists in promoting the reaction between two (or more) compounds by sequential delivery onto a surface of femtolitre-sized droplets of each reagent. If the position of the droplets is precisely controlled, the different reagent solutions can be placed on the same location of a substrate, forming mixed droplets that behave as surface-confined nanoreactors. Due to the high level of precision required by the procedure its popularity is still quite limited; in fact at the moment of elaboration of this manuscript only one article that employed a combination of AFM and microfluidic tips reported this approach in the literature. This pioneering work released in 2013 descripts the use of MPL to mix femtolitre-sized droplets of different reagents. The authors reported an extensive and very complete work that included in-situ acid-base reactions detected by fluorescence microscopy, and synthesis and crystallization of metal-organic frameworks including multiplexed arrays of Prussian Blue analogs.[94]

The vast experience of our group in the synthesis and characterization of coordination polymers as well as in AFM-assisted lithography encouraged us to pursue the confined synthesis and growth of coordination polymer structures on surfaces. In this sense, our group has carried out the miniaturization of the well-known coordination polymer $[Co(CH_3COO)_2(\mu\text{-}4,4'\text{-bipy})]$ (Co-bipy). The synthesis and crystallization of Co-bipy were scaled down in a stepwise manner and the material was characterized in every stage. In the first experiments the reagents were pre-mixed before the delivery of small droplets onto surfaces, so only the crystallization process was confined. In that way, Co-bipy was obtained in bulk, inside microliter-sized droplets obtained by drop-casting and confined into femtolitre droplets delivered onto a Au surface using an AFM tip (Figure 5.6a). Crystalline structures were obtained in all cases showing different morphologies corresponding to the crystal growth stage reached in each case. The coordination reaction of the metal centre and the ligand was also performed directly on surface by handling and mixing femtolitre volumes of separate metal and ligand solutions directly on surface with the aid of an AFM cantilever array. Crystalline structures with analogous morphology to those obtained when the reagents were mixed prior to droplet deposition were obtained in the mixed droplets (Figure 5.6b). MicroRaman was used to characterize the materials and confirmed the formation of the Co-bipy coordination polymer. A scientific article describing this work was in preparation at the time of writing this thesis.

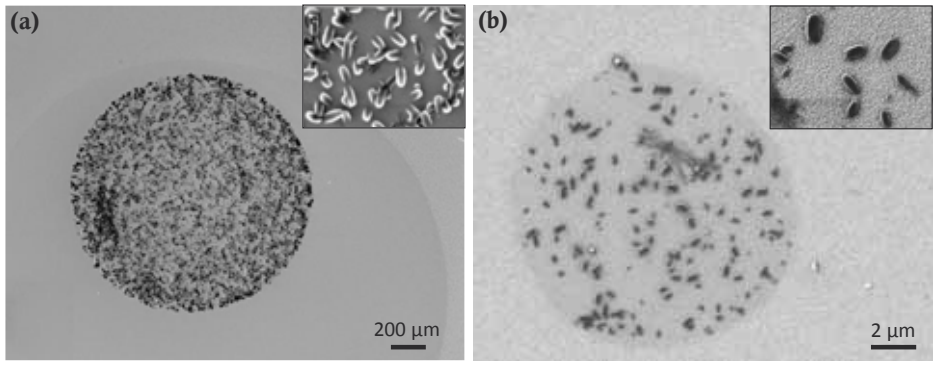

Figure 5.6 Co-bipy crystalline structures obtained by confined growth in femtolitre droplets. (a) Crystals grown after deposition of droplets containing both the metal ion and the di-topic ligand. Inset: detail of the structures grown inside the droplets. (b) Crystals obtained after sequential delivery of each reagent and confined reaction and crystallization.

5.1.4 Aim of the work

As a follow-up of the work previously developed in our group, in this thesis we have implemented the confined synthesis of other catechol-based polymers, namely polydopamine (PDA) and **CPP1**, the VT-CPPs already described in Section 3.4. Both materials show interesting functionalities; whilst PDA is a well-known adhesive and primer,[95] the CPPs exhibit valence tautomerism, and therefore they are potential components of integrated electronic devices.[96] These two materials can only be structured on surfaces through direct-write AFM lithography by confining their synthesis on the surface because, once they are formed, their insolubility precludes their patterning; which adds value and novelty to our approach. In the case of the CPPs our challenge was not only to carry out the coordination reaction in confined environments but also to achieve the structuration of the coordination polymer in the shape of spherical particles. Moreover, given the amorphous nature of the materials, the use of X-ray diffraction techniques to characterize the structures was discarded and we were forced to search for alternative techniques.

5.2 Confined synthesis of Polydopamine in femtolitre reactors: fabrication and properties

In the following section we will describe the experimental work performed on the structuration of PDA by direct-write AFM-assisted lithography and the study of the

adhesive and chemical properties of the patterned material. A schematic representation of the process is shown in Figure 5.7. PDA patterns were easily obtained on Si/SiO_2 surfaces by directly delivering a solution of PDA precursors and confining the polymerization to femtolitre-sized volumes. The adhesive properties of PDA inside the fabricated motifs were also studied and the results were compared to those obtained in continuous films. Finally, the chemical reactivity of PDA allowed the reduction of Ag^+ to obtain metallic silver nanoparticles (AgNP) over the PDA motifs previously fabricated.

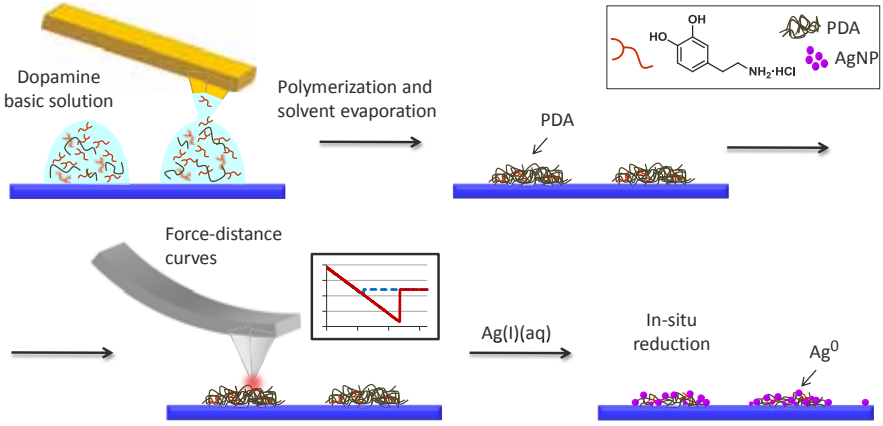

Figure 5.7 Schematic representation of the experimental procedure followed to structure PDA on surfaces. First, a freshly prepared basic solution of dopamine hydrochloride was delivered onto the surface through AFM-assisted lithography in the shape of femtolitre-sized droplets where the polymerization took place. The patterned PDA was subjected to local adhesion measurements through F-d curves and employed to create AgNPs by in-situ reduction.

5.2.1 Fabrication of polydopamine arrays on surfaces through confined polymerization

Our first experiments were directed to find the best conditions to achieve a high degree of control over the lithographic process. Although PDA had been previously structured on surfaces using other lithographic methods,[97–100] AFM-assisted lithography had not been used before this work. First, the ink solution; which consisted of a 2 mg/ml solution of dopamine hydrochloride in Tris·HCl buffer (pH 8.59), was prepared. This was the same solution that is commonly used to obtain film coatings of PDA on surfaces by dip-coating.[101] Immediately after preparation, the mixture was placed in the reservoirs of a microfluidic chip-based ink delivery system (Inkwell) using a micropipette. The inkwell was placed in an O_3/UV cleaner for 10 minutes prior to ink loading in order to favour the flow of the dopamine solution through the microfluidic channels. Then, an AFM tip (A-type, single tip) was functionalized with the ink by dipping it in the solution for approximately two minutes. At this stage fast evaporation of the solvent in the inkwell chip and the functionalized AFM tip was observed

when the experiments were performed under atmospheric conditions, which hampered the patterning process. In order to slow down the evaporation rate of the ink and ensure a controllable coating of the tip and delivery of the ink to the surface, the whole patterning process was performed under controlled environmental conditions (~70% R.H., ~25ºC). Under these conditions, the tips could be homogeneously coated and used to transfer the ink to the desired areas of the target surface in a controlled manner; in our case we chose silicon bearing a native layer of silicon oxide (Si/SiO_2). Note that the polymerization of dopamine starts right after the preparation of the solution, which resulted in an increase of ink viscosity as well as in changes in ink composition throughout the patterning process. For that reason, the use of a specific dopamine solution was limited to two hours after preparation. After the lithographic process, the substrates were kept under high humidity conditions for two more hours to complete the reaction.

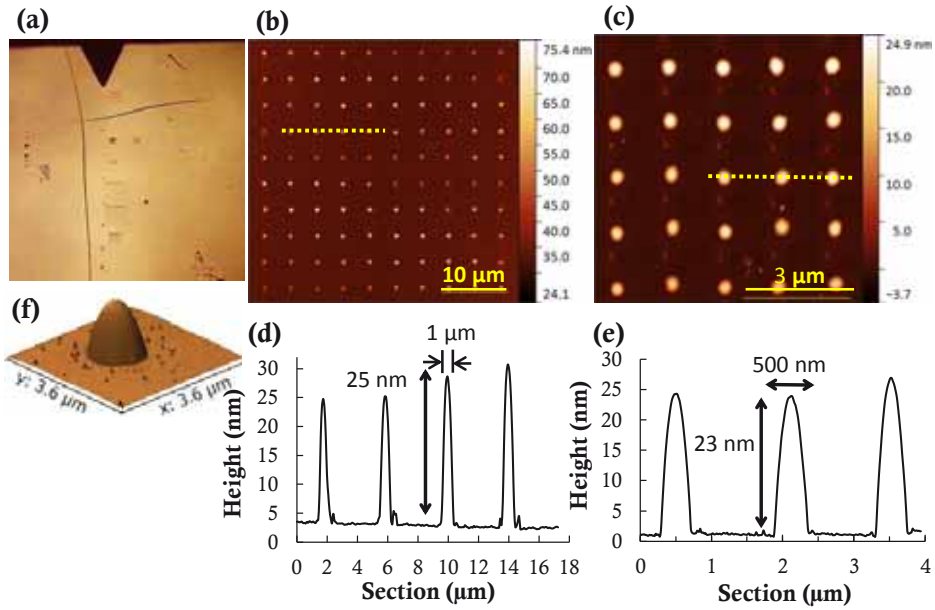

Figure 5.8 (a) Optical microscopy image of a patterned area immediately after the lithographic process. Several bleeding dots can be seen together with dot-like feature arrays of different sizes. Panels (b) and (c) show AFM topography images of two different PDA arrays and graphs; (d) and (e) are the profiles corresponding to the dotted lines. As seen in panel (e) features as small as 500 nm in diameter could be fabricated. (f) 3D-reconstruction of an AFM topography image of a single PDA dot.

The first step of the patterning process after the functionalization of the tip consisted in eliminating the excess ink on the cantilevers and tips by performing several bleeding steps. After that, we were able to start writing uniform (sub)micron sized dots in the shape of dot-like feature arrays, as shown in Figure 5.8. After the patterning and solvent evaporation, the obtained structures were characterized by tapping mode AFM and optical microscopy,

revealing rounded structures that were both reproducible and uniform in size. Typically, the dots showed diameters between 1.0 and 1.5 μm and maximum height around 20 nm (Figure 5.8d), however these dimensions were tuneable and features with diameters as small as 500 nm were obtained (Figure 5.8e). By controlling parameters such as the amount of ink loaded on the tips, the contact time between the tip and the substrate and the depletion of the ink, the height and diameter of the features could be varied.

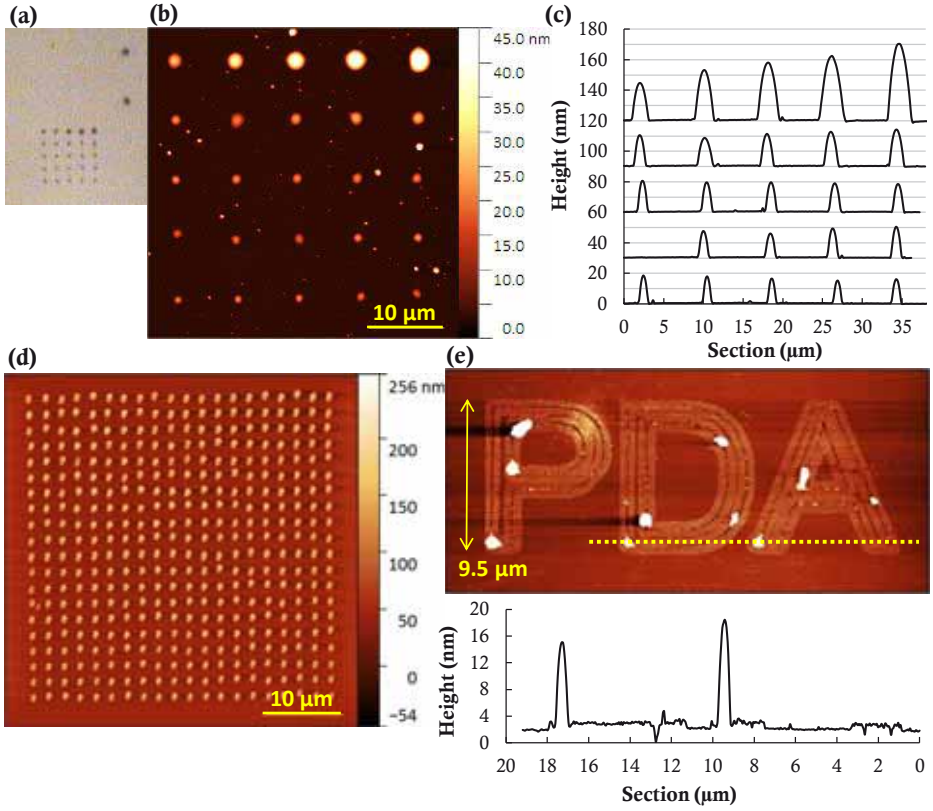

Figure 5.9 Panels (a), (b) and (c) show the optical microscopy image, AFM topography image and profiles of a 5×5 dot array in which depletion of the ink caused gradual reduction of the feature size. Profiles in (c) correspond to each one of the rows in the array in panel (b). (d) AFM topography image of a 20×20 dot array of homogeneous PDA features. (e) AFM topography image and corresponding height profile of microscale letters forming the word PDA written with the basic dopamine solution.

A direct relationship between the deposited ink volume and the final dimensions of the features could be deduced form the results. In Figure 5.9a the optical microscopy image of a just-deposited 5×5 dot array is displayed. It can be clearly seen in the image that depletion of the ink caused a gradual reduction in size (height and diameter) of the deposited droplets. When the same array was examined by tapping mode AFM, a decrease in feature dimensions was also observed (Figure 5.9b,c). The decrease is more noticeable in the first

dots of the array (first two rows), after that the writing became stable and highly uniform dots were obtained in the last three rows. The uniformity in writing could be maintained for long periods of time and large amounts of homogeneous features could be fabricated, as demonstrated in Figure 5.9d, that shows an array of 400 highly uniform dots 1240 nm (± 7 nm) in diameter and 114 nm (± 2 nm) in height. Finally, the performace of the ink was tested also in dynamic writing and we were able to create complex shapes forming the word "PDA" (Figure 5.9e).

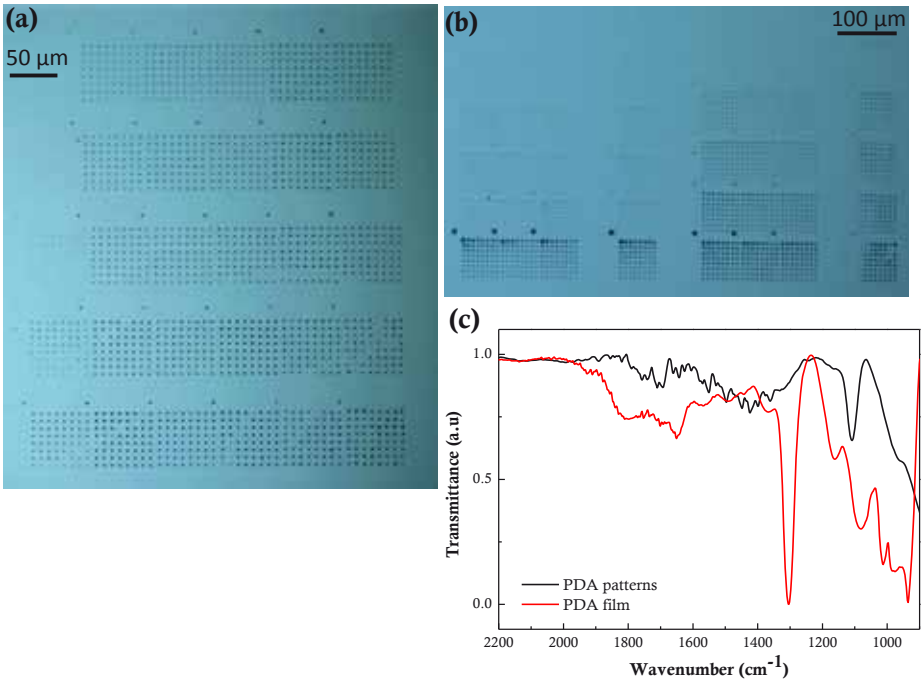

Figure 5.10 (a, b) Optical microscopy images of PDA patterns obtained over large areas (total height of panel (a) is 0.5 mm). (c) GA-IR spectra of a PDA film and PDA patterns.

Also, the use of multiple tip arrays (M-type probe arrays, 66 µm pitch) with up to 12 cantilevers allowed for the fabrication of uniform patterns over large areas, as shown in Figure 5.10a,b. The slight differences in the size of the dots written by the different pens that can be observed in the optical micrographs are related to the geometry of each particular tip, slight variations in the ink loading and surface features. The fabrication of patterns over large areas allowed to record the IR spectrum of the deposited material through Grazing Angle Infrared spectroscopy (GA-IR) to compare it to the spectrum of a PDA film deposited on Si/SiO_2 (Figure 5.10c). Both presented the typical poorly defined signals commonly observed in PDA, mostly located in the 1800-1200 cm^{-1} range.[102,103] A detailed assignment of

the bands is complicated however, given the high degree of chemical disorder and the unknown chemical structure of PDA.

5.2.2 Structured polydopamine properties: Adhesion

Once the PDA microarrays were obtained, the adhesive properties of the in-situ synthesized polymer were studied by performing Force-distance (F-d) curves on the PDA dot-like features. For that, we made use of the Flex-Grid tool of PicoScan5, which allows to record force-distance curves in pre-defined points of an area while scanning. As detailed in Section 4.2.2, the force of adhesion (F_{adh}) was extracted from the jump-out of contact during the retraction of the tip. First, the PDA dots in the arrays were located by previously scanning the surface with the same tip. In order to minimize the possible contamination of the tip during this process, the cantilever deflection was kept as low as possible during the whole experiment and the contact time between the surface and the tip was minimized. Also, during the measurements we recorded F-d curves on non-functionalised spots inside the arrays (between the dots) and made sure that the adhesion values in those points were not increasing. After every experiment, five F-d curves were obtained on a clean Si/SiO_2 surface to corroborate the cleanliness of the tip. This procedure allowed us to measure around 20 force-distance curves without changing the tip.

Additionally, PDA coatings were prepared on Si/SiO_2 substrates and were used as a reference to compare the results. For that, the classical dip-coating procedure described in Section 4.2.2 was employed. By varying the immersion time of the substrates in the dopamine hydrochloride solution it was possible to obtain two different coating thicknesses, 8-11 nm (for 1 hour immersion) and 33-39 nm (for overnight) (Figure 5.11a, b). The adhesion measurements in the thinner coating provided a clear median F_{adh} of 10-11 nN, however the coating obtained by overnight immersion showed a high statistical dispersion whereupon a clear adhesion value could not be extracted (Figure 5.11a, b). This observation is in agreement with the results reported in Section 4.2.2 for the adhesion of a PDA film deposited on epitaxial gold. In that case a high dispersion of the results was also observed, which can be attributed to the diminished homogeneity of these coatings that are considerably deformable and soft, with a large tendency to retain water.[104]

Going back to the dot-like features obtained through confined PDA synthesis, multiple F-d curves were recorded on a variety of patterned areas. The results exhibit a low dispersion of values and an average adhesion force of 15-16 nN independent of the feature dimensions (Figure 5.11c). This observation not only probed that the patterned material acts

as an adhesive at the local scale but it also showed slightly enhanced adhesive properties of the patternswhen compared to the PDA films. The average F_{adh} was higher than that measured on the ~10 nm thick coating and the statistical dispersion of the results was considerably lower than in the case of the ~35 nm thick PDA coating. Also, the adhesion in the areas of the patterned surfaces that were not functionalized was consistent with that of bare Si/SiO_2, confirming the cleanliness and precision of the patterning procedure.

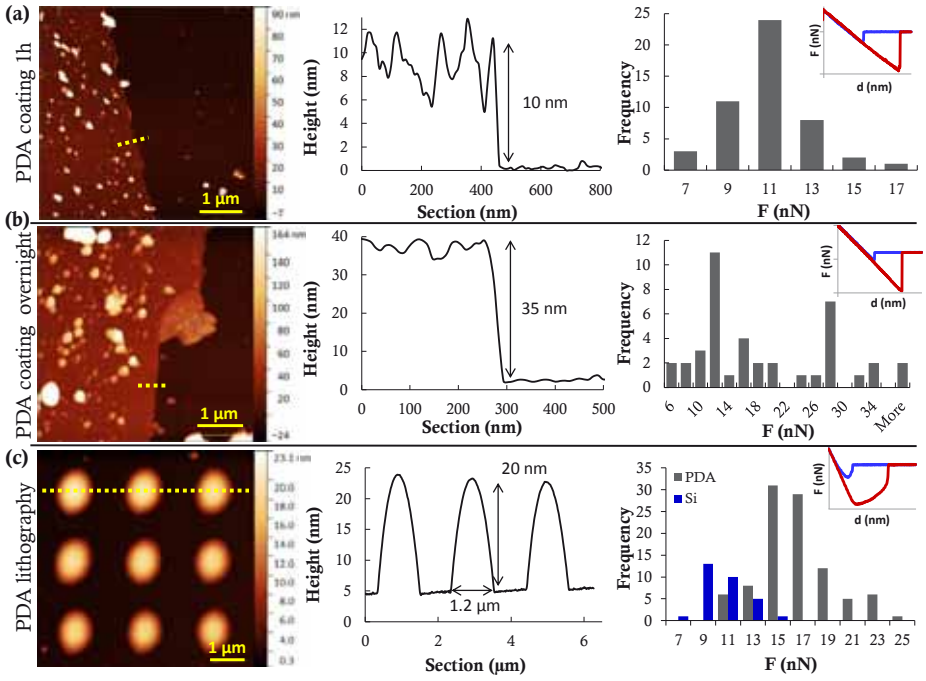

Figure 5.11 Tapping mode AFM topography images (left), profiles corresponding to dashed lines in the images (centre) and histograms of the F_{adh} values (right) measured in each one of the studied substrates. (a) 1 hour PDA coating, (b) overnight PDA coating and (c) structured PDA. On the PDA coatings, a scratch was intentionally made on the polymer using a needle in order to measure their thickness. The image and profile of the structured substrate are a representative example but the histogram summarizes the results obtained in several lithographies with differently sized features.

5.2.3 Structured polydopamine properties: Redox activity

Among the multiple chemical properties of PDA, its ability to spontaneously reduce some metal cations to their zero-valent state is one of the most interesting and has been applied to the fabrication of organic-inorganic hybrid materials for many applications.[105–108] In the early studies about PDA and its properties, its ability to behave as a reducing agent was attributed to the presence of 5,6-dihydroxyindole units in the polymeric chain; but according to Ball et.al. the free dopamine trapped inside the polymer is the actual

responsible for that ability,[109] as was recently confirmed by Lee and co-workers.[110] We took advantage of this property of PDA to in-situ synthesize silver nanoparticles confined to the micropatterned areas. In our case, these experiments also served as a robustness and stability test of the in-situ synthesized material.

Previously to the use of the patterned substrates, the reaction was assayed in continuous PDA films. These were obtained on Si/SiO_2 substrates by immersing them overnight in a basic dopamine hydrochloride solution. Then, the PDA coated substrates were immersed in a $AgNO_3$ solution (50 mM in H_2O) without stirring and kept in the dark for 24 h. After that time the substrates were rinsed with copious amounts of Milli-Q water and examined by FE-SEM. Good amounts of AgNPs were found distributed along the whole sample surface (Figure 5.12a). The backscattered electrons image indicated that the particles were composed of a material that was much heavier than the background, as shown in Figure 5.12b, as would be expected for AgNPs on a substrate composed of Si, O, C and N. The formation of metallic AgNPs was confirmed by XPS, which showed the appearance of the characteristic Ag^0 bands (Figure 5.12c).

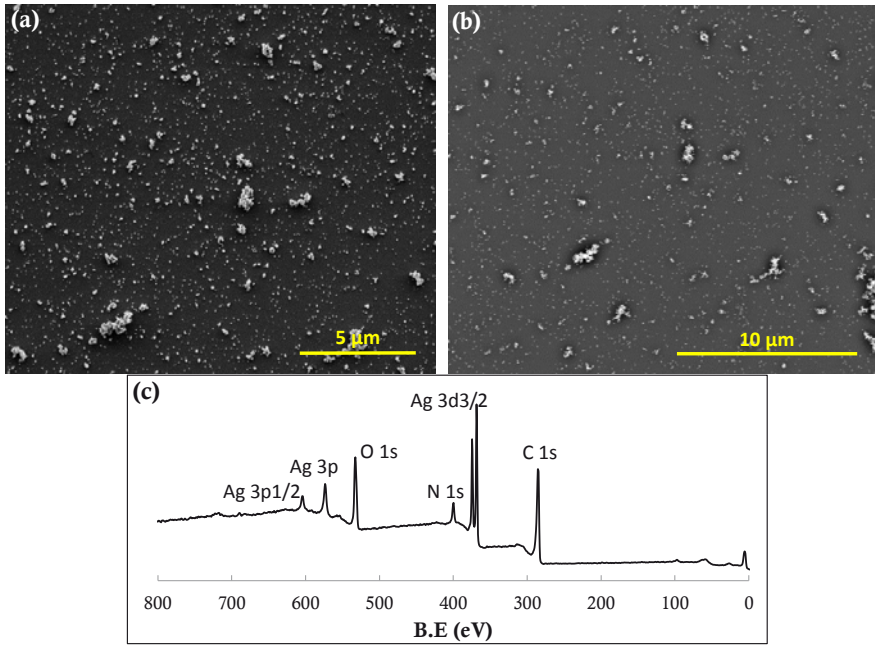

Figure 5.12 (a) FE-SEM secondary electrons image of a Si wafer coated with PDA overnight and then immersed in a $AgNO_3$ 50 mM solution for 24 hours showing the formation of AgNP on the surface. (b) Backscattered electrons image of the same sample. (c) XPS spectra of the sample, the formation of Ag particles is showed by the appearance of characteristic Ag^0 bands.

The same methodology was then reproduced using the PDA arrays by immersing a patterned substrate in a $AgNO_3$ solution (50 mM) overnight and subsequently rinsing with Milli-Q water. However, examination of the substrate by FE-SEM showed the loss of the 2D organization. Although the AgNPs were successfully formed on the PDA, the motifs moved from their original locations probably due to weak binding to the surface (Figure 5.13a). Alternatively, a gentle washing of the substrate was performed after the treatment with $AgNO_3$ in order to avoid the loss of the motifs just by dipping the substrate in Milli-Q water, although this procedure also resulted in the material being displaced from its original position (Figure 5.13b). Additionally, a thermal treatment of the PDA patterns was carried out in order to provide higher stability to the polymer[111] by placing the patterned substrates in an oven at 90 ºC for 24 hours prior to their immersion in the $AgNO_3$ solution. In this case, the patterns were maintained but the central part of the dots was washed away in most cases and almost no AgNPs were found on the surface (Figure 5.13c). A blank experiment was also performed by placing a PDA-patterned substrate in water overnight. After rinsing the substrate, examination of the patterned areas by optical microscopy showed that the motifs had disappeared; therefore the treatment with $AgNO_3$ was not the cause for the reduced robustness of the in-situ synthesized material.

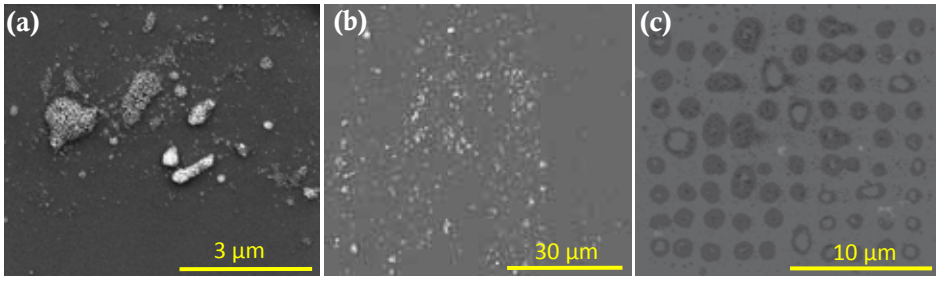

Figure 5.13 (a) FE-SEM image of PDA patterns immersed overnight in a 50 mM $AgNO_3$ solution and rinsed with water, it can be seen that the organization was lost after the procedure . (b) FE-SEM micrograph of a patterned substrate subjected to the same treatment and washed by dipping in water, the gentle washing did not avoid the loss of the motifs. (c) FE-SEM images of PDA arrays treated at 90ºC for 24 hours and immersed in a 50 mM $AgNO_3$ solution for 1 hour showing partial disappearance of the polymer and no AgNPs.

Finally, the localized in situ reduction of Ag^+ was achieved whilst preserving the PDA patterns after a slight modification of the methodology. A patterned substrate was immersed in a 10 mM solution of $AgNO_3$ and placed in an oven at 60 ºC for an hour.[106] After that, the substrate was gently washed with water and examined by FE-SEM. In this case, the dot-like feature arrays fabricated before maintained their position and lateral resolution and each one of the features contained a number of rounded AgNPs (Figure 5.14a, b). The patterned areas were also examined by tapping mode AFM after the in-situ formation of the AgNPs (Figure 5.14c) revealing a considerable decrease in the height of the dots, which was now under 10

nm as seen in the height profile in Figure 5.14d. This meant that only the PDA layer closer to the surface was maintained after the treatment and that the material obtained through confined polymerization presented a rather low cohesion.

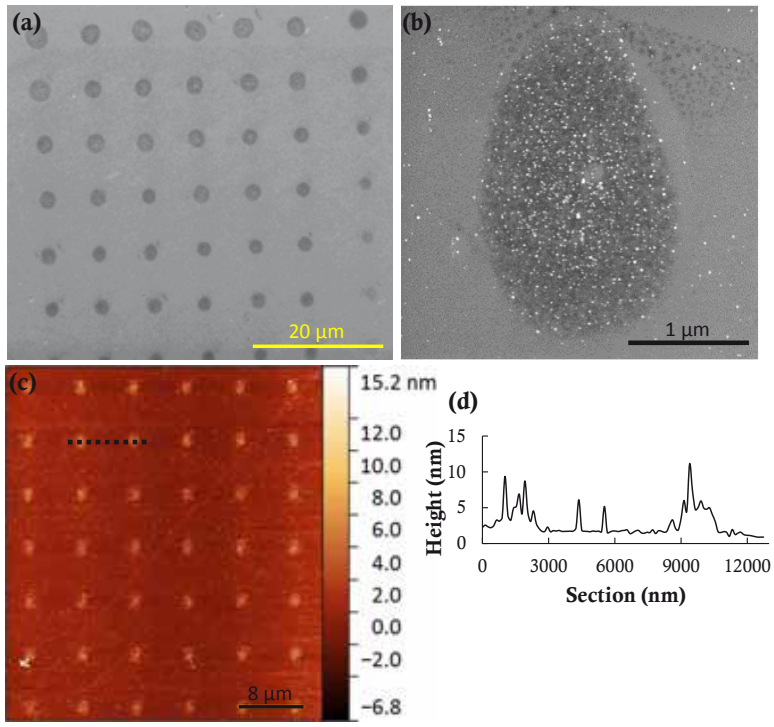

Figure 5.14 Panels (a) and (b) show FE-SEM images of the PDA-AgNP motifs obtained after performing the in situ reduction at 60 °C during 1h. The AgNPs can be clearly seen in the picture in (b) (c) AFM image of a PDA dot array after the treatment with $AgNO_3$ solution in the same conditions. (d) Height profile corresponding to the dashed line in (c).

During the examination of the substrates, we observed that a continuous and highly homogeneous silver layer had formed on the larger PDA dots created during the bleeding of the cantilevers (Figure 5.15a, b). The electrical resistivity of these Ag/PDA islands was measured by Dr. M. J. Esplandiu, from the ICN2, using a two-point conductivity method. For this, conventional electron beam lithography and lift-off methods were used to fabricate two small circuits formed by two titanium/gold electrodes fabricated on top of the Ag/PDA structures and separated by a 10 µm gap (Figure 5.15c). These small electrodes were connected to larger gold pads where the two point contact methodology was applied. The I-V curves were acquired by applying a bias voltage ranging between -100 mV and 100 mV (Figure 5.15d). Using this method, resistances (R) of 134 and 122 Ω were calculated for the two circuits. Taking into consideration the gap length between the electrodes (L) and an averaged contact area (A) of $1.7 \cdot 10^{-10}$ m^2, a Ag/PDA structure resistivity (ρ) of 2.2 10^{-3} Ω·m

was estimated (ρ = RA/L). Although this result denotes a rather poor conductivity of the Ag/PDA islands compared to the results reported for other similar systems,[108,112,113] further development of this methodology is expected to lead to improved results either by extended optimization of the Ag reduction process or by introducing a protective coating that prevents the oxidation of the silver layer.

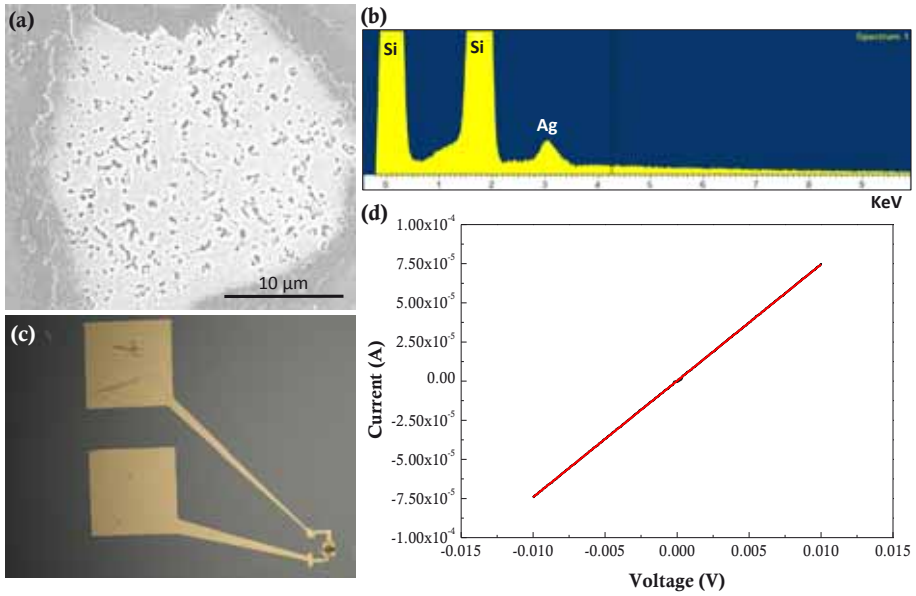

Figure 5.15 (a) FE-SEM image of a Ag island obtained by in-situ reduction of Ag^+ over a large PDA dot fabricated during the bleeding steps. (b) EDX analysis performed on this spot showing the presence of Ag. (c) Optical microscopy image of a Ag/PDA island contacted with gold electrodes fabricated by electron beam lithography and connected to gold pads used to measure the electrical conductivity of the Ag/PDA island. (d) Ohmic I-V profile obtained by the two-point contact methodology in the circuit in (c).

5.3 Surface-confined synthesis of coordination polymer particles using direct-write AFM-assisted lithography

In the following section, the synthesis of coordination polymer particles in femtolitre-sized vessels fabricated by AFM-assisted lithography will be addressed. In this case, multiple cantilever arrays were used to mix femtolitre volumes of two reagent solutions by sequential delivery on the same position of a surface. Alternatively, the mixing of the reagents was promoted during the functionalization of the tip and the reacting mixture was delivered on the surface. Both methodologies led to the controlled growth of a single CPP per dot. The general experimental procedure is schematically represented in Figure 5.16.

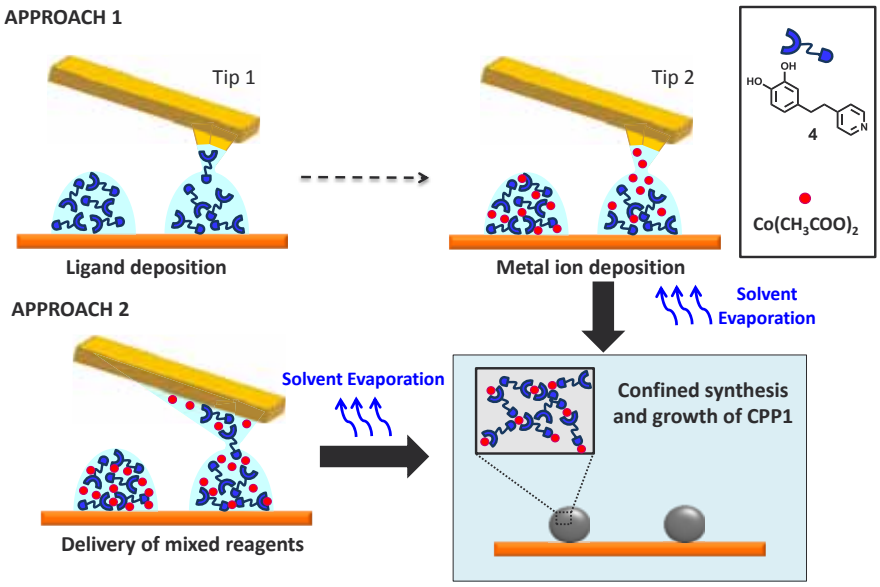

Figure 5.16 Schematic representation of the different approaches followed to synthesize and grow CPPs through femtolitre-confined reaction

5.3.1 Bulk synthesis: solvent optimization

For the confined synthesis and growth of CPPs on surfaces we chose the coordination polymer already described in Section 3.4 (**CPP1**). This material is formed through the coordination of ligand **4**; that combines a catechol and a pyridine unit, with a cobalt salt. This election was based in several factors; first of all the reaction only requires the participation of two reagents. In that way complex mixtures were avoided, and the experimental procedure was simplified. Also, the coordination polymer spontaneously organizes in the shape of rounded particles, as exposed in Section 3.4; which facilitated the routine assessment of the experimental results using SEM.

The synthesis of **CPP1** in bulk had been previously optimized using EtOH/H_2O mixtures as solvent (see Section 3.4). However, this combination is not appropriate for AFM assisted lithography, which requires the use of ink solutions that fulfil the requirements specified in Section 5.1.1. Unfortunately EtOH/H_2O mixtures evaporate very easily and show low viscosity, which impedes their use in the formulation of inks for direct-write AFM-assisted lithography. Therefore, our first experimental steps were directed towards the

optimization of the reaction using appropriate solvent mixtures. With that aim, a screening of the reaction was performed both in bulk and by drop casting experiments.

High boiling point solvents such as DMF and DMSO and combinations of them with H_2O were used to synthesize **CPP1** in bulk. These experiments were performed by Dr Fernando Novio at the ICN2. Solutions of $Co(COOCH_3)_2$ (0.25 mmols) in water and **4** (0.5 mmols) in either DMF or DMSO were mixed, leading to the almost immediate appearance of a precipitate that was stirred for 30 minutes, washed several times and dried under vacuum. In all cases the formation of spherical particles was observed (Figure 5.17). For the drop casting experiments, microliter volumes (typically 1-3 μL) of solutions containing each one of the reagents were sequentially casted onto a polycrystalline gold substrate and then left undisturbed until the solvents were completely evaporated. The used solvents were the same as in the experiments in bulk and the solutions were slightly more concentrated; the $Co(COOCH_3)_2$ was 34 mM and the ligand **4**, 20 mM. The FE-SEM images of the substrates revealed the formation of round-shaped nanoparticles frequently accompanied by a film that was attributed to the presence of non-structured coordination polymer (Figure 5.17). After performing these tests and some preliminary lithography experiments the best results were obtained using an aqueous solution of $Co(COOCH_3)_2$ and a solution of ligand **4** in DMSO. In order to increase the viscosity and boiling point of the inks (which probed necessary in the first lithography experiments), a 2% v/v of glycerol was added to the mixture. Using these conditions, the particles obtained in bulk showed an average diameter of 811 ± 27 nm whilst the ones obtained by drop casting were 214 ± 14 nm in diameter (Figure 5.17d).

It is worth to mention that the direct delivery of **CPP1** particles onto the surface through the AFM tip was attempted without success. For that the two inks were mixed in estequiometric ratios in a vial and the resulting turbid mixture was immediately transferred to the ink reservoir of an inkwell. Then, an AFM tip was functionalised by dipping it in the solution for a few minutes, however all the attempts to directly deliver the particles were unsuccessful. Examination of the AFM probe by FE-SEM showed the presence of an amorphous material on the tip (most probably excess reagents) but no particles were observed, meaning that these were not able to transfer to the tip (Figure 5.17e). Consequently, the only feasible strategy to structure **CPP1** particles on surface by direct-write AFM lithography was to deposit the precursors and promote the reaction and particle growth directly on the surface.

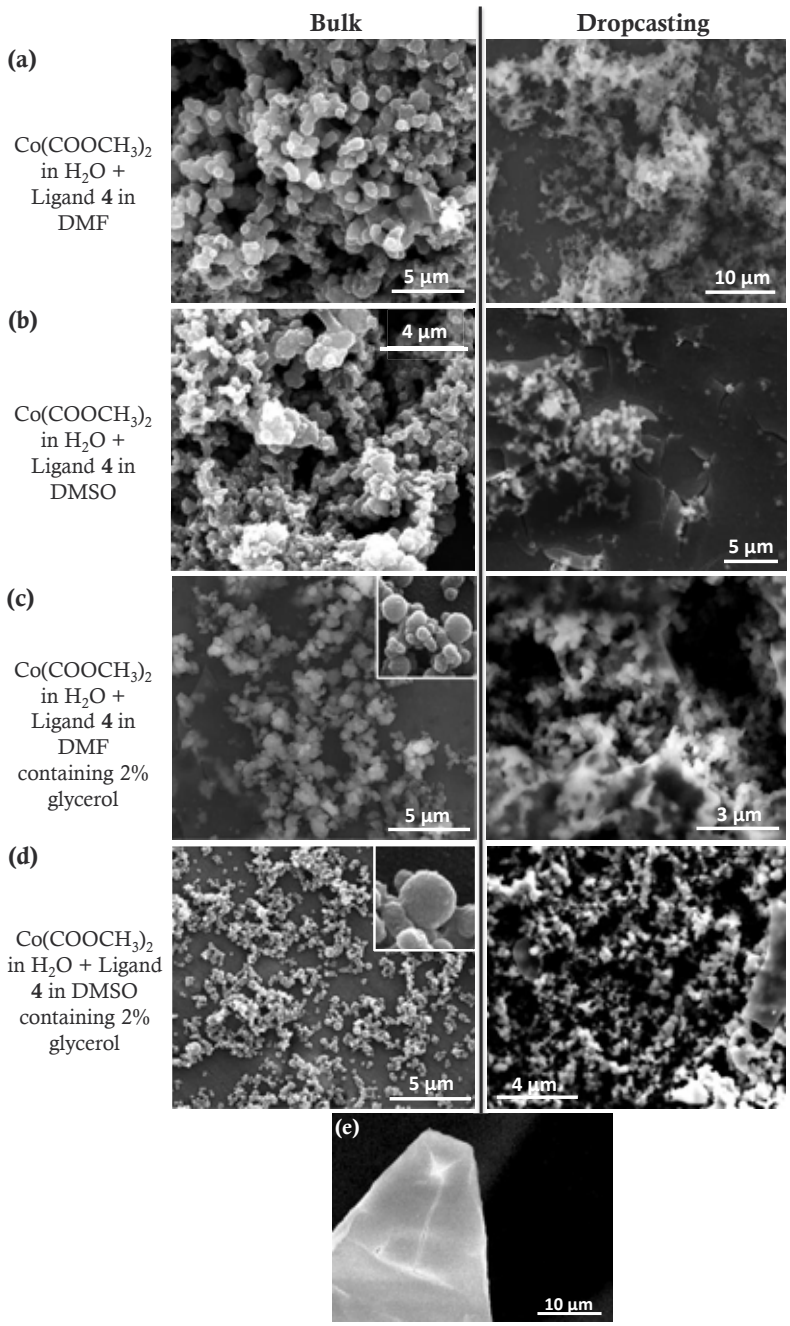

Figure 5.17 (a)-(d) FE-SEM images of the materials resulting from the preliminary assays of **CPP1** synthesis in bulk (left) and by dropcasting (right) using different solvent combinations. (e) FE-SEM of an AFM tip dipped in a suspension of the particles and showing that only non-structured material transferred to it.

5.3.2 Approach 1: Confined synthesis of coordination polymer particles by sequential delivery of reagent solutions

The first strategy employed consisted on the sequential delivery of the two reagents onto specific positions of the substrate, as schematically represented in Figure 5.18. First, the ink solutions containing the Co^{2+} salt and ligand **4** were prepared and transferred to adjacent channels of an inkwell (they appear in red and blue colours in Figure 5.18). Then, M-type probe arrays (66 μm pitch) were dipped into each solution (b) to obtain two differently functionalized tips located side by side. The coated tips were then brought into contact with a polycrystalline gold surface to deposit drops of controlled size and dot-like feature arrays of the two separated inks were fabricated by traversing the tip over the surface in the shape of the desired patterns (c). Then, a lateral translation of the tips (66 μm) allowed to perform an additional lithography following exactly the same pattern to deliver the second reagent over the previously deposited one (d). In this way femtolitre-sized droplets of the reacting mixture were fabricated in-situ to act as confined nanoreactors.

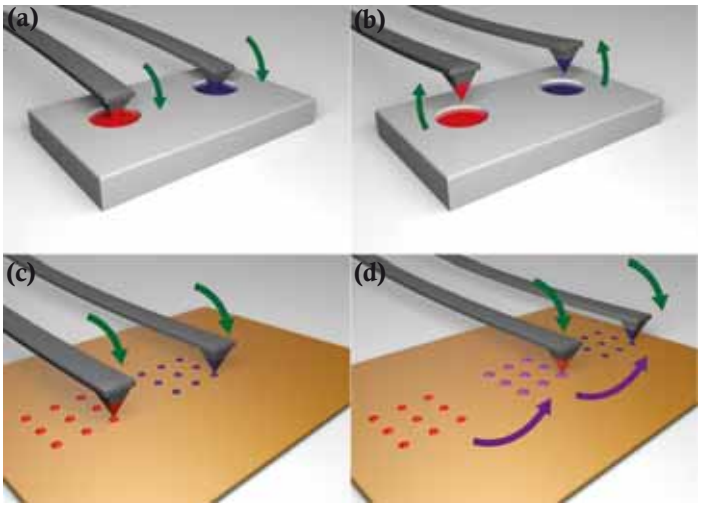

Figure 5.18 Schematic representation of the mixture of $Co(COOCH_3)_2$ and ligand **4** through superimposed lithographies. Two adjacent tips of a pen array were functionalised with each one of the inks (a,b); then dot-like feature arrays were obtained with the separate inks (c) and a lateral movement of the tips was performed to superimpose a second lithography over the first one (d) creating nanovessels were the reaction and growth of **CPP1** took place.

No significant dependence with the order in which the reagents where added (metal over ligand or *viceversa*) was detected. However, the $Co(COOCH_3)_2$ ink demonstrated higher writing stability so the mixtures were always performed by adding the metal over the ligand. Note that the ink solutions used here were highly concentrated compared to those employed in the drop casting and bulk experiments, as they consisted in a 200 mM solution of the

ligand in DMSO (2% glycerol) and a 100 mM solution of the metal ion in H_2O (1% glycerol). This was motivated by the reduced amount of material observed on the surface patterns in the first lithography experiments, when diluted solutions were used. Also this increase in concentration resulted in higher ink viscosity, which had a positive impact in the performance of the lithographic process.

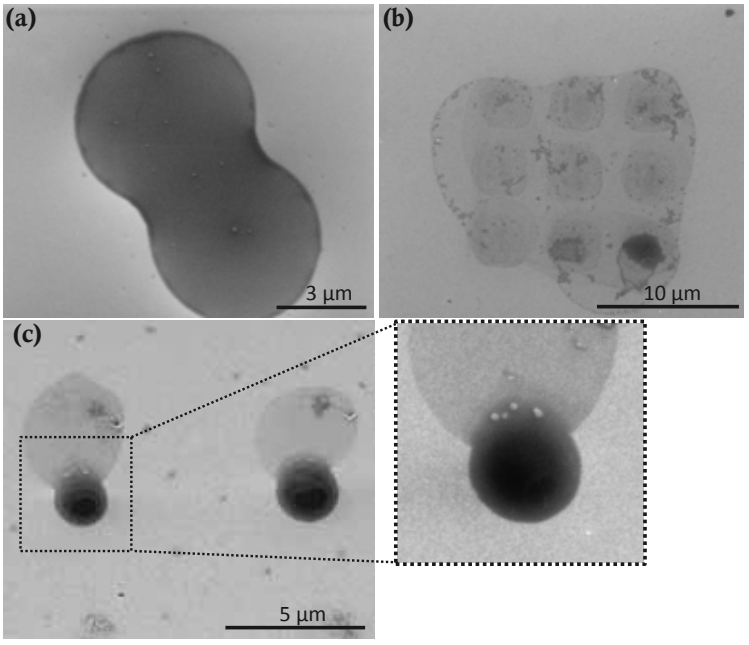

Figure 5.19 FE-SEM images of failed experiments due to several reasons. (a) Fast evaporation of the solvents led to the formation of non-structured material. (b) When an overly saturated DMSO atmosphere was used, vapour droplets condensed on the droplet arrays. (c) In some cases the droplets were not positioned close enough and the inks did not diffuse completely into each other; some particles grew exclusively at the interface of the two liquids.

In addition to the concentration, during the first experiments two additional parameters were found to be determinant for the success of the confined reactions. First of all the residence time of the mixed droplets (or nanoreactors) had to be optimized. It was observed that fast evaporation of the droplets led to the formation of unstructured material occasionally accompanied by some nanoparticles. (Figure 5.19a) In order to maintain the liquid state of the droplets for longer periods of time, the AFM-assisted lithography experiments and droplet mixtures were carried out under high relative humidity conditions (~75%) and afterwards the substrates where placed in an air-tight chamber saturated with DMSO vapours. However, the saturation of the DMSO atmosphere had to be carefully controlled in this step, as an overly saturated environment led to the condensation of solvent over the substrates, which resulted in the disruption of the patterns and fusion of the droplets (Figure 5.19b). The second critical parameter was the precise positioning of the two reagent

droplets exactly on the same point of the surface. Our experience revealed that frequently the two ink solutions were positioned nearby but not exactly on top of each other due to the experimental limitations of our positioning system (minimum steps were 2 μm) and the reduced size of the features; limiting the number of successful experiments. In some cases the two droplets were placed close enough to fuse by capillarity; in those cases the appearance of non-structured material was observed and occasionally some small particles formed in the regions where the droplets overlapped (Figure 5.19c).

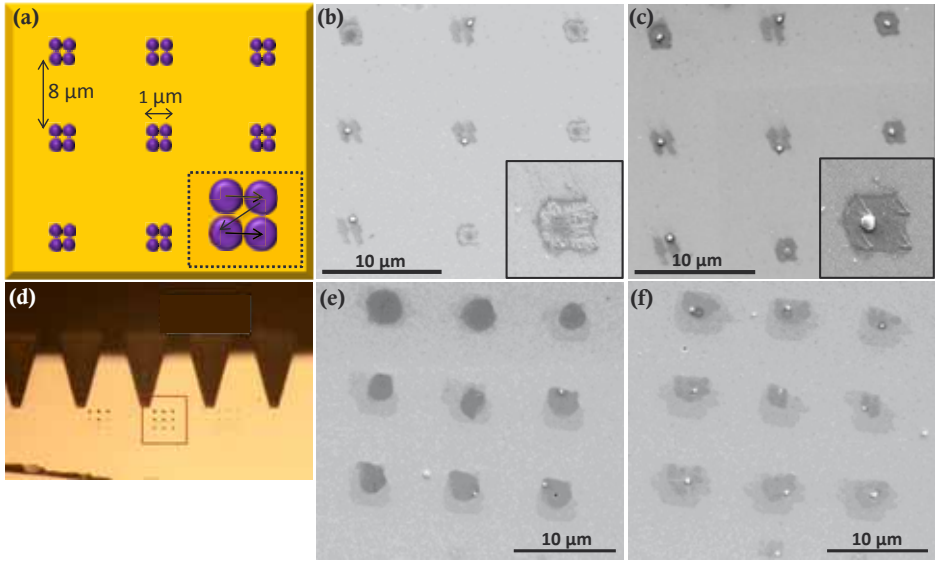

Figure 5.20 (a) Design of the lithographic pattern that allowed the in-situ synthesis and growth of **CPP1** and movement of the tip in each vessel during the lithography. (b) FE-SEM micrograph showing the different morphologies observed in a single dot array after two days of reaction. (c) Evolution of the dendritic structures to form CPPs 48 hours later. Insets: Detail of one of the confined nanoreactors showing dendritic structures in the first days (b) and its final particle shape two days later (c). (d) Optical microscopy image of a just-deposited mixed array (inside the red square) (e) FE-SEM image of a mixed array were only three mixed droplets gave place to a CPP. (f) FE-SEM image of an array composed of mixed droplets where CPPs were grown, in this case more than one particle appeared in some droplets.

Eventually, this limitation was overcome by designing a new lithographic pattern in which each droplet was formed by the fusion of four smaller ones, as schematically depicted in Figure 5.20a. This new pattern was employed in the sequential delivery of the ligand **4** and the Co^{2+} salt ink solutions to obtain 3×3 dot arrays in which each feature was composed of four droplets of each reagent ink. Placing the droplets in this geometry allowed to create reaction vessels with a slightly larger volume and covering more area, which favoured the effective mixing of the inks. Then, the substrates were stored under a DMSO atmosphere for 48 hours and examined by FE-SEM. As can be seen in the micrographs in Figure 5.20b, after that time, some of the mixed droplets showed the presence of rounded particles (with

dimensions ranging from 375 to 485 nm in diameter) though in others a dendritic-like material had formed. The sample was then stored under atmospheric conditions for two more days and then re-examined by FE-SEM. Interestingly, after that time all the dendritic structures had evolved and coarsened into single rounded particles with diameters ranging between 375 and 560 nm, as seen in Figure 5.20c. We assume from these observations that the dendritic-like structures are primitive precursors (seeds) of the final CPPs. The obtention of one particle per dot was reproducible in other analogous experiments (Figure 5.20e,f).

Although in the end we were successful, having full control over the synthesis of the coordination polymer and growth of the particles following this approach proved to be a real challenge. Given the extremely small volumes of reagents that were used, the positioning of the droplets had to be highly accurate, which was not always achieved. Also, there exist a vast amount of non-controllable external parameters with an unpredictable influence in the reaction outcome (such a temperature and humidity fluctuation). Thus, in order to simplify the methodology and improve the reproducibility, an alternative experimental procedure was used consisting in mixing the two inks during the functionalization of the tips. The experimental work and the results obtained using this approach are described in the next section.

5.3.3 Approach 2: Confined synthesis of coordination polymer particles by delivery of mixed precursors

In the second approach designed for the synthesis of **CPP1** particles in femtolitre reactors we took advantage from a phenomenon that is normally considered an undesired event when probes are functionalized with liquid inks using inkwells. The inking procedure of the tips is always a critical step not only because of the limited reproducibility of the methodology but also because capillary forces may cause an excessive loading of ink on the cantilevers and the solutions may spread over the cantilever array and support chip. This phenomenon was used to promote the mixture of the inks on the cantilevers immediately before the lithographic process. In that way the procedure was simplified because the reagents were already mixed when they were delivered onto the surface.

The procedure is schematically represented in Figure 5.21. First, the same ink solutions used in the previous approach were prepared and immediately transferred to adjacent channels of an inkwell chip (a) (distinguished by different blue and red colours in Figure 5.21) and M-type probe arrays were functionalized with them (b). During this step, an excess of ink was intentionally loaded on the probes by using the middle part of the channels

to dip the AFM tips instead of the edge (Figure 5.21e), forcing the inks to spontaneously mix on the cantilevers (c). After that, the coated tips were immediately used to transfer the mixture of inks to the gold surface (d). In that way, the lithography could be performed during the first stages of the reaction, just before the particles start to form. After removing the excess ink on the cantilevers by performing several bleeding steps it was possible to fabricate dot-like feature arrays of controlled size composed of femtolitre-sized droplets of the reacting mixture.

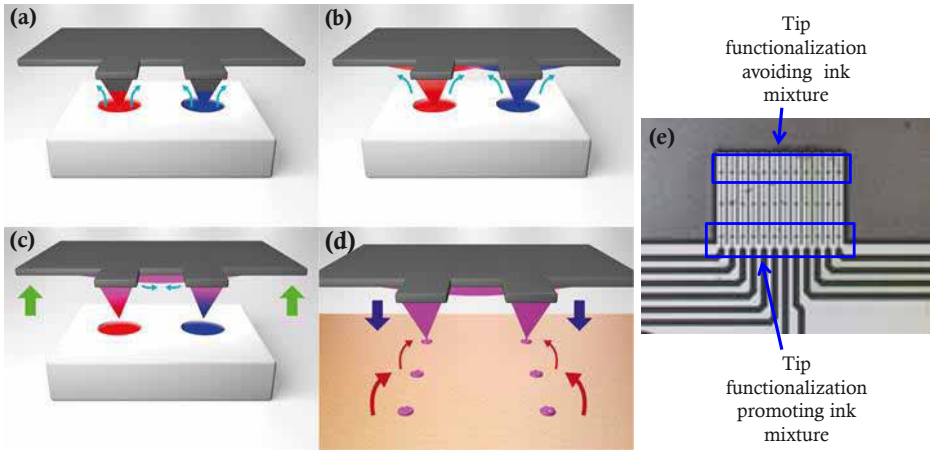

Figure 5.21 Schematic representation of the inking procedure that lead to the mixing of the two inks in the cantilevers. First, the tips were dipped in the inkwells (a) and functionalized each tip. (b) Due to capillarity, the inks went up to the cantilevers and got mixed there (c). Then the mixture of inks was transferred to the surface and femtolitre-sized droplets of the reacting solution were deposited (d). (e) Optical image of the tip functionalization area of an inkwell. The parts of the channels used for each one of the described procedures have been highlighted. The end of the channels was used for the functionalization of the tips with small amounts of ink, avoiding ink mixture. The area closer to the wide channels or even the beginning of them was used to load higher amounts of ink on the cantilevers and force their mixture.

As already observed in the previous approach, the treatment of the sample after the patterning was almost as important as the deposition procedure itself. If the samples were just exposed to the lab atmosphere after the patterning, the droplets quickly evaporated and the particles did not grow. In order to promote the growth of the particles, the substrates were placed in an air-tight chamber with a controlled saturation of DMSO vapours for 48 hours. In this way **CPP1** particle arrays containing one nanoparticle per fabricated dot were obtained (Figure 5.22a, b and c). Alternatively, the growth of single nanoparticles in femtolitre droplet arrays was also achieved by placing the substrate in an oven at 50ºC immediately after deposition (Figure 5.22d). Although these two procedures may seem contradictory, both promoted the formation of **CPP1** in different ways. The vapour-saturated atmosphere increased the residence time of the nanoreactors, allowing the nanoparticles to form slowly at room temperature. On the other hand, the thermal treatment

accelerated the reaction inside the vessels, which compensates for the fast evaporation of the solvents.

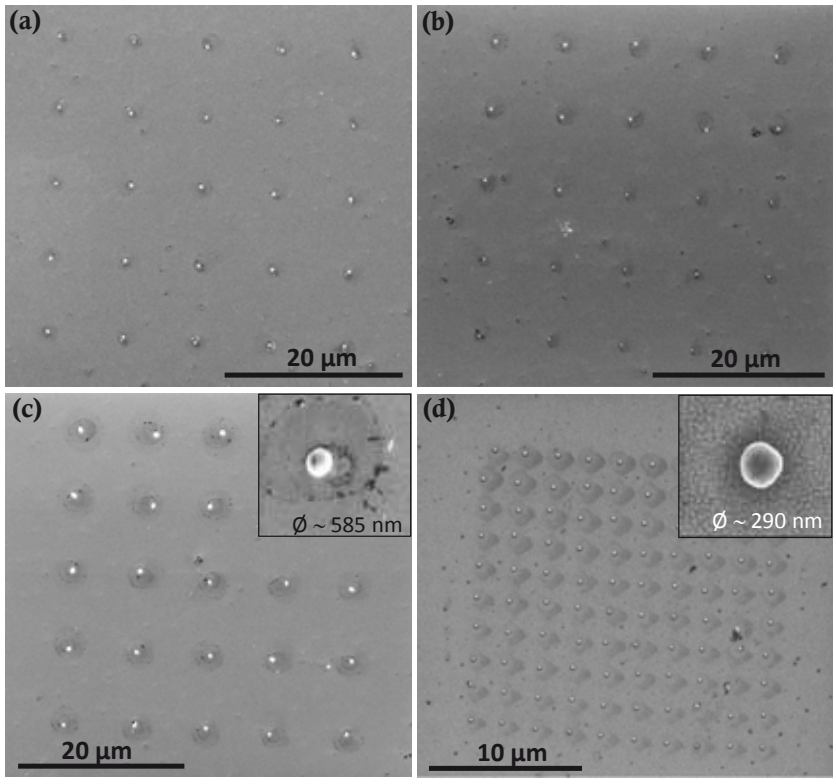

Figure 5.22 FE-SEM images of CPPs obtained after the inks were mixed in the cantilevers during the inking procedure and the mixture delivered onto the surface. Panels (a), (b) and (c) show the growth of one CPP per feature on a substrate kept in DMSO atmosphere after patterning. (d) One CPP per droplet grown on a substrate placed in the oven after patterning. Insets: a single particle and median diameter of the particles in the array.

The growth of large amounts of spherical shaped particles (233 ± 15 nm in diametre) was also observed in the big drops generated during the bleeding of the cantilevers (Figure 5.23a,b) in samples subjected to either of the treatments. Examination of the inkwells and cantilever arrays used in these experiments under FE-SEM also showed the presence of particles formed upon mixture of the inks (Figure 5.23c,d). Through all these experiments, we were able to show the potentiality of this technique to fabricate single nanoparticle arrays with very good size distributions. Only occasionally, imperfections appeared and some confined reactions gave place to more than one nanoparticle or contiguous droplets fused into one (Figure 5.23e,f).

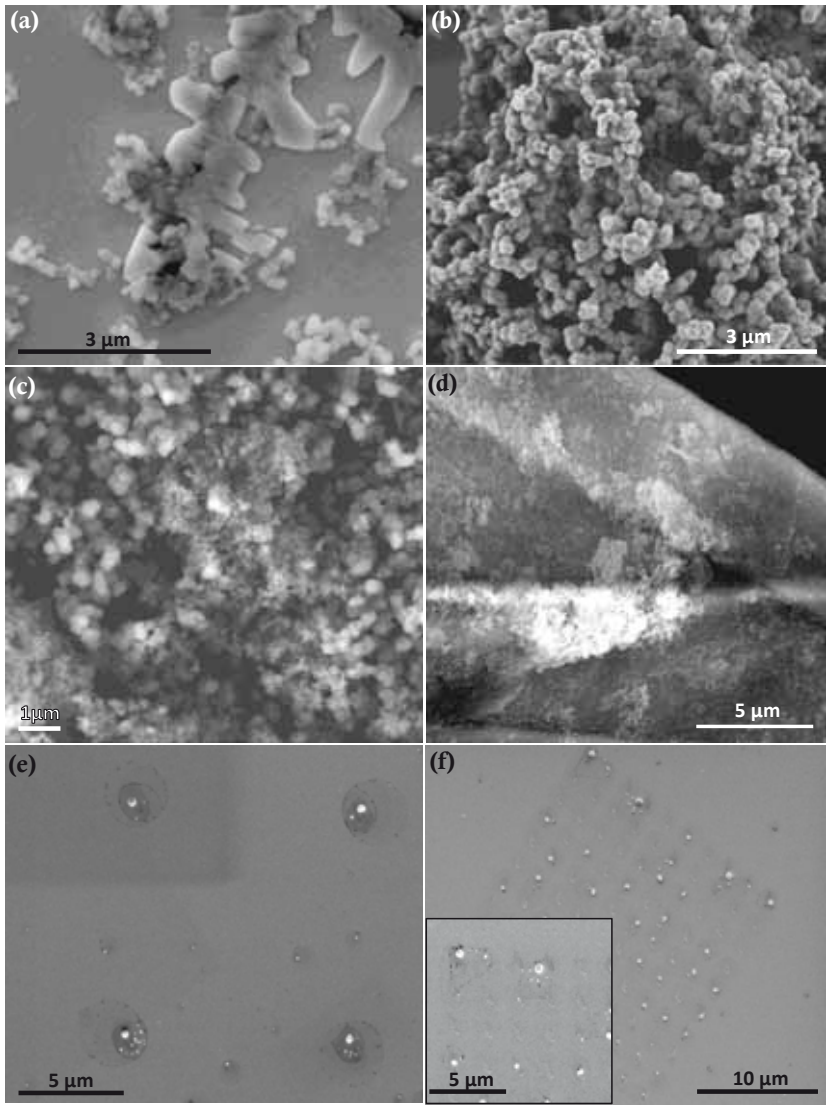

Figure 5.23 FE-SEM images of **CPP1** particles grown inside big droplets fabricated during the bleeding of the cantilevers on a substrate kept in DMSO vapours (a) and placed in the oven after patterning (b). (c) FE-SEM image of CPP1 particles grown in an inkwell used to synthesize them through approach 2. (d) FE-SEM image of one of the tips used in approach 2 showing the formation of CPPs on the cantilever. (e) FE-SEM image showing the growth of more than one particle per feature. (f) FE-SEM showing a dot array where closely positioned droplets fused into one and formed larger CPPs. Inset: magnified image of a small part of the array. Both (e) and (f) micrographs correspond to substrates exposed to DMSO atmosphere after patterning.

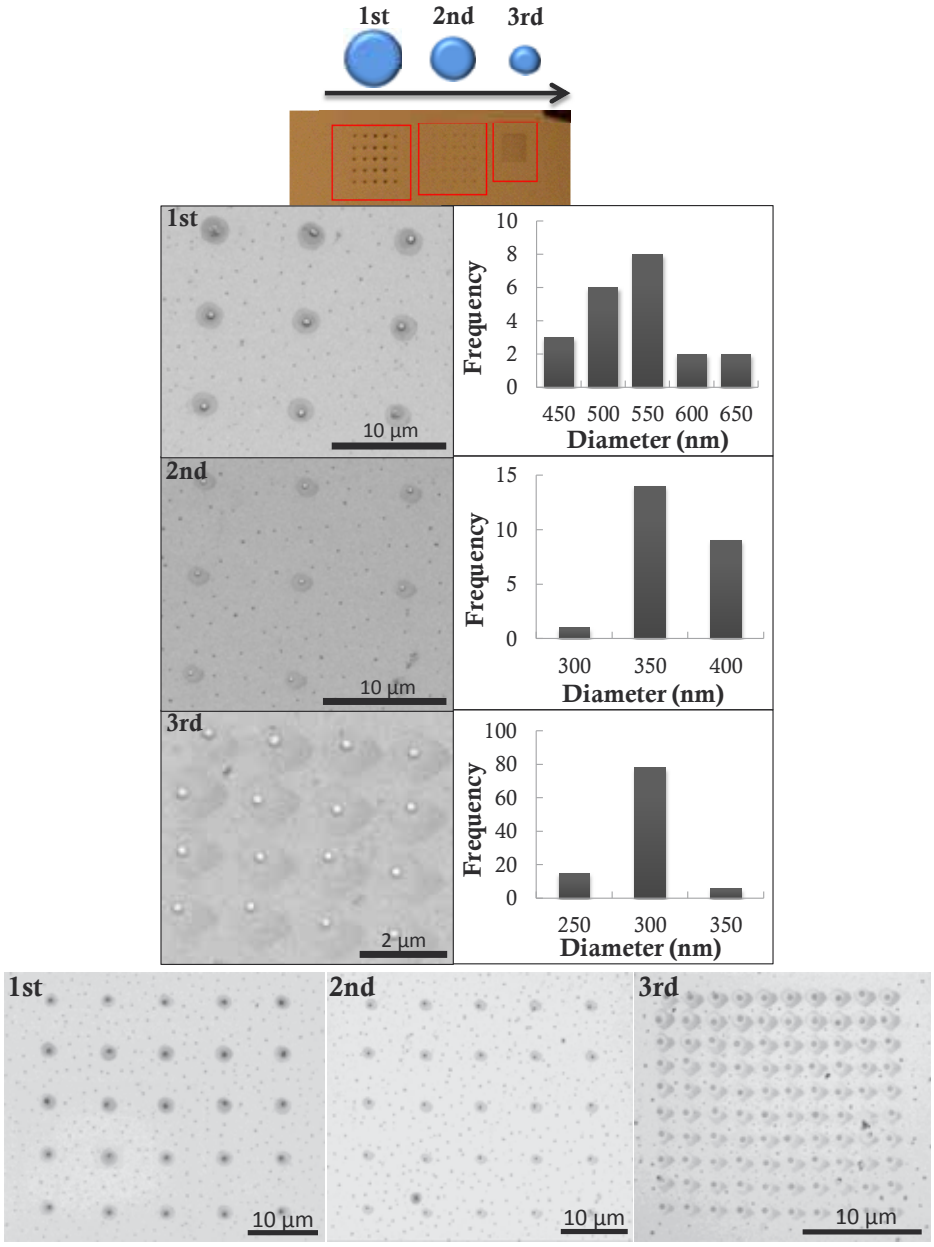

Figure 5.24 Optical microscopy image (top) showing a decrease of the deposited volume in successive arrays. SEM images of the particles obtained inside each one of the arrays (left column) after the substrate was placed in an oven at 50°C. The reduction in size is clearly seen in the diameter measurements (right column). FE-SEM images of the complete arrays (bottom row).

It was also observed that the volume of the deposited droplets had a direct influence on the final size of the CPPs that grew inside each nano-vessel. Also, the particles obtained by this method were highly monodisperse within each array. This observation is consistent

with the reported results on the synthesis of coordination polymers confined into reverse micelles, where a high monodispersity is observed thanks to the template effect of the micro-emulsions.[114,115] Figure 5.24 shows three arrays fabricated in series where the volume of the dots decreased with the successive lithographies due to depletion of the ink. This is visible in the optical microscopy image in Figure 5.24 (top row) where the dots can be distinguished in the first two lithographies but only a rectangular shadow is seen in the third one due to the smaller size of the features. Accordingly, the average size of the resulting nanoparticles systematically decreased with successive lithographies. The FE-SEM images in Figure 5.24 show the formation of one particle per dot with high size reproducibility within each array. In the first lithography the diameters range between 630 and 450 nm; in the second, between 280 and 390 nm and in the third one between 230 and 330 nm. This direct relationship between the deposited volume and the particle size can be attributed not only to the variable amounts of material contained in different sized droplets but also to the confinement of the reaction, as the droplets can act as templates to induce a certain particle shape.

5.3.4 Spectroscopic characterization

The coordination polymer nanostructures obtained directly on surfaces were finally characterized by using Grazing Angle Infrared Spectroscopy (GA-IR) and MicroRaman spectroscopy. First, the **CPP1** particles obtained by drop-casting were examined through GA-IR and their spectrum showed good agreement with that of the material obtained in bulk (Figure 5.25a). In both cases the presence of a C-O stretching band from the catechol groups was clearly observed (~1230 cm^{-1}, doublet), as well as a pyridine band centered at 1485 cm^{-1} ($\upsilon_{C=C/C-N}$) and the skeletal vibrations of the aromatic rings, which appeared at approximately 1600 cm^{-1}. Moreover, comparison of the spectra obtained for both **CPP1** bulk and drop casted samples with that of the pure ligand **4** revealed band shifts attributed to the coordination to cobalt (υ_{C-O} doublet separation). The material deposited in the large droplets generated during the bleeding of the cantilevers (after mixture of the inks during tip functionalization, approach 2) was also examined (Figure 5.25a). The GA-IR spectrum showed the same characteristic peaks than those of the **CPP1** nanoparticles synthesized in solution, confirming the formation of the desired material on surface.

Finally, MicroRaman spectroscopy was used as an additional characterization technique. These experiments were performed by Dr Gábor Molnár, from the Laboratoire de Chimie de Coordination (CNRS) in Toulousse. The spectra were recorded in the 1700-500 cm^{-1} range in bulk samples as well as in droplets generated by AFM-assisted

lithography. The spectra obtained in the large drops deposited using the second approach were in good agreement with the spectrum of the material obtained in bulk (Figure 5.25b). We the bands associated to aromatic moieties (1480, 1190 cm^{-1}) were clearly distinguished and also the small band corresponding to the stretching of the Co-O bond (640 cm^{-1}) was visible, confirming the coordination of the metal to the catechol ring. The reduced amount of material present in the patterns fabricated by approaches 1 and 2 (one particle grown inside each droplet) complicated the obtaining of a clear spectrum due to the large noise to signal ratio. However, the more intense bands were clearly seen in the spectra recorded over areas with a high density of particles. These bands were clearly coincident with the spectrum of the bulk material, suggesting the formation of **CPP1**.

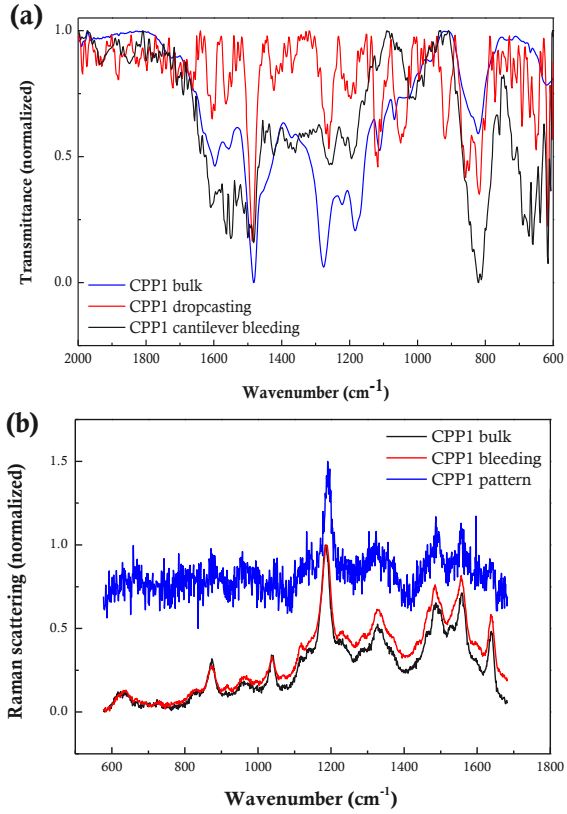

Figure 5.25 (a) GA-IR spectra of the CPPs obtained in bulk (blue), the ones synthesized by drop-casting (red) and those grown in the large drops generated through cantilever bleeding (black) showing good agreement. (b) MicroRaman spectra of **CPP1** in bulk (black), the particles grown inside the large drops obtained during the cantilever bleeding steps fabricated by approach 2 (red) and those in the patterned areas (blue). As seen, the signal to noise ratio in the patterned areas is very poor, but the most intense bands can be distinguished.

As we have described in Section 3.4 the coordination of the catechol moiety to Co^{2+} ions, provides valence tautomeric properties to the **CPP1** particles. Therefore, it would be highly interesting to know if the CPPs synthesized by confined reaction on surface also present this switchable behaviour. MicroRaman spectroscopy was used with that aim, as it has already been employed for the characterization of related spin-crossover materials at the nanoscale.[116–118] Unfortunately, the changes in the Raman spectrum of **CPP1** particles associated to the VT interconversion were already hard to see in bulk and no conclusions could be extracted from the experiments performed on patterned surfaces due to the low amount of material present in the samples.

5.4 Summary

The fabrication of polymeric structures inside femtolitre-sized reaction vessels using direct write AFM-assisted lithography has been describedin this chapter.

First of all the synthesis of polydopamine, an extensively used mussel-mimetic adhesive and primer, was confined. Femtolitre volumes of a standard basic solution of dopamine hydrochloride were delivered onto a surface and the polymerization reaction proceeded inside the fabricated droplets. By doing so, dot-like feature arrays of PDA with variable dimensions and over extended areas were fabricated in a straightforward process. The adhesive properties of the structured PDA were addressed by measuring F-d curves inside the fabricated motifs. The F_{adh} results were comparable to those obtained on PDA films and even showed lower statistical dispersion than those of thick (~35 nm) films. Also, the adhesion did not depend on the dimensions of the dots, and was uniquely related to the material itself. As opposite to what was observed in patterned catechol-terminated SAMs, (Section 4.2.4 of this manuscript) the adhesive properties of PDA were not altered due to confinement of its synthesis and the local adhesion of surface-patterned PDA was measurable. It is important to note here that the PDA structures were much bigger in size than the catechol-terminated sub-monolayers, which clearly simplified the location of the structures on the surface and the measurement of the local adhesion. Additionally, the redox properties of surface-confined PDA were explored and AgNPs were fabricated over the polymeric patterns by in-situ reduction of Ag^{+} ions. This process unveiled some stability issues of the patterned PDA that we were able to overcome after optimization of the methodology.

The second case of study was the confined synthesis of **CPP1** particles through surface deposition of femtolitre-sized droplets containing the metal and the ligand precursors. In a first approach, the two reagents were mixed by sequentially delivering them on the surface. After facing several difficulties including the precise positioning of the droplets and control of solvent evaporation, we were able to carry out the confined reaction and even observed the evolution of the particles from their primary stages to their final shape. An alternative methodology involving the mixture of the inks during the tip functionalization step was developed in order to increase the reproducibility and simplicity of the procedure. This approach allowed us to fabricate CPPs in a controlled manner, creating high-density arrays of precisely positioned particles which size was clearly dependent on the volume of the deposited droplets.

All in all, we have probed that AFM-assisted lithography is a powerful tool to perform reactions in femtolitre volumes with fine control over the position and size of the target materials. The intrinsic nature of the technique allows to directly synthesize the desired materials on precise locations of the substrates by delivering their soluble precursors. This allowed us to pattern PDA and **CPP1** particles on surfaces. Due to the high insolubility of these two materials, their patterning on surface through AFM-assisted lithography is not viable if they are previously synthesized in bulk. Probably the main impediment that we found during these experiments was the characterization of the obtained polymers. The extremely small amount of analyte present in the samples, which is close to the detection limit of most commonly used techniques, largely complicated the chemical characterization of the materials. For this reason, the development of both confined synthesis methodologies and analytical techniques to characterize the materials remain important challenges to continue facing in the future.

5.5 Experimental Section

Materials: Dopamine hydrochloride, Tris(hydroxymethyl)aminomethane (99.0%), Tris(hydroxymethyl)aminomethane hydrochloride (99.0%), $AgNO_3$ (ACS reagent, 99%), $Co(COOCH_3)_2{\cdot}4H_2O$ (ACS Reagent, 98.0%), DMF (anhydrous, 99.8%), DMSO (99.5%) and glycerol (≥ 99%) were purchased from Sigma-Aldrich and used as received.

5.5.1 Polydopamine synthesis and structuration

5.5.1.1 Polydopamine synthesis and coating: Polydopamine was obtained following a previously described and widely used procedure.[101] Dopamine hydrochloride (2 mg/mL) was dissolved in 10 mM Tris·HCl (pH 8.59) solution. Prior to coating, substrates were cleaned by sonication during 15 min in Acetone, EtOH and Milli-Q water and dried in a N_2 stream. Substrates were placed in vertical orientation into the solution for 1 hour or overnight (~15h) while stirring to minimize non-specific deposition. Afterwards, the substrates were rinsed with Milli-Q water and dried under a nitrogen stream. For AFM-assisted lithography experiments, the freshly prepared basic solution of dopamine was used as ink without further modification.

5.5.1.2 Direct-write AFM lithography experiments: PDA lithographies were performed using a commercial dip-pen writer DPN 5000 System (Nanoink Inc.). Commercial silicon nitride A-type tips and M-type probe arrays (Nanoink Inc.) with a spring constant of 0.05 $N{\cdot}m^{-1}$ or tip arrays from Nanosensors™ (0.3 $N{\cdot}m^{-1}$) were used for patterning. The tips were coated with the ink solution described before using a microfluidic ink delivery chip-based system (Inkwell, Nanoink Inc.) that had been placed in an O_3/UV cleaner for 10 min before the experiments were performed in order to facilitate the flow of the ink solution through the channels. The reservoirs were filled with fresh ink and the tips were loaded by dipping them into the microwells for a given time (typically 2-5 min). Afterwards, the tips were carefully brought into contact with the surface to fabricate the desired patterns by traversing the tip over the surface.

5.5.1.3 AFM imaging and Force-distance measurements: AFM imaging and adhesion force measurements were performed using an Agilent 5500 AFM/SPM microscope. Tapping mode AFM was used for topographical characterization using beam shaped silicon cantilevers (Nanosensors) with nominal force constants of 42 $N{\cdot}m^{-1}$ and ~7 nm tip radius.

Contact mode imaging and force-distance measurements were carried out using aluminum-coated silicon cantilevers with nominal force constant of 0.2 $N \cdot m^{-1}$. Adhesion data were extracted from deflection-separation data by measuring the jump-out of the tip during the retraction movement. After the adhesion experiments, all the cantilevers were calibrated (in sensitivity and spring constant). On PDA coatings, F-d curves were recorded all along the surface. On PDA patterns, the exact location of the dot-like features was first found by scanning the patterned areas in contact mode while keeping the deflection to a minimum. Then, the FlexGrid tool of PicoScan5 was used to obtain the F-d curves in the desired specific locations. After each series of measurements F-d curves on clean areas of the same substrate were obtained in order to check if the tip had been damaged or contaminated.

5.5.1.4 On-surface Ag+ reduction by PDA: The substrates coated with PDA were immersed in a 50 mM $AgNO_3$ solution in Milli-Q water and kept in the darkness for 24 hours. Afterwards, they were thoroughly rinsed with copious amounts of water and dried under a nitrogen stream.

For the reduction of Ag^+ the patterned substrates, they were immersed in a 10 mM solution of $AgNO_3$ and placed in the oven at 60 ºC for an hour. After that time, the samples were removed from the oven and carefully rinsed with Milli-Q water.

5.5.1.5 Electrical resistivity: The electrical resistivity of the samples was measured with a two-point contact resistance method. Conventional electron beam lithography and lift-off methods were used to deposit two small titanium/gold electrodes on top of the Ag/PDA structures. The gap between these two small electrodes was about 10 μm. These were connected to large gold pads on which the two point contact methodology was performed. The electrical characteristics of the silver islands were measured with a Karl Suss probe station and a semiconductor parameter analyzer HP4155. The I–V curves were acquired by applying a bias voltage ranging between –100 mV and 100 mV while recording the current.

5.5.2 Confined synthesis of CPPs

5.5.2.1 Synthesis of CPP1 in bulk: An aqueous solution (1 mL) of $Co(COOCH_3)_2 \cdot 4H_2O$ (60.7 mg, 0.25 mmol) was added dropwise to a solution of **4** (108.0 mg, 0.5 mmol) in DMSO (5 mL) under continuous gentle magnetic stirring and immediately a black precipitate formed. After 30 minutes the precipitate was centrifuged and washed several

times with water and EtOH, and dried under vacuum. The resulting solid product was obtained in 65% yield. FE-SEM analysis showed the formation of spherical particles (mean size: 811 ± 17 nm), and XRD measurements indicate the amorphous nature of the particles. IR-ATR and elemental analysis corroborated the obtaining of the corresponding coordination polymer, analogous to the previously obtained using EtOH as solvent; as described in Section 3.4. The same methodology was employed in the experiments performed using other solvents.

5.5.2.2 Drop-casting experiments: As a first step of the reaction miniaturization, several drop-casting experiments were performed. In general, the experiments consisted in sequentially adding microliter volumes of metal and ligand solutions onto a gold substrate and allowing the solvents to evaporate. Aqueous $Co(COOCH_3)_2{\cdot}4H_2O$ solutions (34 mM) and either DMSO or DMF solutions of ligand **4** (20 mM) containing 0-2% of glycerol were used and the volume of each solution was calculated in order to mix the two reagents in stequiometric ratios (2:1 ligand/metal ratio). In all cases the formation of spherical CPPs was observed under examination by FE-SEM.

5.5.2.3 Confined reaction and particle growth using direct-write AFM-assisted lithography: A commercial dip-pen writer Nscriptor™ DPN System (from NanoInk, Inc.) was used to fabricate the femtolitre sized reaction vessels through direct delivery of ink droplets onto a surface. Type M Probe Arrays were coated using a microfluidic ink delivery chip-based system (Inkwell, NanoInk). For that, contiguous channels of the inkwells were filled with the two ink solutions of choice (a 200 mM solution of **4** in DMSO (2% glycerol) and a 100 mM solution of $Co(COOCH_3)_2{\cdot}4H_2O$ in H_2O (1% gly)) and the tips were functionalized with each one of them in a way that they either coated each tip separately (approach 1) or they mixed in the cantilever array during the process (approach 2). Once coated, the tips were brought in close contact with clean polycrystalline gold substrates (40 nm gold thickness) to deliver femtolitre-sized droplets of the inks. After the deposition of the droplets, the substrates were kept in closed vessels saturated with DMSO vapours (a droplet of DMSO was casted on a piece of filter paper and introduced in the chamber) or alternatively placed in an oven at 50ºC in order to control the solvent evaporation rate and the reaction velocity.

5.5.2.4 MicroRaman spectroscopy: Raman spectra were acquired at room temperature using a Dilor triplemate spectrograph (1800 1 mm grating, 100 Lm entrance slit, 1 cm1 spectral resolution) coupled to a Princeton Instruments CCD detector. The 647.1 nm line of a Kr^+ laser (Coherent Radiation Innova) was used as an excitation source with laser power output of 10 mW. The laser beam was focused on a spot approximately 3 mm in diameter

and the Raman signal was collected in a backscattering geometry. The same procedure was carried out for the sample in bulk, on the CPPs obtained by drop casting and on the nanoparticles synthesized directly on the gold surface.

More information on the used instruments, consumables and characterization methods can be found in Chapter 7.

5.6 References

(1) ENIAC: Celebrating Penn Engineering History. University of Pennsylvania, School of Engineering and Applied Science. http://www.seas.upenn.edu/about-seas/eniac/operation.php.

(2) Geissler, M.; Xia, Y. *Adv. Mater.* **2004**, *16*, 1249–1269.

(3) Lei, Y.; Yang, S.; Wu, M.; Wilde, G. *Chem. Soc. Rev.* **2011**, *40*, 1247–1258.

(4) Ito, T.; Okazaki, S. *Nature* **2000**, *406*, 1027–1031.

(5) Cavallini, M.; Albonetti, C.; Biscarini, F. *Adv. Mater.* **2009**, *21*, 1043–1053.

(6) Xia, Y.; Whitesides, G. M. *Annu. Rev. Mater. Sci.* **1998**, *28*, 153–184.

(7) Garcia, R.; Knoll, A. W.; Riedo, E. *Nat. Nanotechnol.* **2014**, *9*, 577–587.

(8) Daniel T. Chiu Gavin D. M. Jeffries, R. M. L. *Anal. Chem.* **2009**, *81*, 5111–5118.

(9) Gorris, H. H.; Walt, D. R. *Angew. Chem. Int. Ed.* **2010**, *49*, 3880–3895.

(10) Collier, C. P.; Simpson, M. L. *Curr. Opin. Biotechnol.* **2011**, *22*, 516–526.

(11) Ganguli, A. K.; Ganguly, A.; Vaidya, S. *Chem. Soc. Rev.* **2010**, *39*, 474–485.

(12) Song, H.; Chen, D. L.; Ismagilov, R. F. *Angew. Chem. Int. Ed.* **2006**, *45*, 7336–7356.

(13) Nightingale, A. M.; Demello, J. C. *Adv. Mater.* **2013**, *25*, 1813–1821.

(14) Marre, S.; Jensen, K. F. *Chem. Soc. Rev.* **2010**, *39*, 1183–1202.

(15) Nakano, M.; Komatsu, J.; Matsuura, S. I.; Takashima, K.; Katsura, S.; Mizuno, A. *J. Biotechnol.* **2003**, *102*, 117–124.

(16) Pietrini, A. V.; Luisi, P. L. *ChemBioChem* **2004**, *5*, 1055–1062.

(17) Noireaux, V.; Libchaber, A. *Proc. Natl. Acad. Sci. USA* **2004**, *101*, 17669–17674.

(18) Stamou, D.; Duschl, C.; Delamarche, E.; Vogel, H. *Angew. Chem. Int. Ed.* **2003**, *42*, 5580–5583.

(19) Chiu, D. T.; Wilson, C. F.; Ryttsén, F.; Strömberg, A.; Farre, C.; Karlsson, A.; Nordholm, S.; Gaggar, A.; Modi, B. P.; Moscho, A.; Garza-López, R. A.; Orwar, O.; Zare, R. N. *Science* **1999**, *283*, 1892–1895.

(20) Martin, K.; Henkel, T.; Baier, V.; Grodrian, A.; Schön, T.; Roth, M.; Michael Köhler, J.; Metze, J. *Lab Chip* **2003**, *3*, 202–207.

(21) Capek, I. *Adv. Colloid Interfac.* **2004**, *110*, 49–74.

(22) Qi, D.; Cao, Z.; Ziener, U. *Adv. Colloid Interfac.* **2014**, *211*, 47–62.

(23) Vaucher, S.; Li, M.; Mann, S. *Angew. Chem. Int. Ed.* **2000**, *39*, 1793–1796.

(24) Duraiswamy, S.; Khan, S. A. *Small* **2009**, *5*, 2828–2834.

(25) Faustini, M.; Kim, J.; Jeong, G. Y.; Kim, J. Y.; Moon, H. R.; Ahn, W. S.; Kim, D. P. *J. Am. Chem. Soc.* **2013**, *135*, 14619–14626.

(26) Paseta, L.; Seoane, B.; Julve, D.; Sebastián, V.; Téllez, C.; Coronas, J. *ACS Appl. Mater. Interfaces* **2013**, *5*, 9405–9410.

(27) Sanchez-Dominguez, M.; Pemartin, K.; Boutonnet, M. *Curr. Opin. Colloid In.* **2012**, *17*, 297–305.

(28) Jaschke, M.; Butt, H.-J. *Langmuir* **1995**, *11*, 1061–1064.

(29) Piner, R. D.; Zhu, J.; Xu, F.; Seunghun, H.; Mirkin, C. A. *Science* **1999**, *283*, 661–663.

(30) Hong, S.; Zhu, J.; Mirkin, C. A. *Langmuir* **1999**, *15*, 7897–7900.

(31) Hong, S. *Science* **1999**, *286*, 523–525.

(32) Hong, S.; Mirkin, C. A. *Science* **2000**, *288*, 1808–1811.

(33) Basnar, B.; Willner, I. *Small* **2009**, *5*, 28–44.

(34) Ginger, D. S.; Zhang, H.; Mirkin, C. A. *Angew. Chem. Int. Ed.* **2004**, *43*, 30–45.

(35) Barsotti, R. J.; O'Connell, M. S.; Stellacci, F. *Langmuir* **2004**, *20*, 4795–4798.

(36) Zhang, H.; Chung, S.; Mirkin, C. A. *Nano Lett.* **2003**, *3*, 43–45.

(37) Wu, C.-C.; Reinhoudt, D. N.; Otto, C.; Subramaniam, V.; Velders, A. H. *Small* **2011**, *7*, 989–1002.

(38) Brinkmann, F.; Hirtz, M.; Greiner, A. M.; Weschenfelder, M.; Waterkotte, B.; Bastmeyer, M.; Fuchs, H. *Small* **2013**, *9*, 3266–3275.

(39) Irvine, E. J.; Hernandez-Santana, A.; Faulds, K.; Graham, D. *Analyst* **2011**, *136*, 2925–2930.

(40) Xie, Z.; Zhou, X.; Tao, X.; Zheng, Z. *Macromol. Rapid Commun.* **2012**, *33*, 359–373.

(41) Kooi, S. E.; Baker, L. a.; Sheehan, P. E.; Whitman, L. J. *Adv. Mater.* **2004**, *16*, 1013–1016.

(42) Demers, L. M.; Ginger, D. S.; Park, S.-J.; Li, Z.; Chung, S.-W.; Mirkin, C. A. *Science* **2002**, *296*, 1836–1838.

(43) Agarwal, G.; Naik, R. R.; Stone, M. O. *J. Am. Chem. Soc.* **2003**, *125*, 7408–7412.

(44) Brown, K. a.; Eichelsdoerfer, D. J.; Liao, X.; He, S.; Mirkin, C. A. *Front. Phys.* **2014**, *9*, 385–397.

(45) Rosa, L. G.; Liang, J. *J. Phys.: Condens. Matter* **2009**, *21*, 483001.

(46) Rozhok, S.; Piner, R.; Mirkin, C. A. *J. Phys. Chem. B* **2003**, *107*, 751–757.

(47) Salaita, K.; Amarnath, A.; Higgins, T. B.; Mirkin, C. A. *Scanning* **2010**, *32*, 9–14.

(48) Rozhok, S.; Sun, P.; Piner, R.; Lieberman, M.; Mirkin, C. A. *J. Phys. Chem. B* **2004**, *108*, 7814–7819.

(49) Wu, C.-D.; Fang, T.-H.; Lin, J.-F. *Langmuir* **2010**, *26*, 3237–3241.

(50) Wu, C.-D.; Fang, T.-H.; Lin, J.-F. *J. Colloid Interface Sci.* **2011**, *361*, 316–320.

(51) Heo, D. M.; Yang, M.; Kim, H.; Saha, L. C.; Jang, J. *J. Phys. Chem. C* **2009**, *113*, 13813–13818.

(52) Hampton, J. R.; Dameron, A. A.; Weiss, P. S. *J. Am. Chem. Soc.* **2006**, *128*, 1648–1653.

(53) Weeks, B. L.; Noy, A.; Miller, A. E.; De Yoreo, J. J. *Phys. Rev. Lett.* **2002**, *88*, 255505.

(54) O'Connell, C. D.; Higgins, M. J.; Marusic, D.; Moulton, S. E.; Wallace, G. G. *Langmuir* **2014**, *30*, 2712–2721.

(55) O'Connell, C. D.; Higgins, M. J.; Sullivan, R. P.; Moulton, S. E.; Wallace, G. G. *Small* **2014**, 1–12.

(56) Zhong, J.; Sun, G.; He, D. *Nanoscale* **2014**, *6*, 12217–12228.

(57) Wang, W. M.; Stoltenberg, R. M.; Liu, S.; Bao, Z. *ACS Nano* **2008**, *2*, 2135–2142.

(58) Lee, K.-B.; Park, S.-J.; Mirkin, C. A.; Smith, J. C.; Mrksich, M. *Science* **2002**, *295*, 1702–1705.

(59) Jung, H.; Dalal, C. K.; Kuntz, S.; Shah, R.; Collier, C. P. *Nano Lett.* **2004**, *4*, 2171–2177.

(60) Huang, L.; Braunschweig, A. B.; Shim, W.; Qin, L.; Lim, J. K.; Hurst, S. J.; Huo, F.; Xue, C.; Jang, J. W.; Mirkin, C. A. *Small* **2010**, *6*, 1077–1081.

(61) Wu, J.; Zan, X.; Li, S.; Liu, Y.; Cui, C.; Zou, B.; Zhang, W.; Xu, H.; Duan, H.; Tian, D.; Huang, W.; Huo, F. *Nanoscale* **2013**, *6*, 749–752.

(62) Liu, G.; Zhou, Y.; Banga, R. S.; Boya, R.; Brown, K. A.; Chipre, A. J.; Nguyen, S. T.; Mirkin, C. A. *Chem. Sci.* **2013**, *4*, 2093–2099.

(63) Salaita, K.; Wang, Y.; Fragala, J.; Vega, R. A.; Liu, C.; Mirkin, C. A. *Angew. Chem. Int. Ed.* **2006**, *45*, 7220–7223.

(64) Lenhert, S.; Sun, P.; Wang, Y.; Fuchs, H.; Mirkin, C. A. *Small* **2007**, *3*, 71–75.

(65) Xie, Z.; Chen, C.; Zhou, X.; Gao, T.; Liu, D.; Miao, Q.; Zheng, Z. *ACS Appl. Mater. Interfaces* **2014**.

(66) Mao, Z.; Ganesh, M.; Bucaro, M.; Smolianski, I.; Gross, R. A.; Lyons, A. M. *Biomacromolecules* **2014**, *15*, 4627–4636.

(67) Giam, L. R.; Massich, M. D.; Hao, L.; Shin Wong, L.; Mader, C. C.; Mirkin, C. A. *Proc. Natl. Acad. Sci. USA* **2012**, *109*, 4377–4382.

(68) Huo, F.; Zheng, Z.; Zheng, G.; Giam, L. R.; Zhang, H.; Mirkin, C. A. *Science* **2008**, *321*, 1658–1660.

(69) Giam, L. R.; Mirkin, C. A. *Angew. Chem. Int. Ed.* **2011**, *50*, 7482–7485.

(70) Eichelsdoerfer, D. J.; Brown, K. A.; Boya, R.; Shim, W.; Mirkin, C. A. *Nano Lett.* **2013**, *13*, 664–667.

(71) Bellido, E.; Cardona-Serra, S.; Coronado, E.; Ruiz-Molina, D. *Chem. Commun.* **2011**, *47*, 5175–5177.

(72) Bellido, E. Ph.D. Thesis, Universitat Autónoma de Barcelona, 2011.

(73) Chui, S. S. Y.; Lo, S. M. F.; Charmant, J. P. H.; Orpen, A. G.; Williams, I. D. *Science* **1999**, *283*, 1148–1150.

(74) Carbonell, C.; Imaz, I.; Maspoch, D. *J. Am. Chem. Soc.* **2011**, *133*, 2144–2147.

(75) Xu, J.; Lynch, M.; Huff, J. L.; Mosher, C.; Vengasandra, S.; Ding, G.; Henderson, E. *Biomed. Microdevices* **2004**, *6*, 117–123.

(76) Chai, J.; Huo, F.; Zheng, Z.; Giam, L. R.; Shim, W.; Mirkin, C. A. *Proc. Natl. Acad. Sci. USA* **2010**, *107*, 20202–20206.

(77) Liu, G.; Eichelsdoerfer, D. J.; Rasin, B.; Zhou, Y.; Brown, K. A.; Liao, X.; Mirkin, C. A. *Proc. Natl. Acad. Sci. USA* **2013**, *110*, 887–891.

(78) Giam, L. R.; He, S.; Horwitz, N. E.; Eichelsdoerfer, D. J.; Chai, J.; Zheng, Z.; Kim, D.; Shim, W.; Mirkin, C. A. *Nano Lett.* **2012**, *12*, 1022–1025.

(79) Chai, J.; Liao, X.; Giam, L. R.; Mirkin, C. A. *J. Am. Chem. Soc.* **2012**, *134*, 158–161.

(80) Long, D. a.; Unal, K.; Pratt, R. C.; Malkoch, M.; Frommer, J. *Adv. Mater.* **2007**, *19*, 4471–4473.

(81) Oberhansl, S.; Hirtz, M.; Lagunas, A.; Eritja, R.; Martinez, E.; Fuchs, H.; Samitier, J. *Small* **2012**, *8*, 541–545.

(82) Chen, H. Y.; Hirtz, M.; Deng, X.; Laue, T.; Fuchs, H.; Lahann, J. *J. Am. Chem. Soc.* **2010**, *132*, 18023–18025.

(83) Bian, S.; He, J.; Schesing, K. B.; Braunschweig, A. B. *Small* **2012**, *8*, 2000–2005.

(84) Bian, S.; Scott, A. M.; Cao, Y.; Liang, Y.; Osuna, S.; Houk, K. N.; Braunschweig, A. B. *J. Am. Chem. Soc.* **2013**, *135*, 9240–9243.

(85) Porter, L. A.; Choi, H. C.; Schmeltzer, J. M.; Ribbe, A. E.; Elliott, L. C. C.; Buriak, J. M. *Nano Lett.* **2002**, *2*, 1369–1372.

(86) Chu, H.; Jin, Z.; Zhang, Y.; Zhou, W.; Ding, L.; Li, Y. *J. Phys. Chem. C* **2008**, *112*, 13437–13441.

(87) Maynor, B. W.; Li, Y.; Liu, J. *Langmuir* **2001**, *17*, 2575–2578.

(88) Fu, L.; Liu, X.; Zhang, Y.; Dravid, V. P.; Mirkin, C. A. *Nano Lett.* **2003**, *3*, 757–760.

(89) Ding, L.; Li, Y.; Chu, H.; Li, X.; Liu, J. *J. Phys. Chem. B* **2005**, *109*, 22337–22340.

(90) Chu, H.; Ding, L.; Wang, J.; Li, X.; You, L.; Li, Y. *J. Phys. Chem. C* **2008**, *112*, 18938–18942.

(91) Su, M.; Liu, X.; Li, S. Y.; Dravid, V. P.; Mirkin, C. A. *J. Am. Chem. Soc.* **2002**, *124*, 1560–1561.

(92) Carnally, S. A. M.; Wong, L. S. *Nanoscale* **2014**, *6*, 4998.

(93) Smetana, A. B.; Pacley, S.; Boeckl, J.; Adamczyk, P.; Nettikadan, S. *J. Mater. Chem. C* **2013**, *1*, 1798–1803.

(94) Carbonell, C.; Stylianou, K. C.; Hernando, J.; Evangelio, E.; Barnett, S. A.; Nettikadan, S.; Imaz, I.; Maspoch, D. *Nat. Commun.* **2013**, *4*, 2173.

(95) Liu, Y.; Ai, K.; Lu, L. *Chem. Rev.* **2014**, *114*, 5057–5115.

(96) Sato, O.; Tao, J.; Zhang, Y. Z. *Angew. Chem. Int. Ed.* **2007**, *46*, 2152–2187.

(97) You, I.; Kang, S. M.; Lee, S.; Cho, Y. O.; Kim, J. B.; Lee, S. B.; Nam, Y. S.; Lee, H. *Angew. Chem. Int. Ed.* **2012**, *51*, 6126–6130.

(98) Ogaki, R.; Bennetsen, D. T.; Bald, I.; Foss, M. *Langmuir* **2012**, *28*, 8594–8599.

(99) Ku, S. H.; Lee, J. S.; Park, C. B. *Langmuir* **2010**, *26*, 15104–15108.

(100) Sun, K.; Xie, Y.; Ye, D.; Zhao, Y.; Cui, Y.; Long, F.; Zhang, W.; Jiang, X. *Langmuir* **2012**, *28*, 2131–2136.

(101) Lee, H.; Dellatore, S. M.; Miller, W. M.; Messersmith, P. B. *Science* **2007**, *318*, 426–430.

(102) Wang, X.; Jin, B.; Lin, X. *Anal. Sci.* **2002**, *18*, 931–933.

(103) Liebscher, J.; Mrówczyński, R.; Scheidt, H. A.; Filip, C.; Hădade, N. D.; Turcu, R.; Bende, A.; Beck, S. *Langmuir* **2013**, *29*, 10539–10548.

(104) Bernsmann, F.; Ponche, A.; Ringwald, C.; Hemmerlé, J.; Raya, J.; Bechinger, B.; Voegel, J.; Schaaf, P.; Ball, V. *J. Phys. Chem. C* **2009**, *113*, 8234–8242.

(105) Xu, H.; Liu, X.; Su, G.; Zhang, B.; Wang, D. *Langmuir* **2012**, *28*, 13060–13065.

(106) Hong, S.; Lee, J. S.; Ryu, J.; Lee, S. H.; Lee, D. Y.; Kim, D.-P.; Park, C. B.; Lee, H. *Nanotechnology* **2011**, *22*, 494020.

(107) Long, Y.; Wu, J.; Wang, H.; Zhang, X.; Zhao, N.; Xu, J. *J. Mater. Chem.* **2011**, *21*, 4875–4881.

(108) Jin, Y.; Cheng, Y.; Deng, D.; Jiang, C.; Qi, T.; Yang, D.; Xiao, F. *ACS Appl. Mater. Interfaces* **2014**, *6*, 1447–1453.

(109) Ball, V.; Nguyen, I.; Haupt, M.; Oehr, C.; Arnoult, C.; Toniazzo, V.; Ruch, D. *J. Colloid Interface Sci.* **2011**, *364*, 359–365.

(110) Hong, S.; Na, Y. S.; Choi, S.; Song, I. T.; Kim, W. Y.; Lee, H. *Adv. Funct. Mater.* **2012**, *22*, 4711–4717.

(111) Proks, V.; Brus, J.; Pop-Georgievski, O.; Večerníková, E.; Wisniewski, W.; Kotek, J.; Urbanová, M.; Rypáček, F. *Macromol. Chem. Phys.* **2013**, *214*, 499–507.

(112) Hung, S. C.; Nafday, O. A.; Haaheim, J. R.; Ren, F.; Chi, G. C.; Pearton, S. J. *J. Phys. Chem. C* **2010**, *114*, 9672–9677.

(113) Fu, Y.; Liu, L.; Zhang, L.; Wang, W. *ACS Appl. Mater. Interfaces* **2014**, *6*, 4–11.

(114) Boldog, I.; Gaspar, A. B.; Martínez, V.; Pardo-Ibañez, P.; Ksenofontov, V.; Bhattacharjee, A.; Gütlich, P.; Real, J. A. *Angew. Chem. Int. Ed.* **2008**, *47*, 6433–6437.

(115) Volatron, F.; Catala, L.; Rivière, E.; Gloter, A.; Stéphan, O.; Mallah, T. *Inorg. Chem.* **2008**, *47*, 6584–6586.

(116) Molnár, G.; Bousseksou, A.; Zwick, A.; McGarvey, J. J. *Chem. Phys. Lett.* **2003**, *367*, 593–598.

(117) Bedoui, S.; Molnár, G.; Bonnet, S.; Quintero, C.; Shepherd, H. J.; Nicolazzi, W.; Salmon, L.; Bousseksou, A. *Chem. Phys. Lett.* **2010**, *499*, 94–99.

(118) Wolny, J. a.; Diller, R.; Schünemann, V. *Eur. J. Inorg. Chem.* **2012**, 2635–2648.

Chapter 6

General conclusions

In the present thesis, the chemical properties of catechol moieties have been exploited for the construction and study of functional nanostructures on surfaces. To achieve this challenging objective, a diversity of experimental techniques has been employed; ranging from classical organic synthesis to advanced microscopies and high resolution lithographic techniques. The results are summarized next:

1. Two new catechol derivatives have been synthesized and fully characterized. The catechol-terminated thiol **3** was obtained in 9 synthetic steps with 16% overall yield. The convergent design of the synthesis allowed synthesizing the ditopic ligand **4** in 56% yield in only two synthetic steps from the common intermediate **13**.
2. The ditopic ligand **4** was used in the synthesis of nanoscale coordination polymer particles (**CPP1**) approximately 110 nm in diameter showing valence tautomeric interconversion and small thermal hysteresis.
3. Well-ordered catechol-terminated SAMs of **3** have been obtained on atomically flat Au surfaces and their interaction with an AFM tip has been measured by means of F-d curves. These experiments revealed the capability of the interfacial catechol moieties to strongly interact with the tip, surpassing the results obtained on a polydopamine film in both absolute value and statistical dispersion.
4. The influence of external factors such as surface roughness, equilibration time and deposition method on the interfacial properties of the SAM was also studied. The equilibration time proved to be a determinant parameter, as monolayers in their primary stages showed essentially non-adhesive character. However, it was also seen that molecules forming the final SAMs still showed large tilt angles, meaning that higher catechol densities could be achieved if the molecules of **3** were vertically aligned with the surface. According to the MD simulations performed, this situation would be theoretically possible.
5. On the contrary, the catechol-terminated thiol **3** was unable to effectively stabilize AuNPs either alone or in combination with other alkanethiols in spite of the numerous experiments and approaches attempted.
6. The confined synthesis of catechol-based materials has been achieved for the first time by depositing femtolitre-sized droplets of reagents onto surfaces using direct write AFM-assisted lithography. In that way, we demonstrated that direct write AFM-assisted lithography is a valuable tool for the fabrication of nanostructures with precise positioning on a surface.

7. The delivery of ultrasmall droplets of a basic solution of dopamine allowed to obtain polydopamine in the shape of (sub-)micrometre features. Moreover, the measurement of localized F-d curves inside the fabricated motifs proved that the material retained its adhesive character after the confined synthesis. Additionally, nanostructures composed of AgNPs were obtained on the PDA-patterned substrates thanks to the reductive character of the polymeric material.
8. **CPP1** particles were also synthesized through confined coordination polymerization reaction in femtolitre-sized droplets. Two different strategies were used with that aim, either the sequential delivery of the reagents or the patterning of a pre-mixed ink solution. In both cases, single particles were obtained inside the fabricated droplets showing a high homogeneity in size within the arrays.
9. Characterization of the nanostructures obtained through reactions performed in confined femtolitre droplets represents nowadays a real challenge, being limited by the sensibility of the analytical methods. For instance, MicroRaman was shown to be a useful technique to address the chemical composition of the particles obtained in confined volumes but not sensible enough to follow their variable-temperature dependence.

The methodologies described in this work represent a novel and innovative approach towards the fabrication of catechol-based nanostructures and interfaces and provide valuable information about the behaviour of catechol groups at the interface of solids. As we have seen, the orientation of the catechol moieties with respect to the surface, as well as their packing density have a clear influence on the F_{adh} measured at the local scale. Therefore, we suggest that exploring new ways of inducing specific molecular orientations and increase the functionalization density on catechol-based coatings and adhesives could lead to the improvement of their adhesive strength.

On the other hand, we have demonstrated the feasibility of constructing functional nanostructures by carrying out confined reactions using direct-write AFM-assisted lithography. The universality of this technique makes it appropriate to position almost any material in specific locations of a surface. Thus, endless possible applications arise from the development of processes similar to those described in this thesis. However, for that to become a reality, both the fabrication methodologies and the characterization of the materials have to be perfected.

Chapter 7

General procedures and equipment

7.1 Characterization of organic compounds

Nuclear magnetic resonance spectra (NMR) were registered at the *Servei de Ressonància Magnètica Nuclear* of the *Universitat Autònoma de Barcelona*. ^{1}H-NMR spectra were recorded on Bruker DPX250 (250 MHz), Bruker DPX360 (360 MHz) and Bruker AR430 (400 MHz) spectrometers. Proton chemical shifts are reported in ppm (CDCl3, 7.26 ppm, MeOH-d4, 3.31 ppm and DMSO-d6, 2.50 ppm). ^{13}C-NMR spectra were recorded with complete proton decoupling on Bruker DPX250 (62.5 MHz), Bruker DPX360 (90 MHz) and Bruker AR430 (100.6 MHz) spectrometers. Carbon chemical shifts are reported in ppm (CDCl3, 77.16 ppm, MeOH-d4, 49.00 ppm and DMSO-d6, 39.52 ppm). NMR signals were assigned with the help of COSY, DEPT 135 HSQC, and HMBC experiments. All spectra were measured at 298 K.

The abbreviations used to describe signal multiplicities are: s (singlet), br s (broad singlet), d (doublet), t (triplet), q (quartet), dd (double doublet), m (multiplet), and *J* (coupling constant).

Infrared spectra (IR) were recorded on a Bruker Tensor 27 Spectrophotometer equipped with a Golden Gate Single Refraction Diamond ATR (Attenuated Total Reflectance) accessory at *Servei d'Anàlisi Química* of the *Universitat Autònoma de Barcelona.* Peaks are reported in cm^{-1}.

High resolution mass spectra (HRMS) were recorded at the *Servei d'Anàlisi Química* of the *Universitat Autònoma de Barcelona* in a Bruker micrOTOFQ spectrometer using ESIMS (QTOF).

Thin-layer chromatography (TLC) was used to monitor all reactions using silica gel 60 F254 pre-coated aluminium plates (0.25 mm thickness). Development was made using an UV lamp at 254 nm and/or by staining using a $KMnO_4$/KOH aqueous solution or *p*-anisaldehyde/H_2SO_4/acetic acid solution. Flash column chromatography was performed using silica gel 60 Å, particle size 35–70 μm (230-400 mesh).

Melting points (Mp) were determined on a REICHERT Koffler hot stage melting point apparatus, and are uncorrected.

7.2 Preparation and characterization of nanoparticles and surfaces

Materials: The solvents used for cleaning the substrates (acetone, EtOH and in some cases MeOH) were all HPLC grade and were purchased from Fisher. Milli-Q water (18.2 mΩ.cm) was used in all cases.

Polycrystalline gold substrates were obtained by evaporation of gold onto silicon wafers bearing a native oxide layer (Si/SiO_2) using an Electron Beam Evaporator (from AJA International Inc.). Si/SiO_2 substrates were obtained from *Centro Nacional de Microelectrónica* (CNM) and were prepared by initially cutting silicon wafers into 1 cm × 1 cm or 0.5 cm × 0.5 cm pieces. Then, each Si/SiO_2 substrate was washed in an ultrasonic bath for 15 min in Acetone, EtOH, and Milli-Q water and dried under a nitrogen stream. In the evaporator, the substrates where first coated with a Ti (99.99%) layer (~10 nm) to act as a primer and then a ~40 nm layer of Au (99.99%) was deposited on top at a rate of ~1 $Å \cdot s^{-1}$. During the whole process, the pressure inside the evaporator was $\sim 10^{-8}$ Torr. Prior to their use, the polycrystalline gold substrates were cleaned by sonication in Acetone, EtOH and Milli-Q water and dried in a nitrogen stream.

Epitaxial gold (300 nm) on mica substrates were purchased from Georg Albert PVD and stored under vacuum. Prior to the SAM formation, the epitaxial gold substrates were cleaned by thoroughly rinsing with acetone, EtOH and Milli-Q water and dried under a nitrogen stream.

Polarization modulation infrared reflection-absorption spectra (PM-IRRAS) were recorded by Dr. J. Saiz-Poseu on a FT-IR spectrometer Vertex 70(Bruker) combined with a PMA50 accessory at the *Institut Català de Nanociència i Nanotecnologia (ICN2)*. The angle of incidence during the acquisition of the spectra was 80°. Two separated spectra were recorded with the photoelastic modulator set at 2900 cm^{-1} for the OH and CH_2 stretching region and at 1600 cm^{-1} for C=C and CO stretching and OH bending region. To obtain the spectrum, a 300 nm thick Au layer was deposited on a Si/SiO_2 substrate with ~10 nm of Ti as primer and the substrate was immersed overnight in the thiol solution.

The notation used to describe the spectra are ν (stretching), δ (bending), ip (in-plane).

X-Ray Photoelectron Spectroscopy (XPS) measurements were carried out by Dr. G. Sauthier at the *ICN2* using a Phoibos 150 analyzer (SPECS GmbH, Berlin,Germany)) in ultra-high vacuum conditions (base pressure $1 \cdot 10^{-10}$ mbar). A monochromatic Kα X-ray

source (1486.6 eV) was used. The spectra were based on photoelectrons with a takeoff angle of 0° for the overall spectra and S 2p core level and 30° for the C 1s core level (takeoff angle considered with respect to the surface normal).

Spectroscopic Ellipsometry (SE) was carried out in order to determine the thickness and refractive index of the layered structures using a Semilab Sopra GES5E spectroscopic ellipsometer and was performed by Dr. S. Tatay at the *Instituto de Ciencia Molecular (ICMOL)*. During the investigation the incident angle of the light beam was set to 65, 70 or 75° and the wavelength was varied from 300 to 800 nm. Measurements were carried out at least on three macroscopically spaced points of the sample. Ellipsometric data was fitted with multilayer models using the Semilab's WinElli II analysis software. Clean gold substrates were modelled first. Next, a Cauchy model (A = 1.49) was used to model the organic film.

UV-Vis spectroscopy (UV-VIS) was carried out at the *ICN2* in a Varian Cary 4000 spectrometer at room temperature using 1 cm path length quartz cuvettes.

Temperature dependent UV-VIS absorption measurements were performed in the same spectrometer, using a refrigerating circulator bath thermostate (Huber MPC-K6) coupled to the sample holder.

Infrared Spectroscopy (IR) was used for the characterization of the AuNP functionalization and the CPPs. For that, a concentrated solution of the AuNPs was mixed with KBr and dried under a N_2 stream, then the dry mixtures were pressed into pellets and measured in a Tensor 27 spectrophotometer (Bruker) at the *ICN2*. A KBr pellet was used as blank. Alternatively the ATR accessory of the equipment was used to record the IR spectra of CPPs that were placed in the diamond window as a powder.

Dynamic Light Scattering (DLS) was used to determine the size distribution of the CPPs using a ZetasizerNano 3600 instrument from Malvern Instruments located at the *ICN2*. The size range limit of the instrument is 0.6 nm to 6 mm. The measurements were recorded at 25 ºC using a folded capillary cell (Malvern).

Grazing Angle Reflection IR Spectroscopy (GA-IR) was used to characterize the PDA and coordination polymer structures obtained on surfaces. It was performed using an Hyperion 2000 FT-IR microscope coupled to a Vertex 80 spectrophotometer. The grazing IR objective of the instrument is optimized for measurements of very thin layers on highly reflecting surfaces such as metals using p-polarized light incident at 83º and allows

visualizing the sample (x15 augmentation) and the area of interest and recording the IR spectra of the selected area without changing the objective. The microscope is equipped with an MCT nitrogen-cooled detector that works in the middle IR spectral region. For these measurements, a clean gold mirror was used as a reference.

Variable-temperature magnetic characterization was performed for the VT sample in solid state in a Quantum Design MPMS XL SQUID on the 35-370 K temperature range operating at a magnetic field strength of 0.1 T. The dried powder sample, (10 to 20 mg) was placed inside a gelatine capsule that was mounted in a straw and placed in the instrument.

MicroRaman spectroscopy: Raman spectra were acquired at room temperature using a Dilor triplemate spectrograph (1800 1 mm grating, 100 Lm entrance slit, 1 cm^{-1} spectral resolution) coupled to a Princeton Instruments CCD detector. The 647.1 nm line of a Kr^{+} laser (Coherent Radiation Innova) was used as an excitation source with laser power output of 10 mW. The laser beam was focused on a spot approximately 3 mm in diameter and the Raman signal was collected in a backscattering geometry.

7.3 Optical and electron microscopies

Optical microscopy images of the patterned substrates were obtained using a Zeiss Axio Observer Z-1 inverted optical/fluorescence microscope with motorized XY stage, halogen lamp excitation source, AxioCam HRc digital camera and standard filters.

Scanning Electron Microscopy (SEM) was used to characterize the samples obtained by drop-casting, dip coating or direct-write AFM-lithography using a Quanta 650 FEG (resolution 1.2 nm at 30 kV) for routine examination of the samples or a Magellan 400L (resolution 0.8 nm at 15 kV) for high resolution images. Both instruments are from FEI™ and are located at the *ICN2*. They were operated in high vacuum mode working at 5 kV for secondary electrons imaging and 10 kV for backscattered electrons. EDS analysis was performed using an Inca 250 SSD XMax20 detector incorporated into the Quanta 650 FEG instrument.

Occasionally a MERLIN® FE-SEM from Carl Zeiss located at the *Servei de Microscopia (UAB)* was used.

Double-sided carbon tape (Ted Pella) was used to adhere the substrates to the sample holders. To examine nanoparticle samples, drops of the particle dispersions were casted onto aluminium tape and left to dry.

Scanning Transmission Electron Miscroscopy (STEM) was performed at the ICN2 to examine the AuNPs using a Magellan 400L from FEI™ operated at 20 kV and 100 pA. Both Bright Field (BF) and High-Angle Annular Dark Field (HAADF) detectors were used simultaneously.

The samples were prepared by casting a drop of AUNP dispersion on TEM grids (ultrathin carbon type-A, 400 mesh Cu grids, Ted Pella) and allowing to dry overnight prior to examination. The digital images were analysed using ImageJ and automatic particle analysis was performed with this software.

7.4 Atomic Force Microscopy

Atomic Force Microscopy (AFM) was employed both for the topographical characterization of surfaces, coatings and lithograpies performed during this thesis and for the study of the interfacial properties of coatings and patterns at the local scale using force-distance (F-d) curves.

The Agilent 5500 AFM/SPM microscope was used combined with PicoScan5 software. The instrument is placed on an anti-vibrations table and enclosed in a vibration isolation chamber to isolate the AFM form external vibrations, air turbulence and acoustic noise. An integrated video system was used to locate the areas of interest and align the laser on the probes.

Two multi-purpose scanners were used: a large scanner, with 7.5 μm z scan range (90 μm × 90 μm x-y range) and a smaller one, with z scan range 1.6 μm (10 μm × 10 μm x-y range). An external X-Y positioning system (closed loop, NPXY100E from nPoint, USA) was used; this system is integrated in the microscope and ensures scanning linearity and position accuracy within a scanning range of 100 μm × 100 μm (linearity error 0.03% and precision 0.5 nm) while significantly reducing the data acquisition time. The samples were mounted on the closed-loop sample holder and fixed using double-sided tape.

The Agilent 5500 can be operated in a variety of imaging modes, contact mode AFM and intermittent contact mode (tapping or AC mode) AFM were used in this thesis. AFM image processing and rendering was done using open source software, WSxM software (version 3.1, Nanotec Electronica, Spain)[1] and Gwyddion data analysis software (version 2.26).[2]

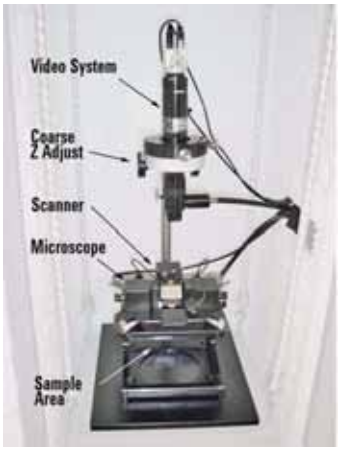

Figure 7.1 Picture showing the components of the Agilent 5500 AFM/SPM microscope.

Local adhesion measurements: (F-d) curves

The interaction of an AFM tip with differently coated surfaces was measured during this thesis. For that, the large AFM scanner was used and a contact mode probe was mounted on the probe holder. Then the laser was positioned at the end of the cantilever and the reflected laser was aligned on the photodiode (0V lateral deflection, -0.1V vertical deflection). The tip was then brought into contact with the surface and retracted 1 μm away from it right after contact was made. Then, the Force Spectroscopy tool of the software was used to record deflection vs. distance curves. The piezo displacement range was determined by trial and error until the surface distance was found. The position of the tip was changed after each measurement and the procedure was repeated in several areas of the samples. The F_{adh} for each of the curves was extracted from the jump-out of the tip during the retraction movement and the results were represented as histograms to obtain mean values.

To perform F-d measurements on specific locations of a surface, the FlexGrid tool of the software was used. The FlexGrid is a Volume Spectroscopy tool that combines AFM imaging and force spectroscopy. It allows to mark up to 25 locations (XY coordinates)

anywhere in an AFM image and record at those locations one or more force-distance curves from a single or multiple approach-retract cycles of force spectroscopy during scanning. Figure 7.2a and b show the positions where the F-d curves would be recorded in an image, and the possibility of placing them anywhere in the scanning area. The dot-like feature arrays or areas of either PDA or **Y1** patterned on surfaces were located by first scanning the surface in contact mode. Then, the markers were positioned on the image to determine the points where the F-d curves were recorded and the height range of the piezo was set. The measurements were performed both inside and outside the dot-like features (Figure 7.2c) and then the F-d curves were analysed separately to determine the F_{adh} in each point. Whenever possible, only a part of the array was scanned in order to reduce contamination and the position of the rest of the features was determined from there.

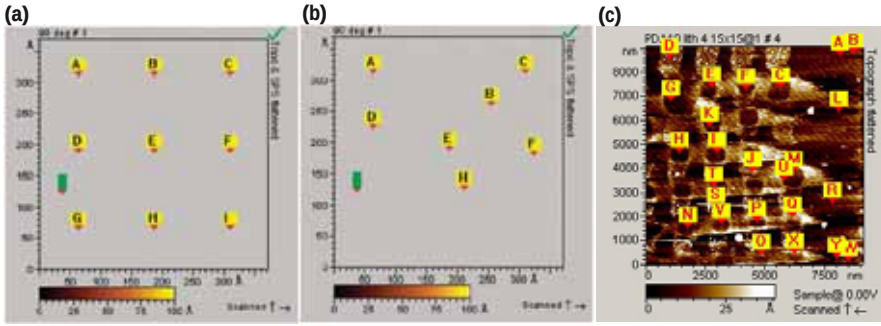

Figure 7.2 Panels (a) and (b) show the FlexGrid markers and and how they can be positioned anywhere in the scan area. (c) Example of a FlexGrid experiment on a PDA array showing the points of the scan where the F-d curves were recorded.

After the adhesion experiments, all the cantilevers were calibrated. Several methods have been described with that purpose.[3] In our case, the sensitivity of the setup (in nm/V) was determined by pressing the used tip over a Si/SiO_2 surface and recording the deflection of the cantilever in the process, we considered that no elastic deformations can occur and therefore the displacement of the piezoelectric actuator was directly proportional to the cantilever deflection. The spring constant of the cantilever (k, in N/m) was determined assuming a linear relationship between k and the cantilever's resonance frequency (f, in kHz). The real f was obtained from the measurement of the maximum resonance frequency and interpolated in the range of frequencies and k provided by the manufacturer.[4] (See Figure 7.3)

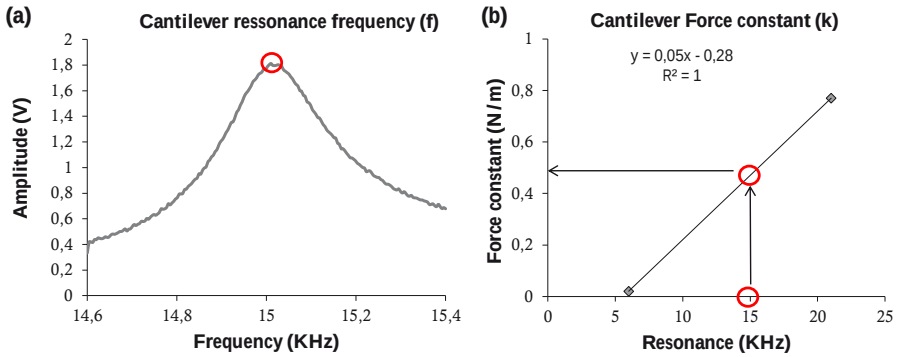

Figure 7.3 Steps followed to calibrate the tips used for Fadh measurements. (a) The resonance frequency was measured and the value was interpolated in the Force constant vs. Resonance (b) plot to obtain the spring constant of the cantilever.

Description of AFM probes

For the topographical characterization of samples, intermittent contact mode AFM was performed using Non-Contact High Ressonance frequency tips (PPP-NCHR, Nanosensors). These probes have beam-shaped cantilevers with nominal force constants of 42 $N \cdot m^{-1}$ and a resonance frequency of ~330 kHz. The sharp tips have asymmetric pyramidal shape of high aspect ratio and 7 nm tip radius (Figure 7.4).

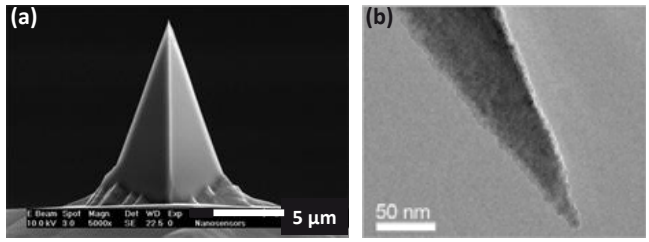

Figure 7.4 (a) SEM and (b) TEM micrographs of the AFM probes used for tapping mode imaging. The tips used for contact mode and F-d curves have the same shape and only the cantilever dimensions change. Reproduced from http://www.nanoandmore.com/

To perform the Force-distance measurements and contact mode AFM images contact mode probes (PPP-CONTR, Nanosensors) were used. These cantilevers have very low force constant values of only 0.2 $N \cdot m^{-1}$ which provide high sensitivity. The tips have 7 nm tip radius.

All the probes are fabricated in n^+-silicon and have a thin alluminum coating at the back of the cantilever to enhance the reflectivity of the laser beam.

7.5 Direct-write AFM-assisted lithography

Direct-write AFM lithography was carried out using the Nscriptor™ DPN System or the DPN 5000 System from Nanoink (Chicago, Illinois). Dip-Pen Nanolithography, DPN® is a patented patterning process that makes use of Nanoink's products to structure functional materials on surfaces using a tip as a delivery system.

The Nscriptor™ DPN system was the first member of the family of Nanoink's nanofabrication instruments and consists of a modified AFM controlled by specific software (InkCAD™) optimized for the DPN® process. The Nscriptor™ uses a closed-loop scanner with inductive position sensors that provide optimum control over the position of the tip (linearity error 1% precision of 10 nm and scan range 90 μm × 90 μm). The design of the instrument and the software allows us to create complex patterns using the lithographic tools and examine them in-situ thanks to the AFM imaging modes included in the software (contact and intermittent contact mode). During lithography the scanner lifts the tip up to 10 μm from the contact height between the elements in the pattern, in order to reduce the amount of undesirable ink drawn between the features. In addition, the Nscriptor™ is placed inside an environmental chamber that allows monitoring and controlling the environmental conditions (i.e. temperature and relative humidity) during the writing process. Also, using the integrated optics (resolution ~3μm) the position of the tip(s) relative to the sample can be controlled. The sample mounted on the sample stage (2.5 cm × 2.5 cm travel, 2 μm minimum step) was fixed using double-sided tape (Figure 7.5).

The Nscriptor™ offers the possibility of working in both constant height mode and constant force mode. During this thesis, both writing modes have been employed. In constant force mode the z-position of the tip is controlled by the displacement of a laser that is reflected in the back of the cantilever, as a classical AFM would do when operating in contact mode. This writing mode was employed for the patterning of the catechol-terminated thiol **3** and required that the tip was functionalised before being mounted on the instrument (see Section 4.5.1.4 for a detailed description of the tip functionalization procedure). Then the functionalised tip was inserted in the tip holder and the laser was positioned at the back of the cantilever. The reflected laser was then aligned on the photodetector and the tip was brought into contact with the substrate. Then the lithographic patterns could be fabricated thanks to the diffusion of the thiols through the water meniscus that naturally formes under environmental conditions.

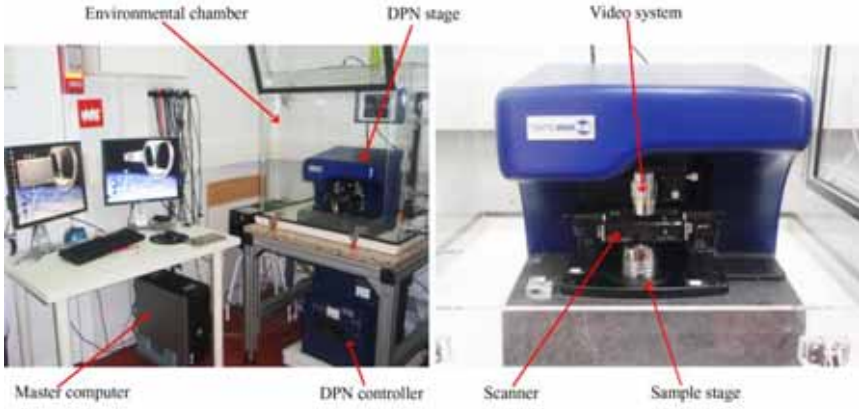

Figure 7.5 *Components of the Nscriptor™ DPN System.*

As opposite, for the obtention of PDA patterns and CPPs in situ the equipment was operated in constant height mode. In this mode the pen is not in feedback, and it remains at a user-controlled height optically determined by the cantilever deflection. In this case we followed a tip coating approach based on dip coating the tip into an ink solution for a given time using a commercial microfluidic system called Inkwell. The coated tips were immediately used in order to deliver the desired amount of the ink solution onto a surface in the form of droplets that, after evaporation of the solvent(s), gave place to the desired patterns.

An example of a deposition procedure using liquid ink and a multiple cantilever array is shown in Figure 7.6.[5] First, the pens are dipped in the ink solution using the microwells of an inkwell chip and kept there for a given time to functionalize the tips (Figure 7.6a). Then, the coated tips are brought into contact with the target surface. Initially, the excess of ink is reduced through cantilever and tip bleeding by bringing the coated tip into contact with the substrate surface (Figure 7.6b). Between depositions, the tips are displaced to new regions of the surface in order to avoid undesirable contact of the tips with already deposited drops. After few bleeding spots, the tip starts writing uniform (sub-)micron sized dots and the desired patterns can be written. In this example, twelve identical rectangular-shaped structures were created in a single step (Figure 7.6c).

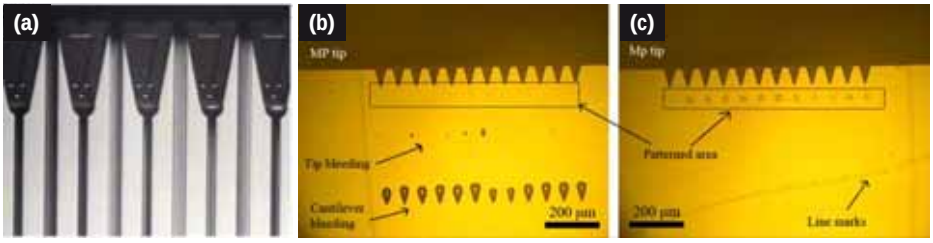

Figure 7. 6 (a) Image captured with the integrated camera to the Nscriptor™ instrument during dipping MP-type tips into the microwells of an inkwell. Panels (b) and (c) show optical images captured during direct-write AFM lithography experiments. Bleeding drops delivered to eliminate the excess of ink coating the tip are indicated in the image in (c). After the excess ink is removed, MP tips fabricate well-defined arrays which can be distinguished on the image by the presence of rectangular-shaped shadows (the patterned area is indicated on the image). These experiments were performed in our lab by Dr. E. Bellido using a ferritin-based ink. Reproduced from ref. 5.

Description of the lithographic probes

Two types of tips were used for the direct-write AFM lithography experiments: single pen (SP) and multiple cantilever pen (MP). These tips are part of a full series of tips (also referred to as pens) that were specially developed by NanoInk to be used in their nanofabrication instruments (such as the Nscriptor™).

SP pens (also known as A-type single pens) feature two different cantilever configurations on each side of the pen chip. One side contains a "diving board" shaped cantilever (spring constant 0.041 $N \cdot m^{-1}$) suited for applications such as contact mode imaging or thiol patterning on gold surfaces. The opposite side contains an "A-frame" cantilever with a higher spring constant of ~0.1 $N \cdot m^{-1}$ specially designed for patterning viscous liquids. The tips exhibit a tip radius of ~15 nm and a symmetric pyramidal shape of low aspect ratio. During this thesis, SP pens with "diving board" shaped cantilevers were used to pattern the catechol-terminated thiol (**3**) on gold surfaces whilst the "A-frame" shaped ones were used to pattern polydopamine precursors (Figure 7.7).

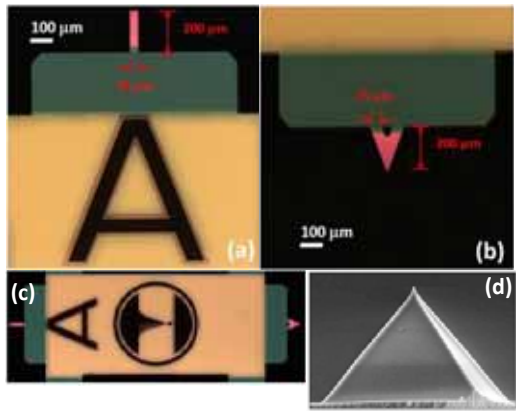

Figure 7.7 Optical images of an SP pen and the dimensions of the cantilevers (a) "Diving-board" shaped cantilever (b) "A-frame" shaped cantilever (c) Configuration of the A-type single pen (d) FE-SEM image of the tip. Reproduced from Nanoink's product datasheet.

Multiple cantilever arrays (also called passive pen arrays, parallel-probe cantilever arrays or M-type pens) were developed to increase the throughput of direct-write AFM lithography thanks to an inherent parallel fabrication process. They also allow the tips to be loaded with different inks for multiplex writing. MP pens consist of two groups of 12 parallel silicon nitride probes. As in SP pens, two cantilever configurations are featured although, during this thesis, only A-frame cantilevers were used. The probes show a force constant of ~0.5 $N \cdot m^{-1}$ and the separation between them is ~ 66 µm, they exhibit a tip radius of ~ 15 nm and a symmetric pyramidal shape of low aspect ratio (Figure 7.8a). Like SP tips, they are optimized for patterning viscous liquids and further modified with a recessed area surrounding the tip to increase loading of ink and extend printing times (Figure 7.8b). MP pens were used during this thesis to pattern polydopamine precursors and to create confined nano-reactors to obtain CPPs in situ.

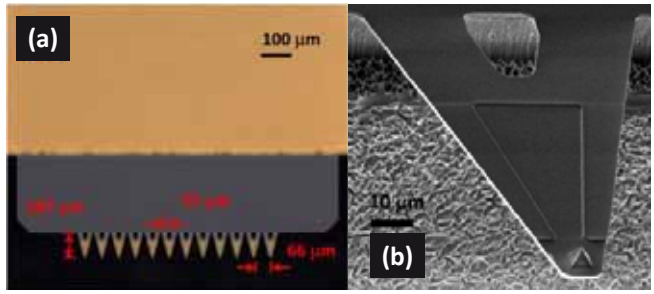

Figure 7.8 (a) Optical image of an MP pen array (A-shaped cantilevers) and its dimensions (b) FE-SEM image one of the cantilevers showing the recessed area surrounding the tip. Reproduced from Nanoink's product datasheet.

When these cantilever arrays are used it is crucial to ensure that the twelve tips are precisely aligned with the Inkwell surface (during coating step) and substrate surface (during deposition step). For this, leveling can be optically determined and corrected by viewing the relative deflection between cantilevers and performing leveling operations using a three z-axis motor leveling system in the Nscriptor™ instrument.

Description of the Inkwells

The controlled coating of the tips with polar ink solutions was performed following standard NanoInk inking routines using a microfluidic ink delivery chip-based system (Inkwell) developed and commercialized by NanoInk. This microfluidic system is specifically engineered to be filled with polar solvents such as aqueous ink solutions. A hydrophobic polymeric coating inhibits polar inks from spreading onto the chip substrate, while the channels, reservoirs and microwells remain uncoated and thus hydrophilic. In particular, we used M-6MW or M-12MW Inkwell chips specifically designed to be used with MP tips. The spacing between the microchannels is 66 μm, corresponding exactly to the spacing between the tips with "A-frame" shaped cantilevers. The Inkwell systems consist on 2 mm diameter reservoirs with a depth of 85 μm. The reservoirs are linked to the 20 μm diameter microwells *via* 40 μm wide channels that lead into 6 μm wide microchannels. These characteristics are identical in both Inkwell systems which only differ in the amount of tips that can be functionalised simultaneously if all the reservoirs are loaded with ink (six tips for the M-6MW Inkwell chip and 12 tips for the M-12MW). In some experiments, a different model of Inkwell with the same channel configuration but lacking the microwells was also used with the same purpose (Figure 7.9).

In a typical experiment, the reservoirs are filled with the same or different inks using a micropipette. Then, the ink solution is transferred by capillary action through the channels that connect the reservoirs with the microwells. The system was designed to keep the microwells full of ink, even if the ink supply slowly evaporates from the reservoir. In the final stage of the ink coating process, each tip is loaded with the desired ink by dipping the tips into the microwells for a given time and immediately used to create the patterns.

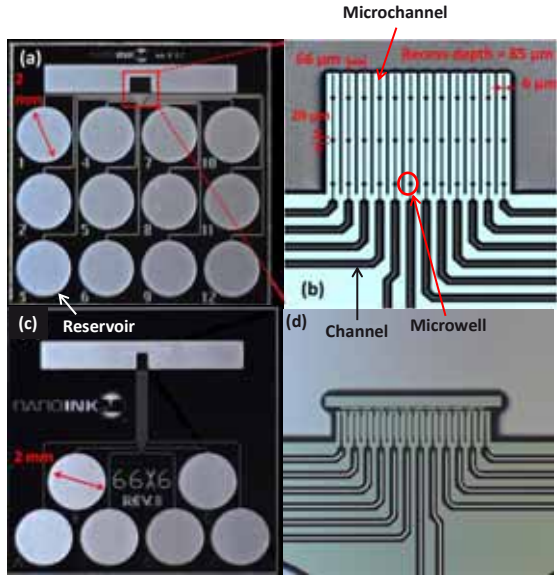

Figure 7.9 Optical microscope images of the Inkwell systems (a) M-12MW Inkwell overview with 12 reservoirs (b) Dimensions of the microchannels and microwells of the 12-channel Inkwell system (c) M-6MW Inkwell overview. The dimensions are the same as those of the 12-channel one. Reproduced from Nanoink's product datasheet.

7.6 References

(1) Horcas, I.; Fernández, R.; Gómez-Rodríguez, J. M.; Colchero, J.; Gómez-Herrero, J.; Baro, a. M. *Rev. Sci. Instrum.* **2007**, *78*, 013705.

(2) Gwyddion – Free SPM (AFM, SNOM/NSOM, STM, MFM, …) data analysis software. http://gwyddion.net/.

(3) Cappella, B.; Dietler, G. *Surf. Sci. Rep.* **1999**, *34*, 1–104.

(4) Segura, J. J. Ph.D. Thesis, Universitat Autónoma de Barcelona, 2012.

(5) Bellido, E. Ph.D. Thesis, Universitat Autónoma de Barcelona, 2011.

Annex

Additional spectra

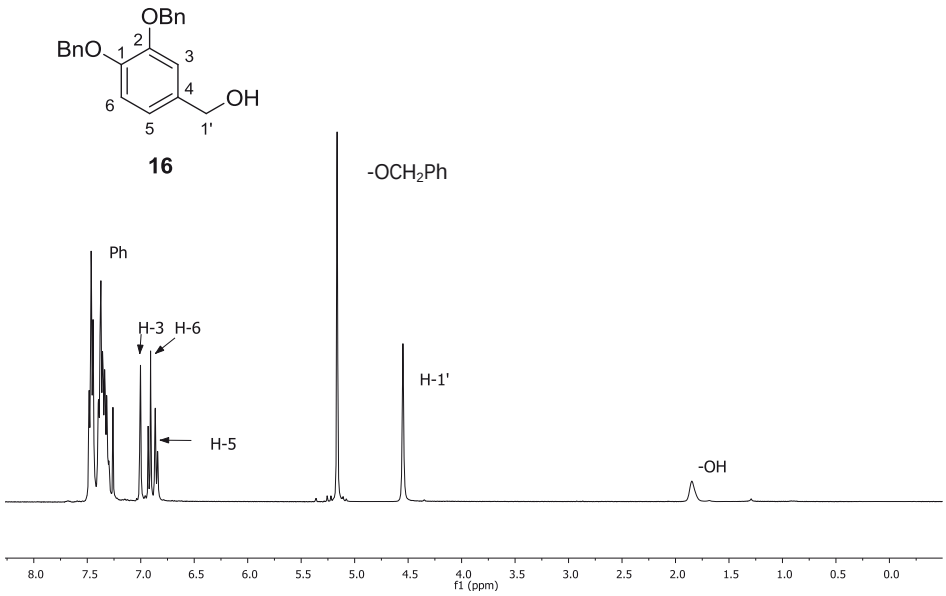

^{1}H NMR (360 MHz, $CDCl_3$)

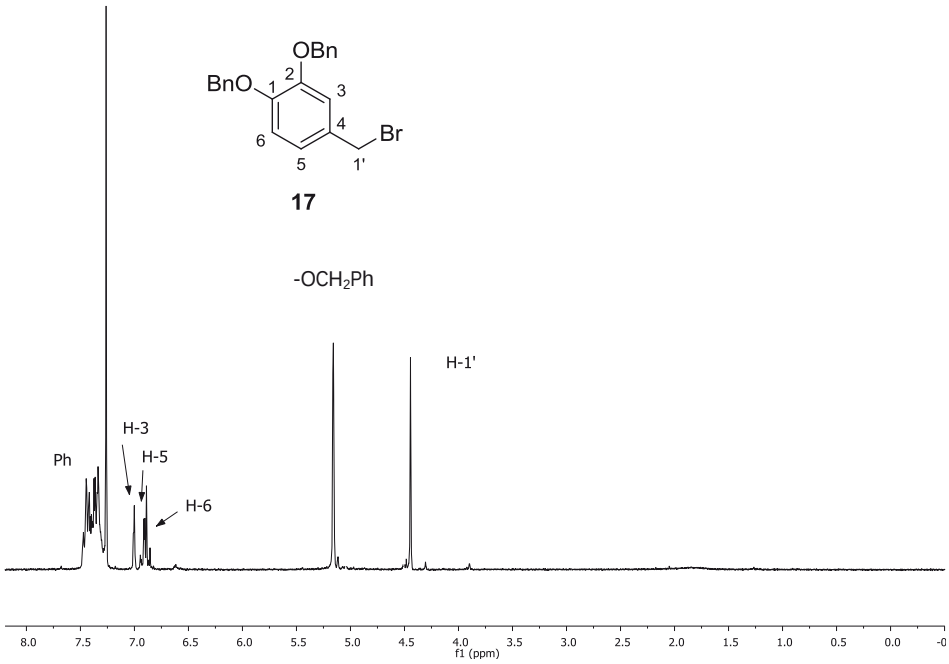

^{1}H NMR (250 MHz, $CDCl_3$)

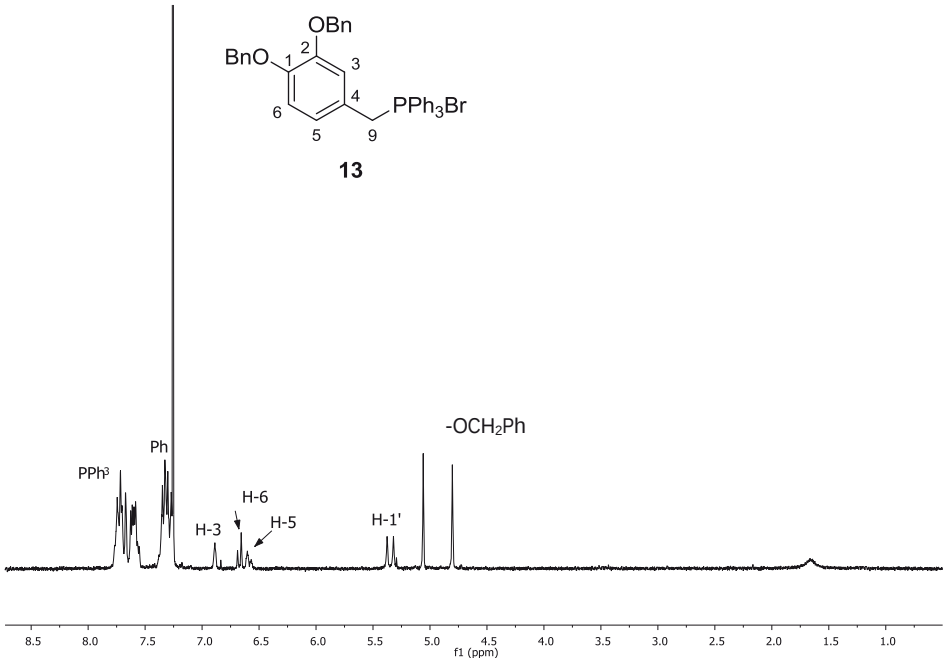

^{1}H NMR (250 MHz, $CDCl_3$)

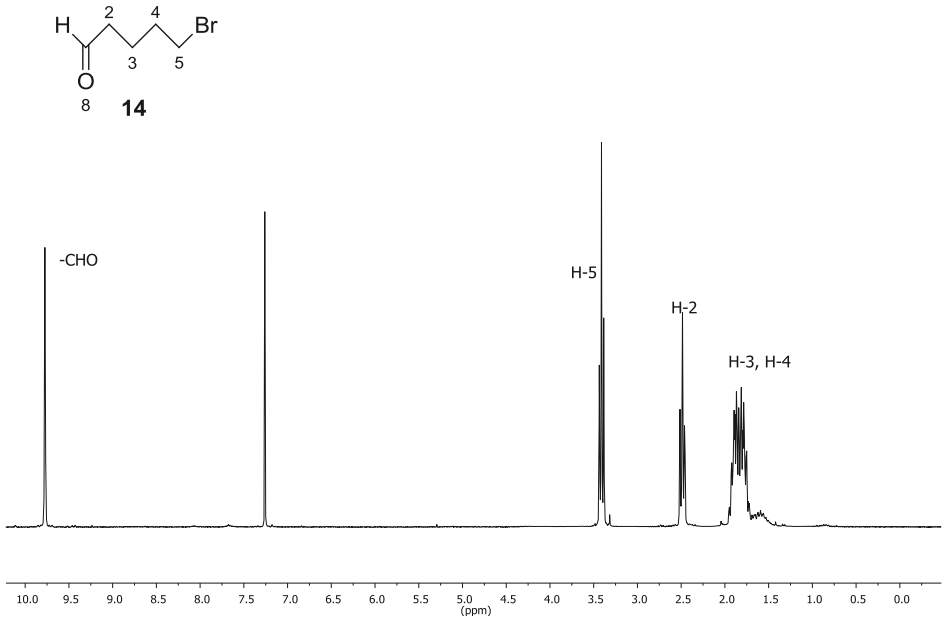

^{1}H NMR (250 MHz, $CDCl_3$)

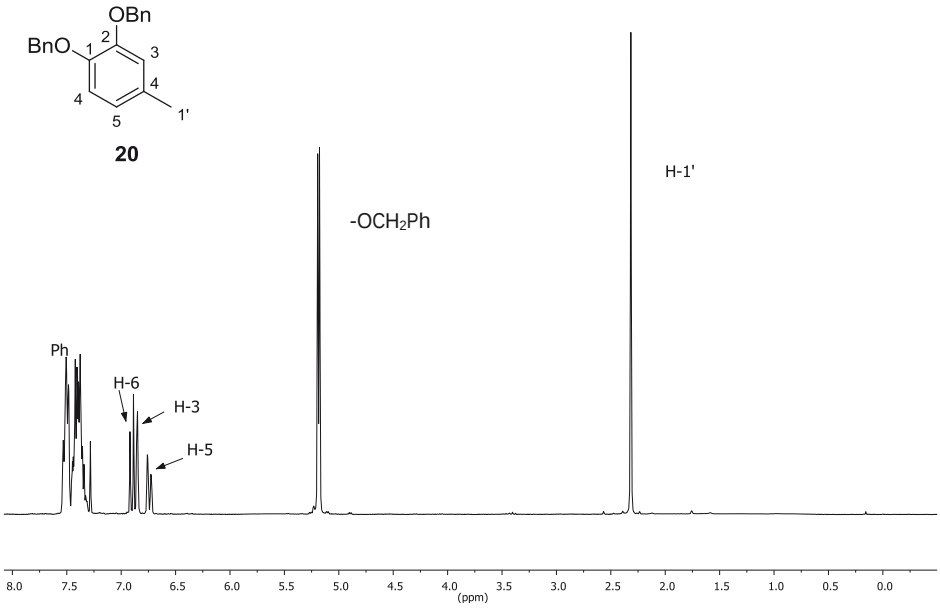

^{1}H NMR (360 MHz, $CDCl_3$)

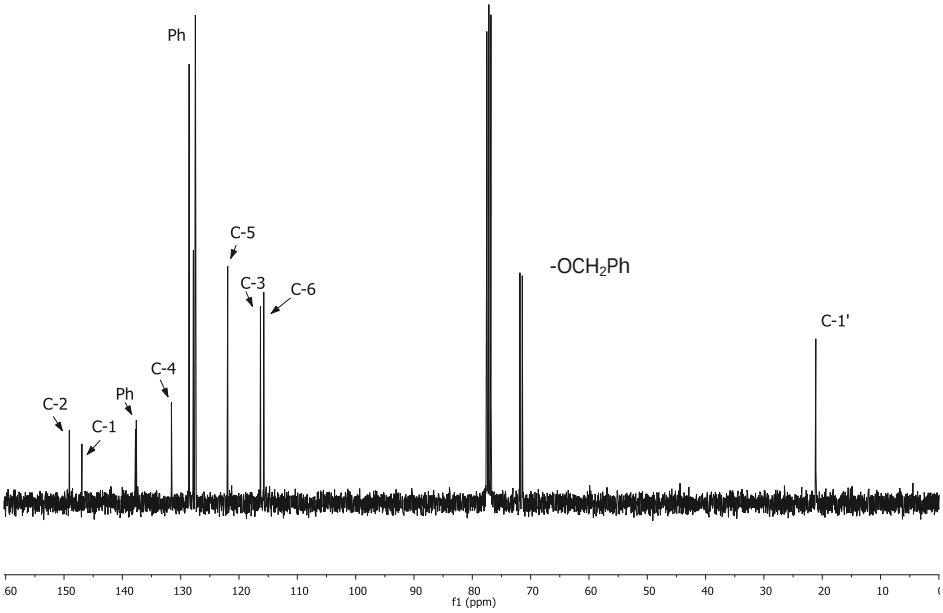

^{13}C NMR (91 MHz, $CDCl_3$)

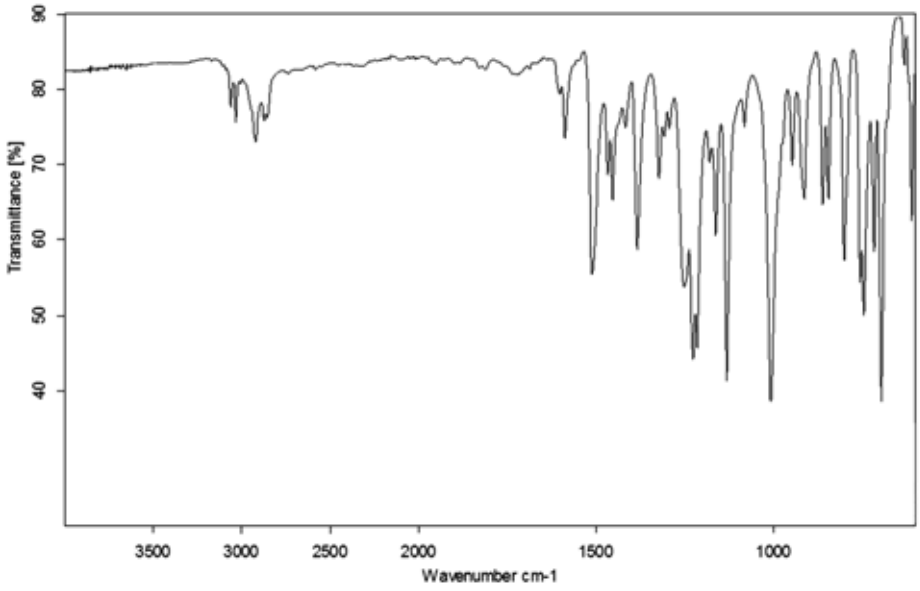

IR (ATR)

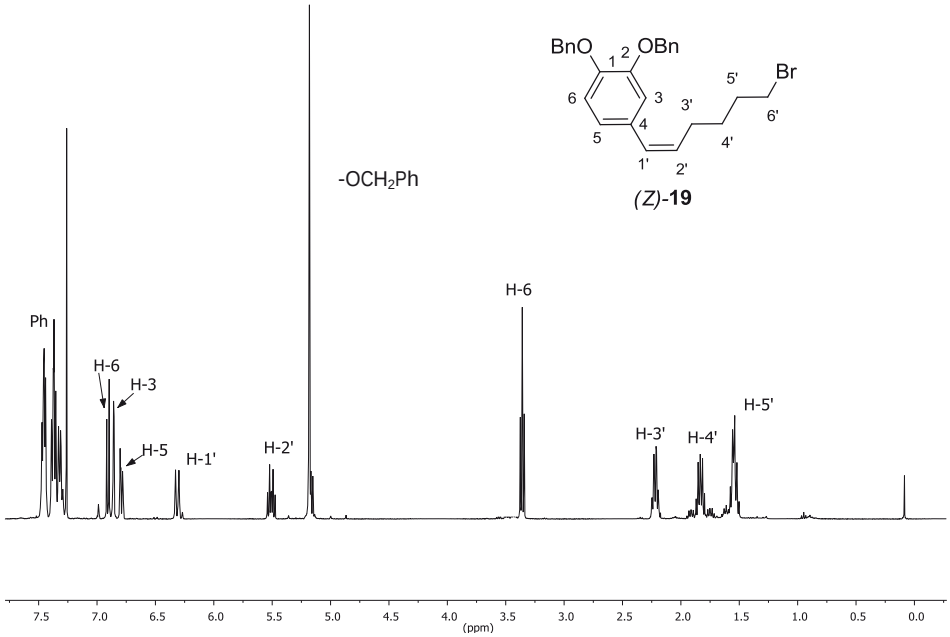

^{1}H NMR (400 MHz, $CDCl_3$)

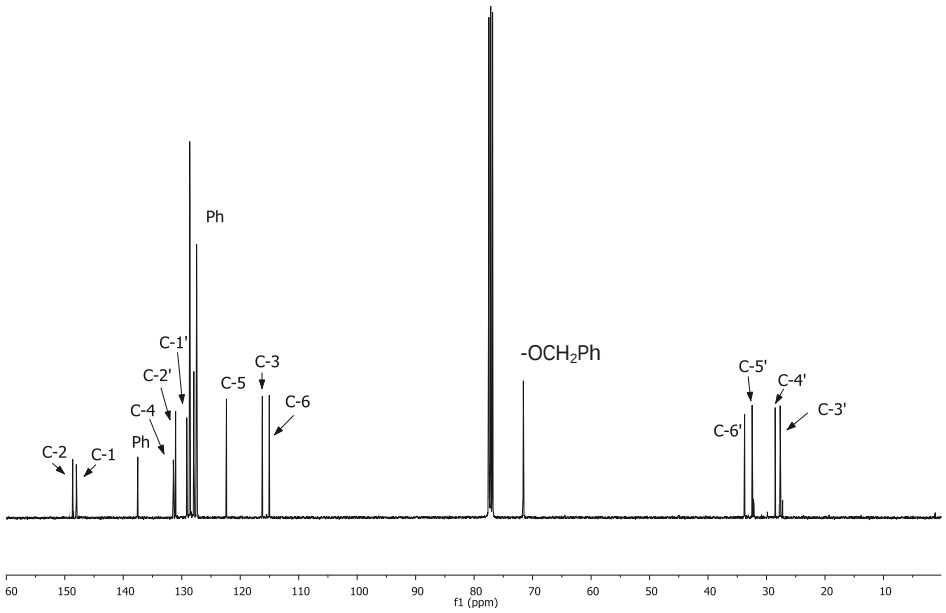

^{13}C NMR (101 MHz, $CDCl_3$)

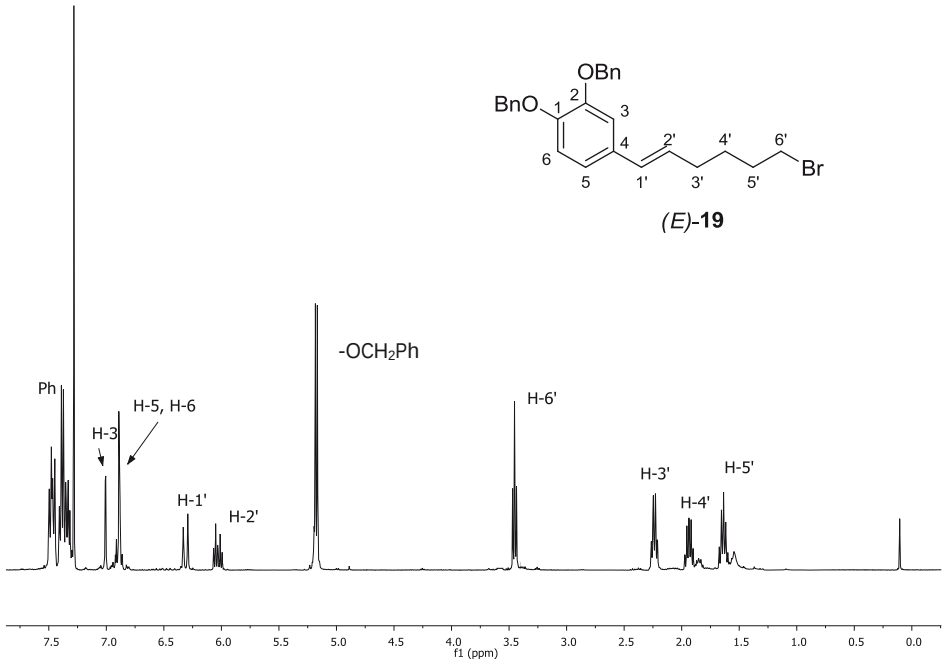

(E)-**19**

^{1}H NMR (400 MHz, $CDCl_3$)

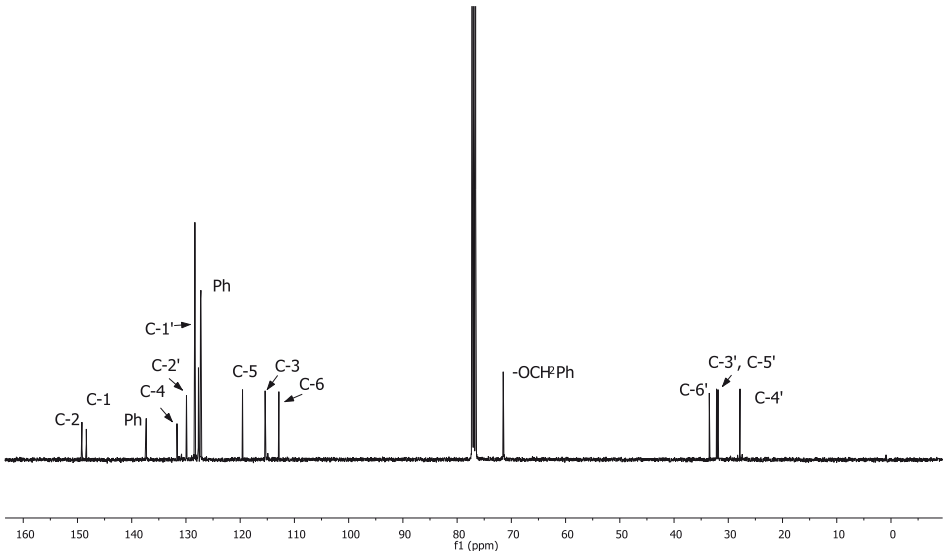

^{13}C NMR (101 MHz, $CDCl_3$)

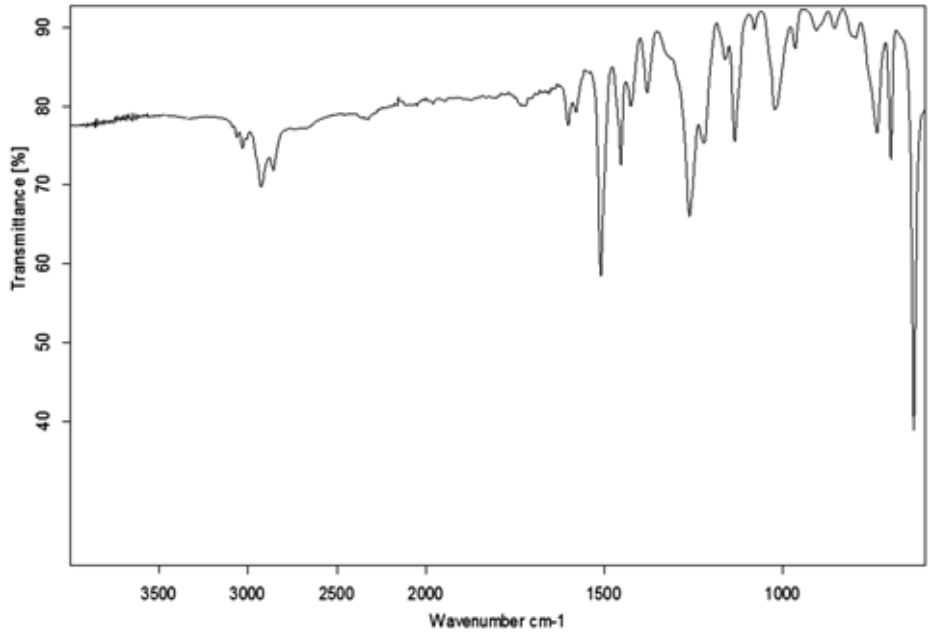

IR (ATR)

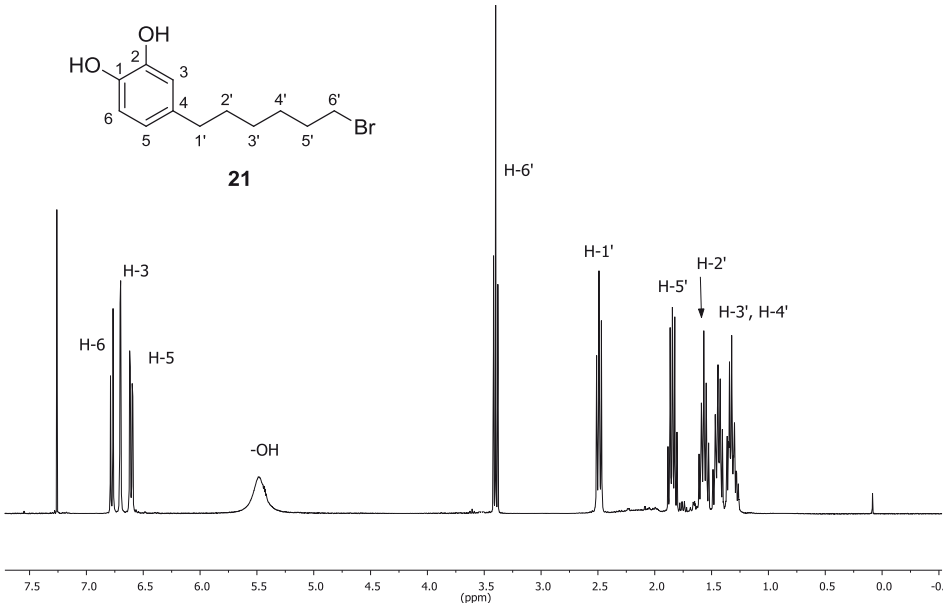

^{1}H NMR (360 MHz, $CDCl_3$)

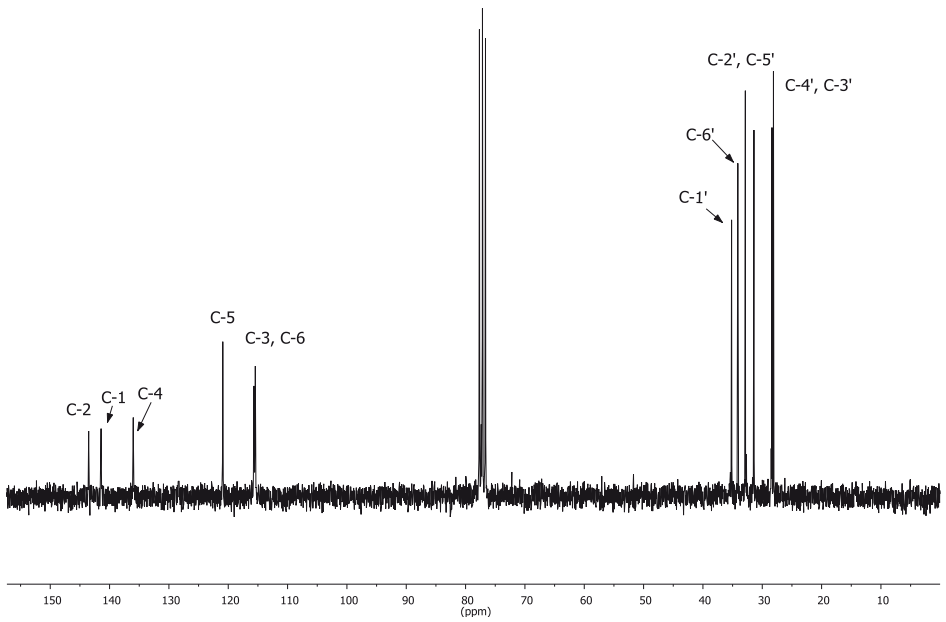

^{13}C NMR (63 MHz, $CDCl_3$)

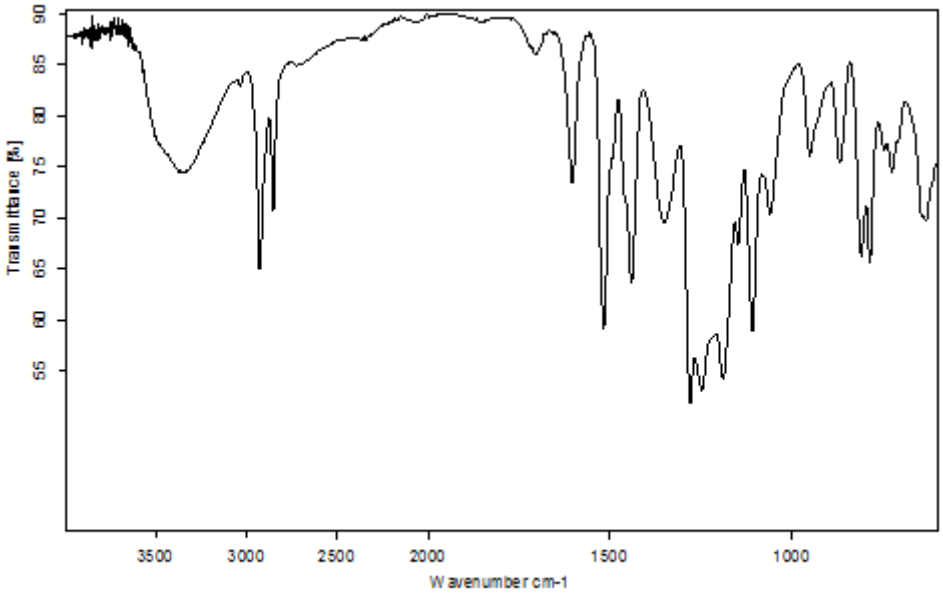
Transmittance [%]
90
85
80
75
70
65
60
55
3500
3000
2500
2000
1500
1000
Wavenumber cm-1

IR (ATR)

OH
OH
1
2
3
4
5
6
1'
2'
3'
4'
5'
6'
S
O

22

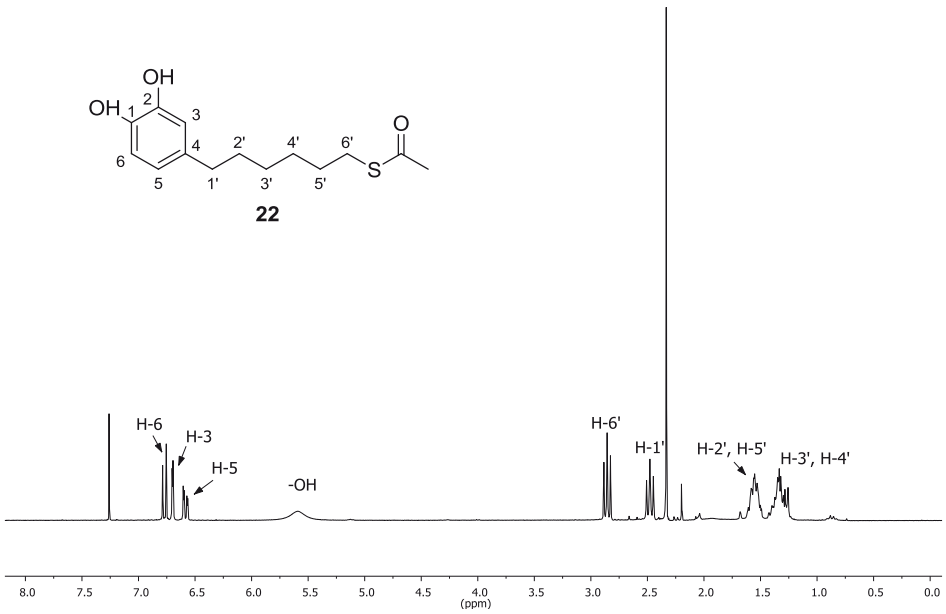
H-6
H-3
H-5
-OH
H-6'
H-1'
H-2', H-5'
H-3', H-4'
8.0
7.5
7.0
6.5
6.0
5.5
5.0
4.5
4.0
3.5
3.0
2.5
2.0
1.5
1.0
0.5
0.0
(ppm)

^{1}H NMR (250 MHz, $CDCl_3$)

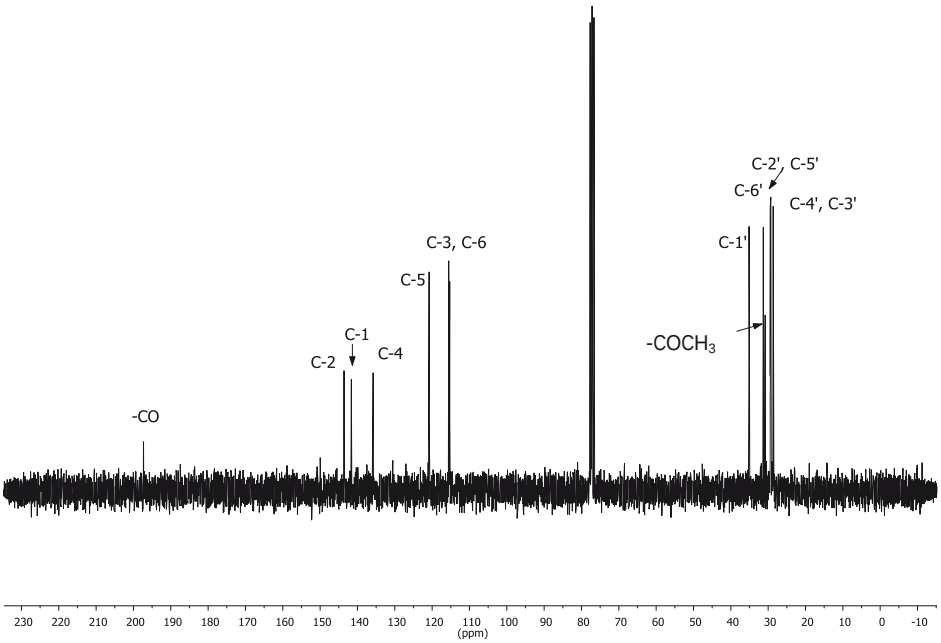

^{13}C NMR (63 MHz, $CDCl_3$)

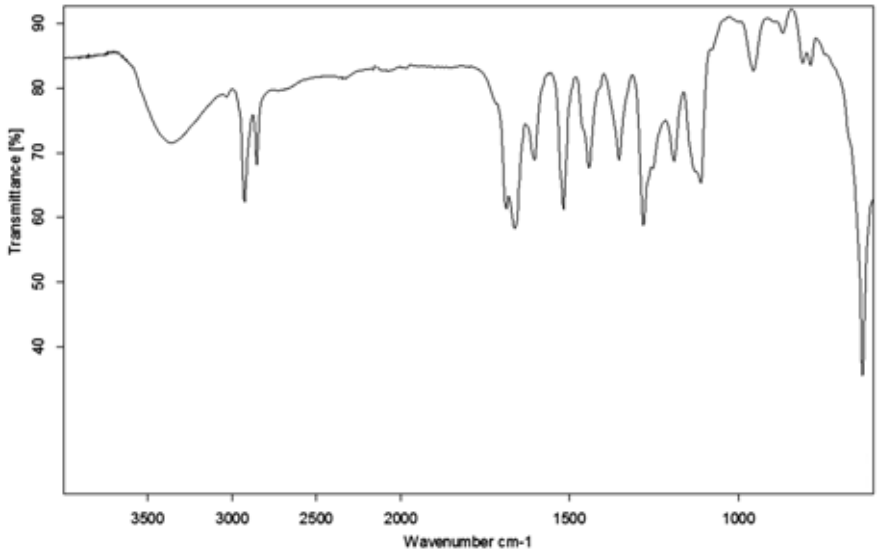

IR (ATR)

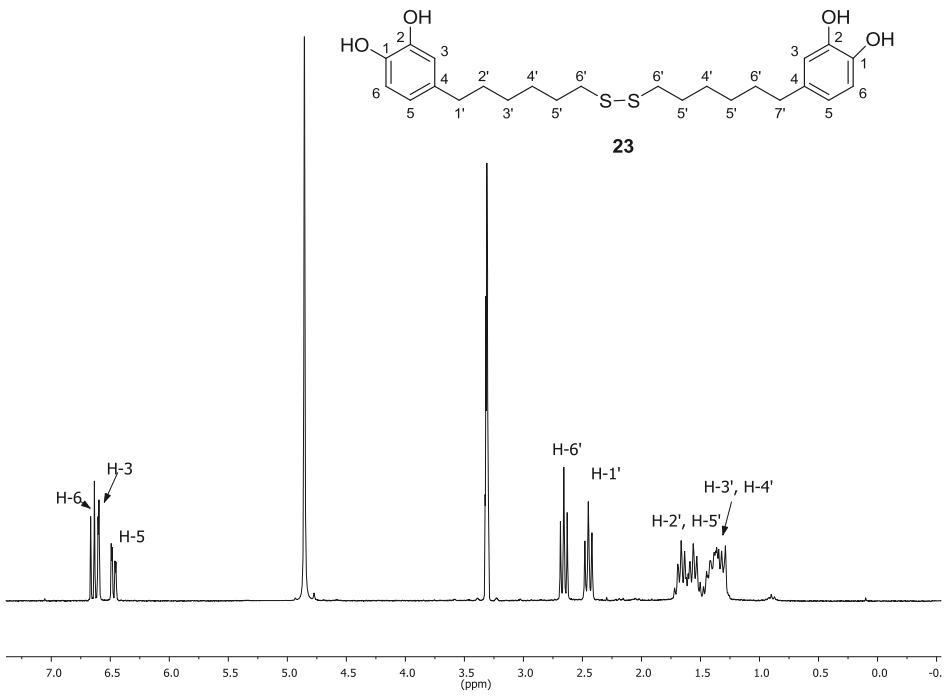

^{1}H NMR (250 MHz, $CDCl_3$)

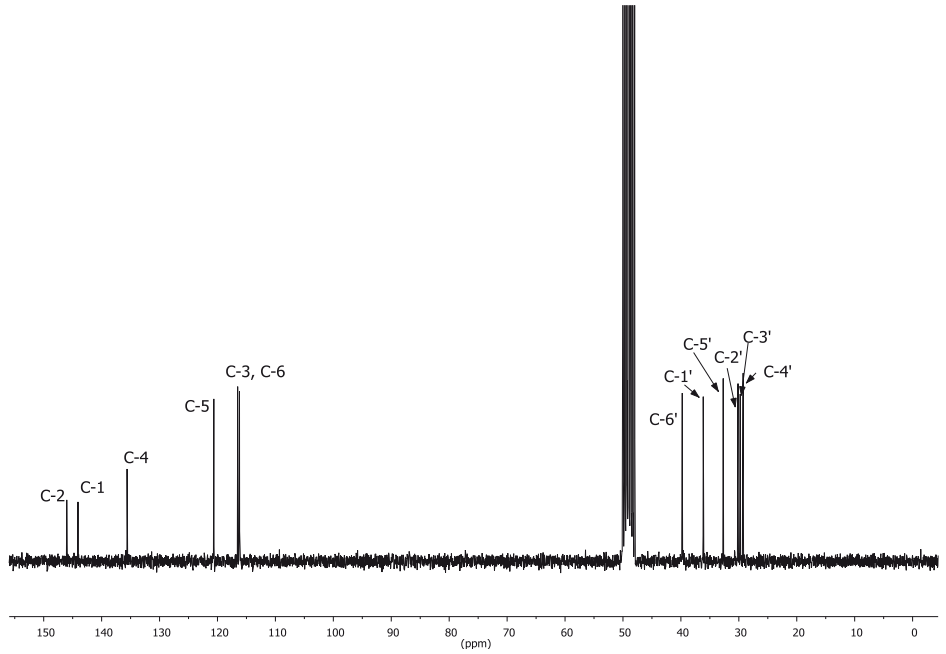

^{13}C NMR (63 MHz, $CDCl_3$)

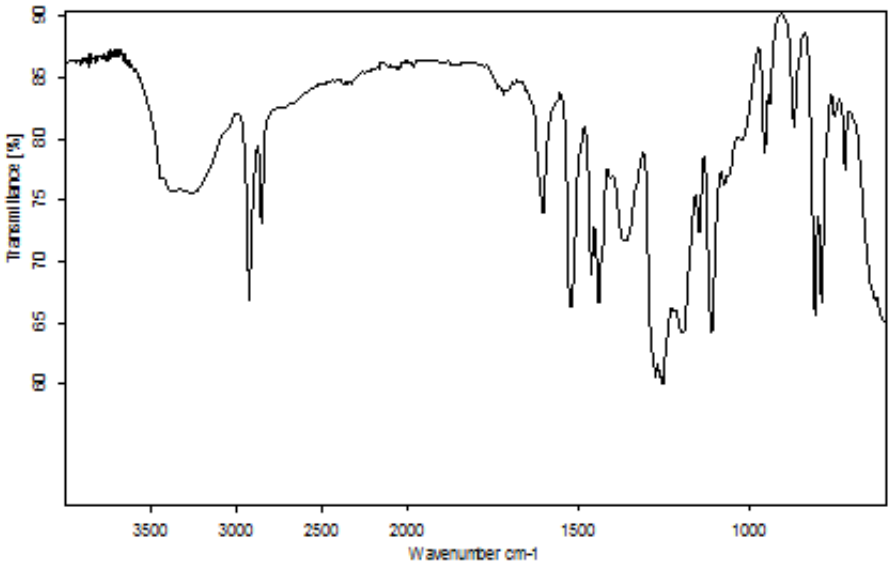

IR (ATR)

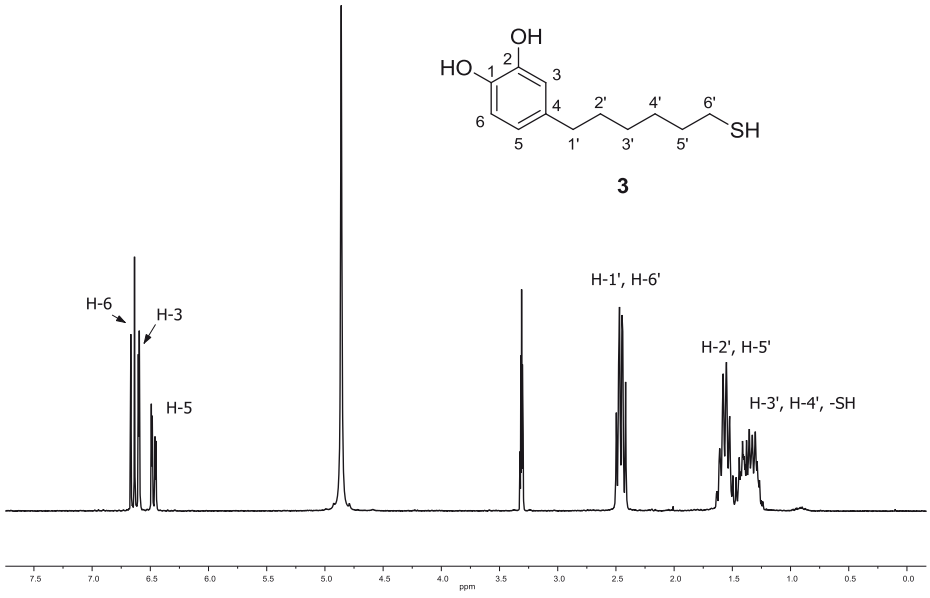

^{1}H NMR (400 MHz, MeOD)

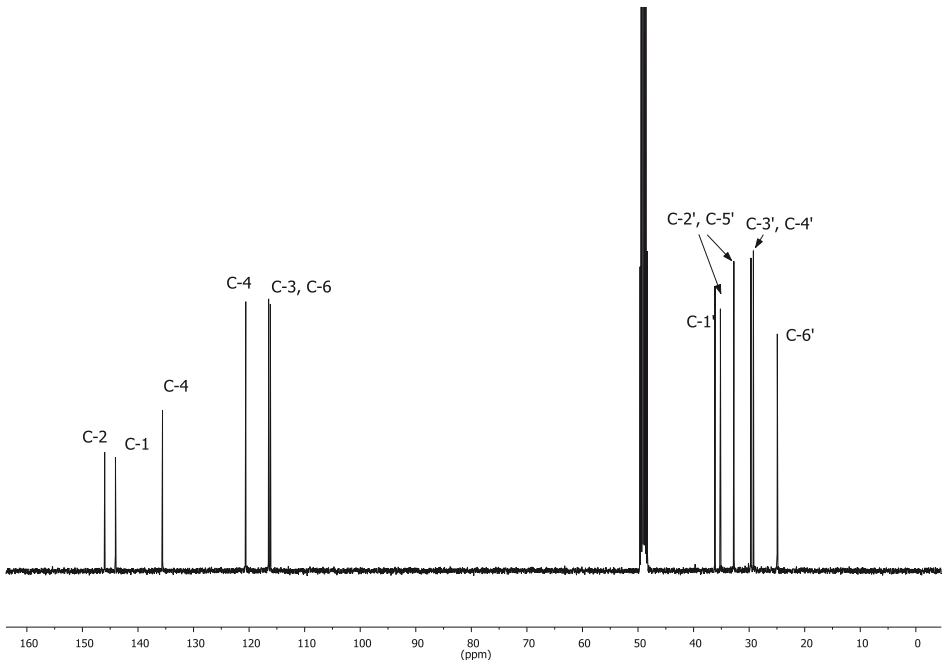

^{13}C NMR (101 MHz, MeOD)

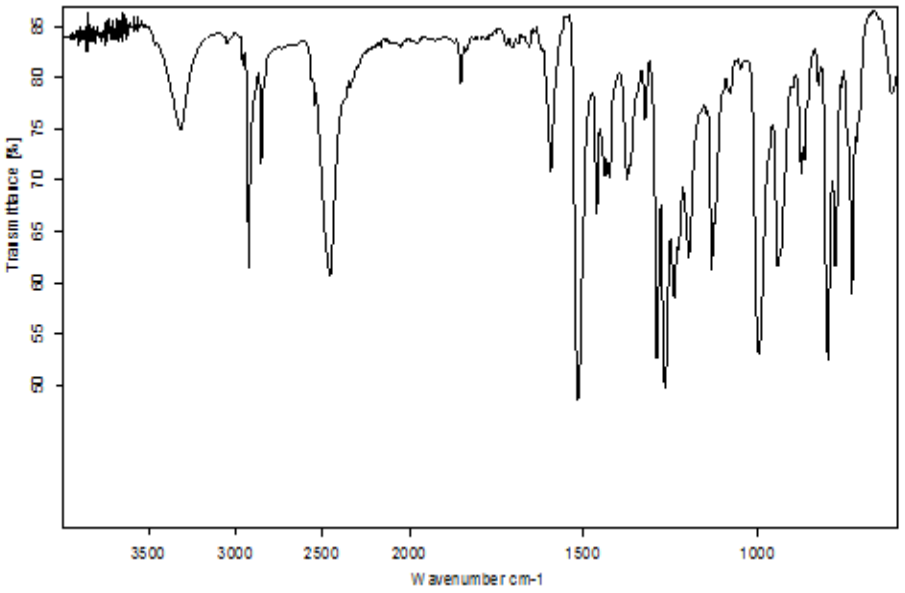

IR (ATR)

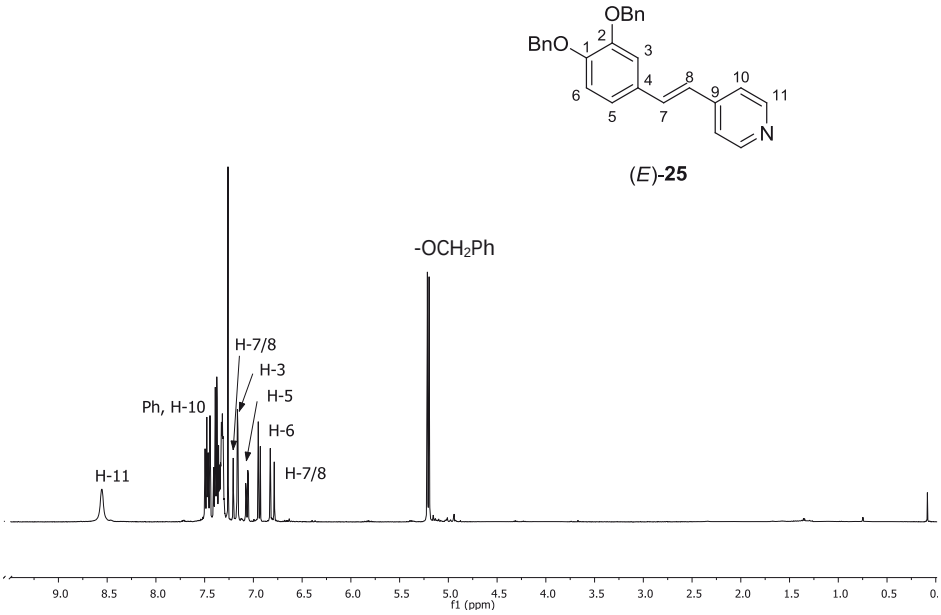

^{1}H NMR (400 MHz, MeOD)

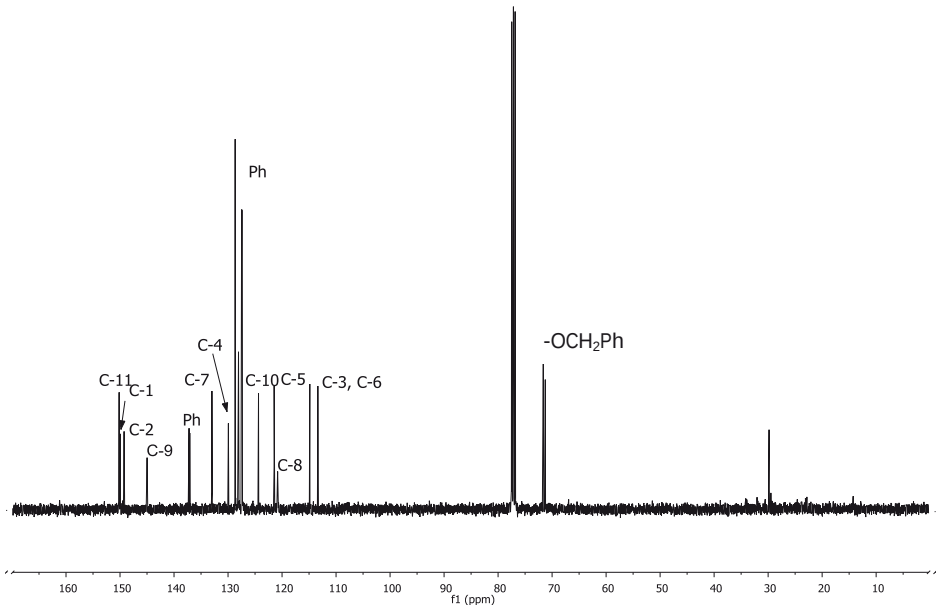

^{13}C NMR (101 MHz, MeOD)

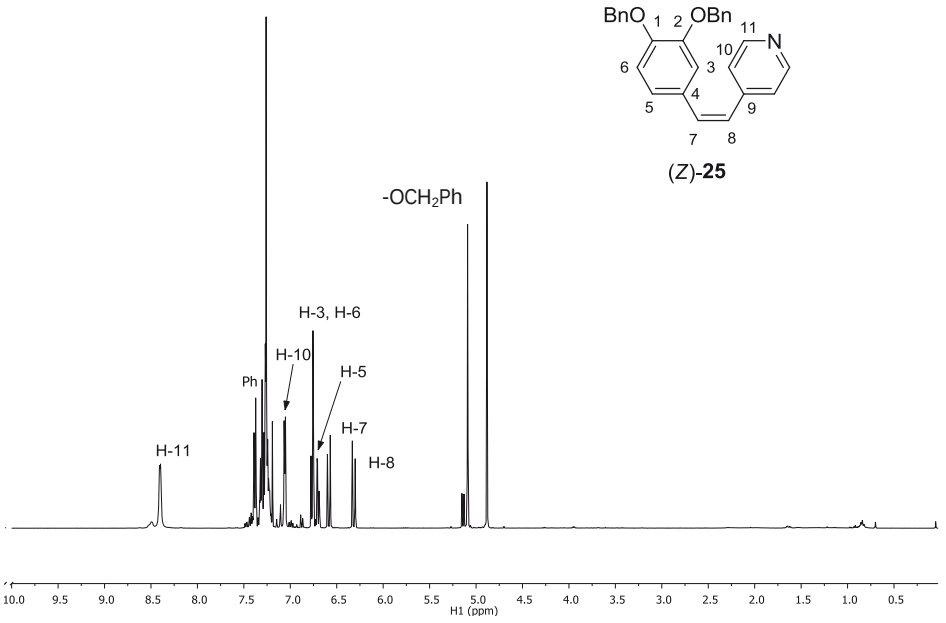

^{1}H NMR (400 MHz, MeOD)

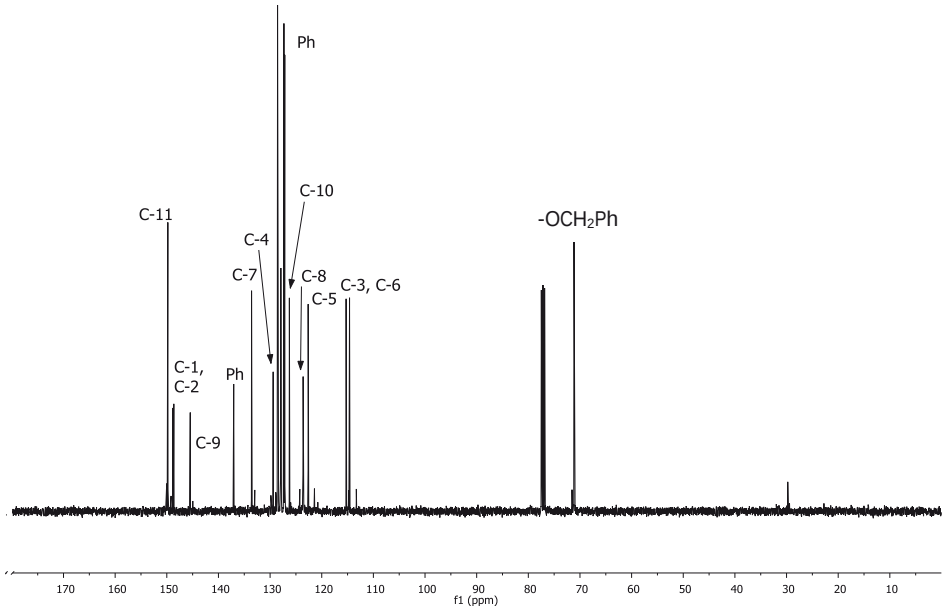

^{13}C NMR (101 MHz, MeOD)

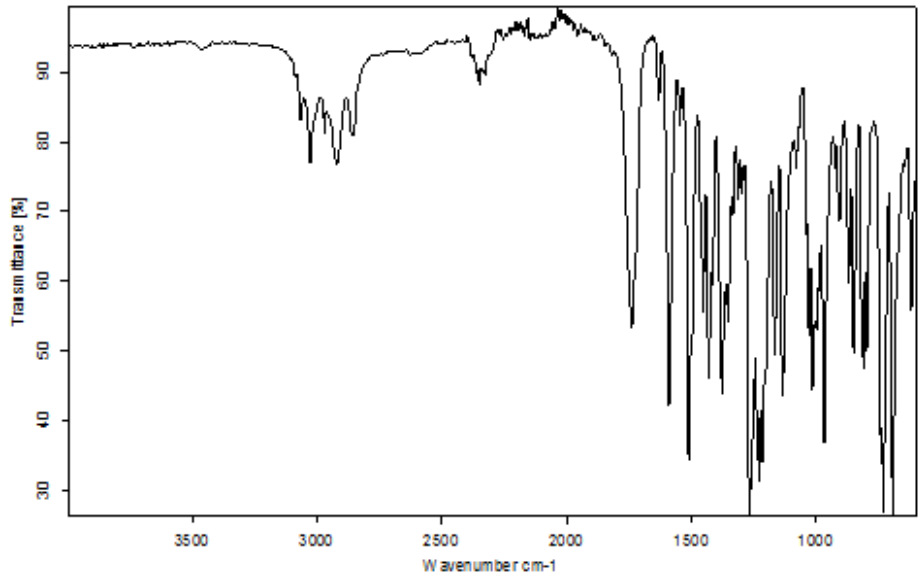

IR (ATR)

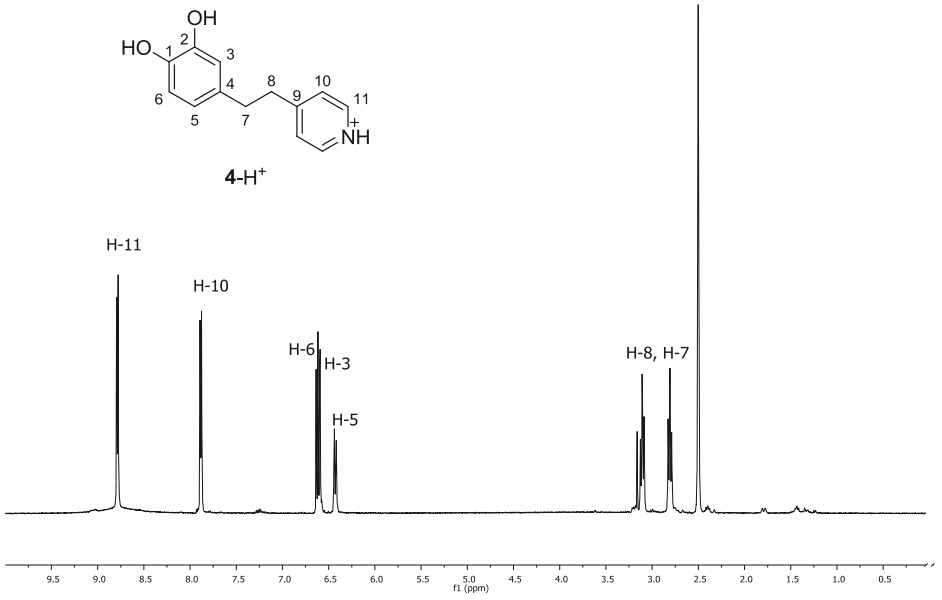

^{1}H NMR (400 MHz, MeOD)

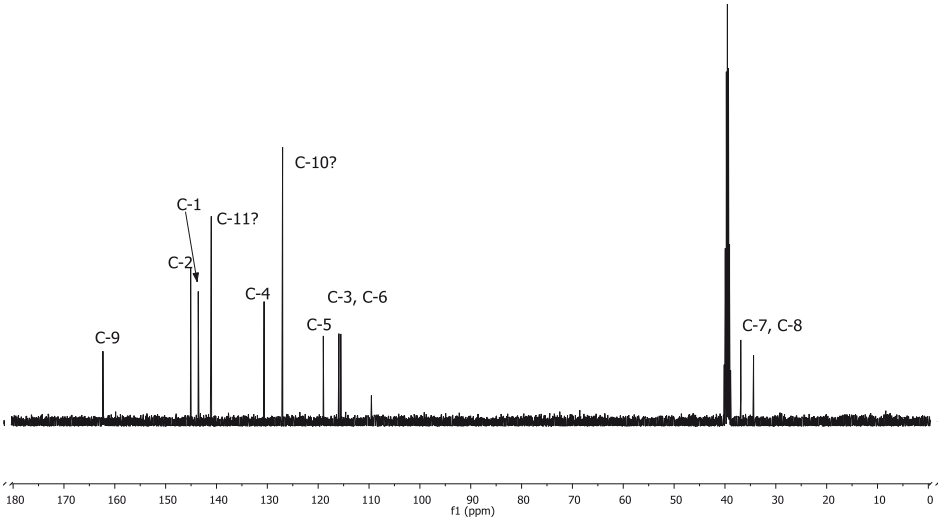

^{13}C NMR (101 MHz, MeOD)

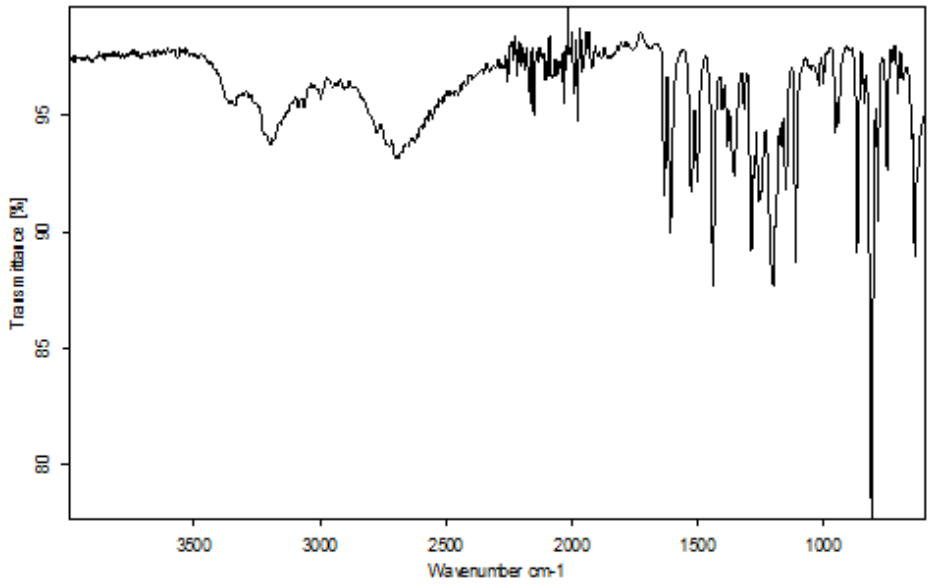

IR (ATR)

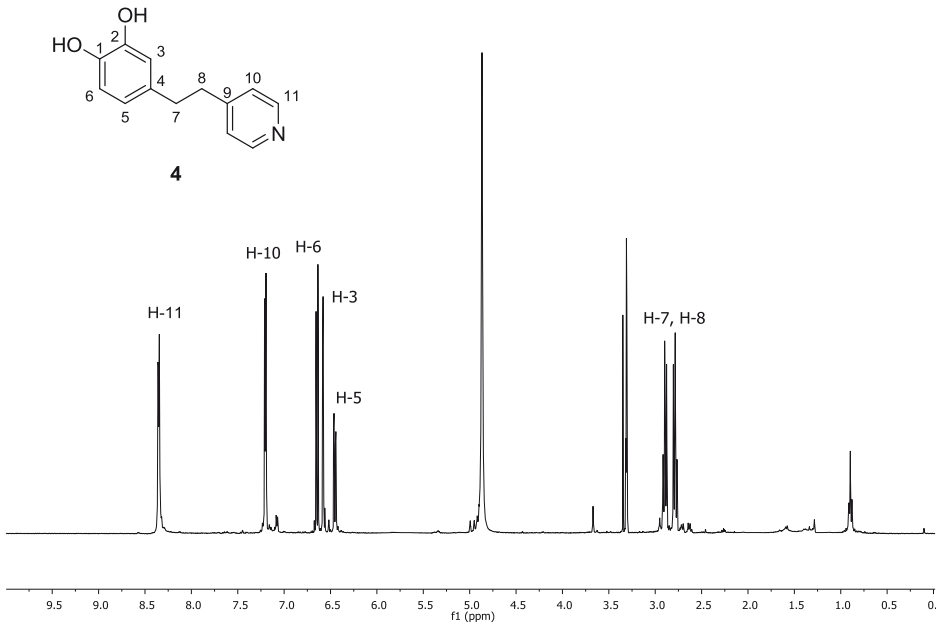

^{1}H NMR (400 MHz, MeOD)

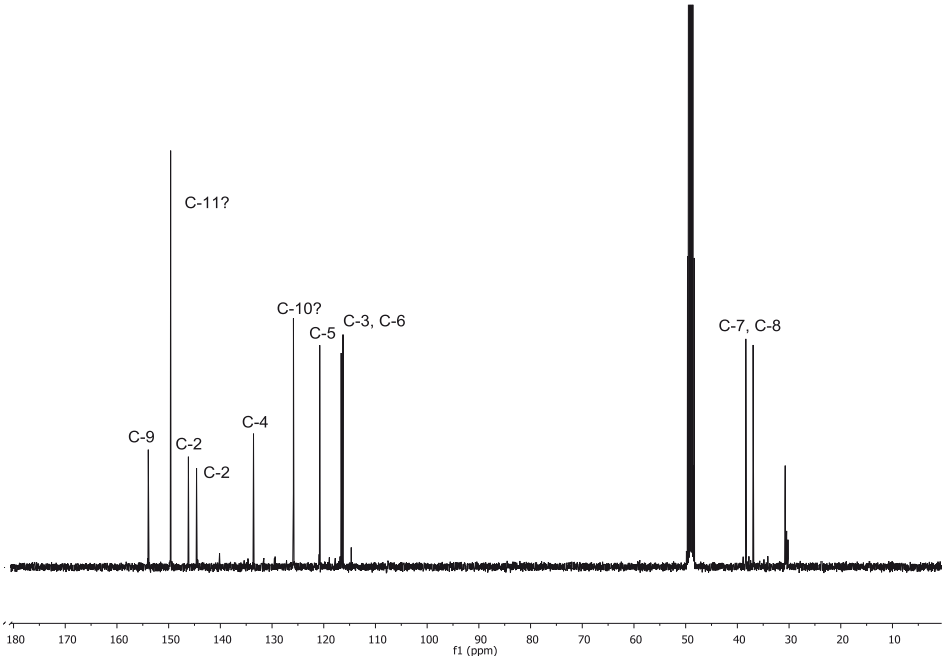

^{13}C NMR (101 MHz, MeOD)

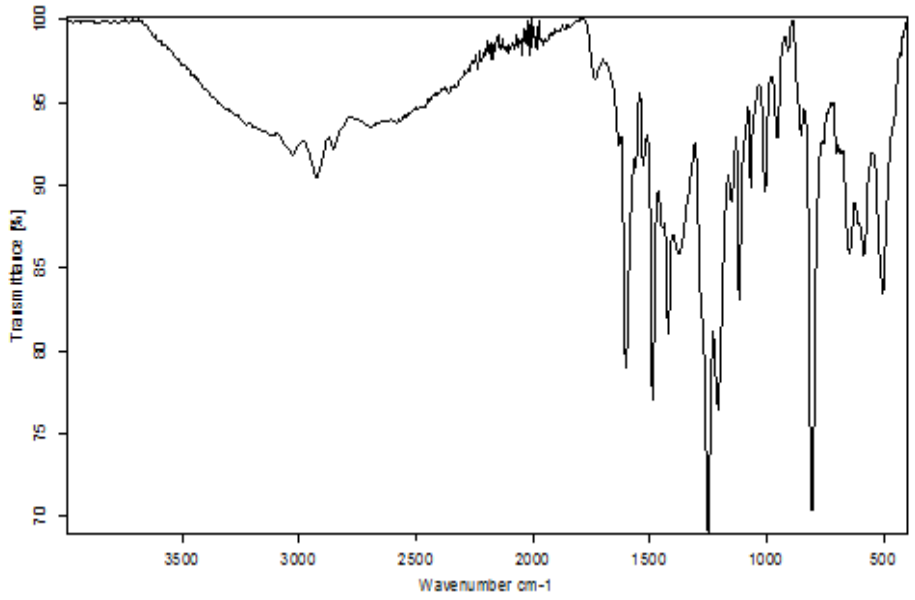

IR (ATR)

CPP1

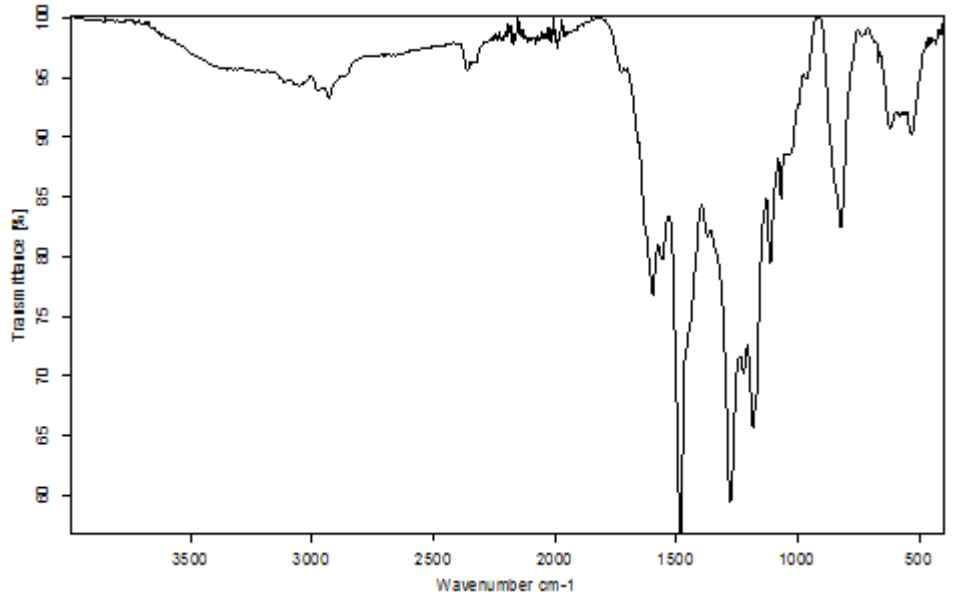

IR (ATR)

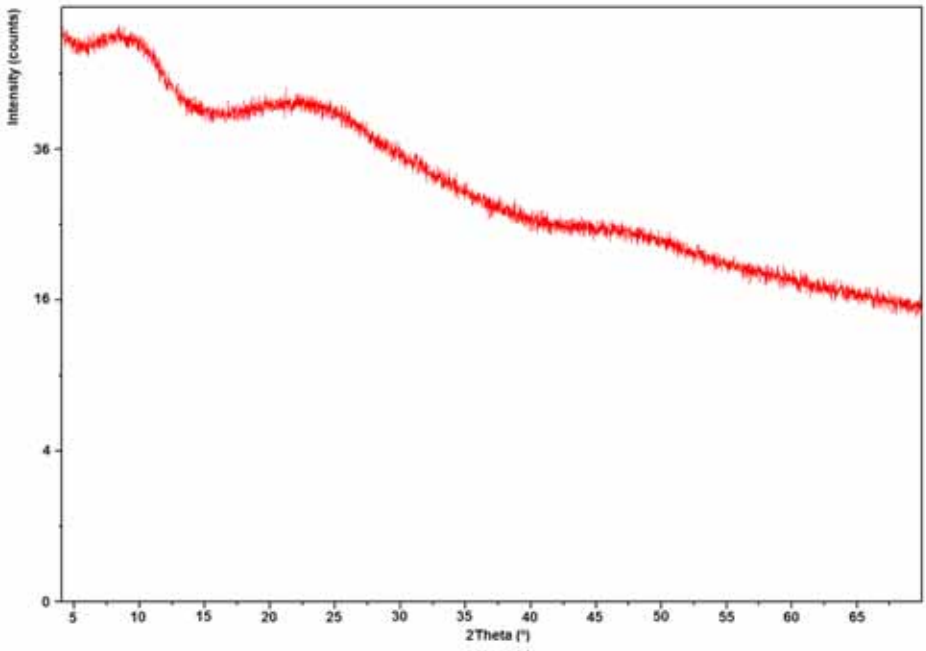

XRD (powder)

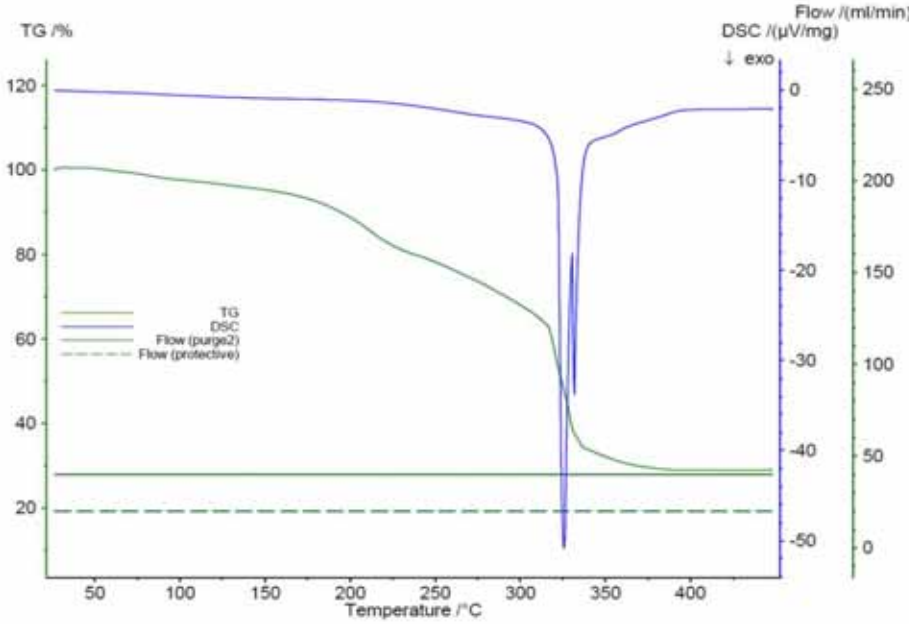

TGA / DSC

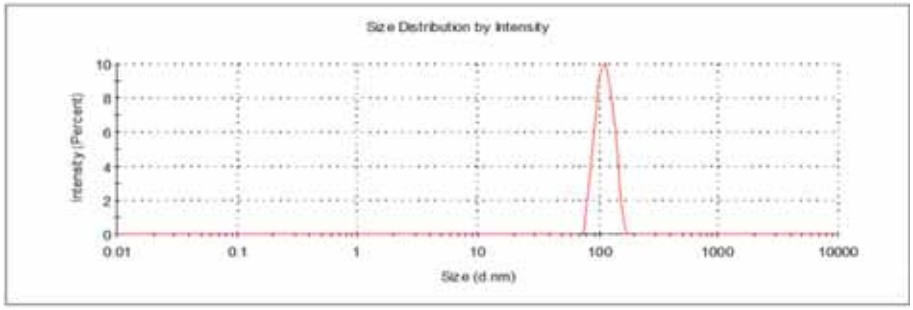
Size Distribution by Intensity
Intensity (Percent)
10
8
6
4
2
0
0.01
0.1
1
10
100
1000
10000
Size (d.nm)

DLS